بسم الله الرحمن الرحیم

مجموعه مقالات

سومین همایش بین‌المللی و پنجمین همایش ملی

ریاضیات زیستی

دانشگاه تبریز

۳ و ۴ مرداد ماه ۱۴۰۳

همایش ریاضیات زیستی

University of Tabriz

انجمن ریاضی ایران

ISC

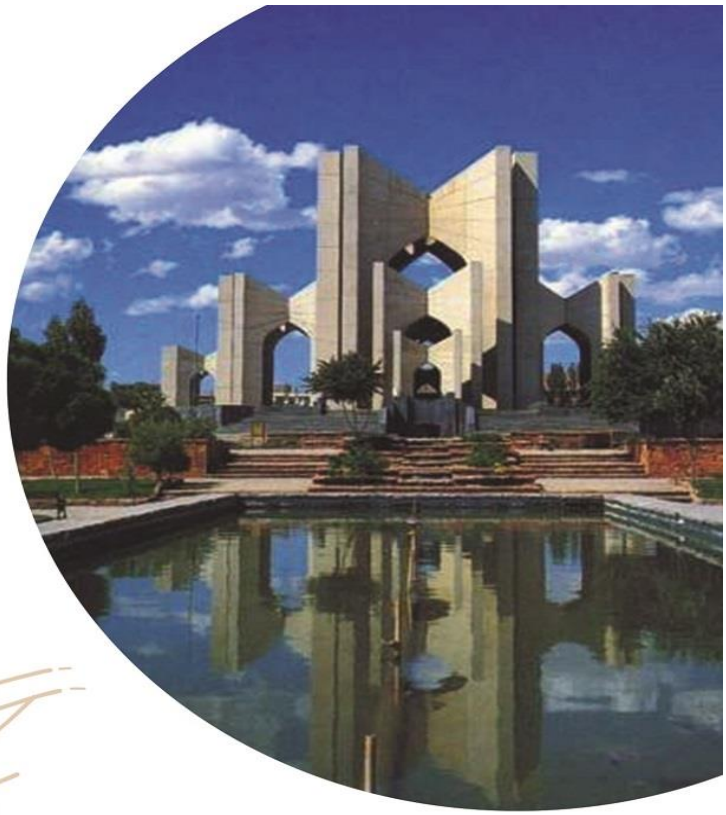

The 3rd International and 5th National Conference on

BIOMATHEMATICS

July 24-25 , 2024 | University of Tabriz

http:\\biomath3.tabrizu.ac.ir

سومین همایش بین المللی و پنجمین همایش ملی ریاضیات زیستی ۳ و ۴ مرداد ماه ۱۴۰۳

دانشگاه تبریز _ دانشکده ریاضی، آمار و علوم کامپیوتر

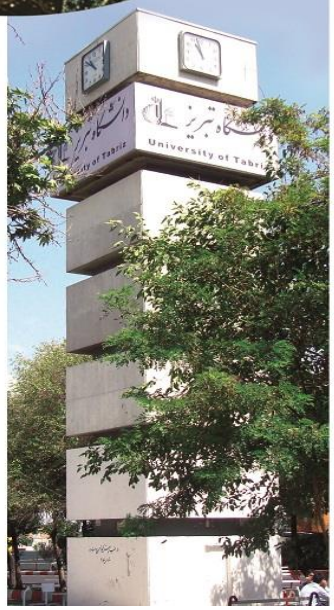

Invited Speakers:

- Dr. Saeed Ranjbar: Maastricht University of Medical center at the Netherlands
- Dr. Mohammadhosein Roozbehani: Iran University of Science & Technology
- Dr. Gholamreza Rokni : University of Tehran

Topics:

- Mathematical Modelling in Biological and Medical Sciences
- Biomathematics
- Biophysics
- Biostatistics
- Bioinformatics
- Optimal Control in the Biosciences
- Computational Methods in Biosciences Models
- Bioenvironmental
- Machine learning and applications in medical and biological sciences

Contact Information:

Faculty of Mathematics, Statistics and Computer Sciense
University of Tabriz, Tabriz, Iran

biomath3@tabrizu.ac.ir / www.biomath3.tabrizu.ac.ir
+98 41 33392893 / +98 41 33392890

مقدمه

همایش ریاضیات زیستی هر دو سال یک بار تحت حمایت انجمن ریاضی ایران در یکی از دانشگاه‌های معتبر ایران برگزار می‌شود. سومین همایش بین المللی و پنجمین همایش ملی ریاضیات زیستی در تاریخ سوم و چهارم مرداد ماه ۱۴۰۳ در دانشگاه تبریز برگزار گردید. نخستین همایش ملی از این رده در سال ۱۳۹۷ در دانشگاه نیشابور، دومین همایش ملی در سال ۱۳۹۹ در دانشگاه تبریز، اولین همایش بین المللی و سومین همایش ملی در سال ۱۴۰۰ در دانشگاه سمنان و دومین همایش بین المللی و چهارمین همایش ملی در سال ۱۴۰۱ در دانشگاه مازندران برگزار شد.

در این همایش پژوهشگران داخلی و خارجی در محورهای همایش، آخرین دست آوردهای خویش را ارائه و در مورد آنها بین شرکت کننده‌ها تبادل نظر صورت می‌گیرد. از نتایج مطالب ارائه شده می‌توان در مدل بندی بیماری‌های عفونی، غیر عفونی و سایر زمینه‌های ریاضیات زیستی استفاده نمود. کنترل کننده‌های گوناگونی را روی مدل می‌توان پیاده نموده و تأثیر گذاری آن‌ها را پیش از اعمال واقعی در جامعه مشاهده نمود.

در ادامه، با توجه به ضرورت تاسیس انجمن ریاضی زیستی و تأثیر آن در بین رشته‌ای شدن ریاضیات زیستی، بیش از ۴۵ مقاله به صورت سخنرانی حضوری و مجازی به دبیرخانه همایش ارسال گردید که اساتید و محققان حاضر در این همایش دو روزه، به ارائه‌ی مقالات و آخرین تحقیقات و دستاوردهای خود در حوزه ریاضیات زیستی پرداختند. لازم است مراتب قدردانی و سپاس خود را از هیأت رئیسه محترم دانشگاه تبریز، دانشکده ریاضی، آمار و علوم کامپیوتر و اساتید، محققان و دانشجویان که ما را در برگزاری این همایش همیاری و همکاری کردند، ابراز نماییم.

در خاتمه، برای حضار بزرگوار، میهمانان گرامی و دست اندرکاران عزیز سومین همایش بین المللی و پنجمین همایش ملی ریاضیات زیستی همواره آرزوی سلامتی و موفقیت روزافزون داریم.

با احترام

دبیر علمی و اجرائی همایش

دکتر حسین خیری

کمیته علمی همایش

دکتر حسین خیری	دانشگاه تبریز
دکتر سید حمید رضا مراثی	دانشگاه تبریز
دکتر علی اصغر جدیری اکبرفام	دانشگاه تبریز
دکتر کریم ایواز	دانشگاه تبریز
دکتر غلامرضا حجتی	دانشگاه تبریز
دکتر صداقت شهمراد	دانشگاه تبریز
دکتر فریبا بهرامی	دانشگاه تبریز
دکتر محمد جاویدی	دانشگاه تبریز
دکتر قدرت عبادی	دانشگاه تبریز
دکتر مهرداد لکستانی	دانشگاه تبریز
دکتر رباب علیخانی	دانشگاه تبریز
دکتر جعفر رزم آرا	دانشگاه تبریز
دکتر علی عبدی	دانشگاه تبریز
دکتر صفر ایراندوست	دانشگاه تبریز
دکتر حبیب ایزدخواه	دانشگاه تبریز
Dr. Ahmet Yildirim	Ege University of Izmir-Turkey
Dr. Mohammad kohandel	University of Waterloo-Canada
Dr. Soheil Rastgou talemi	Harvard Medical School
Dr. Shireen Jawad	University of Baghdad

کمیته علمی همایش

Dr. Subhas Khajanchi	Presidency University Kolkata of India
Cemil Tunc	Van Yuzuncu Yil University
Dr. Saeed Ranjbar	Maastricht University of Medical Center at the Netherlands
دکتر حمیدرضا ظهوری زنگنه	دانشگاه صنعتی اصفهان
دکتر رضا مزروعی سبدانی	دانشگاه صنعتی اصفهان
دکتر رسول عاشقی	دانشگاه صنعتی اصفهان
دکتر سهراب عفتی	دانشگاه فردوسی مشهد
دکتر اله بخش یزدانی	دانشگاه مازندران
دکتر غلامرضا رکنی	دانشگاه تهران
دکتر عزیزه جباری	دانشگاه فنی مهندسی مرند، دانشگاه تبریز
دکتر حسین متولی	دانشکده فیزیک
دکتر بهروز نقیلی	دانشگاه علوم پزشکی تبریز
دکتر فریبرز رحیمی	دانشگاه بناب
دکتر محمد حسین رحمانی دوست	دانشگاه نیشابور
دکتر کاظم قنبری	دانشگاه صنعتی سهند
دکتر محمد جهانشاهی	دانشگاه شهید مدنی
دکتر قربانعلی حقیقت دوست	دانشگاه شهید مدنی
دکتر احمدرضا حقیقی	دانشگاه علامه طباطبایی
دکتر ایلدار صادقی	دانشگاه صنعتی سهند

کمیته علمی همایش

دکتر وحید رومی	دانشگاه شهید مدنی
دکتر بشیر نادری	دانشگاه پیام نور واحد تبریز
دکتر عقیله حیدری	دانشگاه پیام نور واحد تبریز
دکتر آرزوی رضایی	دانشگاه دامغان
دکتر حسین روزبهانی	دانشگاه علم و صنعت
دکتر رضا دهقان	دانشگاه علوم پزشکی تهران
دکتر حسین پوربشاش	دانشگاه گرمسار
دکتر رضا خوش سیر	دانشگاه شهرکرد
دکتر توحید کسبی	دانشگاه امام حسین

کمیته اجرایی همایش

دکتر جلال شیری	معاون پژوهش و فناوری دانشگاه تبریز
دکتر سید حمید رضا مراثی	رئیس دانشکده ریاضی، آمار و علوم کامپیوتر
دکتر غلامرضا حجتی	معاون آموزشی و تحصیلات تکمیلی دانشگاه
دکتر حسین خیری	دبیر همایش
دکتر علیرضا مددی	عضو هیأت اجرایی همایش
دکتر صفر ایراندوست	عضو هیأت اجرایی همایش
دکتر عزیزه جباری	عضو هیأت اجرایی همایش
دکتر مرتضی فغفوری	عضو هیأت اجرایی همایش
دکتر آرزوی رضایی	عضو هیأت اجرایی همایش
دکتر حسین روزبهانی	عضو هیأت اجرایی همایش
دکتر جواد وکیلی	عضو هیأت اجرایی همایش
آقای هادی خیری	عضو هیأت اجرایی همایش
آقای یونس یوسف پور	عضو هیأت اجرایی همایش
خانم معصومه امیری	عضو هیأت اجرایی همایش
آقای مهرداد انواری	عضو هیأت اجرایی همایش
خانم معصومه امیری	مسئول تهیه و تنظیم کتابچه (مجموعه مقالات) همایش

جدول زمان‌بندی برنامه های سومین همایش بین‌المللی و پنجمین همایش ملی ریاضیات زیستی		
چهارشنبه ۳ مرداد ۱۴۰۳		دانشکده ریاضی، آمار و علوم کامپیوتر
۷:۰۰-۱۰:۴۰	پذیرش در دانشکده ریاضی، آمار و علوم کامپیوتر	
۸:۳۰-۹:۰۰	افتتاحیه	
۹:۰۰-۱۰:۰۰	سخنرانی عمومی (دکتر سعید رنجبر)	
۱۰:۰۰-۱۰:۳۰	پذیرایی	
۱۰:۴۰-۱۲:۴۰	سخنرانی‌های تخصصی	
۱۲:۴۰-۱۶:۰۰	نماز و نهار	
۱۶:۰۰-۱۷:۰۰	سخنرانی‌های تخصصی	
۱۷:۰۰-۱۷:۳۰	پذیرایی	
۱۷:۳۰-۱۸:۳۰	سخنرانی عمومی (دکتر غلامرضا رکنی)	
از ساعت ۱۸:۳۰	تبریزگردی و شام ویژه	
پنجشنبه ۴ مرداد ۱۴۰۳		
۹:۰۰-۱۰:۰۰	سخنرانی عمومی (دکتر محمدحسین روزبهانی)	
۱۰:۰۰-۱۰:۳۰	پذیرایی	
۱۰:۴۰-۱۲:۴۰	سخنرانی‌های تخصصی	
افتتاحیه‌ی همایش و تمامی سخنرانی‌های کلیدی در اتاق سمینار دانشکده ریاضی، آمار و علوم کامپیوتر و سخنرانی‌های تخصصی در کلاس‌های مشخص شده برگزار می‌شوند.		

برنامه زمان‌بندی روز اول سمینار (چهارشنبه ۳ مرداد ۱۴۰۳)	
پذیرش در دانشکده ریاضی، آمار و علوم کامپیوتر	۷:۳۰-۱۰:۴۰
افتتاحیه (اتاق سمینار دانشکده ریاضی، آمار و علوم کامپیوتر)	۸:۳۰-۹:۰۰
سخنرانی عمومی (دکتر سعید رنجبر)	۹:۰۰-۱۰:۰۰
پذیرایی	۱۰:۰۰-۱۰:۳۰

سخنرانی‌های تخصصی

مکان ارائه	زمان	کد مقاله	عنوان سخنرانی	سخنران
کلاس A	۱۰:۴۰-۱۱:۰۰	۹۰۰۱۰۴	Application of Skewed Logistic Modeling for Comparison of Traditional and Novel Anthropometric Indices in Discriminating Diabetes: Results of 5-year Follow up Azar Cohort Study	ندا گیلانی
	۱۱:۰۰-۱۱:۲۰	۵۳۰۰۵۹	مدل یادگیری عمیق در تشخیص رتینوپاتی دیابتی	کوثر تارویردیزاده
	۱۱:۲۰-۱۱:۴۰	۵۱۰۰۳۴	تولید مولکول‌های دارویی با استفاده از یادگیری عمیق	ساناز هاشمی‌پور
	۱۱:۴۰-۱۲:۰۰	۷۵۰۰۸۷	رویکرد انتخاب ژن جدید برای بیماری آلزایمر	حامد خیاط عجمی
	۱۲:۰۰-۱۲:۲۰	۴۷۰۰۲۵	مدل سازی و پیش بینی وضعیت جوی از روی داده های ماهواره ایی با استفاده از شبکه های عصبی مصنوعی	غلامرضا زکی
	۱۲:۲۰-۱۲:۴۰	۵۳۰۰۹۴	رادیومیکس: تبدیل تصاویر پزشکی به داده های کمی جهت بهبود تشخیص و درمان	کوثر تارویردیزاده
کلاس B	۱۰:۴۰-۱۱:۰۰		The effect of psychological scare on the dynamics of the tumor-immune interaction	شیرین جواد
	۱۱:۰۰-۱۱:۲۰	۷۱۰۰۸۰	شبیه‌سازی پویایی درمان دارویی ضد ویروسی در شیوع کووید-19 با استفاده از روش موضعی گلرکین بدون شبکه	پوریا عصاری
	۱۱:۲۰-۱۱:۴۰	۶۸۰۰۷۵	تأثیر انشعاب به عقب در مدل سل	عزیزه جباری
	۱۱:۴۰-۱۲:۰۰	۵۷۰۰۴۶	شبیه سازی رفتار تهاجم سلول های سرطانی به بافت اطراف با استفاده از روش پتروف-گالرکین محلی بدون شبکه مستقیم	علی ابراهیمی جهان
	۱۲:۰۰-۱۲:۲۰	۲۰۰۰۲۷	دینامیک سراسری مدل توسعه یافته عفونت ویروسی با دو نوع انتقال، نرخ بهبودی، سلول های عفونی نهفته ایمنی هومورال و ایمنی سلولی	توحید کسبی
	۱۲:۲۰-۱۲:۴۰	۷۱۰۱۰۳	Local radial basis functions to the numerical solution of Volterra integral equations with delay argument	پوریا عصاری
کلاس C	۱۰:۴۰-۱۱:۰۰	۳۰۰۰۱۷	مدل سازي رياضي جريان خون پالسی در رگ با گرفتگی مخروطی	احمد رضا حقیقی
	۱۱:۰۰-۱۱:۲۰	۵۵۰۰۴۰	فیدبک داده های واقعی برای کنترل رفتار تیروئید	آرتا جمشیدی
	۱۱:۲۰-۱۱:۴۰	۳۵۰۰۶۲	الگوریتم یادگیری ماشین برای حل عددی مدل بیماری اپیدمیولوژی	سیما نراقی
	۱۱:۴۰-۱۲:۰۰	۶۷۰۰۷۳	تحلیل قانون و تاثیرات اجتماعی آن بر مدل ریاضی شیوع و کنترل بیماری های واگیر: جنبه های پیچیده مرتبط با پردازش اطلاعات	روزبه آقائی بیک
	۱۲:۰۰-۱۲:۲۰	۲۴۰۰۰۹	مدل سازی آماری داده ها بر اساس آمار توصیفی	مهدی مهدی زاده
	۱۲:۲۰-۱۲:۴۰	۶۱۰۰۴۱	تحلیل انشعاب یک مدل بیماری عفونی با تاخیر	الهه رفیعیان
نماز و نهار				۱۲:۴۰-۱۶:۰۰

سخنرانی‌های تخصصی				
مکان ارائه	زمان	کد مقاله	عنوان سخنرانی	سخنران
کلاس A	۱۶:۰۰–۱۶:۲۰	۴۷۰۱۰۱	Pretreatment of Food Industry Wastewater by Coagulation: Process Modeling and Optimization using by artificial intelligence	غلامرضا زکی
	۱۶:۲۰–۱۶:۴۰	۷۵۰۰۹۱	مدل یادگیری ماشین برای طبقه بندی واریانت های missense ژن BRCA1	حامد خیاط عجمی
	۱۶:۴۰–۱۷:۰۰	۵۸۰۰۳۹	اصلاح قوانین یادگیری سیناپسی در شبکه‌های عصبی اسپایکی الهام گرفته از زیست	فاطمه توانگریان
	۱۷:۳۰–۱۷:۵۰	۴۰۰۳۷	بررسي مدلسازي اپيدمي	آیناز دربای
کلاس B	۱۶:۰۰–۱۶:۲۰	۲۰۰۰۲۴	مدل SEAICR برای کووید-۱۹ با مشتق کاپوتو	بهنام محمدعلئی
	۱۶:۲۰–۱۶:۴۰	۶۰۰۰۴۸	شبیه سازی عددی مدل رشد تومور توسط روش تفاضلات متناهی حافظ بقا	مهدیه سادات فضایل
	۱۶:۴۰–۱۷:۰۰	۱۴۰۰۶۱	دینامیک عملکرد بطن چپ قلب	محدثه ابراهیمی
کلاس C	۱۶:۰۰–۱۶:۲۰	۳۰۰۰۲۹	Effect Of Magnetic, Body Acceleration, And Time Dependency On The Blood Flow with its Application to Diseased Blood	احمدرضا حقیقی
	۱۶:۲۰–۱۶:۴۰	۲۹۰۰۰۸	دینامیک بیماری های عفونی: بررسی انشعاب ها در یک مدل اپیدمی SIR زمان گسسته با رشد لجستیک	زهره اسکندری
	۱۶:۴۰–۱۷:۰۰	۴۰۰۰۱۸	تقریب عددی بر اساس چندجمله ای های برنولی برای حل عفونت HIV مدل سلولی CD4+T	حمیده عبدالهی
۱۷:۰۰–۱۷:۳۰	پذیرایی			
۱۷:۳۰–۱۸:۳۰	سخنرانی عمومی (دکتر غلامرضا رکنی)			
از ساعت ۱۸:۳۰	تبریزگردی و ضیافت شام			

برنامه زمان‌بندی روز دوم سمینار (پنجشنبه ۴ مرداد ۱۴۰۳)	
۹:۰۰-۱۰:۰۰	سخنرانی عمومی (دکتر محمدحسین روزبهانی)
۱۰:۰۰-۱۰:۳۰	پذیرایی

سخنرانی‌های تخصصی

مکان ارائه	زمان	کد مقاله	عنوان سخنرانی	سخنران
کلاس A	۱۰:۴۰-۱۱:۰۰	۴۴۰۰۲۲	بررسی انتشار آلاینده ناشی از نیروگاه حرارتی و گازی تبریز و آسیب های جبران ناپذیر آن	قادر درخوشی
	۱۱:۰۰-۱۱:۲۰	۶۵۰۰۷۹	یک مدل شکار -شکارچی با عفونت در شکار	مهناز عابدینی
	۱۱:۲۰-۱۱:۴۰	۷۸۰۰۸۹	الگوریتمی جدید برای حل مسائل شبه تعادل در فضای آدامار	مهدیه شاکر سار
	۱۱:۴۰-۱۲:۰۰	۹۰۰۳۲	مدل دینامیکی یک تومور سرطانی	زهرا حسن زاده
	۱۲:۰۰-۱۲:۲۰	۱۳۰۰۶۴	مدل ریاضی بیماری ریوی فیبروز کیستسیک و جریان هوا در ریه	فاطمه حسن زاده
	۱۲:۲۰-۱۲:۴۰	۳۶۰۰۱۴	بررسی روند انتشار بیماری با استفاده از شبکه‌های چندلایه	هاله عشّاقی
کلاس B	۱۰:۴۰-۱۱:۰۰	۴۸۰۰۲۶	بررسی اهمیت روش های مقابله ای در پیش بینی سلامت روان با استفاده از مدل جنگل تصادفی	عباس پاک
	۱۱:۰۰-۱۱:۲۰	۶۴۰۰۷۸	Find New Hypergraph for Polynomials Modeling	مرضیه مرادی دالینی
	۱۱:۲۰-۱۱:۴۰	۳۹۰۰۱۹	حل عددی مدل کسری COVID-19 با استفاده از روش تکرار کسری لژاندر-پیکارد	سهیلا انصاری
	۱۱:۴۰-۱۲:۰۰	۲۸۰۰۰۷	Modeling the Dynamics of Cancer Stem Cells Using Nonlinear Integro-Differential Equations	سعیده محمدی
	۱۲:۰۰-۱۲:۲۰	۶۳۰۰۶۰	بررسی آموزش مدلسازی ریاضی و ایجاد ارتباط بین علوم ریاضی و زندگی روزمره بر پیشرفت تحصیلی ریاضی دانش آموزان	فاطمه یوسف زاده
کلاس C	۱۰:۴۰-۱۱:۰۰	۲۲۰۰۰۴	بهینه‌سازی وضعیت و تقریب هم وضعیت مسائل کنترل بهینه کسری به روش شبه طیفی با استفاده چند جمله های مونتز برای درمان سرطان	حسین قاسمی
	۱۱:۰۰-۱۱:۲۰	۵۰۰۰۳۵	ریاضیات زیستی:مدلسازی جمعیت در حال توسعه مقاومت دارویی	لیلا علیزاده
	۱۱:۲۰-۱۱:۴۰	۲۶۰۰۳۸	نمونه هایی از مدل سازی ریاضی در درمان سرطان	مریم مسعودی آرانی
	۱۱:۴۰-۱۲:۰۰	۴۱۰۰۱۵	Study on the behavior and control of a chaotic HIV-1 system	مرضیه پابسته
	۱۲:۰۰-۱۲:۲۰	۷۰۰۰۸۱	ارتباط بین مصرف کانابیس و وضعیت ویتامین D سرم: انالیز و تحلیل داده‌های National Health and Nutrition Examination Survey در سال‌های ۲۰۰۹-۲۰۱۸	سید احسان موسوی

برنامه ارائه پوسترها

زمان	کد مقاله	عنوان مقاله	ارائه کننده
پنجشنبه، ۴ مرداد ۱۴۰۳، از ساعت ۱۰ الی ۱۰:۳۰	۴۹۰۰۴۳	تحلیل داده هاي تابعي با استفاده شبکه هاي عصبي (پوستر)	سیده اوین قیصري
	۷۰۰۸۳	شناسایی رفتار دینامیکی داده‌های رشد-مهار بیماری به‌وسیله‌ی ابزار یادگیری ماشین	یونس یوسف پور

پایان همایش

Contents English Papers

Public lectures ……1

Numerical Approximation based on The Bernoulli Polynomials for Solving HIV infection of CD4+T cells model ……..2

Hamideh Abdollahi Lashaki

A prey-predator model with infection in prey ……..7

Mahnaz Abedini

An analysis of legal and social issues affecting mathematical models of disease control; some complex features of information processing ……12

Roozbeh Aghaieebeiklavasani

The Biomathematics, modelling of populations developing drugs resistance ……..17

Leila Alizadeh

Numerical Solution of a Fractional COVID-19 Model Using the Fractional Legendre-Picard Iteration Method ……21

Soheyla Ansari

Local radial basis functions to the numerical solution of Volterra integral equations with delay argument ……...26

Pouria Assari

Simulation of Antiviral Drug Treatment Dynamics on COVID-19 Spread Using the Local Meshless Galerkin Method ……31

Pouria Assari

Survey To Epidemic Modeling ……..35

Aynaz Darbay

Simulation of thebehavior of cancer cell invasion of surrounding tissue using direct mesh-less local Petrov-Galerkin method ……39

Ali Ebrahimijahan

Dynamics of Infectious Diseases: Exploring Bifurcations in a Discrete-Time SIR Epidemic Model with Logistic Growth ……44

Zohre Eskandari

Numerical simulation of tumor growth model by the conservative finite difference method

Mahdiehalsadat Fazayel ……...……...49

Trajectory optimization and costate estimation of fractional optimal control problems via a M¨untz pseudospectral method: application in cancer treatment ……54

Hussein Ghassemi

Application of Skewed Logistic Modeling for Comparison of Traditional and Novel Anthropometric Indices in Discriminating Diabetes ……59

Neda Gilani

Effect Of Magnetic, Body Acceleration, And Time Dependency On The Blood Flow with its Application to Diseased Blood ……64

Ahmad Reza Haghighi

Mathematical model of cystic fibrosis pulmonary disease and air flow in the lung …….69

Fatemeh Hasanzadeh

Dynamic Behaviour of a Cancer Tumor ……74

Zahra Hasanzadeh

Generating pharmaceutical molecules using deep Learning ……..78

Sanaz Hashemipour

Modeling and forecasting of rainfall from satellite data using radial base and generalized regression neural networks ……83

Nahideh Hossein Babazadeh

Influence of Backward Bifurcation in a Model of Tuberculosis ……87

Azizeh Jabbari

Real Data Feedback to Control Thyroid Behavior ……92

Arta Jamshidi

Global dynamic of generalized viral infection model with two transmission mode, cure rate, latently infected cells, cellular immunity and humoral immunity ……..96

Tohid Kasbi Gharahasanlou

Machine learning model for classifying BRCA1 missense variants ……101

Hamed Khayyateh Ajami

A new gene selection approach for Alzheimer's disease ……..106

Hamed Khayyateh Ajami

SEAICR model for Covid-19 via Caputo derivative ……110

Behnam Mohammadaliee

Modeling the Dynamics of Cancer Stem Cells Using Nonlinear Integro-Differential Equations ……..115

Saeedeh Mohammadi

Find New Hypergraph for Polynomials Modeling ……...120

Marzieh Moradi Daleni

Machine learning algorithm for the numerical solution of the epidemiological disease model ……125

Sima Naraghi

Study on the behavior and control of a chaotic HIV-1 system ……130

Marzieh Pabasteh

Investigating the importance of coping strategies in predicting mental well-being by using random forest model ……134

Abbas Pak

Bifurcation Analysis of Infectious Disease Model with Delay ……139

Khayyam Salehi

A novel method for solving quasi-equilibrium problems in Hadamard space ……....143

Mahdiyeh Shaker Sar

Radiomics: Transforming Medical Imaging into Quantitative Data for Enhanced Diagnosis and Treatment ……..……147

Kosar Tarvirdizade

Deep Learning Model to Diagnose Diabetic Retinopathy ……...151

Kosar Tarvirdizade

A modification of synaptic learning rules in bio-inspired spiking neural networks …….155

Fatemeh Tavangarian

Pretreatment of Food Industry Wastewater by Coagulation: Process Modeling and Optimization using by artificial intelligence ……160

GholamReza Zaki

فهرست مقالات فارسی

دینامیک عملکرد بطن چپ قلب ۱۶۶
محدثه ابراهیمی

مدل سازی ریاضی جریان خون پالسی در رگ با گرفتگی مخروطی ۱۷۰
احمدرضا حقیقی

بررسی انتشار آلاینده ناشی از نیروگاه حرارتی وگازی تبریز و آسیب های جبران ناپذیر آن ۱۷۵
قادر درخوشی

بررسی روند انتشار بیماری با استفاده از شبکه‌های چندلایه ۱۷۹
هاله عشّاقی

تحلیل داده‌های تابعی با استفاده شبکه های عصبی ۱۸۴
سیده اوین قصری

نمونه‌هایی از مدل سازی ریاضی در درمان سرطان ۱۸۸
مریم مسعودی آرانی

مدل سازی آماری داده‌ها براساس آمار توصیفی ۱۹۲
مهدی مهدی زاده

شناسایی رفتاردینامیکی داده های رشد - مهاربیماری به وسیله ی ابزار یادگیری ماشین..... ۱۹۶
یونس یوسف پور

بررسی آموزش مدلسازی ریاضی و ایجاد ارتباط بین علوم ریاضی و زندگی روزمره بر پیشرفت تحصیلی ریاضی دانش آموزان ۲۰۰
فاطمه یوسف زاده درزی

سخنرانی‌های عمومی

دکتر سعید رنجبر

Dr. saeed Ranjbar

Maastricht university of Medical center at the Netherlands

عنوان سخنرانی:

How one can make a bridge from advanced mathematics to medical science?

دکتر غلامرضا رکنی

Dr. Gholamreza Rokni

عضو هیأت علمی دانشگاه تهران

عنوان سخنرانی:

Theoretical Biology: Mathematical and Relational

دکتر محمد حسین روزبهانی

Dr. Mohammadhossein Roozbehani

عضو هیات علمی دانشگاه علم و صنعت ایران

عنوان سخنرانی:

از مدلسازی ریاضی تا هوش مصنوعی در دوقلوهای دیجیتال سلامت و پزشکی

Numerical Approximation based on The Bernoulli Polynomials for Solving HIV infection of CD4+T cells model

Hamideh Abdollahi Lashaki[1]
Department of Mathematics, Faculty of Mathematical Sciences, Farhangian University, Mazandaran, Iran.

Mojgan Akbari
Department of Mathematics, Faculty of Mathematical Sciences,University of Guilan, P.O.Box 1914, Rasht, Iran

Abstract

In this article, an applied matrix method, which is based on Bernouli Polynomials has been presented to find approximate solutions of the mathematical model describing HIV infection of CD4+T cells. The proposed approach is validated through numerical experiments and compared with existing methods to demonstrate its efficacy and computational efficiency.

Keywords: Bernoulli polynomials, Approximation, HIV infection model
Mathematics Subject Classification [2010]: 65R20, 65R99

1 Introduction

The Human Immunodeficiency Virus (HIV) remains a significant global health challenge, with millions of individuals affected worldwide. Understanding the dynamics of HIV infection within the immune system is crucial for developing effective treatment strategies. Mathematical models play a vital role in elucidating the complex interactions between the virus and immune cells. Consider the HIV infection model of CD4+ T cells, characterized by a system of nonlinear ordinary differential equations (ODEs) of the following form[5]

$$\begin{aligned}\frac{dT}{dx} &= p - \alpha T + rT(1 - \frac{T+I}{T_{max}}) - kVT \\ \frac{dI}{dx} &= kVT - \beta I \\ \frac{dV}{dx} &= N\beta I - \gamma V \end{aligned} \tag{1}$$

With physical conditions $I(0) = 0, T(0) = 0.1, andV(0) = 0.1$, T(x) represents the concentration of susceptible CD4+ T cells, I(x) represents CD4+T cells infected by the HIV viruses, and V(x) is free HIV particles in the blood. α, β, and γ reflects natural turnover rates of uninfected CD4+T cells, infected CD4+T cells, and virus particles, respectively, $(1 - \frac{T+I}{T_{max}})$ denotes the logistic development of the healthy CD4+T cells. k is the positive real number representing the infection rate; kVT describes HIV infection of healthy CD4+ T cells. The maximum CD4+T cells in the body are denoted by T_{max}. Here, we set values for each parameter as follows, $p = 0.1, \alpha = 0.02, \beta = 0.3, r = 3, \gamma = 2.4, k = 0.0027, T_{max} = 1500, N = 9$. Since, last decade, several numerical approaches were utilized to solve the HIV infection model of CD4+T cells. For instance, the Bessel collocation method [8], Differential transform technique [10], Multistep differential transform method [3], Homotopy perturbation technique [2] ,Modified Bernoulli wavelets [5] etc. Bernouli polynomials play a main role in a variety of expansions and approximation. We propose a numerical approximation method based on Bernoulli polynomials to solve the differential equations governing the dynamics of HIV infection.

[1]Speaker

1.1 Bernoulli Polynomials

The Bernouli polynomials of order m, are explained in [4] by

$$B_n(x) = \sum_{i=0}^{n} \binom{n}{i} \beta_i x^{n-i}, \tag{2}$$

where $\beta_i, i = 0, 1, ..., n$ are Bernouli numbers. These numbers are a sequence of signed rational numbers, which are obtained from the series extension of trigonometric functions and can be described by

$$\frac{t}{e^t - 1} = \sum_{j=0}^{\infty} \beta_j \frac{t^j}{j!}. \tag{3}$$

The first four Bernouli numbers are

$$\beta_0 = 1, \quad \beta_1 = \frac{-1}{2}, \quad \beta_2 = \frac{1}{6}, \quad \beta_4 = -\frac{1}{30},$$

with $\beta_{2i+1} = 0, \quad i = 1, 2, 3, \cdots$. The first four Bernouli Polynomials are

$$B_0(x) = 1, \quad B_1(x) = x - \frac{1}{2}, \quad B_2(x) = x^2 - x + \frac{1}{6}, \quad B_3(x) = x^3 - \frac{3}{2}x^2 + \frac{1}{2}x.$$

The subsequent features apply to Bernouli polynomials [6], [9]

$$B_n(0) = \beta_n, \quad n \geq 0, \tag{4}$$

$$\tag{5}$$

$$\int_a^x B_n(t)dt = \frac{B_{n+1}(x) - B_{n+1}(a)}{n+1}, \tag{6}$$

$$\tag{7}$$

$$\int_0^1 B_m(t)B_n(t)dt = (-1)^{m-1} \frac{n!m!}{(n+m)!}, \quad n, m \geq 1, \tag{8}$$

$$\tag{9}$$

and

$$\sum_{i=0}^{m} B_i(t) = (m+1)t^m. \tag{10}$$

It can be simply illustrated that any supposed polynomials of degree n can be extended with regard to linear combination of Bernouli polynomials as

$$p(x) = \sum_{k=0}^{m} c_k B_k(x) = C^T B(x),$$

where C and $B(x)$ are defined by

$$C = [c_0, c_1, ..., c_n]^T \tag{11}$$

and

$$B(x) = [B_0(x), B_1(x), ..., B_n(x)]^T, \tag{12}$$

where

$$B_k(x) = \binom{k}{k} B_k + \binom{k}{k-1} B_{k-1}x + ... + \binom{k}{1} B_1 x^{k-1} + \binom{k}{0} B_0 x^k.$$

where

$$B_k(x) = \binom{k}{k} B_k + \binom{k}{k-1} B_{k-1}x + ... + \binom{k}{1} B_1 x^{k-1} + \binom{k}{0} B_0 x^k,$$

for $k = 0, 1, ..., m$, therefore

$$B(x) = MT(x), \tag{13}$$

where

$$T = [1 \;\; x \;\; x^2 \;\; ...x^n], \tag{14}$$

and M is a lower triangular $(n+1) \times (n+1)$ matrix has the form

$$M = \begin{bmatrix} B_0 & 0 & 0 & 0 & 0 & \cdots & 0 \\ \binom{1}{1} B_1 & \binom{1}{0} B_0 & 0 & 0 & 0 & \cdots & 0 \\ \binom{2}{2} B_2 & \binom{2}{1} B_1 & \binom{2}{0} B_0 & 0 & 0 & \cdots & 0 \\ \binom{3}{3} B_3 & \binom{3}{2} B_2 & \binom{3}{1} B_1 & \binom{3}{0} B_0 & 0 & \cdots & 0 \\ \vdots & \vdots & \vdots & \ddots & \vdots & & \\ \binom{n}{n} B_n & \binom{n}{n-1} B_{n-1} & \binom{n}{n-2} B_{n-2} & \binom{n}{n-3} B_{n-3} & \cdots & \binom{n}{0} B_0 & \end{bmatrix}, \tag{15}$$

and $det(M) = 1$, then M is an invertible matrix. Using (14), we have

$$T(x) = M^{-1} B(x). \tag{16}$$

1.2 Approximation of functions

Suppose that $H = L^2[0,1]$ and $\{B_0(x), B_1(x), \cdots B_N(x)\} \subset H$, where $B_i(x)$' s are Bernoulli polynomials and

$$V = span\{B_0(x), B_1(x), \cdots B_N(x)\},$$

and f be an arbitrary member in H. Since V is a finite dimensional vector space, f has the unique best approximation $\hat{f} \in V$, that is

$$\forall v \in V, \quad \|f - \hat{f}\| \leq \|f - v\|.$$

Since $\hat{f} \in V$, then there exists the unique coefficients $f_0, f_1, \cdots f_N$ such that

$$f \approx \hat{f} = \sum_{n=0}^{N} f_n B_n(x) = F^T B(x), \quad F = [f_0, f_1, \cdots f_N]. \tag{17}$$

Theorem 1.1. *[7] For vector $B(t)$ defined in (13), the following formula is defined*

$$\int_0^x B(t)dt \simeq PB(x), \tag{18}$$

where P is the $(N+1)\times(N+1)$ operational matrix of integration, which is obtained from $P = UM^{-1}$, where

$$U = [U_1, U_2, ..., U_N, \Xi^T M]^T,$$

and

$$U_i = [0 \quad \frac{1}{i}\binom{i}{i-1}B_{i-1} \quad \frac{1}{i}\binom{i}{i-2}B_{i-2} \quad ... \quad \frac{1}{i}\binom{i}{1}B_1 \quad \frac{1}{i}B_0 \quad \underbrace{...}_{N-i}],$$

and $\Xi = [c_1, c_2, ..., c_N]^T$ which $\dfrac{B_{N+1}(x) - B_{N+1}(0)}{N+1} \simeq \Xi^T B(x)$, Ξ can be computed by (17).

The operational matrix of integration P is a sparse matrix, for example, for $N = 3$, we have

$$P = \begin{bmatrix} \frac{1}{2} & 1 & 0 & 0 \\ \frac{-1}{12} & 0 & \frac{1}{2} & 0 \\ 0 & 0 & 0 & \frac{1}{3} \\ \frac{1}{129} & 0 & \frac{-1}{14} & 0 \end{bmatrix}.$$

It is not difficult to see that the operation matrix P as N increases, becomes more sparse. This is one of the advantages of using Bernouli polynomials for solving equations.

2 Description of Bernouli matrix method

for solving the proposed HIV infection of D4+T cells model,first, we can approximate the unknown function $\frac{dT}{dx}, \frac{dI}{dx}, \frac{dV}{dx}$ by Bernouli matrix as

$$\frac{dT}{dx} = A^T B(x), \quad \frac{dI}{dx} = C^T B(x), \quad \frac{dV}{dx} = D^T B(x) \tag{19}$$

which A, C, D are the unknown vector. by using theorem (1-1) we have $T(x), I(x), V(x)$ based on operational matrix P, by replacing them in (**??**), we have

$$\begin{aligned} A^T B(x) &= p - \alpha A^T PB(x) + rA^T PB(x)(1 - \frac{A^T PB(x) + C^T PB(x)}{T_{max}}) \\ &\quad - kC^T PB(x)A^T PB(x) \\ A^T B(x) &= kC^T PB(x)A^T PB(x) - \beta C^T PB(x) \\ D^T B(x) &= N\beta\gamma D^T PB(x)D^T PB(x) \end{aligned} \tag{20}$$

Now we collocate (**??**) with the following grid points $t_i = \frac{2i-1}{2(N+1)}, \quad i = 1, \cdots, N+1$ then we have a system of nonlinear algebric equations, with unknown vector A, C, D, we can solve nonlinear system of equations with $fsolve$ function in matlab and approximate the $T(x), I(x), V(x)$.

3 Numerical Examples

Consider (**??**) With physical conditions $I(0) = 0$, $T(0) = 0.1$ and $V(0) = 0.1$, with the following values, $p = 0.1, \alpha = 0.02, \beta = 0.3, r = 3, \gamma = 2.4, k = 0.0027, T_{max} = 1500, N = 9$. The comparison between the

Table 1: Numerical comparison for $T(x), I(x), N(x)$ with different methods

	presented method	Bernoulli wavelet [5]	Haar wavelet [1]
T(x)	0.1000000000000	0.1000000000000	0.1000000000000
I(x)	0.0000000000000	0.0000000000000	0.0000000000000
V(x)	0.1000000000000	0.1000000000000	0.1000000000000

results of presented method for N = 4 and some other methods are shown in table1. The results obtained from this method show no significant different from those of other methods, but it boasts enhanced usability and notably reduced computational complexity compared to its counterparts.

References

[1] H. Alrabaiah, I. Ahmad, R. Amin, K.A. Shah, numerical method for fractional variable order pantograph differential equations based on Haar wavelet. Eng Comput, 38, 3 (2022), 2655–68.

[2] M. Ghoreishi, A. Ismail, A. K. Alomari, *Applications of the homotopy analysis method for solving a model of HIV infection of CD+ T cells* Math Comput Modelling, 54 (2011), 3007–15, Elsevier.

[3] A. Gokdogan, A. Yildirim, M. Merdana, Solving a fractional order model of HIV infection of CD+ T cells, Math Comput Modelling, 45 (2011), 2132–8, Elsevier.

[4] E. Kreyszig, Introductory Functional Analysis with Applications, John Wiley and Sons Press, New York (1978).

[5] S. Kumbinarasaiah, G. Manohara, *Modified Bernoulli wavelets functional matrix approach for the HIV infection of CD4+ T cells model*, Results in Control and Optimization 10 (2023) 1001–97.

[6] S. Mashayekhi, Y. Ordokhani, M. Razzaghi, Hybrid functions approach for nonlinear constrained optimal control problems, Commun. Nonli. Sci. Numer. Simul, 17 (2012), 1831–1843.

[7] J. A. Rad, S. Kazem, M. Shaban, K. Parand, *A new operational matrix based on Bernouli polynomials*, arXiv:1408.2207v1 [cs.NA] 2014.

[8] Y. Suayip. *A numerical approach to solve the model for HIV infection of CD+ T cells*, Appl Math Model, 36 (2012), 587–90, Elsevier.

[9] P. K. Sahu, B. Mallick, Approximate solution of fractional order Lane-Emden type differential equation by orthonormal Bernoulli's polynomials, Int J Appl Comput. Math, 5(2019), 1–9.

[10] V.K Srivastava,M. K. Awasthi, S. Kumar, *Numerical approximation for HIV infection of CD4+ T cells mathematical model*, Ain Shams Eng J 2014. Elsevier.

Email: `abdollahi`$_h l$*@yahoo.co.uk*
`Email: m_`*akbari@guilan.ac.ir*

A prey-predator model with infection in prey

Abedini Mahnaz[1]
Haghighatdoost Ghorbanali[2]
Kheiri Hossein [3]

Abstract

In this article, we study the behavior of a dynamic system that has one prey and one predator, so that one of the prey is diseases. Our goal is to find the equilibrium points and check the stability of the equilibrium points.

Keywords: Dynamical Systems, Equilibrium Points , Stability
AMS Mathematical Subject Classification [2010]: 13D45, 39B42

1 Introduction

Dynamic systems are used in ecology, they are defined by the interactions of species with each other and their environment, which determine population and community structure. Hunting is one of the most important interactions that affect the qualitative behavior of all species, for this reason, the predator and prey system is one of the most important topics in biological mathematics.
The simplest model for the problem of prey and predator was first presented by Lotka Volterra in 1926[1, 2]. After that, prey-predator models were widely considered. Since the biological population also suffers from various diseases and this disease plays a significant role in regulating the population size. Therefore, many scientists and mathematicians started working in this field, and it can be said that the effect of the epidemic or disease on hunting was first studied and investigated by Anderson and May in the reference[3, 4].
Other models were also introduced with disease, for example: study disease in prey [5]. Hunters only consume infected prey [6]. Predators avoid infected prey [7].It can be mentioned [8], where both prey and predator populations are affected by the disease. In this paper, we study a population model with one prey and one predator. The populations prey has two sub-classes: susceptible and infected. So our system has six equilibrium points, two of which are unstable and the rest are stable.

Definition 1.1. The point $\tilde{x} \in R^n$ is an equilibrium point for the differential equation

$$\frac{dx}{dt} = f(x)$$

if $f(\tilde{x}) = 0$ for all t.

[1]Speaker, Department of Mathematics, Azarbaijan Shahid Madani University
[2]Department of Mathematics, Azarbaijan Shahid Madani University
[3]Faculty of Mathematical Sciences, University of Tabriz

Definition 1.2. The equilibrium point q is said to be stable if given$\epsilon > 0$ there is a $\delta > 0$ such that $\|\phi(t,p) - q\| < 0$ for all $t > 0$ and for all p such that $\|p - q\| < \delta$. If δ can be chosen not only so that the solution q is stable but also so that $\phi(t,p) \longrightarrow q$ as $t \longrightarrow \infty$, then q is said to be asymptotically stable. If q is not stable it is said to be unstable.

2 Main results

In this paper, we study a population model with one prey and one predator. The populations prey has two sub-classes: susceptible and infected. At time T; let S(T) denote the density of the susceptible prey, and I(T) denote the density of the infected prey. The predator densities are denoted by X(T). Now we discuss the basic assumptions that we have made in formulating the model.
1. In the absence of predator population and with no disease, the prey population grows logistically with intrinsic growth rate r and environmental carrying capacity K(K > 0).
2. Susceptible prey gets infected in contact with infected prey.
3. By consuming infected prey, the hunter does not become infected.
According to the above assumptions, we have three nonlinear ordinary differential equations as follows:

$$\begin{aligned} \frac{dS}{dT} &= rS(1 - \frac{S+I}{K}) - bSI - cSX \\ \frac{dI}{dT} &= dI + bSI - eIX - fI \\ \frac{dX}{dT} &= -gX + cSX + eIX \end{aligned} \tag{1}$$

with the initial population

$$S(0) \geq 0, I(0) \geq 0, X(0) \geq 0. \tag{2}$$

Next, we obtain the equilibrium points of system(1), which has three disease-free equilibrium points and three endemic equilibrium points. Therefor three disease-free equilibrium points as follows:

$$E_1 = (0,0,0), \qquad E_2 = (k,0,0), \qquad E_3 = (\frac{g}{c}, 0, \frac{r(ck-g)}{c^2k}).$$

And three endemic equilibrium points as follows:

$$E_4 = (0, \frac{g}{e}, \frac{d-f}{e}), \qquad E_5 = (-\frac{d-f}{b}, \frac{r(bk+d-f)}{b(bk+r)}, 0) \qquad E_6 = (S^*, I^*, X^*)$$

Where

$$\begin{aligned} S^* &= \frac{bgk + cdk - cfk - ekr + gr}{r(c-e)} \\ I^* &= -\frac{bcgk + c^2dk - c^2fk - cekr + egr}{er(c-e)} \\ X^* &= \frac{b^2gk + bcdk - bcfk - bekr + bgr + cdr - cfr - der + efr}{er(c-e)} \end{aligned}$$

.

In the following, we check the stability of the equilibrium points using the Jacobian matrix.

2.1 Stability Analysis

The Jacobian matrix $J(S, I, X)$ of system (1) at any pont (S, I, X) is gvein by:

$$J(E_i) = \begin{pmatrix} A & -\frac{rS}{k} - bS & -cS \\ bI & bS - eX + d - f & -eI \\ cX & eX & cS + eI - g \end{pmatrix}, \tag{3}$$

where

$$A = r(1 - \frac{S+I}{k}) - \frac{rS}{k} - bI - cX.$$

The local asymptotic stability of each equilibrium point is studied by computing the Jacobian matrix and finding the eigenvalues evaluated at each equilibrium point. For stability of the equilibrium points, the real parts of the eigenvalues of the Jacobian matrix must be negative

Theorem 2.1. $E_1 = (0, 0, 0)$ *unstable.*

The Jacobian matrix at E_1 given by

$$J(E_1) = \begin{pmatrix} r & 0 & 0 \\ 0 & d - f & 0 \\ 0 & 0 & -g \end{pmatrix}$$

The corresponding eigenvalues are $r, d - f, -g$; since $r > 0$ then E_1 unstable.

The Jacobian matrix at E_2 becomes

$$J(E_2) = \begin{pmatrix} -r & bk - r & -ck \\ 0 & bk + d - f & 0 \\ 0 & 0 & ck - g \end{pmatrix}$$

The corresponding eigenvalues are $-r$, $ck - g$ and $bk + d - f$. Then we have the following theorem for E_2.

Theorem 2.2. $E_2 = (k, 0, 0)$ *is locally asymptotically stable if* $ck < g$, $bk + d < f$.

The corresponding eigenvalues at $E_3 = (\frac{g}{c}, 0, \frac{r(ck - g)}{c^2 k})$ are

$$\lambda_1 = \frac{-rg + \sqrt{-4c^2gk^2r + 4cg^2kr + g^2r^2}}{2ck}$$
$$\lambda_2 = -\frac{rg + \sqrt{-4c^2gk^2r + 4cg^2kr + g^2r^2}}{2ck}$$
$$\lambda_3 = \frac{bgck + dc^2k - fc^2k - cekr + egr}{c^2k}$$

Then we have the following theorem for E_3.

Theorem 2.3. $E_3 = (\frac{g}{c}, 0, \frac{r(ck - g)}{c^2 k})$ *is locally asymptically stable if*

$$-4c^2gk^2r + 4cg^2kr + g^2r^2 > 0$$
$$bgck + dc^2k - fc^2k - cekr + egr < 0.$$

The Jacobian matrix at $E_4 = (0, \frac{g}{e}, \dfrac{d-f}{e})$ given by

$$J(E_4) = \begin{pmatrix} r(1-\dfrac{g}{ek}) - \dfrac{bg}{e} - \dfrac{c(d-f)}{e} & 0 & 0 \\ \dfrac{bg}{e} & 0 & -g \\ \dfrac{c(d-f)}{e} & d-f & 0 \end{pmatrix}$$

The corresponding eigenvalues are

$$\lambda_1 = \sqrt{-dg+fg}, \quad \lambda_2 = -\sqrt{-dg+fg}, \quad \lambda_3 = -\frac{bgk+cdk-cfk-ekr+gr}{ek}.$$

Theorem 2.4. $E_4 = (0, \frac{g}{e}, \dfrac{d-f}{e})$ *unstable.*

The Jacobian matrix at $E_6 = (S^*, I^*, X^*)$ given by

$$J(E_6) = \begin{pmatrix} a_{11} & a_{12} & a_{13} \\ a_{21} & 0 & a_{23} \\ a_{31} & a_{32} & 0 \end{pmatrix}$$

where

$$\begin{aligned}
a_{11} &= (((-d+f)c - bg + er)k - gr)/((c-e)k) \\
a_{12} &= -(bk+r)((-er + (d-f)c + bg)k + gr)/((c-e)kr) \\
a_{13} &= -(k(d-f)c + (bg-er)k + gr)c/((c-e)r) \\
a_{21} &= -b(k(d-f)c^2 + (bg-er)kc + egr)/(er(c-e)) \\
a_{23} &= (k(d-f)c^2 + (bg-er)kc + egr)/((c-e)r) \\
a_{31} &= (((d-f)c + (-ek+g)b - e(d-f))r + b((d-f)c+bg)k)c/(er(c-e)) \\
a_{32} &= (((-ek+g)b + (d-f)(c-e))r + b((d-f)c+bg)k)/((c-e)r)
\end{aligned}$$

After simplifying, the characteristic equation of the Jacobian matrix $J(E_6)$ is as follows:

$$\lambda^3 - a_{11}\lambda^2 - (a_{12}a_{21} + a_{13}a_{31} + a_{23}a_{31})\lambda + a_{11}a_{23}a_{32} - a_{12}a_{23}a_{31} - a_{13}a_{21}a_{32} = 0$$

where

$$A_1 = -a_{11}, \quad A_2 = -a(_{12}a_{21} + a_{13}a_{31} + a_{23}a_{31}), \quad A_3 = a_{11}a_{23}a_{32} - a_{12}a_{23}a_{31} - a_{13}a_{21}a_{32} \tag{4}$$

By Routh-Hurwitz's criterion, the characteristic equation (4) has negative eigenvalues if,

$$A_1 > 0, \qquad A_3 > 0, \qquad A_1A_2 > A_3 \tag{5}$$

Then if condition(5) is satisfied, the equilibrium point E_6 is locally asymptotically stable.

Acknowledgment

The acknowledgements should be in a separate section at the end of the article before the references.

References

[1] A. J. Lotka. *Elements of physical biology*, Williams Wilkins, 1925.

[2] V. Volterra. *Variazioni e fluttuazioni del numero d'individui in specie animali conviventi*, vol.2. Societáanonima tipografica" Leonardo da Vinci", 1927.

[3] R. M. Anderson and R. M. May, *Population biology of infectious diseases: Part i* Nature, vol.280,no.5721, pp.361–367, 1979. 5

[4] R. M. Anderson and R. M. May,*The invasion, persistence and spread of infectious diseases within animaland plant communities* Philosophical Transactions of the Royal Society of London. B, Biological Sciences, vol.314, no.1167, pp.533–570, 1986. 5

[5] M. S. Rahman and S. Chakravarty,*A predator-prey model with disease in prey*, Nonlinear Analysis: Modelling and Control, vol.18, no.2, pp.191–209, 2013.

[6] J. Chattopadhyay and O. Arino, *A predator-prey model with disease in the prey*, Nonlinear analysis,vol.36, pp.747–766, 1999.

[7] M. Haque and D. Greenhalgh, *When a predator avoids infected prey: a model-based theoretical study*, Mathematical Medicine and Biology: A Journal of the IMA, vol.27, no.1, pp.75–94, 2010.

[8] S.P. Bera, A. Maiti, and , G.P. Samanta,*A prey-predator model with infection in both prey and predator*, Filomat, 29(8), pp.1753-1767.

e-mail: `M.abedini@azaruniv.ac.ir`
e-mail: `gorbanali@azaruniv.ac.ir`
e-mail: `h-kheiri@tabrizu.ac.ir`

An analysis of legal and social issues affecting mathematical models of disease control; some complex features of information processing

Aghaieebeiklavasani, R. [1]

Faculty of Law and Political Science, University of Tehran

Rokni Lamouki, G. R.

School of Mathematics, Statistics, and Computer Science, College of Science, University of Tehran

Abstract

In this paper, we investigate how mathematical models in epidemiology are associated with legal and social issues. Such linkage will enable us to address some elements in different cases, like the interplay between negative and positive rights in disease control, the impact of quarantine, and some complex features of information function in assessing the dynamics of disease, which have been unaddressed. A deeper look into the behavior of our system will shed light on finding optimal solutions to address both healthcare and legal issues.

Keywords: Decreasing Information processing, Isolation, Dynamical systems, Legal issues

AMS Mathematical Subject Classification [2010]: 91B14, 92D30

1 Introduction

It would be impossible to address mathematical epidemiology models without considering different elements highlighting the impact of legal and societal issues. One can exemplify the role Media outlets often take in affecting disease dynamics. The psychological consequences of Media reporting can highly overshadow the process of decision-making concerning disease control both on the regional and global levels. A retrospective analysis of governments' response to healthcare crises throughout our history shows factors like overfear, political misuse like Xenophobia, and underestimation of a particular disease can harm attempts at overcoming pandemics [**?**]. Making a connection between human behavior and disease control is facilitated by the fact that people can alter their responses regarding pandemics [**?**]. This approach, called behavioral epidemiology- has some implications for our understanding of pandemics and diseases through the lens of mathematics. For instance, the effect of infected people in a given society during vaccination reflects the complexity of human nature, and thus, our approach should be evaluated as such [**?**], [**?**]. The caveat here is the extent to which efforts to surmount a pandemic cause the law to get into the act. The balance between individuals' rights (negative rights) and the viability of healthcare-related decisions benefiting society as a

[1] Speaker

whole (positive rights) is not an easy task to carry out. During the COVID-19 pandemic, many governments straddle the two sides, and some legal challenges and cases arose due to this inevitable imbalance [**?**]. Therefore, the abovementioned efforts to infuse our model with these themes bring more accuracy to our analysis. In this paper, we extend an analysis of the role of information processing in epidemiological models by adding the legal aspects of non-pharmaceutical in the model to contribute to the existing literature on the multidimensional characteristics of social issues. Such analysis divulges multistability in the disease-inflicted equilibriums of our model, leading to more complexities in higher dimensions.

2 Modeling

To address the problem we laid out above, we extend the model presented by [**?**]. Our goal is to show how the relationship between the process of information in both non-pharmaceutical and pharmaceutical prescriptions and the legal and societal aspects of these solutions are highly intertwined. The information we process is not necessarily increasing over time. On the contrary, we can trace the signs of overlooking problems. On the other hand, turning a blind eye to the comprehension of different trends in various societies and communities is also misleading and can result in undermining authorities's efforts. To extend the model we have

$$\dot{S} = \alpha(1-S) - \beta IS - p(M)S + \eta A, \tag{1}$$
$$\dot{A} = p(M)S - (\alpha+\eta)A, \tag{2}$$
$$\dot{I} = \beta IS - (\mu+\omega+\alpha)I + q(M)I, \tag{3}$$
$$\dot{M} = a\left(g(I) - M\right) \tag{4}$$

Here, S, A, and I correspondingly represent the number of Susceptible, Isolated, and Infected individuals in a Society, M represents the information index [2], and $q(M) = \epsilon p(M)$ for small positive $0 < \epsilon < 1$. To carry out stability analysis we have $\dot{S} = \dot{A} = \dot{I} = \dot{M} = 0$. Then

$$\dot{S} = 0 \to p(M) = \frac{1}{S}\left(\alpha(1-S) - \beta IS + \eta A\right), \tag{5}$$
$$\dot{A} = 0 \to p(M) = \frac{1}{S}\left(\alpha+\eta\right)A, \tag{6}$$
$$\dot{I} = 0 \to \epsilon p(M) = \frac{1}{I}\left((\omega+\mu+\alpha)I - \beta IS\right), \tag{7}$$
$$\dot{M} = 0 \to M = g(I). \tag{8}$$

By doing some simple substitution we have:

$$A = \left(\frac{(\omega+\mu+\alpha) - \beta S}{\epsilon(\eta+\alpha)}\right)S, \tag{9}$$
$$I = \frac{\alpha}{\beta S}\left((1-S) - \frac{(\omega+\mu+\alpha)S - \beta S^2}{\epsilon(\eta+\alpha)}\right), \tag{10}$$
$$M = g\left(\frac{\alpha}{\beta S}\left((1-S) - \frac{(\omega+\mu+\alpha)S - \beta S^2}{\epsilon(\eta+\alpha)}\right)\right). \tag{11}$$

[2] Or negative feedback

Then, we have

$$p(M) = \frac{1}{S}\,(\alpha+\eta)\,A = \epsilon^{-1}\big((\omega+\mu+\alpha)-\beta S\big), \tag{12}$$

$$p(g(I)) = \epsilon^{-1}\big((\omega+\mu+\alpha)-\beta S\big). \tag{13}$$

As we noted above, in this paper, we discuss different types of information processing functions by which individuals adopt a non-monotonic function regarding information about pharmaceutical and pharmaceutical measures. It is worth noting that our option reflects the complexity of the information index in a disease-inflicted community. For this case, we can use the general function

$$p(M) = \frac{n\,M^2 + m\,M + \gamma}{M^2+1} \tag{14}$$

In order to find equilibrium points we use $p(M)$ as

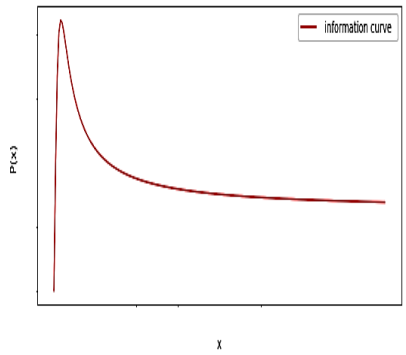

Figure 1: General non-monotonic information processing

$$p(g(I)) = \frac{n\,g^2(I) + m\,g(I) + \gamma}{g^2(I)+1}. \tag{15}$$

The fixed point problem will be

$$\frac{n\,g^2(I) + m\,g(I) + \gamma}{g^2(I)+1} = \epsilon^{-1}\big((\omega+\mu+\alpha)-\beta S\big), \tag{16}$$

or equivalently

$$\overbrace{\Big(n-\epsilon^{-1}\big((\omega+\mu+\alpha)-\beta S\big)\Big)}^{u(S)}\,g^2(I) + m\,g(I) + \overbrace{\Big(\gamma-\epsilon^{-1}\big((\omega+\mu+\alpha)-\beta S\big)\Big)}^{v(S)} = 0. \tag{17}$$

By solving quadratic equation we have

$$g(I) = -\frac{1}{2u(S)}\Big(m \pm \sqrt{m^2-4u(S)v(S)}\Big). \tag{18}$$

The function $g(I)$ is increasing and saturated with $g(0)=0$. Then we use exponential function $g(I) = 1-\zeta^{-\kappa I}$ for $\zeta > 1$. Finally we have:

$$1-\zeta^{-\kappa\frac{\alpha}{\beta S}\left((1-S)-\frac{(\omega+\mu+\alpha)S-\beta S^2}{\epsilon(\alpha+\eta)}\right)} = -\frac{1}{2u(S)}\Big(m \pm \sqrt{m^2-4u(S)v(S)}\Big). \tag{19}$$

We let

$$D_1 := 1 - \zeta^{-\kappa \frac{\alpha}{\beta S}\left((1-S) - \frac{(\omega+\mu+\alpha)S - \beta S^2}{\epsilon(\alpha+\eta)}\right)} + \frac{1}{2u(S)}\left(m - \sqrt{m^2 - 4u(S)v(S)}\right), \tag{20}$$

$$D_2 := 1 - \zeta^{-\kappa \frac{\alpha}{\beta S}\left((1-S) - \frac{(\omega+\mu+\alpha)S - \beta S^2}{\epsilon(\alpha+\eta)}\right)} + \frac{1}{2u(S)}\left(m + \sqrt{m^2 - 4u(S)v(S)}\right). \tag{21}$$

Then, the zero-level of D_1 and D_2 curves in $(D, S)-$plane determines the equilibria. For the biological meaningful solutions of $D_1(S) = 0, D_2(S) = 0$, we need $0 < S < (\omega + \mu + \alpha)/\beta$, and $0 < A < 1 - S$ which implies $4\beta > \epsilon(\eta + \alpha)\big(1 + \frac{\omega+\mu+\alpha}{\epsilon(\eta+\alpha)}\big)^2$. Based on variations of parameters, the typical form of these functions are illustrated in Figure (2).

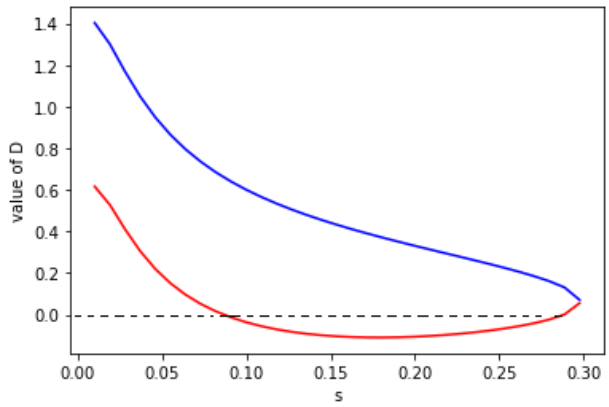

Figure 2: Curves of D1 (red) and D2 (blue). For $\alpha = 0.01$, $\beta = 0.96$, $\omega = 0.29993$, $a = 0.13$, $n = 3$, $m = 0.1$, $k = 4$, $\epsilon = 0.772$, $\eta = \mu = 0.23$, $\gamma = 0.33$, and $\zeta = 3$.

3 Conclusion

We have concluded that the social impact of the regulatory policies set out by authorities may lead to the leakage of infectious members of the society and thus worsen the epidemic condition by creating a multi-stability situation. We have investigated the occurrence of extra infectious equilibria which may be left unnoticed due to neglecting the social effect of imposing the law. There are the possibilities of folds, cusps, pitchforks, and Hopf bifurcation. Thus, the system has the potential to suffer chaos. The stability analysis of equilibria needs separate comprehensive studies.

Acknowledgment

This work is partially supported by Vision Daru (https://visiondaru.com/) as its support for young researchers in health and society.

References

[1] G. Chowell & J. M. Hyman, (Eds.), *Mathematical and statistical modeling for emerging and re-emerging infectious diseases*, pp. 344, Springer, 2016.

[2] R. López-Cruz, Global stability of an SAIRD epidemiological model with negative feedback, *Advances in Continuous and Discrete Models*, **1**, 41, 2022.

[3] P. Manfredi, & A. D'Onofrio, (Eds.), *Modeling the interplay between human behavior and the spread of infectious diseases*, Springer, 2013.

[4] A. d'Onofrio, P. Manfredi, & E. P. Salinelli, Vaccinating behaviour, information, and the dynamics of SIR vaccine preventable diseases, *Theoretical population biology*, **71**, 3, pp. 301-317, 2007.

[5] W. E. Parmet, *Constitutional Contagion: COVID, the Courts, and Public Health*, Cambridge University Press, pp. 68-70, 2023.

[6] N. Ribeiro, & C. Schwarzenegger, (Eds.), *Media and the Dissemination of Fear: Pandemics, Wars and Political Intimidation*, Springer, 2021.

e-mail: `rouzbeh.aghaieeb@ut.ac.ir`
e-mail: `rokni@ut.ac.ir`

The Biomathematics, modelling of populations developing drugs resistance

Leila Alizadeh[1]

Islamic Azad University, Yadegar-e-Imam branch in Shahre Ray

Abstract

The main motivation which led us to work with Biomathematics is that we could understand some mechanisms of biological phenomena using techniques which came from Mathematics. This existing interface between Biology and Mathematics, characterized by a great contact range, experiences a process of fast-track deepening nowadays.

Keywords: Biomathematics, Optimal control, populations, modelling developing drugs resistance

AMS Mathematical Subject Classification [2010]: 13D45, 39B42

1 Introduction

The contemporary Biomathematics can be classified in three distinct branches concerning methods and approaches: the traditional interface offered by biophysical and biomechanical issues; the most recent one dedicated to the genomic analyses and a third one called Population Dynamics. The field of greatest emphasis in the IMECC graduate programs was directed to the Population Dynamics which, in its broader meaning encompasses the study of population of molecules, cells, micro organisms, higher organisms, diseases and human societies. The synthesis and the foundation of this broad line of research proceed from a variety of mathematical models described by variational equations: ordinary and partial, continuous and discrete differential equations and afterwards, variational equations which envisage the subjectivity of parameters and state variables (fuzzy systems).

The use of Mathematics in the formulation of biological laws is still in its initial stage if compared to the development and use in the Physical Sciences; however, in the past years, along with the evolution of the computer sector, it has demonstrated to be a crucial tool in cutting-edge research in several fields. The practical models which involve inter-relationships of a great number of variables are formulated through equation systems with countless parameters. In these cases, an analytical treatment is usually impossible and the resolution qualitative methods must be used, which favors the computational resolutions. And, the more complex or realist the model is, the more difficult it will be to statistically show that it describes the reality!

[1]Speaker

The first Biomathematics paper at a master's level that we assisted took place as a partner in the FUEL postgraduate program it was a dissertation about the dynamics of biodigesters.

The Biomathematics at the IMECC was considered as a field of research of applied mathematics just in 1990.

papers presented can be gathered in two main topics: Dynamic Population Systems (Optimal control of tumors and bacteria, dengue evolution, resistance to fungicides and enzymatic kinetics) and numerical analysis of parabolic-hyperbolic PDE (river and sea pollution, hemodialysis and potato drying).

The Biomathematics group began, then, to develop integrated research projects: "Growth and Treatment of Cancerous Tumors", "Mathematical Modeling for Medicine Optimization in Cancerous Tumors".

We believe that the reason for the active continuity of this group is the result of modeling in biological processes supported by instruments resulting from the Fuzzy Theory.

The first Biomathematical paper using fuzzy logic arguments occurred when we used, along with Heriberto, the structure of a foundation of fuzzy rules to study the process of medical diagnosis of childhood diseases.

2 Initial discussion

The Group published some texts which became essential for those who intend to research in Biomathematics and/or Fuzzy Logic: "Differential Equations with Applications", "Theory of the fuzzy sets with applications", SBMAC - Notas em Matem´atica Aplicada, Vol.17, 2005; "Topics of Fuzzy Logic and Biomathematics".

"The First Course in Fuzzy Logic, Fuzzy Dynamical Systems and Biomathematics - Theory and Applications".

In 1989, Professor Lee. A. Segel from the Weizmann Institute in Israel, one of the most renowned biomathematician in the world, was present, as a guest of the Group, and he lectured several times emphasizing the research in Biomathematics.

2.1 Mathematical Modeling for tumor growth and the problem of cellular resistance to antiblastic drugs

This work demonstrated the importance of pharmacon resistance from spontaneous mutations, as an intrinsic property of a tumor. The formal mathematical models show in this context different factors which can influence the efficacy of chemotherapy, such as tumor size, degree of cell resistance at the initiation of therapy, therapeutic program, the frequency of mutations resistant cells, tumor kinetics, etc. The results that were obtained suggest directions to be taken by therapists for the best choice of chemotherapy of its program, which is usually done empirically. The proposed model initially considersC: tumor cells; S: sensitive cells; R_1: cells resistant to the first drug and R_2: second drug resistant cells.

$$\begin{cases} \dfrac{dS}{dt} = rS(1-kN) - \alpha_1 rS(1-kN) - \alpha_2 rS(1-kN) \\ \dfrac{dR_1}{dt} = rR_1(1-kN) + \alpha_1 rS(1-kN) - \alpha_2 rR_1(1-kN) \\ \dfrac{dR_2}{dt} = rR_2(1-kN) + \alpha_2 rS(1-kN) - \alpha_2 rR_2(1-kN) \\ \dfrac{dR_d}{dt} = rR_d(1-kN) + \alpha_2 rR_1(1-kN) - \alpha_1 rR_2(1-kN) \end{cases} \tag{1}$$

$$\frac{R_1}{N} = N^{-\alpha_2} - N^{-\alpha_1+\alpha_2}$$

$$\frac{R_1}{N} = N^{-\alpha_1} - N^{-\alpha_1+\alpha_2}$$

In this paper, models with A and B alternative therapies having immediate effects and effects at fixed period intervals were also analyzed.

$$\begin{cases} \frac{dS}{dt} = rS(1-kN) - \alpha_1 rS(1-kN) - \alpha_2 rS(1-kN) - F(t)S \\ \frac{dR_1}{dt} = rR_1(1-kN) + \alpha_1 rS(1-kN) - \alpha_2 rR_1(1-kN) - F_B(t)R_1 \\ \frac{dR_2}{dt} = rR_2(1-kN) + \alpha_2 rS(1-kN) - \alpha_2 rR_2(1-kN) - F_A(t)R_2 \\ \frac{dR_d}{dt} = rR_d(1-kN) + \alpha_2 rR_1(1-kN) - \alpha_1 rR_2(1-kN) \end{cases}$$

Simulations carried out show the therapeutic advantage of using a program of alternate drugs over the mono-chemotherapy.

2.2 Optimal chemical control of populations developing drug resistance (Michel I. da S. Costa, J. L. Boldrini and R. C. Bassanezi) - IMA Journal of Mathematics Applied in Medicine & Biology, 1992.

A system of differential equations for the control of tumor cells growth in a cyclenonspecific chemotherapy is presented. Drug resistance and toxicity are also taken into account. The aim of the control is to minimize the final tumor level and the toxicity. The analysis resorted to the Optimal Control Theory and the results showed that maximum drug concentration featured in all treatments - in some cases it was the sole optimal strategy. Treatments dependent on tumor level were also optimal whereas alternating maximum drug concentration and rest periods proved to be suboptimal or an alternative strategy when there is no optimal solution. Specifically, the considered model is given by the following systems of ordinary differential equations:

$$\begin{cases} \frac{dx}{dt} = xf(y) + \alpha f(y)(y-x) \\ \frac{dy}{dt} = yf(y) - u(t)g(y-x) \\ x(0) = x_0; y(0) = y_0 \end{cases} \tag{2}$$

”Optimal chemotherapy: A Case study with drug resistance; saturation effect and toxicity”.

3 conclusion

From this two-way process, not only basic Biology issues have been solved, but also new lines of research in Mathematics have arisen and taken on a life of their own. Moreover, it is important to notice the emerging of new fields in Applied Mathematics, such as genetic algorithms, neural networks, sociobiological algorithms, fuzzy logic, etc., which we could call Biological Mathematics since, in many cases, they owe their basic concepts to Theoretical Biology.

References

[1] Brossard, Ludovic, Jean-Yves Dourmad, and Florence Garcia-Launay. "Modelling nutrient requirements for pigs to optimize feed efficiency Jaap van Milgen, PEGASE, INRA–Agrocampus Ouest, France." In Achieving sustainable production of pig meat Volume 2, pp. 207-230. Burleigh Dodds Science Publishing, 2018.

[2] Jordan, B. W., and E. Polak. "Theory of a class of discrete optimal control systems." International Journal of Electronics 17, no. 6 (1964): 697-711.

[3] El-Samad, Hana, and Mustafa Khammash. "Coherence resonance: a mechanism for noise induced stable oscillations in gene regulatory networks." In Proceedings of the 45th IEEE Conference on Decision and Control, pp. 2382-2387. IEEE, 2006.

[4] Torres, Delfim FM, Iván Area, César Silva, and Cristiana J. Silva. "The Portuguese Meeting in Biomathematics." Statistics, Optimization & Information Computing 7, no. 3 (2019): 530-532.

[5] Harris, Matthew Wade. "Lossless convexification of optimal control problems." PhD diss., 2014.

[6] Yang, Chayu, Xueying Wang, Daozhou Gao, and Jin Wang. "Impact of awareness programs on cholera dynamics: two modeling approaches." Bulletin of Mathematical Biology 79 (2017): 2109-2131.

[7] Kunhippurayil, Sheril, and Matthew W. Harris. "Strong observability as a sufficient condition for non-singularity and lossless convexification in optimal control with mixed constraints." Control Theory and Technology 20, no. 4 (2022): 475-487.

e-mail: `le_alizad@yahoo.com`

Numerical Solution of a Fractional COVID-19 Model Using the Fractional Legendre-Picard Iteration Method

Soheyla Ansari[1], and Mohammad Hossein Akrami
Department of Mathematical Sciences, Yazd University, Yazd, Iran

Abstract

This paper focuses on a numerical approach for solving nonlinear fractional differential equations using Picard's iteration method combined with shifted Legendre polynomials, known as the fractional Legendre-Picard iteration method. Towards the end of the paper, numerical approximations of a fractional COVID-19 pandemic model are presented to demonstrate and validate the proposed method. The numerical results indicate that our method is efficient.

Keywords: An epidemic model of COVID-19, Shifted Legendre polynomials, Legendre-Picard iteration

Mathematics Subject Classification [2010]: 13D45, 39B42

1 Introduction

In the past few decades, there has been significant progress in fractional differential equations (FDEs) due to their applicability in various fields of science and engineering [1, 2]. FDEs offer an advantage in modeling real-life phenomena as they help reduce errors that may arise from ignored parameters. There are numerous examples of mathematical models in biology, physics, natural sciences, and other fields of science that can be effectively represented by FDEs such as the fractional-order COVID-19 model [2, 5]. It has been observed that obtaining analytical solutions for systems of FDEs can be a challenging task and, in some cases, even impossible. Therefore, the development of efficient numerical methods is essential for studying the solutions of these equations. Researchers have recently achieved various approximate methods for the numerical solution of systems of fractional differential equations, such as spectral Galerkin method [2], Computational method [1] and Adams-Bashforth method [5]. One of numerical techniques used to solve FDEs consists of semi-analytical methods [6]. Picard's method is a simple yet efficient semi-analytical technique that can be employed to solve a wide range of FDEs [6]. Picard's method is a frequently used approach for solving equations but can have difficulty with non-linear problems. In this research, we utilized a combination of shifted Legendre polynomials, the Legendre-Gauss quadrature formula, and the Picard iteration technique. This allowed us to develop the Legendre-Picard iteration method (LPIM) to solve nonlinear fractional integral equations. First, we recall some basic concepts.

Definition 1.1. The analytic form of the shifted Legendre polynomial on the interval $\Lambda = [0, L]$ is defined as:

$$\mathbb{L}_n^*(x) = \sum_{k=0}^{n} \frac{(-1)^{n-k}\Gamma(n+k+1)}{\Gamma(k+1)(n-k)!k!L^k} x^k. \tag{1}$$

[1]Speaker

Hence, the orthogonality condition is

$$\int_{\Lambda} \mathbb{L}_n^*(x)\mathbb{L}_m^*(x)dx = (\frac{L}{2m+1})\delta_{nm},$$

where, δ_{nm} is Kronecker delta function. Thus, for any function

$$g(x) = \sum_{i=0}^{\infty} g_i \mathbb{L}_i^*(x),$$

where the cofficients g_i are given by

$$g_i = \frac{2i+1}{L}\int_0^L g(x)\mathbb{L}_i^*(x)dx, \qquad i = 0, 1, 2, \cdots . \tag{2}$$

The integral of Equation (2) can be calculated numerically using the shifted Legendre-Gauss quadrature rule as:

$$g_i(x) \simeq \frac{2i+1}{L}\sum_{j=0}^{N} g(x_j)\mathbb{L}_i^*(x_j)\omega_j,$$

where

$$x_j = \frac{L}{2}(t_j + 1),$$

and $\{t_j\}_{j=0}^N$ are zeros of $\mathbb{L}_{N+1}(x)$ and $\{\omega_j\}_{j=0}^N$ are corresponding weights introduced in [6] as

$$\begin{aligned}\omega_j &= \frac{2}{(1-x_j^2)(\mathbb{L}'_{N+1}(t_j))^2} \\ &= \frac{(2N+2)}{(N+1)^2\mathbb{L}_N(t_j)\mathbb{L}'_{N+1}(t_j)}, \qquad j = 0, 1, \cdots, N.\end{aligned}$$

Definition 1.2. For a function say $y(t)$ we define fractional integral (Riemann-Liouville fractional integral) corresponding to t as

$$I^\gamma y(x) = \frac{1}{\Gamma(\gamma)}\int_0^x (x-\tau)^{\gamma-1}y(\tau)d\tau, \qquad \gamma > 0.$$

For the Riemann-Liouville fractional integral, we have

$$\mathcal{I}_a^\gamma (x)^k = \frac{\Gamma(k+1)}{\Gamma(\gamma+k+1)}(x)^{\gamma+k}. \tag{3}$$

Definition 1.3. Caputo's fractional derivative of order γ is defined as:

$${}^c\mathbb{D}^\gamma u(x) = \mathcal{I}_0^{n-\gamma}u^{(n)}(x) = \frac{1}{\Gamma(n-\gamma)}\int_0^x (x-\tau)^{n-\gamma-1}u^{(n)}(\tau)d\tau, \quad n-1 \le \gamma \le n,$$

For the Caputo derivative, we have

$$\mathcal{I}_0^\gamma \mathbb{D}^\gamma u(x) = u(x) - \sum_{k=0}^{n-1}\frac{u^{(k)}(0)}{k!}x^k, \qquad x > 0, \tag{4}$$

$$\mathbb{D}^\gamma \mathcal{I}_0^\gamma u(x) = u(x). \tag{5}$$

2 Main results

In this section, we introduce our proposed method, called the Fractional Legendre-Picard's Iteration Method (FPLIM), which offers an iterative algorithm for solving system of fractional ordinary differential equations.

Theorem 2.1. *Let $\mathbb{L}_n^*$ be the shifted Legendre polynomials of degree n. Then we have*

$$\mathcal{I}_0^\gamma \mathbb{L}_i^*(x) = \sum_{j=0}^{N} \phi(i,j)\mathbb{L}_j^*(x), \qquad i = 0, 1, \cdots, N, \tag{6}$$

where $\phi(i,j) = \sum_{k=0}^{i} \Theta_{ijk}$, *and*

$$\begin{aligned}\Theta_{ijk} &= \frac{(-1)^{i-k}\Gamma(i+k+1)}{\Gamma(k+1)\Gamma(k+\gamma+1)(i-k)!} \\ &\times \sum_{h=0}^{j} \frac{(-1)^{j-h}\Gamma(j+h+1)\Gamma(h+k+\gamma+1)(2j+1)j!}{\Gamma(j+1)\Gamma(h+1)\Gamma(h+\gamma+k+2)(j-h)!h!} L^\gamma.\end{aligned} \tag{7}$$

Remark 2.2. [3] Based on Theorem 2.1, in the vector form we have

$$\mathcal{I}_0^\gamma \mathbb{L}_i^*(x) \simeq [\phi(i,0), \phi(i,1), \cdots, \phi(i,N)]\psi(t), \qquad i = 0, 1, \cdots, N. \tag{8}$$

A proposed method called fractional Legendre-Picard iteration method (FLPIM) for solving system of fractional ordinary differential equations (FODEs) as

$$^c\mathbb{D}^\gamma \mathcal{U}_j(x) = G_j(x, \mathcal{U}_j(x)), \qquad 0 \le x \le L, \qquad n-1 \le \gamma \le n, \quad n \in \mathbb{N}, \tag{9}$$

$$\mathcal{U}_j^{(l)}(0) = \mathcal{U}_{j0}^{(l)}, \qquad l = 0, 1, \ldots m_j - 1, \qquad 0 \le j \le n. \tag{10}$$

By applying the fractional integral to equation (10), we have

$$\mathcal{U}_j(x) = \sum_{l=0}^{m_j-1} \frac{x^l \mathcal{U}_{j0}^{(l)}}{l!} + \frac{1}{\Gamma(\gamma)} \int_0^x (x-s)^{\gamma-1} G_j(s, \mathcal{U}_j(s))ds. \tag{11}$$

According to (11), the iteration sequence is generated in the following way

$$\mathcal{U}_j^i(x) = \sum_{l=0}^{m_j-1} \frac{x^l \mathcal{U}_{j0}^{(l)}}{l!} + \frac{1}{\Gamma(\gamma)} \int_0^x (x-s)^{\gamma-1} G_j(s, \mathcal{U}_j^{i-1}(s))ds, \tag{12}$$

where $\mathcal{U}_j^0(t)$ is an appropriate initial function that corresponds to the initial conditions of the problem. The first step of the FJPIM is to approximate the function $f(s, \mathcal{U}_j^{i-1}(s))$ using $\{\mathbb{L}_n^*(s)\}_{n=0}^N$. Therefore

$$G_j(s, \mathcal{U}_j^{i-1}(s)) \simeq \sum_{k=0}^{N} \tilde{G}_{jk}^{i-1} \mathbb{L}_k^*, \tag{13}$$

where $\{\tilde{G}_{jk}^{i-1}\}_{j=0}^N$ obtained as $\tilde{G}_{jk}^{i-1} = \frac{2k+1}{2} \sum_{r=0}^{N} G_j(s_r, \mathcal{U}_j^{i-1}(s_r))\mathbb{L}_k^*(s_r)\omega_r$ With the placement of equation (13) at (12), and according to (6) we have

$$\begin{aligned}\mathcal{U}_d^i(x) &= \sum_{l=0}^{m_j-1} \frac{x^l \mathcal{U}_{d0}^{(l)}}{l!} + \mathcal{I}^\gamma(G_d(s, \mathcal{U}_d^{i-1}(s))) \\ &= \sum_{l=0}^{m_j-1} \frac{\mathcal{U}_{d0}^{(l)}}{l!} \sum_{j=0}^{N} C_{lj}\mathbb{L}_j^*(x) + \sum_{k=0}^{N} \tilde{G}_{dk}^{i-1} \sum_{j=0}^{N} \sum_{k=0}^{i} \Theta_{ijk}\mathbb{L}_j^*(x) \\ &= \sum_{j=0}^{N} \mathbb{L}_j^*(t) \Big(\sum_{l=0}^{m_j-1} \frac{\mathcal{U}_{d0}^{(l)}}{l!} C_{lj} + \sum_{k=0}^{N} \tilde{G}_{dk}^{i-1} \sum_{k=0}^{i} \Theta_{ijk} \Big), \qquad 0 \le d \le n.\end{aligned} \tag{14}$$

where $C_{lj} = \frac{(2j+1)\Gamma(j+1)L^l}{\Gamma(j+1)} \sum_{f=0}^{j} \frac{(-1)^{j-f}\Gamma(j+f+1)\Gamma(f+l+1)}{\Gamma(f+\beta+1)\Gamma(f+l+2)(j-f)!f!}$. We assume that the approximate solution in the i-th step is shown as

$$\begin{aligned}\mathcal{U}_d^i(x) \simeq \sum_{j=0}^{N} K_j^i \mathbb{L}_j^*(t) \simeq \mathbb{L}_0^*(x)\Big(\sum_{l=0}^{n-1} \frac{\mathcal{U}_{d0}^{(l)}}{l!} C_{l0} + \sum_{k=0}^{N} \tilde{G}_{dk}^{i-1} \sum_{k=0}^{i} \Theta_{i0k}\Big) \\ + \cdots + \mathbb{L}_N^*\Big(\sum_{l=0}^{n-1} \frac{\mathcal{U}_{d0}^{(l)}}{l!} C_{lN} + \sum_{k=0}^{N} \tilde{G}_{dk}^{i-1} \sum_{k=0}^{i} \Theta_{iNk}\Big).\end{aligned} \tag{15}$$

We obtain the coefficients $\{K_j^i\}_{j=0}^N$ directly from (15), as follows:

$$K_j^i = \sum_{l=0}^{n-1} \frac{\mathcal{U}_{d0}^{(l)}}{l!} C_{lj} + \sum_{k=0}^{N} \tilde{G}_{dk}^{i-1} \sum_{k=0}^{i} \Theta_{ijk}, \qquad j = 0, 1, \cdots N, \qquad 0 \le d \le n.$$

After updating the cofficients, the new estimated solution is generated. The proposed algorithm continues to iterate until the stopping criterion is met, which is defined as $\|\mathcal{U}_d^i(x) - \mathcal{U}_d^{i-1}(x)\|_\infty < \epsilon$,.

3 Numerical example

Consider the following non-linear dynamical model of COVID-19 disease [1, 2, 5]:

$$\begin{aligned}{}^c\mathbb{D}^\gamma \mathcal{X}(t) &= \sigma - \rho\mathcal{Z}(t)\mathcal{X}(t)(1+\nu\mathcal{Z}(t)) - \xi\mathcal{X}(t), \\ {}^c\mathbb{D}^\gamma \mathcal{Y}(t) &= \rho\mathcal{Z}(t)\mathcal{X}(t)(1+\nu\mathcal{Z}(t)) - (\xi+\kappa)\mathcal{Y}(t), \\ {}^c\mathbb{D}^\gamma \mathcal{Z}(t) &= \delta + \nu\mathcal{Y}(t) - (\theta+\xi+\mu)\mathcal{Z}(t), \\ {}^c\mathbb{D}^\gamma \mathcal{M}(t) &= \mu\mathcal{Z}(t) - \xi\mathcal{M}(t), \qquad t \in [0, 15], \qquad 0 < \gamma \le 1,\end{aligned}$$

where $\rho = \frac{\mathcal{M}(0)\xi(\xi+\kappa)(\theta+\xi+\mu)}{\nu\sigma}$ is proportionality constant. This model contains four compartments at time t (day) healthy or susceptible population $\mathcal{X}(t)$, the exposed class $\mathcal{Y}(t)$, the infected population $\mathcal{Z}(t)$ and the removed class $\mathcal{M}(t)$. The other parameters in model and their corresponding values are provided in Table 1.

Table 1: Description of the parameters of model

Parameter	Description	Value
σ	The group of people whose is negative test result	0.00250281 million
ν	Rate at which individuals who have recovered lose their immunity	0.00009 million
ξ	The mortality rate due to natural causes	0.0000004 million
κ	The constant rate that determines the progression of the infection	0.000024
δ	The group of people whose is positive test result	0.006656 million
θ	Fatalities resulting from the coronavirus	0.0109
μ	Recovery rate	0.75

By applying the proposed method, we can evaluate this example by setting the initial conditions as follows, (scaled in million)

$$\mathcal{X}(0) = 0.323, \qquad \mathcal{Y}(0) = 0.21, \qquad \mathcal{Z}(0) = 0.22, \qquad \mathcal{M}(0) = 0.21,$$

When using numerical methods to solve problems where the exact solution is unknown, it is important to assess the accuracy and errors of the numerical approach. Table 2 shows the maximum absolute error of solution by our method for two consecutive iteration ($l = 8$ and $N = 10$). For this model, in the absence of a solution for direct error calculation, the numerical errors are using alternative means:

$$E_u = \max_{0 \le t \le L} |u_l(t) - u_{l+1}(t)|.$$

Table 2 quantitatively analyzes the reliability and discretization independence of the numerical approach used for model simulations. The obtained findings are compared with the findings of the FDE12 technique solver. FDE12 Solves an initial value problem for a non-linear differential equation of fractional order (FDE). The code implements the predictor-corrector PECE method of Adams-Bashforth Moulton (A-BM) type described in [4]. Here, the step length of A-BM method , $\frac{15}{5000}$ is considered.

Table 2: The maximum absolute error of solution by our method ($l = 8$ and $N = 10$) for $\gamma = 0.5$ and comparison of the absolute error with the method FDE12.

	$E_{\mathcal{X}(t)}$	$E_{\mathcal{Y}(t)}$	$E_{\mathcal{Z}(t)}$	$E_{\mathcal{M}(t)}$
Our method	$1.4e-34$	$4e-29$	$1.5e-28$	0
FDE12	$1.1e-6$	$2.2e-7$	$3.5e-6$	$7.1e-6$

Conclusion

In this paper, we introduced the fractional Legendre-Picard iteration method as an effective numerical technique for solving nonlinear fractional differential equations. In conclusion, the results of our study demonstrate the effectiveness and accuracy of the new method proposed for solving the Covid-19 model. By comparing the outcomes with those obtained using the Adams Bashforth Moulton method, we have shown that our approach not only performs well but also offers efficient solutions. This validation underscores the potential of our method as a valuable tool for modeling and analyzing infectious disease dynamics.

References

[1] Abderrazak, Nabti, and Behzad. Ghanbari, *Global stability analysis of a fractional SVEIR epidemic model*, Mathematical Methods in the Applied Sciences, 11, (44), (2021).

[2] Amin. Faghih, P. Mokhtary, *Non-linear system of multi-order fractional differential equations: theoretical analysis and a robust fractional Galerkin implementation*, Journal of Scientific Computing, 02, (91), (2022).

[3] A. H. Bhrawy, E. H. Doha, D. Baleanu, and S. S. Ezz-Eldien. *A spectral tau algo- rithm based on Jacobi operational matrix for numerical solution of time fractional diffusion-wave equations.* Journal of Computational Physics, 293, (2015), 142–156.

[4] K. Diethelm, N.J. Ford, A.D. Freed, *Detailed error analysis for a fractional Adams method*, Numer. Algorithms, 36 (1), (2004).

[5] Rahman. Mati ur, Arfan. Muhammad, Shah. Kamal and Gómez-Aguilar. JF, *Investigating a nonlinear dynamical model of COVID-19 disease under fuzzy caputo, random and ABC fractional order derivative*, Chaos, Solitons & Fractals, 140, (2020).

[6] Tafakkori-Bafghi, M and Barid Loghmani, G and Heydari, M and Bai, X, *JacobiPicard iteration method for the numerical solution of nonlinear initial value problems*, . Math Methods Appl Sci. 43(3), (2020).

Email: `sansari@stu.yazd.ac.ir`
Email: `akrami@yazd.ac.ir`

Local radial basis functions to the numerical solution of Volterra integral equations with delay argument

Pouria Assari[1]

Department of Mathematics, Faculty of Sciences, Bu-Ali Sina University, Hamedan 65178, Iran

Alireza Hosseinian

Department of Mathematics, Faculty of Sciences, Bu-Ali Sina University, Hamedan 65178, Iran

Abstract

The effect of the past values of some natural physical phenomena in understanding the current and predicting their future dynamics behavior is undeniable. Delay systems describe their behavior; hence special attention has been given to them recently. In this investigation, we deal with the delay Volterra integral equations as one of the most important tools in this field, applying the collocation method based on the locally supported radial basis functions. Discretization of integrals obtained has been done through the Gauss-Legendre integration rule. The presented scheme estimates the unknown function utilizing a small set of data instead of all points in the solution domain and subsequently uses much less computer memory and volume computing compared to global cases. In addition, the presented example confirms that the new approach is powerful in solving these kinds of integral equations.

Keywords: Delay integral equations, Local radial basis functions, Discrete collocation method, Numerical solution

AMS Mathematical Subject Classification [2010]: 45D05, 65D12

1 Introduction

To reflect more closely on the measured performance in comparison with the output of some problems, delay Volterra integral equations have emerged in mathematical modeling processes describing physical phenomena with memory effects. These equations are widely used in medicine, bio-mathematics, engineering, and other sciences. In the present work, we establish the numerical solution of the nonlinear DIEs with the constant delay $\tau > 0$, which are presented as follows

$$u(t) - \int_{t-\tau}^{t} K(t, s, u(s))\mathrm{d}s = g(t), \qquad 0 \leq t \leq T, \tag{1}$$

with the initial function

$$u(t) = \varphi(t), \qquad -\tau \leq t \leq 0. \tag{2}$$

The kernel function $K(t, s, u(s))$ is nonlinear with respect to the variable u, the function $g(t)$ is given, and the unknown function $u(t)$ must be determined. Equation (1) can be considered as the general form of

[1]Speaker

the various problems in the growth of single-species populations, the growth of capital or certain epidemics proposed by Cooke [1], in which immigration or the importation of capital is allowed.

The complexity of the delay integral equations has made it impossible to solve them analytically, so numerical methods are considered in solving such equations. We apply local radial basis functions with the collocation method which is based on the use of a set of scattered data. To construct the discrete collocation method, the uniform composite Gauss-Legendre quadrature formula has been employed. Finally, a numerical example has been included to show the validity and efficiency of the new technique.

2 Locally supported RBFs

In this section, we focus our study on the locally supported RBFs to approximate a function on the interval $[a, b] \subset \mathbb{R}$ utilizing a radial function. Let $S = \{t_1, ..., t_N\}$ be a set of scattered points selected in $[a, b] \subset \mathbb{R}$ and $\phi(|t|)$ be a global radial function on $\mathbb{R}$. To approximate a function $u(t)$ at an arbitrary point $t \in [a, b]$ using the function $\phi(t)$ based on the nodal set S, consider the following linear combination [4]:

$$u(t) \approx \mathcal{G}_N u(t) = \sum_{i=1}^{N} c_i \phi(|t - t_i|), \qquad t \in [a, b], \tag{3}$$

where the coefficients $\{c_1, ..., c_N\}$ are determined by the interpolation conditions

$$\mathcal{G}_N u(t_i) = u(t_i) = u_i, \quad i = 1, ..., N. \tag{4}$$

Therefore, the solution of the interpolation problem based on the extended expansion (3) reduces to the solution of a system of linear equations of the matrix form

$$A\mathbf{c} = \mathbf{u}, \tag{5}$$

where the pieces are given by $A_{jk} = \phi(|x_j - x_k|)$, $j, k = 1, ..., N$, $\mathbf{c} = [c_1, ..., c_N]^T$ and $\mathbf{u} = [u_1, ..., u_N]^T$. If a radial basis function Φ is strictly positive definite, then the associated interpolation matrix A is positive definite and so non-singular. Therefore, the interpolation problem (5) has a unique solution.
It should be noted that the condition number of the global RBFs grows when the number of nodal points N increases in the domain to obtain accurate results. Therefore, the coefficient matrix of the interpolation by global RBFs is ill-conditioned, i.e., a small perturbation in the initial data may produce a large amount of perturbation in the solution. Useful schemes have been introduced by Fu et al. [2] to eliminate ill-conditioning problems. Suppose $[a_i, b_i] = [t_i - r_i, t_i + r_i]$ in which $r_i > 0$ is chosen such that the set of them establishes an open bounded cover for $[a, b]$. Therefore, a function $u(t)$ on $[a_i, b_i]$, $i = 1, ..., N$, can be estimated as follows:

$$u(t) \approx \mathcal{L}_i u(t) = \sum_{j \in I_i} c_j^i \phi^i(|t - t_j|), \quad t \in [a_i, b_i], \tag{6}$$

where I_i is the set of indexes corresponding to points fallen within the influence domain $[a_i, b_i]$ (or cover) with the cardinal number $|I_i| = n_i$ and

$$\psi_j^i(t) = \sum_{k \in I_i} [\mathbf{B}^{i^{-1}}]_{kj} \phi^i(|t - t_k|), \quad j \in I_i,$$

moreover $\mathbf{B}^i = [\phi(|t_j - t_k|)],\ j,k = 1,...,n_i$, is an $n_i \times n_i$ real symmetric coefficient matrix. Let ϕ be strictly positive definite; then, we know that the matrix $\mathbf{B}^i$ is invertible. In the expansion (6), the coefficients $\{c_j^i\}_{j\in I_i}$ are determined by enforcing the interpolation conditions

$$\mathcal{L}_i u(t_j) = u_j, \quad j \in I_i. \tag{7}$$

The interpolation conditions (7) and the expansion (6) eventually result that the shape functions $\psi_i^i(t)$ satisfying the Kronecker delta condition [3] .i.e. $\psi_i^i(t) = 0$ for every $t \notin [a_i, b_i]$. Therefore, we can assume that

$$u(t) \approx \mathcal{P}_N u(t) = \sum_{i\in I_t} u_i \psi_i^i(t), \quad t \in [a,b], \tag{8}$$

where $I_t = \{i : t \in [a_i, b_i]\}$ and the influence domain of the point t is defined as $D_t = \cup_{i\in I_t}[a_i, b_i]$ and the functions $\psi_i^i(t)$ are called the shape functions for the LRBF interpolation.

3 Description of the method

In this section, a method based on the LRBF collocation scheme is presented to find the solution of delay Volterra integral equations (1) with initial function (2). It is straightforward that, integral equation (1) can be rewritten as follow by using integral properties:

$$u(t) - \int_{t-\tau}^{0} K(t,s,u(s))\mathrm{d}s - \int_0^t K(t,s,u(s))\mathrm{d}s = g(t), \quad 0 \le t \le T, \tag{9}$$

To handle, we need N nodal points $\{t_1, ..., t_N\}$ selected in the interval $[0,T]$; thus the unknown function $u(t)$ is approximated utilizing the LRBFs method by

$$u(t) \approx u_N(t) = \sum_{i=1}^{N} \bar{c}_i \psi_i^i(t), \quad t \in [0,T]. \tag{10}$$

In the collocation technique, the coefficients $\{\bar{c}_1, ..., \bar{c}_N\}$ are evaluated by replacing the expansion (10) with $u(t)$ in the integral equation (9) and placing the nodal points $t_1, t_2, ..., t_N$ in the achieved equation as

$$\sum_{i=1}^{N} \bar{c}_i \psi_i^i(t_j) - \int_{t_j-\tau}^{0} K(t_j, s, \sum_{i=1}^{N} \bar{c}_i \psi_i^i(s))ds - \int_0^{t_j} K(t_j, s, \sum_{i=1}^{N} \bar{c}_i \psi_i^i(s))ds = g(t_j), \quad j = 1, ..., N. \tag{11}$$

Since the support of the shape functions $\psi_i^i(t)$ are $[a_i, b_i] = [t_i - r_i, t_i + r_i]$ and these shape functions satisfy the Kronecker delta condition, (11) becomes

$$\bar{c}_j - \int_{t_j-\tau}^{0} K(t_j, s, \sum_{i=1}^{N} \bar{c}_i \psi_i^i(s))ds - \int_0^{t_j} K(t_j, s, \sum_{i=1}^{N} \bar{c}_i \psi_i^i(s))ds = g(t_j), \quad j = 1, ..., N. \tag{12}$$

The discrete collocation method is obtained by calculating all integrals in the systems (12) associated with the collocation method numerically. To approximate these integrals, we use the composite m_N-point Gauss-Legendre rule with M uniform subdivisions relative to the coefficients $\{v_k\}$ and weights $\{w_k\}$ in the interval $[-1,1]$. Suppose $f \in C^{2m_N}[a,b]$, for any given integer $M > 0$, we have [5]

$$\int_a^b f(t)\mathrm{d}t = \frac{\Delta t}{2} \sum_{k=1}^{m_N} w_k \sum_{q=1}^{M} f(\theta_k^q) + \mathcal{O}(\frac{1}{M^{2m_N}}), \tag{13}$$

where $\Delta t = \frac{b-a}{M}$ and $\theta_k^q = \frac{\Delta t}{2} v_k + (q - \frac{1}{2})\Delta t$. Applying the rule (13) for (12), if $t_j \geq \tau$, we have

$$\hat{c}_j - \frac{\Delta t_1}{2} \sum_{k=1}^{m_N} w_k \sum_{q=1}^{M} K(t_j, \theta_k^q, \sum_{i=1}^{N} \hat{c}_i \psi_i^i(\theta_k^q)) - \frac{\Delta t_2}{2} \sum_{k=1}^{m_N} w_k \sum_{q=1}^{M} K(t_j, \eta_k^q, \sum_{i=1}^{N} \hat{c}_i \psi_i^i(\eta_k^q)) = g(t_j), \tag{14}$$

where $\Delta t_1 = \frac{\tau - t_j}{M}$ and $\theta_k^q = \frac{\Delta t_1}{2} v_k + (q - \frac{1}{2})\Delta t_1$ and $\Delta t_2 = \frac{t_j}{M}$ and $\eta_k^q = \frac{\Delta t_2}{2} v_k + (q - \frac{1}{2})\Delta t_2$. For $t_j < \tau$, using the initial condition (2) results

$$\hat{c}_j - \frac{\Delta t_1}{2} \sum_{k=1}^{m_N} w_k \sum_{q=1}^{M} K(t_j, \theta_k^q, \phi(\theta_k^q)) - \frac{\Delta t_2}{2} \sum_{k=1}^{m_N} w_k \sum_{q=1}^{M} K(t_j, \eta_k^q, \sum_{i=1}^{N} \hat{c}_i \psi_i^i(\eta_k^q)) = g(t_j), \tag{15}$$

Thus, by solving the systems (14) and (15) for the unknowns $\{\hat{c}_1, ..., \hat{c}_N\}$, the values of $u(t)$ at any point $t \in [0, T]$ can be approximated by

$$\hat{u}_N(t) = \sum_{i=1}^{N} \hat{c}_i \psi_i^i(t), \quad t \in [0, T]. \tag{16}$$

4 Numerical example

Here, a delay Volterra integral equation has been solved to study the efficiency and accuracy of the proposed method. In computations, the local Gaussian (LGA) and local inverse multiquadrics (LIMQ) radial basis functions are used to solve the mentioned integral equation. We put $c = 0.1 \times \sqrt{N} (c = 0.2 \times \sqrt{N})$ for LGA and $c = 5/\sqrt{N} (c = 10/\sqrt{N})$ for LIMQ, respectively. Also, the integrals that appeared in the scheme are computed using 6-point GaussLegendre quadrature rule.

Example 4.1. Consider the following delay integral equation

$$u(t) - \int_{t-0.2}^{t} \left(\cos\left(\frac{1}{t+2}\right) + \frac{2\, s \cos\left(u\left(s\right)\right)}{s^2+1} \right) \mathrm{d}s = g(t), \qquad 0 \leq t \leq \frac{\mathrm{e}}{2},$$

where

$$g(t) = -0.2 \cos\left(\frac{1}{t+2}\right) + \ln\left(t^2+1\right) - \sin\left(\ln\left(t^2+1\right)\right) + \sin\left(\ln\left(t^2 - 0.4\, t + 1.04\right)\right),$$

and the exact solution is

$$u(t) = \ln\left(t^2+1\right), \qquad -0.2 \leq t \leq \frac{\mathrm{e}}{2}.$$

Solving these types of integral equations employing previous numerical methods have more difficulties, but we can easily compute the approximate solution for this problem utilizing the meshless method presented in this work based on some random nodes. Table 1 reports $\|e_N\|_\infty$, $\|e_N\|_2$ and the values of ratio at different numbers of N. We also compared the obtained errors for different numbers of N in Fig. 1 drawn in the logarithmic mode.

5 Conclusion

The current work has presented a computational scheme to solve delay Volterra integral equations. The offered technique has approximated the solution by the discrete collocation method based on locally supported RBFs constructed on a set of irregular knots. The appeared integrals are calculated via Gauss-Legendre quadrature formula. The specific structure of the method leads to much less computer memory and volume computing used compared to its global counterpart. The illustrative example shows the reliability and efficiency of the proposed scheme.

Table 1: Some numerical results for Example 4.1 using the proposed method.

	LGA			LIMQ		
N	$\|e_N\|_2$	$\|e_N\|_\infty$	Ratio	$\|e_N\|_2$	$\|e_N\|_\infty$	Ratio
10	1.59×10^{-2}	2.87×10^{-2}	–	1.98×10^{-2}	4.18×10^{-2}	–
20	6.91×10^{-4}	1.26×10^{-3}	4.52	3.88×10^{-3}	7.97×10^{-3}	2.39
30	3.22×10^{-5}	5.53×10^{-5}	7.69	4.75×10^{-4}	9.92×10^{-4}	5.14
40	9.69×10^{-7}	1.72×10^{-6}	12.06	6.01×10^{-5}	1.22×10^{-4}	7.27
50	3.98×10^{-8}	7.19×10^{-8}	14.23	5.69×10^{-6}	1.18×10^{-5}	10.48
60	1.78×10^{-9}	2.93×10^{-9}	17.55	4.72×10^{-7}	9.74×10^{-7}	13.69

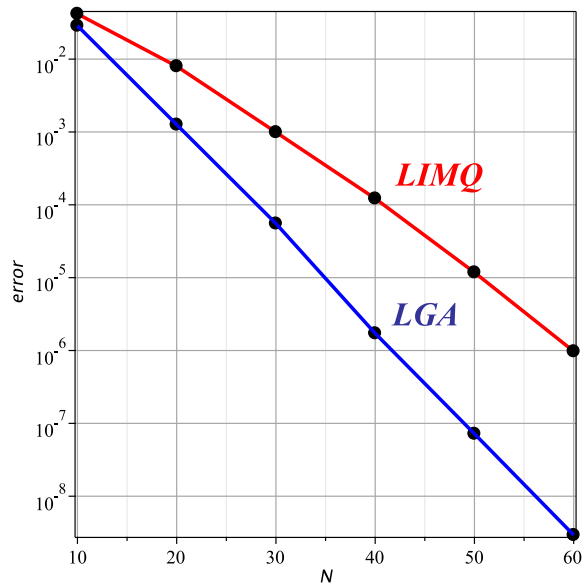

Figure 1: Distribution absolute error for Example 4.1.

References

[1] K. L. Cooke. An epidemic equation with immigration. *Math. Biosci.*, **29**(1-2):135–158, 1976.

[2] Z. Fu, Qiang Xi, Wen C., and A. Cheng. A boundary-type meshless solver for transient heat conduction analysis of slender functionally graded materials with exponential variations. *Comput. Math. Appl.*, 76(4):760–773, 2018.

[3] C. K. Lee, X. Liu, and S. C. Fan. Local multiquadric approximation for solving boundary value problems. *Comput. Mech.*, 30(5-6):396–409, 2003.

[4] H. Wendland. *Scattered Data Approximation.* Cambridge University Press, New York, 2005.

[5] W. Fang, Y. Wang, and Y. Xu. An implementation of fast wavelet Galerkin methods for integral equations of the second kind. *J. Sci. Comput.*, 20(2):277–302, 2004.

e-mail: `a.hosseinian@sci.basu.ac.ir`
e-mail: `passari@basu.ac.ir`

Simulation of Antiviral Drug Treatment Dynamics on COVID-19 Spread Using the Local Meshless Galerkin Method

Pouria Assari[1]

Department of Mathematics, Faculty of Science, Bu-Ali Sina University, Hamedan, Iran

Fatemeh Asadi-Mehreganr

Department of Mathematics, Faculty of Science, Bu-Ali Sina University, Hamedan, Iran

Abstract

The paper aims to develop a computational method for studying the impact of antiviral drugs on the novel coronavirus. The method utilizes the moving least squares (MLS) approximation functions in the discrete Galerkin method. The MLS is an effective technique for approximating unknown functions using locally weighted least squares polynomial fitting. The proposed algorithm is computationally efficient and easily implementable on computers. The validity and efficiency of the method are demonstrated through a numerical example.

Keywords: Antiviral Drug Treatment, Covid-19 pandemic, Moving least squares, Meshless method, Discrete Galerkin Method

AMS Mathematical Subject Classification [2010]: 92C60, 65M70

1 Introduction

To model the spread of a disease in a populations, a very logical choice is to use compartmental models. The three most commonly used compartments are Susceptible, S, which includes those who are healthyand can catch a disease. Infectives, I, which includes those who are infected and can also transmit the disease. Recovered, R, which includes those who are recovered from the disease and are immune to it. In order to estimate the final size of the epidemic when antiviral drugs are used, the SIR model is modified by categorizing infected individuals into two groups: treated (I_{tr}) and untreated (I_u), as described in equation (1). The fraction of infected individuals receiving antiviral drug treatment, denoted by f_0, is assumed to reduce the infection level by a factor σ [3]. As a result, the number of individuals who recover after receiving treatment increases, leading to a reduction in the overall number of infection cases.

$$\begin{cases} \frac{\mathrm{d}S}{\mathrm{d}t} = -\beta(t)\frac{S}{N}\left(I_u + \sigma I_{tr}\right), \\ \frac{\mathrm{d}I_u}{\mathrm{d}t} = (1-f_0)\beta(t)\frac{S}{N}\left(I_u + \sigma I_{tr}\right) - \gamma_u I_u, \\ \frac{\mathrm{d}I_{tr}}{\mathrm{d}t} = f_0\beta(t)\frac{S}{N}\left(I_u + \sigma I_{tr}\right) - \gamma_{tr} I_{tr}, \\ \frac{\mathrm{d}R}{\mathrm{d}t} = \gamma_u I_u + \gamma_{tr} I_{tr}. \end{cases} \tag{1}$$

[1]Speaker

This system is supplemented by initial data

$$S(t_0) = S_0, \qquad I_u(t_0) = I_{u,0}, \qquad I_{tr}(t_0) = I_{tr,0} \qquad \text{and} \qquad R(t_0) = R_0.$$

The parameters γ_u and γ_{tr} are the average recovery rates for the untreated and treated individuals, respectively. The meshless methods are based on scattered data approximations that estimate a function without generating a mesh in the domain. These methods have various advantages, most of which can be explained by what is known in the literature as RBFs, or based on the MLS method [2].

2 Meshless local discrete Galerkin method

Given data values of the function $\mathbf{u}(t)$ at certain data sites $\mathcal{T} = \{t_1, ..., t_N\}$ selected in the interval $[a, b]$. For $t \in [a, b]$, the value $s_{\mathbf{u},\mathcal{T}}(t)$ of the MLS approximation is given by the solution of

$$\min \left\{ \sum_{i=1}^{N} \left[\mathbf{u}(t_i) - p(t_i)\right]^2 w(t, t_i) : p \in \Pi_m(\mathbb{R}) \right\}, \tag{2}$$

where $w : [a, b] \times [a, b] \to [0, \infty]$ is a continuous weight function. Let the set $\{p_0, ..., p_m\}$ form a basis of the space $\Pi_m(\mathbb{R})$ and the data points $\{t_1, ..., t_N\}$ be a set of disjoint points in the interval $[a, b]$, then the problem (2) has a unique solution and the value $s_{\mathbf{u},\mathcal{T}}(t)$ can be considered as

$$s_{\mathbf{u},\mathcal{T}}(t) = \sum_{i=1}^{N} \mathbf{u}(t_i)\psi_i(t), \tag{3}$$

where the basis functions $\psi_i(t)$ are a combination of the weight function.

In the following, we solve the system (1) using the MLS Galerkin method. By employing integration, we reduce the system (1) into two integral equations as follows:

$$I_u(t) = -\frac{S_0}{\beta(t)}(1 - f_0) \exp\left(-\frac{1}{N_0}\int_0^t \beta(\tau)\left(I_u(\tau) + \sigma I_{tr}(\tau)\right) \mathrm{d}\tau\right) \\ -\gamma_u \int_0^t I_u(\tau)\mathrm{d}\tau + I_{u,0}, \tag{4}$$

and

$$I_{tr}(t) = -\frac{S_0}{\beta(t)} f_0 \exp\left(-\frac{1}{N_0}\int_0^t \beta(\tau)\left(I_u(\tau) + \sigma I_{tr}(\tau)\right) \mathrm{d}\tau\right) \\ -\gamma_{tr} \int_0^t I_{tr}(\tau)\mathrm{d}\tau + I_{tr,0}, \tag{5}$$

we require N nodal points $\{t_1, ..., t_N\}$ selected in the interval $[a, b]$ and we estimate the unknown functions $I_u(t)$ and $I_{tr}(t)$by the MLS as follows:

$$I_u(t) \approx I_{u,N}(t) = \sum_{i=1}^{N} c_{u,i}\psi_i(t), \qquad I_{tr}(t) \approx I_{tr,N}(t) = \sum_{i=1}^{N} c_{tr,i}\psi_i(t). \tag{6}$$

By replacing the expansion (6) with $I_u(t)$ and $I_{tr}(t)$ in (4), and taking inner product $\langle ., \psi_j \rangle$ upon both sides, and using the composite m_N-point Gauss-Legendre rule with M uniform subdivisions relative to the coefficients $\{v_k\}$ and weights $\{w_k\}$ in interval $[-1, 1]$, we have

$$\frac{\Delta t}{2} \sum_{k=1}^{m_N} \sum_{q=1}^{M} w_k \left[I_{u,N}(\theta_k^q)\psi_j(\theta_k^q) + \mathcal{H}[j, \theta_k^q, \eta_r^p] - I_{u,0}\psi_j(\theta_k^q)\right] = 0, \tag{7}$$

where

$$\mathcal{H}[j,\theta_k^q,\eta_r^p] = \frac{(1-f_0)S_0}{\beta(\theta_k^q)} \exp\left(\frac{-\Delta s(\theta_k^p)}{2N_0} \sum_{p=1}^{m_N}\sum_{r=1}^{M} w_p \beta(\eta_r^p(\theta_k^q)) \left(I_{u,N}(\eta_r^p(\theta_k^q)) \right.\right.$$
$$\left.\left. + \sigma I_{tr,N}(\eta_r^p(\theta_k^q))\right)\right) \psi_j(\theta_k^q) + \gamma_u \frac{\Delta s(\theta_k^p)}{2} \sum_{p=1}^{m_N}\sum_{r=1}^{M} w_p I_{u,N}(\eta_r^p(\theta_k^q))\psi_j(\theta_k^q).$$

Similarly, equation (5) can also be approximated. Therefore, by the solving systems for the unknowns $\{\hat{c}_{u,i}\}_{i=1}^N$ and $\{\hat{c}_{tr,i}\}_{i=1}^N$ the values of $I_u(t)$ and $I_{tr}(t)$ can be approximated. As a result, we have

$$R_N(t) = \gamma_u I_{u,N} + \gamma_{tr} I_{tr,N}.$$

3 Numerical result

A virus transmission model based on simulating crowd flow is used to simulate the spread of Covid-19 in a population of 1000218 individuals. Among them, 1000000 individuals are susceptible, 200 are receiving treatment for infection, and the rest are untreated infections. The model is solved for a time period of 50 days. For equation (1), the following parameters are chosen [1, 3]:

$$\beta(t) = \ln(1.01)exp(-t/40), \qquad \sigma = 0.5, \qquad \gamma_u = \ln(1.1), \qquad \gamma_{tr} = \ln(1.9).$$

Figure 1 shows the numerical results obtained from the solution of this model using the proposed method, in which we considered $f_0 = 0.1$. This Figure shows that the number of population who recover after receiving treatment increases and leads to a decrease in the overall number of infection cases.

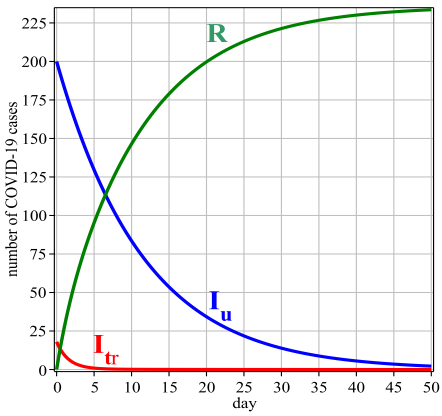

Figure 1: Graphs of $I_u(t)$, $I_{tr}(t)$ and $R(t)$

References

[1] F. Asadi-Mehregan, P. Assari and M. Dehghan. *The numerical solution of a mathematical model of the Covid-19 pandemic utilizing a meshless local discrete Galerkin method*, Engineering with Computers, 39 (2023) 3327–3351.

[2] G. E. Fasshauer. *Meshfree Methods, Handbook of Theoretical and Computational Nan-otechnology*, American Scientific Publishers, (27) (2006) 33–97.

[3] Z. Feng, S. Towers and Y. Yang. *Modeling the effects of vaccination and treatment on pandemic influenza*, An Official Journal of the American Association of Pharmaceutical Scientists, 13 (2011) 427–437.

e-mail: passari@basu.ac.ir
e-mail: f.asadi@sci.basu.ac.ir

Survey To Epidemic Modeling[2]

Aynaz Darbay[3]

Master of Science, Department of BioMathemtics, Faculty of mathematics statistics computer science, University of Tabriz, Tabriz, Iran(a.darbay1402@ms.tabrizu.ac.ir)

Abstract

In this paper, we introduce basic epidemic models without demographics and also compare them with data.that we can optimally control the epidemic by using a dynamical system.SIR and SIS models are the models that are studied in this section. The SIR model is studied for diseases in which there is no possibility of the person becoming infected after contracting the disease (after becoming infected) and passing the recovery period. But the SIS epidemic model is studied for diseases that a person can get the same disease again after passing the recovery period and get infected,like a cold. In the following, assuming that the total population size (N) is constant, we will study the Kermac-McKendrick model, and in the SIS model, we will go through the stages of formulation in order to present the model using the logistic equation.

Keywords: Dynamical Systems, Optimal control, Epidemic
AMS Mathematical Subject Classification [2010]: 13D45, 39B42

1 Introduction

In the history of medical research, there are reports where vaccination did not eradicate the disease. These unexpected failures can be due to the ineffectiveness of vaccination, hiding symptoms of illness in people's bodies,or physical contact rate with infectious people. With this, we have tried to reduce the number of infected people to their minimum amount by prescribing medicine to the infected and quarantining them. Here we divide the population into three separate groups: S(Susceptible), I(Infected), R(Recovery) and also we consider the total population size remains constant. In general, we have two types of prevalence rates, one is the standard prevalence rate and the other is the non-standard prevalence rate, which we have also considered the psychological effects of the epidemic. That is, when the awareness of a disease becomes widespread, and the methods of preventing the disease become known to everyone, people will try to avoid being in crowded places as much as possible, or do not have physical contact with suspicious people. In general, they will prevent the disease with different methods. Therefore, in this case, the number of infected individuals decreases. In general and in summary, in this article, we introduce a special strategy on the SIR model to control infectious disease, where the parameters are time-varying.

Definition 1.1. A disease is infectious if the causative agent, whether a virus, bacterium, protozoa, or toxin, can be passed from one host to another through modes of transmission such as direct physical contact, airborne droplets, water or food, or mother to newborn.

Definition 1.2. If the number of cases rises above the usual average within a short period of time, a disease outbreak occurs.

Definition 1.3. If fresh susceptibles are added to the population, either from birth or migration or if reinfection occures easily, the epidemic may persist and the infection may remain in the population over a long period of time. In this case, the disease is said to endemic in the population.

1.1 SIR Epidemic Model

In SIR epidemic model we have three classes in here:

-susceptible (The size of this class is usually denoted by S)
-infectious/infected (The size of this class is usually denoted by I)
-removed/recovered (The size of this class is usually denoted by R)

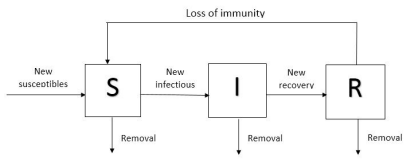

1.2 Kermac-McKendrik Model

The KermackMcKendrick model is based on several assumptions

-There are no births and deaths in the population.
- All recovered individuals have completely immuned and cannot be infected again.
-The population is closed, that is no one from the outside enters the population, and no one leaves the population.
-Total population size N(t)=S(t)+I(t)+R(t)$\Rightarrow$ *constant*.

1.3 Deriving the KermackMcKendrick Epidemic Model

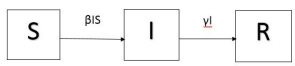

$S'(t) = -\beta IS$
$I'(t) = \beta IS - \gamma I$
$R'(t) = \gamma I$

1.4 SIR model with birth and death

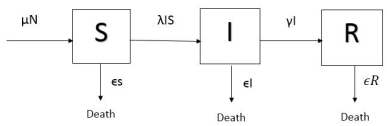

$S'(t) = \mu N - \lambda IS - Death$
$I'(t) = \lambda IS - \gamma I - Death$

$R'(t) = \gamma I - Death$
$N'(t) = \mu N - D_1 S - D_2 I - D_3 R$

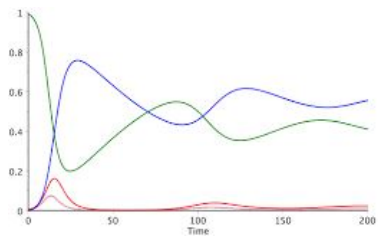

1.5 SEIR Model

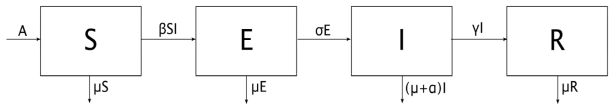

$S'(t) = A - \beta IS - \mu S$
$E'(t) = \beta IS - \sigma E - \mu E$
$I'(t) = \sigma E - (\mu + a)I - \gamma I$
$R'(t) = \gamma I - \mu R$
$N'(t) = S(t) + E(t) + I(t) + R(t)$
total population size N is not constant here.

1.6 SVIR Model(Immunization)

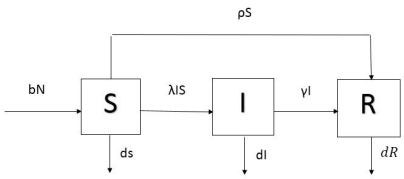

SIR model with vaccination:
$S' = bN - \lambda IS - dS - \rho S$
$I' = \lambda IS - (d + \gamma)I$
$R' = \rho S + \gamma I - dR$
$N = S + I + R$

1.7 SVIR Model

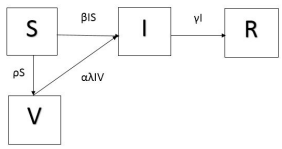

SIR model with a leaky vaccine:
$S' = -\beta IS - \rho S$

$I' = \beta IS + \alpha\lambda IV - \gamma I$
$R' = \gamma I$
$V' = \rho S - \alpha\lambda IV$

1.8 SQIR Model

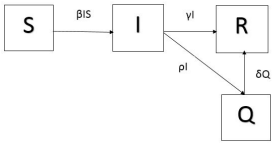

SIR model with Quarantine:
$S' = -\beta IS$
$I' = \beta IS - \gamma I - \rho I$
$R' = \gamma I + \delta Q$
$Q' = \rho I - \delta Q$

1.9 SIR model with medicine effect

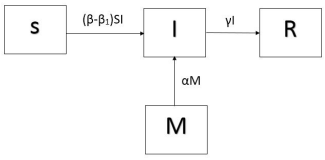

$S' = -(\beta - \beta_1)IS$
$I' = (\beta - \beta_1)IS - \gamma I - \alpha M$
$R' = \gamma I$
$M' = -\alpha M$

References

[1] Michael Y . Li, *An Introduction to mathematical Modeling of Infectious Diseases*, Mathematical and Statistical Sciences, University of Alberta, Edmonton, AB.

[2] L. RASS AND J. RADCLIFFE, Spatial deterministic epidemics, vol. 102 of Mathematical Surveys and Monographs, American Mathematical Society, Providence, RI.

[3] C. RHODES AND R. ANDERSON, Epidemic thresholds and vaccination in a lattice model of disease spread, Theoretical Population Biology, pp.

[4] H. J. ROSE, The use of amantadine and influenza vaccine in a type a influenza epidemic in a boarding school, Journal of Royal College of General Practitioners, pp.

e-mail: `a.darbay1402@ms.tabrizu.ac.ir`

Simulation of thebehavior of cancer cell invasion of surrounding tissue using direct mesh-less local Petrov-Galerkin method

Ali Ebrahimijahan[1]
Department of Mathematics, Faculty of Mathematical Sciences, Alzahra University, Tehran, Iran

Yadollah Ordokhani
Department of Mathematics, Faculty of Mathematical Sciences, Alzahra University, Tehran, Iran

Abstract

In this work, we use a mesh-less weak form based on the direct mesh-less local Petrov-Galerkin (DMLPG) method to numerically solve a mathematical model of cancer cell invasion of tissue. The DMLPG method employs the generalized moving least-square (GMLS) approximation and the local weak form of the equation. Time discretization is achieved using a nine-stage Runge-Kutta method with non-decreasing abscissas, offering flexibility in time step width. The model comprises time-dependent reaction-diffusion-taxis partial differential equations describing interactions between cancer cells, the extracellular matrix, and matrix degradation enzymes. We also present numerical simulations demonstrating cancer cell invasion behavior over time.

Keywords: Cancer invasion, Reaction-diffusion-taxis partial differential equations, Generelized moving least squares approximation, Mathematical biology,
Mathematics Subject Classification [2010]: 81T80, 92B05, 80M22

1 Introduction

Mathematical modeling of tumor growth has evolved significantly since Hill's 1928 work on oxygen diffusion in tissues. In 1955, Thomlinson and Gray introduced a model for oxygen diffusion and consumption by tumor cells. Over the years, modeling various cancer growth phases has garnered extensive research attention. Hanahan and Weinberg identified and later expanded the hallmarks of cancer in 2000 and 2011. Subsequent models addressed tissue invasion, including contributions by Gatenby, Gawlinski, Perumpanani, Anderson, Chaplain, and others, focusing on factors like cell adhesion and the role of the extracellular matrix in cancer invasion. In this paper, we investigate the mathematical modeling of cancer cell invasion into tissue (solid tumor growth at the avascular stage) within a two-dimensional space using the following system of time-dependent partial differential equations over the square domain $\Omega = [0,1]^2 := \left\{\boldsymbol{x} := (x,y)^T \in \mathbb{R}^2 : 0 \le x, y \le 1\right\}$ in nondimensionalized form [1, 3].

$$\begin{cases} \frac{\partial n}{\partial t} = d_n \nabla^2 n - \gamma \nabla \cdot (n \nabla f), \\ \frac{\partial f}{\partial t} = -\eta m f, \\ \frac{\partial m}{\partial t} = d_m \nabla^2 m + \alpha n - \beta m, \end{cases} \tag{1}$$

where d_n is a constant denoting the tumor cell random motility coefficient, γ is a constant representing the haptotactic coefficient, η is a positive constant for the degradation coefficient of the extracellular matrix

[1]Speaker

(ECM). Additionally, d_m is the diffusion coefficient for matrix degrading enzymes (MDEs), α is the constant production coefficient of MDE by tumor cells, and β is a constant representing natural decay. The initial conditions are specified as follows [1, 3]:

$$n(\boldsymbol{x},0) = \exp\left(-\frac{r^2}{\epsilon}\right), \quad f(\boldsymbol{x},0) = 1 - 0.5n(\boldsymbol{x},0), \quad m(\boldsymbol{x},0) = 0.5n(\boldsymbol{x},0), \quad \text{in } \Omega, \tag{2}$$

where $r := \left\|\boldsymbol{x} - (0.5, 0.5)^T\right\|_2$, with boundary conditions specified as follows:

$$n.\left(-d_n \nabla n + n\chi \nabla f\right) = 0, \quad n.(\nabla f) = 0, \quad n.\left(-d_m \nabla m\right) = 0, \tag{3}$$

on $\partial\Omega$, where $\mathbf{n}$ denotes the outward normal vector on the boundary $\partial\Omega$. In Eq. (1), $n(\boldsymbol{x},t)$ represents the concentration of tumor cells, $f(\boldsymbol{x},t)$ denotes the concentration of ECM, and $m(\boldsymbol{x},t)$ indicates the concentration of matrix metalloproteinases (MMPs), all as functions of spatial and temporal variables.

2 The generalized MLS approximation

Weighted residual methods are widely employed for numerically solving differential equations. These methods underpin various numerical techniques such as spectral methods, finite element methods, finite volume methods, and mesh-less methods. The core idea of these approaches is to represent the approximate solution as a linear combination of known basis functions. To demonstrate the GMLS approximation, consider a set of scattered nodes along the boundary of the problem domain, denoted by $\Omega \cup \partial\Omega$. These nodes are represented as $\mathbf{X} = \{\mathbf{x}_i\}_{i=1}^N$ (see Fig. 1) with i ranging from 1 to N. The GMLS method seeks to approximate the functional $\{u_i(\phi)\}_{i=1}^N$, where ϕ is an unknown function in the dual space of $C(\Omega)$, denoted by $\mathbb{C}(\Omega)^\star$. The approximation of $u(\phi)$ in the GMLS method is expressed as [4]:

$$u(\phi) = \widehat{u}(\phi) = \sum_{i=1}^{N} \lambda_i(u)\phi(\mathbf{x}_i), \quad \forall \phi \in \mathbb{P}_m^h \subset \mathbb{C}^m(\Omega), \tag{4}$$

where λ_i are the linear coefficients, and $\widehat{u}(\phi)$ represents a linear combination of $\phi(\mathbf{x}_i)$, $\mathbb{P}_m^h = \text{span}\{p_1, p_2, \ldots, p_Q\}$ is a d-dimensional subspace and Q is the total number of basis monomials.

The coefficients λ_i are determined through the GMLS approximation by minimizing the weighted residual:

$$\sum_{i=1}^{N} \omega_i \left(p(\mathbf{x}_i) - \phi(\mathbf{x}_i)\right)^2, \tag{5}$$

for all $p \in \mathbb{P}_m^h$.

The GMLS approximation $\widehat{\lambda(u)}$ is given by $u(p^*)$, where p^* is the minimizer of this quadratic form. Consequently, the optimal solution $\lambda^*(u) \in \mathbb{R}^N$ for (5) is:

$$\lambda^*(u) = u(\mathbf{p}^T)(\mathbf{P}^T\mathbf{W}\mathbf{P})^{-1}\mathbf{P}^T\mathbf{W}, \tag{6}$$

where $\mathbf{P}^T$ represents the basis monomials evaluated at the scattered nodes, W is a diagonal weight matrix, and $u(\mathbf{p}^T)$ denotes the evaluations of the functional u on the basis monomials.

3 DMLPG formulation and time discretization for governing equation

To develop the DMLPG (Discrete Moving Least Squares Particle Galerkin) methods for solving Eq. (1), it is essential to derive the local weak formulation. This process involves considering a set of internal and boundary nodes, denoted by $\mathbf{X} = \{\mathbf{x}_i\}_{i=1}^N$, within the problem domain. The arrangement of these nodes can be either regular or irregular. Additionally, local subdomains $\Omega_r \subset \bar{\Omega}$ are defined around each node. The shapes of Ω_r can vary, including geometries such as circles or squares of different sizes (see Fig. 1). The

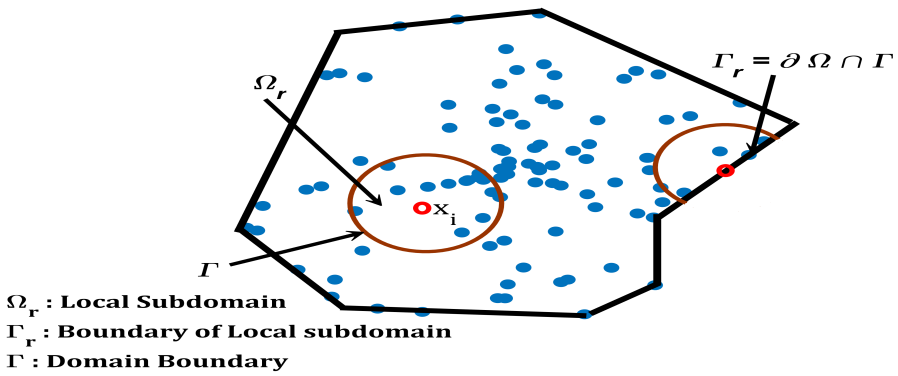

Figure 1: Arrangement of scattered nodes within an irregular domain

local weak form of (1) is derived by multiplying both sides of the equation with a suitable test function, such as v_n, v_f and v_m.

$$\begin{cases} \int_\Omega \frac{\partial n}{\partial t} v_n d\Omega = \int_\Omega \left(d_n \nabla^2 n - \gamma \nabla \cdot (n \nabla f)\right) v_n d\Omega \\ \int_\Omega \frac{\partial f}{\partial t} v_f d\Omega = -\int_\Omega \eta m f v_f d\Omega, \\ \int_\Omega \frac{\partial m}{\partial t} v_m d\Omega = \int_\Omega d_m \nabla^2 m v_m d\Omega + \int_\Omega \alpha n v_m d\Omega - \int_\Omega \beta m v_m d\Omega, \quad \forall v_n, v_f, v_m \in H^1(\Omega). \end{cases} \tag{7}$$

Using divergence theorem for the global weak form (7) gives

$$\begin{cases} \frac{\partial}{\partial t} \int_\Omega n v_n d\Omega = -d_n \int_\Omega \nabla n . \nabla v_n d\Omega + \gamma \int_\Omega n \nabla f . \nabla v_n d\Omega \\ \frac{\partial}{\partial t} \int_\Omega f v_f d\Omega = -\eta \int_\Omega m f v_f d\Omega \\ \frac{\partial}{\partial t} \int_\Omega m v_m d\Omega = -d_m \int_\Omega \nabla m . \nabla v_m d\Omega + \alpha \int_\Omega n v_m d\Omega - \beta \int_\Omega m v_m d\Omega, \quad \forall v_n, v_f, v_m \in H^1(\Omega) \end{cases} \tag{8}$$

the linear system of algebraic equations will be obtained:

$$\frac{\partial w}{\partial t} = G(w). \tag{9}$$

where

$$\frac{\partial w}{\partial t} = \begin{cases} \frac{\partial}{\partial t} \int_\Omega n v_n d\Omega \\ \frac{\partial}{\partial t} \int_\Omega f v_f d\Omega \\ \frac{\partial}{\partial t} \int_\Omega m v_m d\Omega \end{cases}, \quad and \quad G(w) = \begin{cases} -d_n \int_\Omega \nabla n . \nabla v_n d\Omega + \gamma \int_\Omega n \nabla f . \nabla v_n d\Omega \\ -\eta \int_\Omega m f v_f d\Omega \\ -d_m \int_\Omega \nabla m . \nabla v_m d\Omega + \alpha \int_\Omega n v_m d\Omega - \beta \int_\Omega m v_m d\Omega, \end{cases}$$

The integrals in Eq. (8) can be approximated using the GMLS method as follows.

$$\begin{aligned} u_{1,k}(\phi) &:= \int_{\Omega_r} u \nu d\Omega &&\approx \widehat{u_{1,k}(\phi)} = \textstyle\sum_{i=1}^N \lambda_{1,i}(x_k)\, u(x_i), \\ u_{2,k}(\phi) &:= \int_{\Omega_r} \nabla u \nabla \nu d\Omega &&\approx \widehat{u_{2,k}(\phi)} = \textstyle\sum_{i=1}^N \lambda_{2,i}(x_k)\, u(x_i), \\ u_{3,k}(u) &:= \int_{\Omega_r} \nabla u \nu d\Omega &&\approx \widehat{u_{3,k}(\phi)} = \textstyle\sum_{i=1}^N \lambda_{3,i}(x_k)\, u(x_i), \end{aligned} \tag{10}$$

where u and v can be n, f, m and v_n, v_f, v_m, respectively. Different variants of DMLPG methods can be devised by choosing particular functions as test functions. The primary distinction among these methods

lies in the selection of test functionals used to formulate the local weak forms of the problem. In DMLPG1, the test functionals are the point values of the solution and its derivatives at specific nodes. In DMLPG2, the test functionals consist of integrals of the solution and its derivatives over subdomains. In DMLPG5, the test functionals are integrals of the solution and its derivatives over subdomains, multiplied by a Heaviside step function. The selection of test functionals influences the accuracy and efficiency of the DMLPG method. For instance, in DMLPG1, certain functionals can be excluded if the test function vanishes on the boundary, whereas in DMLPG5, some functionals are unnecessary due to the presence of the Heaviside step function. In our numerical calculations, we utilize the following Gaussian weight function [4]:

$$\omega_i(\mathbf{x}) = \begin{cases} \frac{\exp\left(-\mu^2 d_i^2\right)-\exp\left(-\mu^2 d_0^2\right)}{1-\exp\left(-\mu^2 d_0^2\right)}, & 0 \le d \le d_0, \\ 0, & \text{elsewhere} \end{cases}.$$

For discretization of time variable, some preliminary is required. We define $t_n = n\tau, \quad n = 0, 1, \ldots, N_t$, in which $\tau = \frac{T}{N_t}$, denotes the step size of time variable. In this manuscript, we utilize the third-order explicit SSP Runge-Kutta method with non-decreasing abscissas ($eSSPRK^+(9,3)$) with 9-stage for Eq. (9) as follows [2]:

$$\begin{aligned} &w^{(0)} = w^n, \quad w^{(i)} = w^{(i-1)} + \frac{1}{6}\tau G\left(w^{(i-1)}\right) \text{ for } i = 1, \ldots, 4, \\ &w^{(5)} = \frac{1}{5}w^n + \frac{4}{5}\left(\frac{1}{6}\tau G\left(w^{(4)}\right) + w^{(4)}\right), \quad w^{(6)} = \frac{1}{4}\left(w^n + \frac{1}{6}\tau G\left(w^n\right)\right) + \frac{3}{4}\left(\frac{1}{6}\tau G\left(w^{(5)}\right) + w^{(5)}\right) \\ &w^{(7)} = \frac{1}{3}w^{(2)} + \frac{2}{3}\left(\frac{1}{6}\tau G\left(w^{(6)}\right) + w^{(6)}\right), \quad w^{(8)} = \frac{1}{6}\tau G\left(w^{(7)}\right) + w^{(7)}, \quad w^{n+1} = w^{(8)} + \frac{1}{6}\tau G\left(w^{(8)}\right). \end{aligned} \tag{11}$$

4 Numerical result

Example 4.1. In this model, following [14, 20], we assume the tumor cell equation (the first equation of (1.1)) has no birth or death terms. The parameters are set as $d_n = 0.001$, $d_m = 0.001$, $\gamma = 0.005$, $\eta = 10$, $\alpha = 0.1$, $\beta = 0$, and $\epsilon = 0.0025$. The initial conditions for the concentrations of tumor cells and MDE are given by:

$$n(x, y, 0) = \exp\left(-\frac{(x-0.5)^2 + (y-0.5)^2}{\epsilon}\right), \quad m(x, y, 0) = 0.5n(x, y, 0), \quad (x, y)^T \in [0, 1]^2,$$

and

$$f(x, y, 0) = \begin{cases} 1 - 0.5n(x, y, 0), & x^2 + y^2 \le 0.25, \\ 1 - 0.5|\sin(\frac{\pi}{2}(x-0.5))| - 0.5\exp\left(-\frac{0.25}{\epsilon}\right), & \text{o.w.} \end{cases}$$

The numerical simulations of n and f with spatial step $h = \frac{1}{80}$ and time step $\tau = \frac{1}{1000}$ are illustrated in Fig. 2 at various time points. This figure shows that at $t = 4$, the symmetry of the tumor cell distribution breaks, leading to regions of high tumor cell density. As time progresses, these high-density regions continue to invade further. Additionally, it is observed that a significant concentration of tumor cells migrates along collagen fibers and degrades ECM proteins by secreting MDEs. Notably, two crucial factors influencing the final tumor cell density are the heterogeneity of the ECM and the haptotactic response of cancer cells to the MDEs resulting from matrix degradation.

Acknowledgments

We announce that this research was done in the Scientific Computing and Modeling Research Laboratory of Alzahra University.

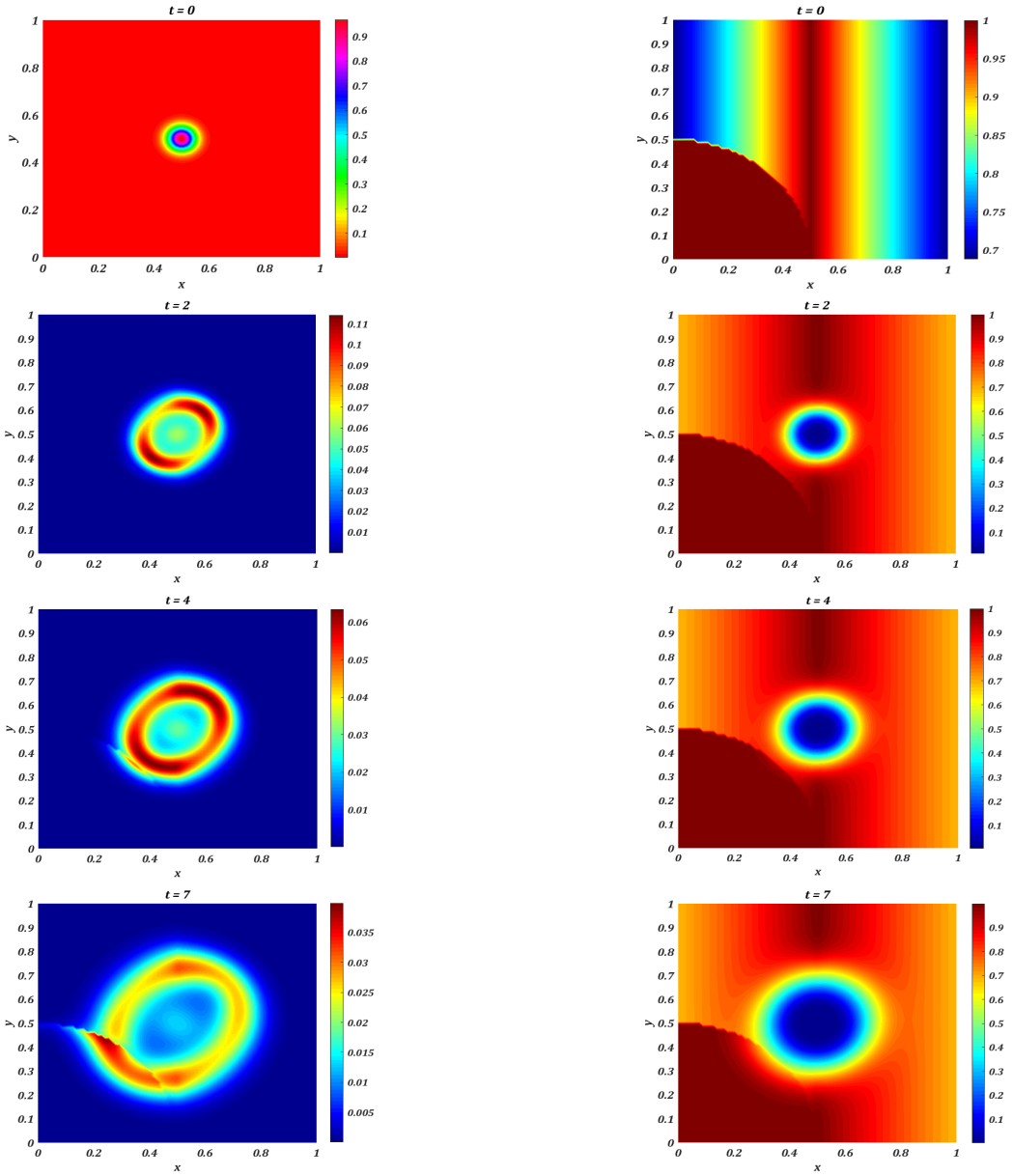

Figure 2: Spatio-temporal evolution of tumor cell density (left) and ECM (right) from the numerical simulation with EFG method at $t = 0, 2, 4$ and $t = 7$

References

[1] A.R.A. Anderson, M.A.J. Chaplain, E.L. Newman, R.J.C. Steele, A.M. Thompson, *Mathematical modelling of tumour invasion and metastasis*, J. Theory Med. 2 (2000) 129-154.

[2] S. Gottlieb, C. W. Shu and E. Tadmor, *Strong stability-preserving high-order time discretization methods*, SIAM Rev. 43 (2001) 89-112.

[3] L. Preziosi, *Cancer Modelling and Simulation*, First ed., Chapman Hall/CRC, USA, 2003.

[4] Mirzaei, D., and Schaback, R. *Direct mesh-less local petrov-galerkin (DMLPG) method: a generalized MLS approximation*, Applied Numerical Mathematics 68 (2013), 73-82.

Email: `A.Ebrahimijahan@alzahra.ac.ir`
Email: `ordokhani@alzahra.ac.ir`

Dynamics of Infectious Diseases: Exploring Bifurcations in a Discrete-Time SIR Epidemic Model with Logistic Growth

Zohre Eskandari[1]

Department of Mathematics, Faculty of Science, Fasa University, Fasa, 74616-86131, Iran

Abstract

This research paper explores the dynamics of infectious diseases using a discrete-time SIR epidemic model with logistic growth, focusing on local bifurcations analytically and numerically.

Keywords: Discrete-time SIR model, Logistic growth, Bifurcations

AMS Mathematical Subject Classification [2010]: 13D45, 39B42

1 Introduction

Infectious diseases continue to pose a significant threat to global health, necessitating a deep understanding of their dynamics for the development of effective control and prevention strategies. The complexity of disease transmission, exacerbated by seasonal variations, underscores the need for mathematical models like the SIR model to unravel these intricacies.

Previous research has emphasized the chaotic oscillations inherent in infectious diseases, highlighting the importance of comprehensive models that can capture the nuances of disease spread. Studies focusing on epidemic models with constraints such as limited medical resources and treatment capacity have shed light on the multifaceted nature of disease dynamics.

In epidemiological models, the exponential increase in susceptible individuals in the absence of infection is a critical factor to consider. While some models discuss constant input saturation rates, the logistic growth hypothesis for susceptible populations appears more reasonable and applicable in real-world scenarios.

The SIR epidemic model, with its incorporation of logistic growth and modified saturated incidence rates, offers a nuanced perspective on disease dynamics. By exploring parameter variations and critical values for bifurcations, this study aims to enhance our understanding of infectious disease dynamics and improve disease management strategies.

[1]Speaker

2 Mathematical Model

In epidemiological models, the number of susceptible individuals increases exponentially in the absence of infection. Reference [1] discusses models with a constant input saturation rate. However, the logistic growth hypothesis for the susceptible population appears more reasonable and applicable. Surprisingly, the potential population's logistic growth has not garnered significant attention.
The SIR epidemic model,

$$\begin{cases} \dot{S} = \rho S\left(1 - \frac{S}{\kappa}\right) - \frac{bSI}{1+\alpha S}, \\ \dot{I} = \frac{bSI}{1+\alpha S} - (a+m+g)\, I, \\ \dot{R} = gI - mR, \end{cases} \tag{1}$$

as proposed by Akrami and Atabaigi [5], addresses the susceptible population by incorporating a modified saturated incidence rate. In the epidemic model described by Equation (1), $S(t)$, $I(t)$ and $R(t)$ represent the numbers of susceptible, infective and recovered individuals at time t, respectively. The dot notation indicates the derivative with respect to t. The parameters in the model are:

- ρ: the intrinsic growth rate of the susceptible population.
- κ: the carrying capacity
- α: the disease-induced death rate
- g: the recovery rate of the infective individuals
- m: the death rate of the population
- b: a positive constant
- α: a positive constant

The term $\frac{bSI}{1+\alpha S}$ represents the saturated contact rate, which models the transmission of the disease from infective to susceptible individuals.
To analyze the epidemic model, we can isolate the first two equations in Equation (1) because they are independent of the third. Therefore, we focus on the reduced system:

$$\begin{cases} \frac{dS}{dt} &= \rho S\left(1 - \frac{S}{\kappa}\right) - \frac{bSI}{1+\alpha S}, \\ \frac{dI}{dt} &= \frac{bSI}{1+\alpha S} - dI, \end{cases} \tag{2}$$

where $d = a + m + g$.
In managing short-term outbreaks, discrete-time models prove invaluable for informed decision-making. Specifically tailored for SIR epidemic scenarios, discrete-time systems offer enhanced suitability. This study delves into the dynamics of a discrete-time SIR epidemic model.

Utilizing the Euler method on the continuous-time formulation yields the following set of discrete equations:

$$\begin{cases} S_{n+1} &= S_n + \sigma\left(\rho S_n\left(1 - \frac{S_n}{\kappa}\right) - \frac{bS_nI_n}{1+\alpha S_n}\right), \\ I_{n+1} &= I_n + \sigma\left(\frac{bS_nI_n}{1+\alpha S_n} - dI_n\right), \end{cases} \tag{3}$$

Here, σ denotes the time step interval.

3 Analytical Investigation of the Discrete-Time SIR Epidemic Model

In this section, we analytically investigate the dynamical behaviors of the discrete-time SIR epidemic model. We focus on the stability and bifurcations of the model.

To analyze the dynamics of the discrete-time SIR epidemic model given by Equation (3), we first need to determine the fixed points of the system. The fixed points are the values of (S, I) that satisfy the following equations:

$$\begin{cases} S &= S + \sigma\left(\rho S\left(1 - \frac{S}{\kappa}\right) - \frac{bSI}{1+\alpha S}\right), \\ I &= I + \sigma\left(\frac{bSI}{1+\alpha S} - dI\right). \end{cases}$$

Solving these equations, we find that the model has three fixed points:

1. $F^{(0)} = (0, 0)$,
2. $F^{(1)} = (\kappa, 0)$,
3. $F^{(*)} = \left(-\frac{d}{\alpha d - b}, -\frac{\rho(\alpha d\kappa - b\kappa + d)}{(\alpha d - b)^2\kappa}\right)$.

The existence of the fixed point $F^{(*)}$ is subject to the condition $\frac{\kappa b}{d(1+\alpha\kappa)} > 1$.

3.1 Bifurcation Analysis

Considering the fixed points, the fixed point $F^{(*)}$ holds greater significance from a biological perspective. Therefore, we investigate the local bifurcations of model (3) at this particular point.

Theorem 3.1. *The fixed point $F^{(*)}$ experiences a period doubling bifurcation when the parameter κ reaches the critical value κ_*, which is given by:*

$$\kappa_* = -\frac{\sigma\rho d\left(\alpha d^2\sigma - bd\sigma - 2\alpha d - 2b\right)}{\alpha^2 d^3\rho\sigma^2 - 2\alpha b d^2\rho\sigma^2 - 2\alpha^2 d^2\rho\sigma + b^2 d\rho\sigma^2 + 2\alpha b d\rho\sigma - 4\alpha b d + 4b^2}.$$

This critical value marks the onset of a period doubling bifurcation, where the fixed point $F^{(*)}$ loses its stability and the system exhibits a period-doubled oscillation.

Theorem 3.2. *The fixed point $F^{(*)}$ experiences a Neimark-Sacker bifurcation when the parameter κ reaches the critical value κ_*, which is given by:*

$$\kappa_* = -\frac{\alpha d^2\sigma - bd\sigma - \alpha d - b}{\alpha^2 d^2\sigma - 2\alpha b d\sigma - \alpha^2 d + b^2\sigma + \alpha b}.$$

At this critical value of κ, the fixed point $F^{(*)}$ loses its stability, and a stable invariant closed curve bifurcates from the fixed point. This bifurcation leads to quasi-periodic oscillations in the system, where the trajectories converge to a torus in the phase space.

4 Numerical Investigation of the Discrete-Time SIR Epidemic Model

In this section, we explore the dynamical behavior of the discrete-time SIR epidemic model described by Equation (3) through numerical investigation. We employ the numerical continuation method, which enables systematic exploration of the parameter space. By doing so, we identify bifurcations and transitions in the

system's behavior, leading to a comprehensive understanding of the model's dynamics. In this section for dynamical behavior of the model (3) numerically, we use the numerical continuation method, [6].
In this section, we fix the following parameter values:

$$b = 1,\ \alpha = 0.4,\ d = 1,\ \rho = 6, \sigma = 1.$$

We treat the parameter κ as a free parameter, allowing it to vary while the other parameters remain constant. By systematically varying the parameter κ, we identify the following codimension one bifurcation:

1. As the parameter κ crosses the critical value $\kappa_* = 2.741935484$, the fixed point

$$F^{(*)} = (1.666666667, 3.921568627)\,,$$

   undergoes a period-doubling bifurcation, which is characterized by the critical normal form $b_{PD} = -1.260363$.

2. As the parameter κ crosses the critical value $\kappa_* = 3.333333$, the fixed point

$$F^{(*)} = (1.666666, 5.00000)\,,$$

   undergoes a Neimark-Sacker bifurcation, which is characterized by the critical normal form $c_{NS} = -1.427143$.

The bifurcation diagram of the model (3) is presented in figure 1.

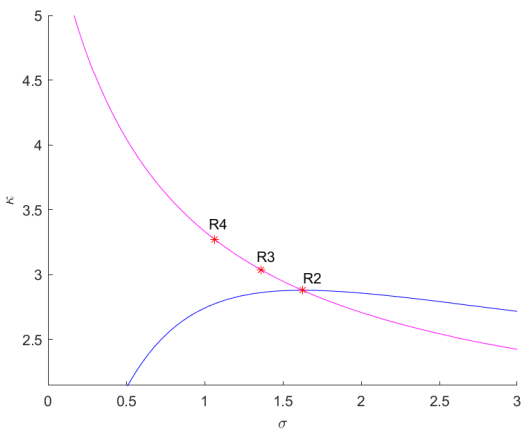

Figure 1: Bifurcation diagram of the model (3).

Acknowledgment

The author expresses sincere gratitude to Fasa University for their support of this paper.

References

[1] Li, Jinhui, Zhidong Teng, Guangqing Wang, Long Zhang, and Cheng Hu. "Stability and bifurcation analysis of an SIR epidemic model with logistic growth and saturated treatment." Chaos, Solitons & Fractals 99 (2017): 63-71.

[2] Eskandari, Zohreh, and Javad Alidousti. "Stability and codimension 2 bifurcations of a discrete time SIR model." Journal of the Franklin Institute 357, no. 15 (2020): 10937-10959.

[3] Maurício de Carvalho, João PS, and Alexandre A. Rodrigues. "SIR model with vaccination: bifurcation analysis." Qualitative theory of dynamical systems 22, no. 3 (2023): 105.

[4] Hu, Zhixing, Ping Bi, Wanbiao Ma, and Shigui Ruan. "Bifurcations of an SIRS epidemic model with nonlinear incidence rate." Discrete Contin. Dyn. Syst. Ser. B 15, no. 3 (2011): 93-112.

[5] Akrami, Mohammad Hossein, and Ali Atabaigi. "Hopf and forward bifurcation of an integer and fractional-order SIR epidemic model with logistic growth of the susceptible individuals." Journal of Applied Mathematics and Computing 64, no. 1 (2020): 615-633.

[6] Govaerts, Willy, R. Khoshsiar Ghaziani, Yu A. Kuznetsov, and Hil GE Meijer. "Numerical methods for two-parameter local bifurcation analysis of maps." SIAM journal on scientific computing 29, no. 6 (2007): 2644-2667.

[7] A. Jabbari, H. kheiri, A. Jodayree Akbarfam and A. Bekir, *Dynamical analysis of the avian-human influenza epidemic model using multistage analytical method*, Int. J. biomath., 09, 1650090 (2016) DOI: 10.1142/S179352451650090X.

[8] H. Kheiri, M. Jafari, *Stability analysis of a fractional order model for the HIV/AIDS epidemic in a patchy environment*, Journal of Computational and Applied Mathematics, 346 (2019) 323-339

e-mail: `z-eskandari@fasau.ac.ir`

Numerical simulation of tumor growth model by the conservative finite difference method

Mahdiehalsadat Fazayel[1]
Farhad Fakhar-Izadi
Mehdi Dehghan
Department of Applied Mathematics, Faculty of Mathematics and Computer Sciences, Amirkabir University of Technology (Tehran Polytechnic), No. 424, Hafez Ave.,15914, Tehran, Iran

Abstract

Mathematical modeling has long been essential for simulating dynamic biological processes. In this work, we focus on a tumor growth model, which conceptualizes tumor growth as a biological mechanism that can be effectively modeled using the Cahn-Hilliard (CH) equation. The CH model, a diffuse interface model, is employed to capture the complexities of tumor growth dynamics. We implement a conservative finite difference scheme to numerically simulate this model. Our results confirm that the numerical method preserves both mass and energy, ensuring the fidelity of these fundamental physical properties throughout the simulations.

Keywords: Cahn-Hilliard equation, Diffuse-interface tumor-growth model, Conservative finite difference scheme
Mathematics Subject Classification [2010]: 65L80, 65N06

1 Introduction

In a healthy body, cells meticulously regulate their proliferation and programmed cell death (apoptosis) within various tissues to optimize repair and healing processes. This delicate balance ensures that cellular growth and regeneration occur as needed, while damaged or unnecessary cells are efficiently removed. However, in cancer, this carefully regulated mechanism breaks down. Cancer cells begin to proliferate uncontrollably or resist apoptosis, leading to the alteration of the microenvironment to favor their survival. These aberrant cells can migrate and metastasize to regions far from the primary tumor site, ultimately posing a severe threat to the host body by causing physical obstructions or organ malfunction [4].

Normal cellular behavior is orchestrated through the expression of genes and regulatory networks within cells. In cancer, genes that promote proliferation (oncogenes) and those responsible for apoptosis (tumor suppressor genes) may malfunction, and regulatory signals can be ignored. This dysfunction within an abnormal cell population can lead to additional mutations and epigenetic changes, resulting in different subgroups of cells, or 'clones,' each with distinct characteristics. As these cancerous cells accumulate to form microscopic nodules without access to the vascular network, they rely on nutrients and growth factors diffusing through the neighboring healthy tissue. Consequently, these nodules typically remain small, growing at most to a few millimeters in diameter.

The accumulation of tumor cells can lead to acute and chronic shortages of oxygen (hypoxia) and nutrients (e.g., glucose, causing hypoglycemia), as well as the build-up of metabolites (e.g., lactic acid, leading to acidosis). As tumor cells continue to proliferate, the existing vasculature becomes insufficient to

[1]Speaker

deliver oxygen and nutrients to all the cells, which may induce neovascularization. Under these stressful conditions, cells release pro-angiogenic growth factors to drive angiogenesis—the process by which existing blood vessels grow from the main circulatory system to supply blood to the tissue, similar to the process occurring during wound healing. This angiogenesis provides the tumor with a direct supply of nutrients and growth-promoting factors, allowing it to grow larger and potentially shed cells into the bloodstream, leading to the formation of satellite tumors in distant parts of the body (metastases). Metastasis is the leading cause of cancer-related mortality. By the time a tumor reaches a clinically detectable size, it is usually in the vascular growth phase, indicating that the transition to metastasis and malignancy often begins with angiogenesis.

Hypoxia, hypoglycemia, and acidosis are exacerbated by the tumor-induced microvasculature, which, unlike the normal wound healing vasculature, tends to be highly disorganized and poorly functioning. This results in considerable heterogeneity in oxygen and nutrient delivery and metabolite removal, conditions that correlate with poor clinical outcomes and an increased risk of cancer spread throughout the body. Moreover, these harsh conditions may select for apoptosis-resistant tumor cells, induce further blood vessel formation, and increase invasiveness [4].

Understanding the complex interplay between tumor growth, nutrient acquisition, and the resulting microenvironmental changes is crucial for developing effective cancer treatments. This paper aims to provide deeper insights into tumor growth model by simulations and our numerical approach ensures that mass and energy are conserved throughout all simulations.
In this research, a coseravtive scheme is proposed for CH tumor growth model [5, 3]

$$\begin{cases} u_t(\mathbf{x},t) = \Delta\mu_u(\mathbf{x},t) + \gamma_u(\mathbf{x},t), \quad (\mathbf{x},t) \in \Omega \times (0,T], \\ \mu_u(\mathbf{x},t) = f'(u(\mathbf{x},t)) - \varepsilon^2 \Delta u(\mathbf{x},t), \quad u(\mathbf{x},t)(\mathbf{x},t) \in \Omega \times (0,T], \\ v_t(\mathbf{x},t) = \Delta\mu_v(\mathbf{x},t) - \gamma_u(\mathbf{x},t), \quad (\mathbf{x},t) \in \Omega \times (0,T], \\ \mu_v(\mathbf{x},t) = \frac{v(\mathbf{x},t)}{\delta}, \quad (\mathbf{x},t) \in \Omega \times (0,T], \\ u(\mathbf{x},0) = u_0, \\ \nabla u \cdot \mathbf{n} = \nabla\mu_u \cdot \mathbf{n} = \nabla v \cdot \mathbf{n} = \nabla\mu_v \cdot \mathbf{n} = 0, \quad (\mathbf{x},t) \in \partial\Omega \times (0,T], \end{cases} \tag{1}$$

which $\delta > 0$, $p \geq 0$ and $\Delta = \nabla^2$. The tumor cell function and nutrient-rich cell function are represented as u and v respectively. μ_u and μ_v are chemical potentials corresponding to u and v. γ_u is the chemical reaction defined as $\gamma_u = P(u)\left(\mu_v - \mu_u\right)$ and

$$P(u) = \begin{cases} \delta p\left(1-u^2\right), \quad |u| \leq 1, \\ 0, \quad u > 1 \quad \text{and} \quad u < -1. \end{cases} \tag{2}$$

The CH tumor growth model is formulated based on the classical CH equation [3]

$$\begin{cases} \frac{\partial u(\mathbf{x},t)}{\partial t} = \Delta\mu(\mathbf{x},t), \quad (\mathbf{x},t) \in \Omega \times (0,T], \\ \mu(\mathbf{x},t) = f'(u(\mathbf{x},t)) - \varepsilon^2 \Delta u(\mathbf{x},t), \quad (\mathbf{x},t) \in \Omega \times (0,T], \\ \nabla u \cdot \mathbf{n} = \nabla\mu \cdot \mathbf{n} = 0 \quad (\mathbf{x},t) \in \partial\Omega \times (0,T], \end{cases} \tag{3}$$

where ε is a constant that represents the equilibrium interface thickness and n is the exterior unit normal vector on the boundary, ∇u, $\nabla\mu$ are gradient vector, $f(u)$ is the free-energy density function in terms of

$$f(u) = \begin{cases} (u-1)^2, \quad u > 1, \\ 0.25\left(u^2-1\right)^2, \quad |u| \leq 1, \\ (u+1)^2, \quad u < -1. \end{cases} \tag{4}$$

Interested readers can refer to [1] for the existence of an inviscid aqueous phase. The CH model is known to possess two significant properties. For Eq. (1), these properties are represented by the total mass, denoted as $\mathbf{M}$, and the total energy, denoted as $\mathbf{E}$ [5, 3]

$$\mathbf{M} = \int_\Omega (u+v)\mathrm{d}\mathbf{x}, \tag{5}$$

$$\mathbf{E} = \int_\Omega \left(\frac{\varepsilon^2}{2}|\nabla u|^2 + f(u) + \frac{v^2}{2\delta}\right)\mathrm{d}\mathbf{x}. \tag{6}$$

In this part, we propose a conservative finite difference scheme for the CH equation in $\Omega = [a,b] \times [c,d]$. For positive integers N_x, N_y and M, let time-step $\tau = \dfrac{T}{M}$, $t_n = n\tau$, $n = 0, 1, ..., M$ and space-steps $h_x = \dfrac{b-a}{N_x}$, $x_i = ih_x$, $0 \le i \le N_x$ and $h_y = \dfrac{d-c}{N_y}$, $y_j = jh_y$, $0 \le j \le N_y$. The difference operators are defined for function u as

$$\begin{gathered}
\left(u_{i,j}^n\right)_x^+ = \frac{u_{i+1,j}^n - u_{i,j}^n}{h_x}, \quad \left(u_{i,j}^n\right)_x^- = \frac{u_{i,j}^n - u_{i-1,j}^n}{h_x}, \quad \left(u_{i,j}^n\right)_x = \frac{1}{2}\left(\left(u_{i,j}^n\right)_x^+ + \left(u_{i,j}^n\right)_x^-\right)^n, \\
\left(u_{i,j}^n\right)_y^+ = \frac{u_{i,j+1}^n - u_{i,j}^n}{h_y}, \quad \left(u_{i,j}^n\right)_y^- = \frac{u_{i,j}^n - u_{i,j-1}^n}{h_y}, \quad \left(u_{i,j}^n\right)_y = \frac{1}{2}\left(\left(u_{i,j}^n\right)_y^+ + \left(u_{i,j}^n\right)_y^-\right)_x, \\
\left(u_{i,j}^n\right)_{xx} = \left(\left(u_{i,j}^n\right)_x^-\right)_x^+, \quad \left(u_{i,j}^n\right)_{yy} = \left(\left(u_{i,j}^n\right)_y^-\right)_y^+, \\
\nabla_h u_{i,j}^n = \left(\left(u_{i,j}^n\right)_x + \left(u_{i,j}^n\right)_y\right), \quad \Delta_h u_{i,j}^n = \left(\left(u_{i,j}^n\right)_{x,x} + \left(u_{i,j}^n\right)_{yy}\right), \\
\left(u_{i,j}^n\right)_t = \frac{u_{i,j}^{n+1} - u_{i,j}^n}{\tau}.
\end{gathered} \tag{7}$$

Discretizing Eq. (1) using the finite difference method yields the following relation

$$\begin{aligned}
& u^{n+1^{(S+1)}} - \frac{\tau}{2}\Delta_h \mu_u^{n+1} = u^n + \frac{\tau}{2}\Delta_h \mu_u^n + 2\,\gamma_u^{n+1^{(S)}} - \gamma_u^n, \\
& \frac{\varepsilon^2}{2}\Delta_h u^{n+1^{(S+1)}} + \mu_u^{n+1} = -\frac{\varepsilon^2}{2}\Delta_h u^n + 2\,f'\left(u^{n+1^{(S)}}\right) - f'\left(u^n\right), \\
& v^{n+1} - \frac{\tau}{2}\Delta_h \mu_v^{n+1} = v^n + \frac{\tau}{2}\Delta_h \mu_v^n + 2\,\gamma_u^{n+1^{(S)}} - \gamma_u^n, \\
& -\frac{1}{\delta}v^{n+1} + \mu_v^{n+1} = 0,
\end{aligned} \tag{8}$$

which has iterative step. This discrete scheme can be represented in matrix form as follows:

$$\begin{bmatrix} I & -\frac{\tau}{2}\Delta_h & 0 & 0 \\ \frac{\varepsilon^2}{2}\Delta_h & I & 0 & 0 \\ 0 & 0 & I & -\frac{\tau}{2}\Delta_h \\ 0 & 0 & -\frac{1}{\delta}I & I \end{bmatrix} \begin{bmatrix} u \\ \mu_u \\ v \\ \mu_v \end{bmatrix} = \begin{bmatrix} u^n + \frac{\tau}{2}\Delta_h \mu_u^n + 2\,\gamma_u^{n+1} - \gamma_u^n \\ -\frac{\varepsilon^2}{2}\Delta_h u^n + 2\,f'\left(u^{n+1}\right) - f'\left(u^n\right) \\ v^n + \frac{\tau}{2}\Delta_h \mu_v^n + 2\,\gamma_u^{n+1} - \gamma_u^n \\ 0 \end{bmatrix}. \tag{9}$$

2 Main results

Example 2.1. Consider the two-dimensional CH equation [3]

$$\frac{\partial u(\mathbf{x},t)}{\partial t} + \Delta\left[\varepsilon^2 \Delta u(\mathbf{x},t) - f'(u(\mathbf{x},t))\right] = g(\mathbf{x},t), \quad (\mathbf{x},t) \in \Omega \times (0,T], \tag{10}$$

in the domain $\Omega = [0,1]^2$, where $\varepsilon^2 = 0.1$ and the analytical solution $u(x,y,t) = e^{-t}\sin^2(\pi x)\sin^2(\pi y)$ applies. The initial condition is given by $u(x,y,0) = \sin^2(\pi x)\sin^2(\pi y)$ and the boundary condition is $\dfrac{\partial u}{\partial \mathrm{n}} = \dfrac{\partial}{\partial \mathrm{n}}\left(f'(u) - \varepsilon^2 \Delta u\right) = 0$. The potential function is derived directly from the exact solution.

Table 1 displays the errors and accuracy rates, which closely match the theoretical predictions of the proposed method.

Example 2.2. In this example, we conduct simulations of the CH model (1) over the domain $\Omega = [-1,1]^2$ [2, 3]. The chosen parameters are $p = 300$, $\delta = 0.01$, and $\varepsilon = 0.02$. The free-energy function utilized is

$Space\ step(h)$	$e_2(method\ in\ [3])$	$e_2(present\ method)$	C_{order}
$\frac{1}{20}$	3.58992×10^{-1}	4.6943×10^{-2}	$---$
$\frac{1}{40}$	1.54646×10^{-1}	1.1065×10^{-2}	2.0849
$\frac{1}{60}$	1.12945×10^{-1}	4.8265×10^{-3}	2.0462

Table 1: The error and convergence order with $dt = 10^{-5}$ at $T = 0.1$.

$f(u) = 0.25\left(u^2 - 1\right)^2$. The initial condition applied is

$$\begin{cases} u_0(x,y) = \tanh\left(\frac{0.15-\sqrt{x^2+y^2}}{\sqrt{2}\varepsilon}\right), \\ v_0(x,y) = 1. \end{cases} \tag{11}$$

Fig. 1 provides a visual representation of the tumor cell evolution at $t = 0.0001, 0.008, 0.032$. Utilizing a

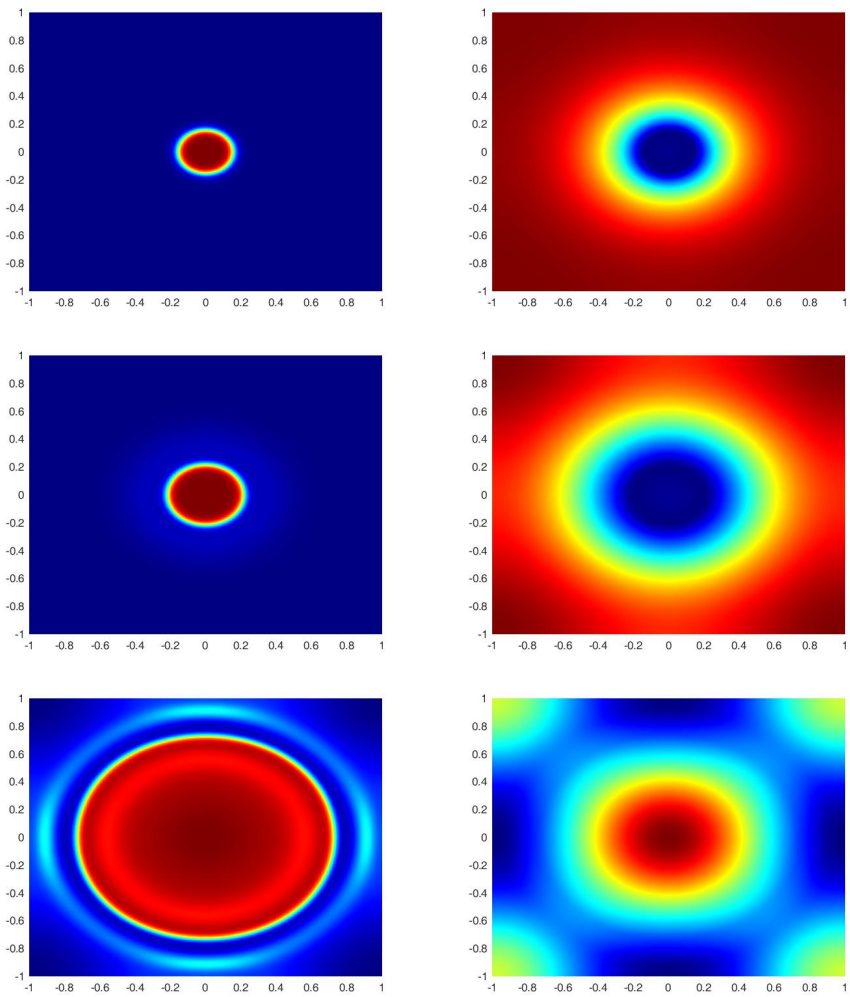

Figure 1: The simulation of tumor cell $u(left)$ and nutrient-rich cell $v(right)$ for single tumor cell in $t = 0.0001, 0.008, 0.032$ respectively

110×110 spatial grid with a time step of $\tau = 1 \times 10^{-6}$, the left column illustrates the tumor cell volume

fraction u, while the right column depicts the nutrient-rich volume fraction v. It is evident from the Fig. 1 that the tumor cells progressively consume the nutrient-rich environment, leading to an expansion in tumor size over time, a trend consistent with findings in prior research [5, 2, 3].

Fig. 2 depicts the temporal evolution of mass and energy. The mass remains invariant regardless of the time

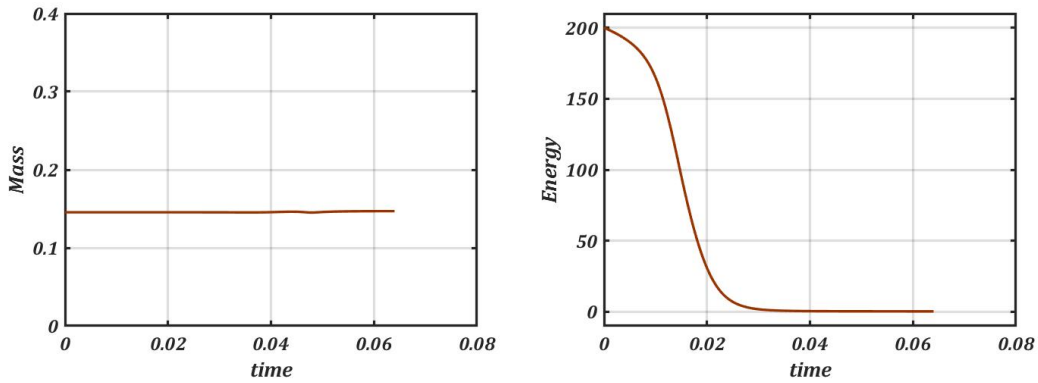

Figure 2: The change of mass and energy versus time of single tumor cell

step size, while the energy consistently decreases monotonically until reaching a steady state. These results confirm the theoretical predictions of mass conservation and energy dissipation, validating the robustness of our method.

3 Conclusion

In conclusion, this study underscored that by employing a conservative finite difference scheme, we successfully simulated the CH model while preserving critical physical properties such as mass and energy. The preservation of these properties throughout our simulations highlighted the robustness and reliability of the numerical method. These findings paved the way for further exploration and refinement of mathematical models in cancer research.

References

[1] C. J. Breward, H. M. Byrne, C. E. Lewis, A multiphase model describing vascular tumour growth, Bulletin of mathematical biology, 65(4) (2003) 609-640.

[2] M. Dehghan, V. Mohammadi, *Comparison between two meshless methods based on collocation technique for the numerical solution of four-species tumor growth model*, Communications in Nonlinear Science and Numerical Simulation, 44 (2017) 204-219.

[3] J. Huang, Y. Xu, J. Zhao and T. Jiang, *A highly efficient semi-implicit corrective SPH scheme for 2D/3D tumor growth model*, Engineering Analysis with Boundary Elements, 155 (2023) 839-849.

[4] J. S. Lowengrub, H. B. Frieboes, F. Jin, Y. L. Chuang, X. Li, P. Macklin, S. M. Wise, V. Cristini, *Nonlinear modelling of cancer: bridging the gap between cells and tumours*, Nonlinearity, 23(1) (2009) R1.

[5] X. Wu, G. J. Van Zwieten, K. van der Zee, *Stabilized second-order convex splitting schemes for Cahn–Hilliard models with application to diffuse-interface tumor-growth models*, International Journal for Numerical Methods in Biomedical Engineering, 30(2) (2014) 180-203.

Email: `m.fazayel@aut.ac.ir`
Email: `f.fakhar@aut.ac.ir`
Email: `mdehghan@aut.ac.ir`

Trajectory optimization and costate estimation of fractional optimal control problems via a Müntz pseudospectral method: application in cancer treatment

Hussein Ghassemi[a,1], Mohammad Maleki[b,2], Masoud Allame[a,3]
[a]Department of Mathematics, Isfahan (Khorasgan) Branch, Islamic Azad University, Isfahan, Iran
[b]Department of Mathematics Education, Farhangian University, P.O. Box 14665-889, Tehran, Iran

Abstract

We study a fractional optimal control problem that models cancer treatment. By introducing Müntz–Legendre polynomials and presenting a stable scheme for their Caputo fractional derivative, a new pseudospectral is derive for trajectory optimization. We also construct a novel costate estimation procedure based on the first order optimality conditions. This method is particularly suitable for problems whose solutions contain non-integer exponent factors. Numerical result are presented to demonstrate the performance and accuracy of the proposed method.

Keywords: Fractional optimal control; Cancer treatment; Pseudospectral; Costate estimation; Müntz polynomials

1 Introduction

Numerical solution of some applied models represented by fractional optimal control problems (FOCPs) has been considered by some authors [1, 2, 3]. Recently, a fractional optimal control problem with Caputo derivative has been presented for modeling tumor burden under immune suppression [4]. More specifically, if we consider t as time, $T(t)$ as tumor cells, $I(t)$ as immune cells, $\widetilde{N}(t)$ as normal cells, $F(t)$ as fat cells and $\widetilde{D}(t)$ as chemotherapeutic drugs, then the following cancer model describes the interactions between $T(t)$, $I(t)$, $\widetilde{N}(t)$ and $F(t)$ at time t near tumor site, while chemotherapeutic drugs $\widetilde{D}(t)$ is injected into the body:

$$Min \quad J = \int_0^1 \Big(\omega_1 T(t) - \omega_2 \widetilde{N}(t) + \omega_3 u^2(t)\Big) dt, \tag{1}$$

subject to the following nonlinear fractional dynamical system

$$\begin{cases} {}_0^C D_t^\alpha T(t) = r_1 T(t)\Big(1 - p_1 T(t)\Big) - a_1 T(t) I(t) - a_2 T(t)\widetilde{N}(t) + c_1 T(t) F(t) - \gamma_1 \widetilde{D}(t) T(t), \\ {}_0^C D_t^\alpha I(t) = s_1 + b_1 \frac{T(t)I(t)}{h+T(t)} - a_3 T(t) I(t) - \mu_1 I(t) - \gamma_2 \widetilde{D}(t) I(t), \\ {}_0^C D_t^\alpha \widetilde{N}(t) = r_2 \widetilde{N}(t)\Big(1 - p_2 \widetilde{N}(t)\Big) - a_4 T(t)\widetilde{N}(t) - \gamma_3 \widetilde{D}(t)\widetilde{N}(t), \\ {}_0^C D_t^\alpha F(t) = r_3 F(t)\Big(1 - p_3 F(t)\Big) - a_5 T(t) F(t) - \gamma_4 \widetilde{D}(t) F(t), \\ {}_0^C D_t^\alpha \widetilde{D}(t) = u(t) - \zeta \widetilde{D}(t), \end{cases} \tag{2}$$

and initial conditions $T(0) = T_0, \quad I(0) = I_0, \quad F(0) = F_0, \quad \widetilde{N}(0) = \widetilde{N}_0, \quad \widetilde{D}(0) = \widetilde{D}_0$, where ${}_0^C D_t^\alpha f(t)$ denotes the Caputo derivative of order $0 < \alpha < 1$ defined by [5]

$${}_a^C D_t^\alpha f(t) = \frac{1}{\Gamma(1-\alpha)} \int_a^t (t-\tau)^{-\alpha} f'(\tau) d\tau, \quad t > a. \tag{3}$$

Note that, $u(t)$ is the dose of injection to be controlled. Here, we propose a Mntz–Legendre pseudospectral method for trajectory optimization and costate estimation of the cancer model (1)–(2).

[1]Corresponding author and speaker. E-mail addresses: *hussein_ghassemi@yahoo.com*.
[2]E-mail addresses: *mm.maleki2013@gmail.com*.
[3]E-mail addresses: *allame@khuisf.ac.ir*.

2 Müntz-Legendre polynomials

Let $\alpha > 0$ be a real number and $t \in [0, T]$. The shifted Müntz-Legendre polynomials [6] are related to a class of Jacobi polynomials as follows:

$$L_n(t;\alpha) = J_n^{(0,\frac{1}{\alpha}-1)}\left(2\left(\frac{t}{T}\right)^{\alpha} - 1\right), \tag{4}$$

Hence, using the three-term recursive relation of Jacobi polynomials, one has

$$L_0(t;\alpha) = 1, \quad L_1(t;\alpha) = (\frac{1}{\alpha}+1)\left(\frac{t}{T}\right)^{\alpha} - \frac{1}{\alpha}, \quad b_{1,n}L_{n+1}(t;\alpha) = b_{2,n}(t)L_n(t;\alpha) - b_{3,n}L_{n-1}(t;\alpha). \tag{5}$$

where

$$b_{1,n} = a_{1,n}^{(0,\frac{1}{\alpha}-1)}, \qquad b_{2,n}(t) = a_{2,n}^{(0,\frac{1}{\alpha}-1)}\left(2\left(\frac{t}{T}\right)^{\alpha} - 1\right), \qquad b_{3,n} = a_{3,n}^{(0,\frac{1}{\alpha}-1)}.$$

Let $0 < \alpha < 1$ be a real number and $t \in [0, T]$. It can be easily shown that the representation

$${}_0^C D_t^{\alpha} L_n(t;\alpha) = \frac{1+n\alpha}{\alpha\Gamma(1-\alpha)T^{\alpha}} \int_0^1 \left(1 - x^{\frac{1}{\alpha}}\right)^{-\alpha} J_{n-1}^{(1,\frac{1}{\alpha})}\left(2\left(\frac{t}{T}\right)^{\alpha} x - 1\right) dx, \tag{6}$$

holds true. For the numerical evaluation of the integral on the right-hand side of Eq. (6), the N-point Gaussian quadrature rule, can be utilized to arrive at

$$\int_0^1 \left(1 - t^{\frac{1}{\alpha}}\right)^{-\alpha} f(t)dt = \sum_{k=1}^{N} w_k^{(\alpha)} f(\tau_k^{(\alpha)}), \qquad f \in \mathcal{P}_{2N}. \tag{7}$$

Clearly, the weight function $w(t;\alpha) = \left(1 - t^{\frac{1}{\alpha}}\right)^{-\alpha}$ is a nonclassical one and for each value of α the GolubWelsch algorithm can be used for calculating the weights $\{w_k^{(\alpha)}\}_{k=1}^N$ and nodes $\{\tau_k^{(\alpha)}\}_{k=1}^N$ of a Gaussian quadrature [7]. Therefore, since the quadrature rule (7) with $N = [n/2]$ becomes exact, Eq. (6) is equivalent to

$${}_0^C D_t^{\alpha} L_n(t;\alpha) = \frac{1+n\alpha}{\Gamma(1-\alpha)T^{\alpha}} \sum_{k=1}^{[\frac{n}{2}]} w_k^{(\alpha)} J_{n-1}^{(1,\frac{1}{\alpha})}\left(2\left(\frac{t}{T}\right)^{\alpha} \tau_k^{(\alpha)} - 1\right). \tag{8}$$

3 Formulation of the Müntz PS method

For brevity, we consider the following nonlinear FOCP in Bolza form: Minimize the cost functional

$$J = \mathbf{h}\Big(t_f, \mathbf{X}(t_f)\Big) + \int_0^{t_f} \mathbf{g}\Big(t, \mathbf{X}(t), \mathbf{U}(t)\Big) dt, \tag{9}$$

subject to the fractional order system dynamics

$${}_0^C D_t^{\alpha} \mathbf{X}(t) = \mathbf{f}\Big(t, \mathbf{X}(t), \mathbf{U}(t)\Big), \quad t \in [0, t_f], \tag{10}$$

the initial conditions and the terminal state constraints

$$\mathbf{X}(0) = \mathbf{x}_0, \quad \boldsymbol{\psi}\Big(t_f, \mathbf{X}(t_f)\Big) = 0, \tag{11}$$

where t_f is a fixed terminal time, $\mathbf{X}(t) \in \mathbb{R}^m$ is the state vector, $\mathbf{U}(t) \in \mathbb{R}^n$ is the control vector and $\mathbf{X}_0$ is a given initial state. We assume that the problem is controllable. Now, we set $T = t_f$ and approximate the state and control vector functions as the finite sums

$$\mathbf{X}(t) \approx P^N\mathbf{X}(t) = \sum_{j=0}^{N} \mathbf{X}_j L_j(t;\alpha), \qquad \mathbf{U}(t) \approx P^N\mathbf{U}(t) = \sum_{j=0}^{N} \mathbf{U}_j L_j(t;\alpha), \tag{12}$$

where $\mathbf{X}_j$ and $\mathbf{U}_j$ are totally $(m+n)(N+1)$ unknown variables to be determined. Collocating the fractional system dynamics (10) at the $N+1$ points $\{t_l = (x_l)^{\frac{1}{\alpha}}\}_{l=0}^{N}$, where $\{x_l\}_{l=0}^{N}$ are Legendre–Gauss-Radau points associated with the interval $[0, t_f)$, we obtain

$$ {}_0^C D_t^\alpha \mathbf{X}(t_l) = \mathbf{f}\Big(t_l, \mathbf{X}(t_l), \mathbf{U}(t_l)\Big), \qquad {}_0^C D_t^\alpha (P^N \mathbf{X})(t_l) = \sum_{j=0}^{N} d_{lj} \mathbf{X}_j, \quad l = 0, \ldots, N. \tag{13} $$

where

$$ d_{lj} = \frac{1 + j\alpha}{\Gamma(1-\alpha) T^\alpha} \sum_{k=1}^{[\frac{j}{2}]} w_k^{(\alpha)} J_{j-1}^{(1,\frac{1}{\alpha})} \left(2 \left(\frac{t_l}{T} \right)^\alpha \tau_k^{(\alpha)} - 1 \right). $$

Substituting Eq. (12) into Eq. (13), for $\{l\}_{l=0}^{N}$ we obtain $m(N+1)$ collocation conditions

$$ \sum_{j=0}^{N} d_{lj} \mathbf{X}_j - \mathbf{f}\Big(t_l, P^N \mathbf{X}(t_l), P^N \mathbf{U}(t_l)\Big) = 0. \tag{14} $$

Moreover, approximating the initial and terminal state constraints (11), gives m algebraic constraints as

$$ P^N \mathbf{X}(0) - \mathbf{x}_0 = 0, \qquad \boldsymbol{\psi}\Big(t_f, \sum_{j=0}^{N} \mathbf{X}_j\Big) = 0. \tag{15} $$

Finally, the cost functional is approximated by substituting Eq. (12) into Eq. (9) and utilizing the standard Legendre-Gauss-Radau quadrature rule, to arrive at

$$ J \simeq J_N = \mathbf{h}\Big(t_f, \sum_{j=0}^{N} \mathbf{X}_j\Big) + \sum_{l=0}^{N} \widehat{w}_l \; \mathbf{g}\Big(x_l, P^N \mathbf{X}(x_l), P^N \mathbf{U}(x_l)\Big), \tag{16} $$

where $\widehat{w}_l$ and x_l are the standard Legendre-Gauss-Radau weights and nodes on the interval $[0, t_f)$, respectively. The finite-dimensional NLP problem arising from the above Radau PS discretization is to minimize Eq. (16) subject to Eqs. (14)–(15). This NLP problem can be solved by an appropriate globally convergent algorithm.

4 Costate estimation

Let $\mathcal{H} = \mathbf{g}(t, \mathbf{X}, \mathbf{U}) + \boldsymbol{\lambda}^T \mathbf{f}(t, \mathbf{X}, \mathbf{U})$ be the Hamiltonian function where the vector function $\boldsymbol{\lambda}(t)$ is the costate. Using the Pontryagin Minimum Principle, the first-order optimality conditions of the continuous-time FOCP (9)–(11) can be derived. Suppose that we have obtained the approximations $\mathbf{X}^N(t)$ and $\mathbf{U}^N(t)$ to $\mathbf{X}(t)$ and $\mathbf{U}(t)$ using the Müntz PS discretization of Section 3. By substituting $\mathbf{X}^N(t)$ and $\mathbf{U}^N(t)$ into the first-order optimality conditions, we obtain

$$ -\mathcal{H}_{\mathbf{x}} \Big|_{(\mathbf{X}^N, \mathbf{U}^N)} = {}_0^C D_t^\alpha \boldsymbol{\lambda}(t) = -\mathbf{g}_{\mathbf{x}}^N - \mathbf{f}_{\mathbf{x}}^N \boldsymbol{\lambda}(t), \quad \boldsymbol{\lambda}(t_f) = \mathbf{h}_{\mathbf{X}}\Big(t_f, \mathbf{X}^N(t_f)\Big) - \boldsymbol{\upsilon}^T \boldsymbol{\psi}_{\mathbf{X}}\Big(t_f, \mathbf{X}^N(t_f)\Big), \tag{17} $$

$$ \mathcal{H}_{\mathbf{U}} \Big|_{(\mathbf{X}^N, \mathbf{U}^N)} = 0 = \mathbf{g}_{\mathbf{U}}^N + \mathbf{f}_{\mathbf{U}}^N \boldsymbol{\lambda}(t). \tag{18} $$

Eq. (17) is a system of linear FDEs of order $0 < \alpha < 1$ with boundary conditions, and Eq. (18) is a system of linear algebraic equations for the unknowns of the vector $\boldsymbol{\lambda}(t)$. Using a combination of these two equations, estimations to costates can be obtained.

Table 1: Values of the parameters for the FOC cancer model.

Description	Units	Estimate value	Description	Units	Estimate value
r_1	day^{-1}	1.5	$c1$	$cells^{-1}day^{-1}$	1.5
r_2	day^{-1}	1	γ_1	day^{-1}	0.08
r_3	day^{-1}	0.75	γ_2	day^{-1}	2×10^{-11}
p_1	$cells^{-1}$	1	γ_3	day^{-1}	0.008
p_2	$cells^{-1}$	1	γ_4	day^{-1}	0.008
p_3	$cells^{-1}$	1.5	s_1	$cells^{-1}day^{-1}$	0.33
a_1	$cells^{-1}day^{-1}$	0.5	b_1	day^{-1}	0.01
a_2	$cells^{-1}day^{-1}$	1	h	$cells^2$	0.3
a_3	$cells^{-1}day^{-1}$	0.5	μ_1	day^{-1}	0.2
a_4	$cells^{-1}day^{-1}$	1	ζ	day^{-1}	0.1
a_5	$cells^{-1}day^{-1}$	0.1			

Table 2: Computational results of J and costate estimation errors for $\alpha = 0.8, 0.9, 1$ and various alues of N.

N	J_N	ε_{dyn}	$\varepsilon_{\mathcal{H}_{\mathbf{X}}}$	$\varepsilon_{\mathcal{H}u}$
$\alpha = 0.8$				
10	9.556	4.59×10^{-5}	4.08×10^{-2}	9.64×10^{-2}
15	9.55443	1.96×10^{-6}	1.56×10^{-2}	8.25×10^{-2}
$\alpha = 0.9$				
15	9.43610	8.76×10^{-6}	4.29×10^{-3}	2.97×10^{-2}
20	9.4360997	3.80×10^{-6}	9.34×10^{-3}	2.30×10^{-3}
$\alpha = 1$				
10	9.288	1.49×10^{-6}	7.42×10^{-3}	9.23×10^{-3}
20	9.28790775	3.41×10^{-7}	6.27×10^{-4}	2.58×10^{-3}

5 Numerical result

By substituting $\mathbf{U}^N(t)$ into Eq. (10), we have ${}_0^C D_t^\alpha \mathbf{X}(t) = \mathbf{f}\Big(t, \mathbf{X}(t), \mathbf{U}^N(t)\Big), \quad \mathbf{X}(0) = \mathbf{x}_0$. To solve this FDE, we have utilized the Müntz collocation method to obtain the approximate solution $\widetilde{\mathbf{X}}(t)$. Then we define

$$\varepsilon_{dyn} = \left\| \widetilde{\mathbf{X}}(t) - \mathbf{X}^N(t) \right\|_{L^\infty(I)}.$$

Moreover, let $\boldsymbol{\lambda}^N(t)$, be the costate estimations obtained using Eqs. (17)–(18). We define the accuracy criterions for costate estimation as

$$\varepsilon_{\mathcal{H}_{\mathbf{X}}} = \max\left\{ \left\| {}_0^C D_t^\alpha \boldsymbol{\lambda}^N + \mathcal{H}_{\mathbf{X}} \right\|_{L^\infty(I)} \right\}, \qquad \varepsilon_{\mathcal{H}_{\mathbf{U}}} = \max\left\{ \left\| \mathcal{H}_{\mathbf{U}} \right\|_{L^\infty(I)} \right\}.$$

Now, consider the cancer model (1)–(2). The values of the weights are $\omega_1 = 20$, $\omega_2 = 1$ and $\omega_3 = 1$ and the values of other parameters are given in Table 1. Also, initial conditions are $T(0) = 1, \quad I(0) = 0.001, \quad F(0) = 4, \quad \widetilde{N}(0) = 0.25, \quad \widetilde{D}(0) = 0.5$. We solved this problem for various values of N and α and the numerical results are summarized in Table 2. In Fig. 1 and Fig. 2, the graphs of approximated state variables, the control variable and costate variables are depicted. In this problem, Eqs. (17)–(18) evaluated at $T^N(t)$, $I^N(t)$, $\widetilde{N}^N(t)$, $F^N(t)$, $\widetilde{D}^N(t)$ and $u^N(t)$, are used to estimate the costate functions. Indeed, Eq. (18) gives an algebraic equation for estimating $\lambda_5(t)$ and then we solve the system of linear FDEs (17) for estimating the remaining costates $\{\lambda_i(t)\}_{i=1}^4$ (see Fig. 2). Based on the obtained numerical results, we have the following observations: For all the considered values α, the tumor population decreases and the normal cell population is renewed as functions of time. Furthermore, the immune cell population and the number of fat cells increases over time. Moreover, after half of the time and eradicating most of the tumor population, the drug concentration $\widetilde{D}(t)$ and dose $u(t)$ decrease.

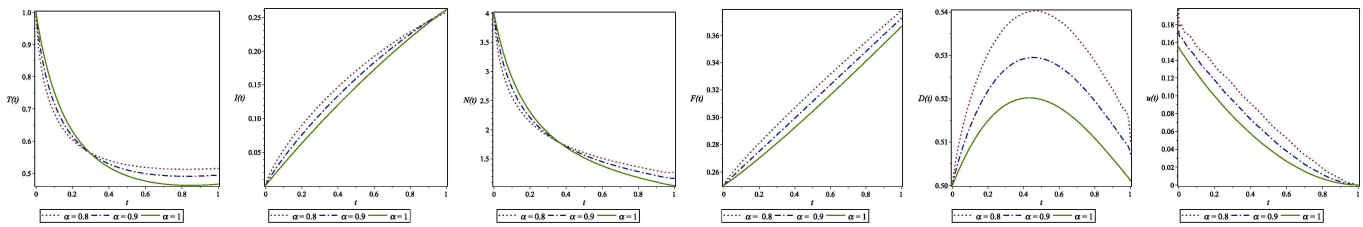

Figure 1: Approximate states and control for $N = 15$ and different values of α.

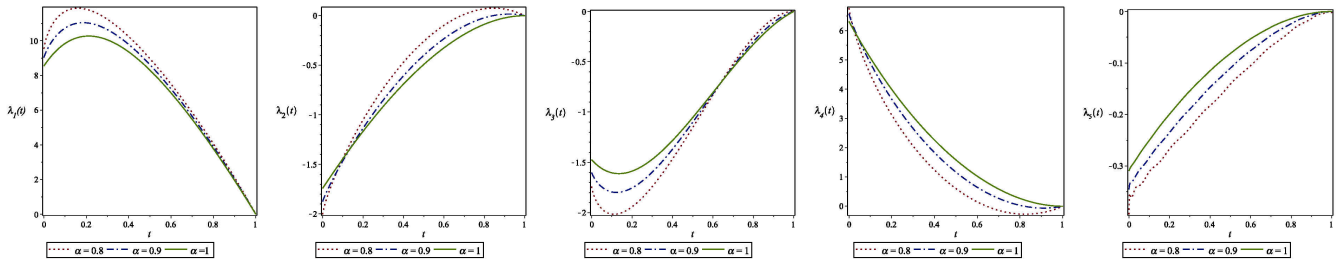

Figure 2: Approximate costates for $N = 15$ and different values of α.

6 Conclusions

In this article, the pseudospectral method has been adopted for numerical solution of a class of FOCPs with application to a fractional cancer model. A special family of the Müntz–Legendre polynomials was used as an approximation basis. The proposed pseudospectral method is characterized by its simplicity, efficiency, and high accuracy and can be readily implemented. A novel costate estimation procedure was also established based on the first order optimality conditions. The accuracy and validity of the presented method were demonstrated through numerical simulations.

References

[1] H. Kheiri, M. Jafari, Fractional optimal control of an HIV/AIDS epidemic model with random testing and contact tracing, J. Appl. Math. Comput. 60 (2019) 387–411.

[2] M. Vellappandi, P. Kumar, V. Govindaraj, W. Albalawi, An optimal control problem for Mosaic disease via Caputo fractional derivative, Alexandria Engineering Journal, 61 (2022) 8027–8037.

[3] K.R. Cheneke,K.P. Rao, G.K. Edessa, Fractional derivative and optimal control analysis of Cholera epidemic model, J. Math. vol. 2022 (2022) Article ID 9075917, https://doi.org/10.1155/2022/9075917.

[4] N.H. Sweilam, S.M. AL-Mekhlafi, Optimal control for a nonlinear mathematical model of tumor under immune suppression: a numerical approach, Optim. Control Appl. Meth. 39(5) (2018), 1581–1596.

[5] I. Podlubny, Fractional Differential Equations, Academic Press, San Diego, CA, 1999.

[6] S. Esmaeili, M. Shamsi, Yury Luchko, Numerical solution of fractional differential equations with a collocation method based on Müntz polynomials, journal Computers and Mathematics with Applications 62 (2011) 918-929.

[7] G.H. Golub, J.H. Welsch, Calculation of Gauss quadrature rules, Math. Comp. 23 (1969) 221-230.

Application of Skewed Logistic Modeling for Comparison of Traditional and Novel Anthropometric Indices in Discriminating Diabetes

Neda Gilani[1]

Liver and Gastrointestinal Diseases Research center, Tabriz University of Medical Sciences,Tabriz, Iran. Department of Statistics and Epidemiology, Faculty of Health, Tabriz University of Medical Sciences, Tabriz, Iran.

Rouhollah Haghshenas

Corresponding author: Department of Sport Sciences, Faculty of Humanities, Semnan University, Semnan, Iran.

Mohammad hossein Somi

Liver and Gastrointestinal Diseases Research center, Tabriz University of Medical Sciences,Tabriz, Iran.

Elnaz Faramarzi

Liver and Gastrointestinal Diseases Research center, Tabriz University of Medical Sciences,Tabriz, Iran.

Abstract

Background: Anthropometric indices (AI) play a crucial role in identifying individuals at risk for various metabolic disorders, including diabetes.The purpose of this study was to identify the diagnostic ability of these indices to discriminate diabetes in the Azar cohort population. Materials and Methods: Subjects who were diabetic in the baseline phase from 15006 participants in study of azar cohort population were excluded and to follow up, a total of 13253 people was included in the analysis. Demographic characteristics and 11 AI were measured. Skewed logistic regression modeling and adjusted risk ratio (aRR) coefficients were used to evaluate the association between the anthropometric indices and diabetes. The receiver operating characteristic (ROC) curve analysis was performed to compare the discrimination of different anthropometric measures. Results: During the follow-up years, a total of 685 participants developed diabetes. The measurements of the AI were significantly higher in subjects with diabetes ($P < .001$). Body Roundness Index (BRI) and Waist height ratio (WHtR) exhibited the largest AUCs for predicting diabetes onset risk (both AUC=0.6989) among these anthropometric measures. Significant aRR for BRI and WhtR were3.69 and 7.89, respectively. Conclusions: The BRI and WtHR demonstrated superior efficacy in detecting diabetes within the Azar Cohort population.

Keywords: Anthropometric, Incidence Diabetes, Modeling

1 Introduction

Diabetes is a non-communicable disease that manifests in both developed and developing nations. Anthropometric indices (AI) play a crucial role in identifying individuals at risk for various metabolic disorders, including diabetes. On the other hand, AI are recognized as cost-effective, straightforward, and non-invasive

[1]Speaker

techniques for screening populations and early detection of obesity. Body mass index (BMI), waist circumference (WC), waist-to-height ratio (WHtR), and waist-to-hip ratio (WHR) have historically been the most utilized measurements in routine clinical practice (1). However, in recent years, new AI have been developed as an alternative to traditional anthropometric measurements to enhance the evaluation of fat distribution and its relationship to incidence rate of diabetes (2). The A Body Shape Index (ABSI) evaluates overall and visceral fatness and is more closely linked to abdominal fat than BMI (3). The Body Roundness Index (BRI) forecasts the quantity of total and regional fat and is regarded as a predictor of metabolic syndrome in diverse populations, proving to be more effective than BMI in several research studies (4). The Body Adiposity Index (BAI) is calculated from hip circumference and height to estimate the level of body fat (5). The abdominal volume index (AVI) quantifies the amount of abdominal fat and is positively correlated with metabolic syndrome (6). The weight-adjusted waist index (WWI) has been linked to cardiovascular morbidity and mortality (7). The conicity index (CI) utilizes weight, height, and abdominal circumference measurements to assess the level of obesity and fat distribution (8). Several studies have compared traditional and novel AI to discriminate diabetes and other related conditions. Zhang et al. (2016) found that waist-to-height ratio (WHtR) and lipid accumulation product (LAP) were better indices for screening metabolic syndrome (MetS) in the Kazakh adult population (9). Kavaric et al. (2017) aimed to assess the reliability of visceral adiposity index (VAI) and LAP in individuals with type 2 diabetes mellitus (DM2) (10). Yang et al. (2018) conducted a prospective study among elderly Chinese individuals to evaluate the prediction ability of different anthropometric indices, including traditional ones like body mass index (BMI) and novel ones like VAI, in predicting diabetes risk (11). Furthermore, Nayak et al. (2020) evaluated the predictive performance of traditional and novel lipid combined anthropometric indices in identifying prediabetes (12). These studies collectively emphasize the importance of comparing traditional and novel AI in discriminating diabetes and other metabolic disorders. Therefore, theaim of this study was to identify the diagnostic ability of AI to discriminate diabetes in the Azar cohort.

2 Materials and Methods

2.1 Study Design and measurements

The data from the Azar cohort study that were collected from 15006 participants (aged between 35 and 70 years from a pool of 33,000 eligible individuals) were used in this research (13). For our study, subjects who were diabetic in the baseline phase were excluded from the study. Although the follow-ups of the Azar Cohort study are still ongoing, in this study the follow-ups until April 2022 were analyzed. Finally, a total of 13253 people was included in the analysis. Full details of the Azar cohort study are provided in another published article (14). This study was approved by the Ethics Committee of Tabriz University of Medical Sciences (IR.TBZMED.REC.1402.943) with grant no.73580.

2.2 Statistical Analysis

Since in this study, the proportion of diabetic and non-diabetic people is not the same, we used skwed logistic modeling approach for quantifying the relationship between antropometric indices and incidence of diabetes events. The area of this curve was used to evaluate the diagnostic ability of a variable to discriminate the true disease status of a patient. Data analysis was done using Stata software (version 17, Stata Crop, College Station, Texas).

3 Results

An overall 13,253 subjects (6,019 [45.4%] men, the average age of 48.9 ± 9.17 years) were studied. During the follow-up, a total of 685 participants developed diabetes. The measurements of the AI were significantly higher in subjects with diabetes ($P < .001$)-not shown. As outlined in Figure 1, the AUC values of all the AI ranged from 0.58 to 0.70. BRI and WHtR exhibited the largest AUCs for predicting diabetes onset risk (both AUC=0.6989) among these anthropometric measures. Table 1 and Figure 2 show the association between AI and Diabetes event. It can have been seen that Significant aRR for BRI and WhtR were 3.69 and 7.89, respectively.

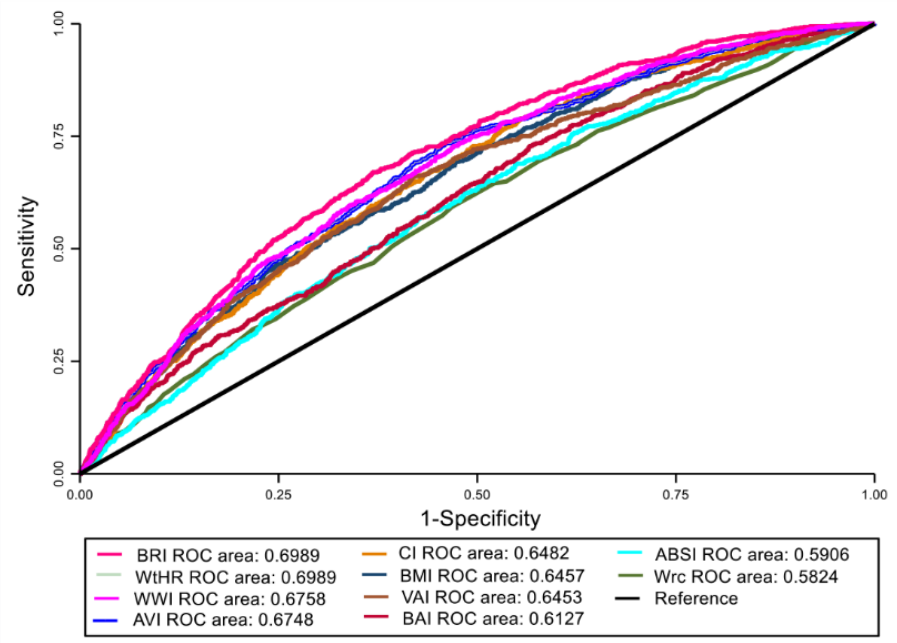

Figure 1: Comparison of the receiver operating characteristic (ROC) curves for separate anthropometric indices

Table 1: Incidence Risk Ratio of antropometric indices base on skewed binary logistic modeling*

Index	aRR^{**}	95% Lower CI IRR	95% Upper CI IRR	P
BRI	3.69	1.79	7.61	$< .001$
WWI	7.89	2.40	18.90	$< .001$
AVI	1.39	1.17	1.68	$< .001$
BMI	1.12	1.10	1.14	$< .001$
BAI	1.06	1.05	1.07	$< .001$
Wrc	1.21	1.15	1.27	$< .001$
WC	1.06	1.04	1.09	$< .001$

*4 AI removed from model because of collinearity

**Risk Ratio Adjusted by demographic factors

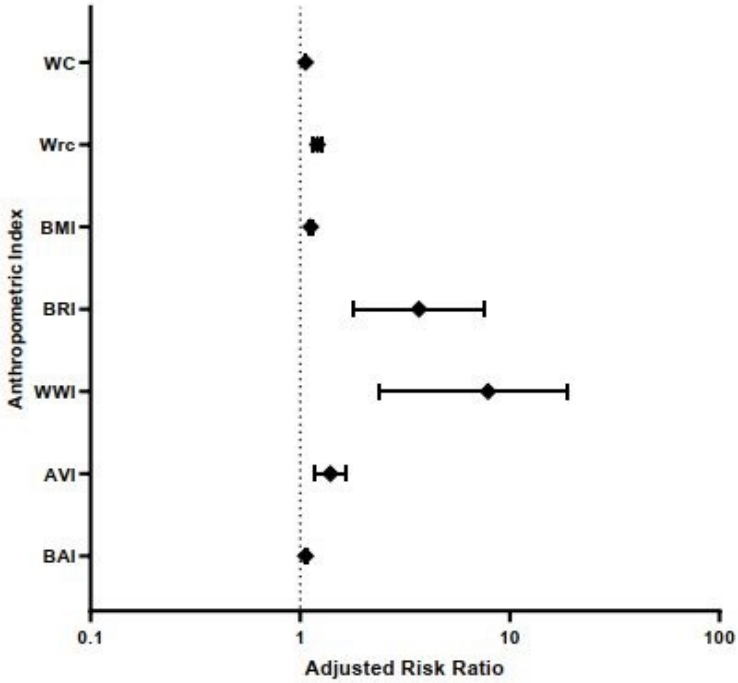

Figure 2: Forest Plot of adjusted risk ratio of AI

4 Discussion and Conclusion

The present study showed that The BRI and WtHR demonstrated superior efficacy in detecting diabetes within the Azar Cohort population. After them, WWI and AVI were in the next ranks5 with AUC respectively. In this relationship, Chen et al (2023) recently published a study indicating that there is a noteworthy correlation between WHtR and the occurrence of diabetes /impaired fasting glucose in both the sub-cohort and the authors recommended WHtR as a valuable predictor for diabetes (15). Park et al (2023) reported that the WWI is a reliable anthropometric measurement for predicting sarcopenic obesity in individuals with type 2 diabetes, and it could serve as a suitable indicator for predicting various cardiometabolic risk factors in the elderly population (16). Of course, in their study, 515 participants were investigated, while in our study, 15,006. The present study showed that The BRI and WtHR demonstrated superior efficacy in detecting diabetes within the Azar Cohort population. After them, WWI and AVI were in the next ranks with AUC respectively.

References

[1] Jensen MD, Ryan DH, Apovian C, Ard J, Comuzzie A, Donato K, et al, *Reprint: 2013 AHA/ACC/TOS guideline for the management of overweight and obesity in adults*, 54(1) (2014)

[2] Jayawardena R, Ranasinghe P, Ranathunga T, Mathangasinghe Y, Wasalathanththri S, Hills AP, *Novel anthropometric parameters to define obesity and obesity-related disease in adults: a systematic review*, J Nutrition Reviews. 78(6) (2020) 498-513

[3] Krakauer NY, Krakauer JC, *A new body shape index predicts mortality hazard independently of body mass index*, PloS one, 7(7) (2012) e39504.

[4] Bergman RN, Stefanovski D, Buchanan TA, Sumner AE, Reynolds JC, Sebring NG, et al, *A better index of body adiposity. Obesity Reviews*, 19(5) (2011) 1083-9

[5] Guerrero-Romero F, Rodrguez-Morn M, *Abdominal volume index. An anthropometry-based index for estimation of obesity is strongly related to impaired glucose tolerance and type 2 diabetes mellitus*, Archives of medical research. 34(5) (2003) 428-32

e-mail: gilanin@tbzmed.ac.ir
e-mail: rhm@semnan.ac.ir

Effect Of Magnetic, Body Acceleration, And Time Dependency On The Blood Flow with its Application to Diseased Blood

Ahmad Reza Haghighi[1]

Full Professor, Department of Mathematics, Faculty of Statistics, Mathematics, and Computer, Allameh Tabataba'i University, Tehran, Iran

Abstract

A size effect in blood flows has been studied in the present investigations with a view to include effects of pulsatile magnetic and body acceleration in the flow situations. The importance of the studies in the cardio-vascular system studies with its applications in blood diseases has been highlighted. The model has been compared to that of non-pulsatile models and shown that the present model yields better results.

Keywords: Physiological fluid dynamics, Heart Attack, Blood flow modelingShear Stress factors

AMS Mathematical Subject Classification [2010]: 76A05, 76DXX, 76BXX

Introduction

Modeling and simulation has paved the way in grater details for understanding system under study. Be it a heat engine, space science or design of remotely controlled robots for defense applications, modeling has not only given effective results but also simplified financial aspect to greater details. In view of its importance modeling in Bio-fluid dynamics has been taken up in the present investigations. Blood flow modeling has been studied by various authors [1] with a view to include various aspects of characteristics of blood flow of in their model [Anomalies of blood flow (FLE, IFLE)[2], time independent [3], time dependent [4] elastic nature [5] and so forth]. In the present model the study is aimed at including most of the aspect in the model and to apply the system studies for various blood diseases. Also the model has been accounted for the size effects nature of flow [effects of blood cells in bulk flow which produces net effects which are different then Navier-Stokes equations considered by continuum approach].There are extensive theories [6] to account size effects in blood flows. In the present model, micro-continuum approach proposed by V.K.Stokes [7] has been used. One of the advantages of taking Stokes approach over other theories is that, the present approach is simple and do not account for coupled equation for both blood cells and bulk flow independently.

[1] Ahmad Reza Haghighi

Analysis

The basic equation governing the flow for the pulsatile nature of blood is given by

$$\rho\frac{\partial u}{\partial t} = -\frac{\partial p}{\partial z} + \mu\nabla^2 u - \eta\nabla^4 u \tag{1}$$

It is assumed that flow is laminar and turbulent effects in the body are neglected. Equation (1) in cylindrical polar co-ordinates under the periodic body acceleration in the presence of magnetic field is given by

$$\rho\frac{\partial u}{\partial t} + \ \eta\nabla^2(\nabla^2 u) - \mu\nabla^2 u + \ \sigma B_0^2 u = \ -\frac{\partial p}{\partial z} + \rho G \tag{2}$$

Where $u(r,t)$ is the velocity in the axial direction, ρ *and* μ are the density and viscosity of blood, η is the couple stress parameter, σ is the electrical conductivity, B_0 is the external magnetic filed and r is the radial coordinate.

$$\nabla^2 = \ \frac{1}{r}\frac{1}{\partial r}\left(r\frac{\partial}{\partial r}\right) \tag{3}$$

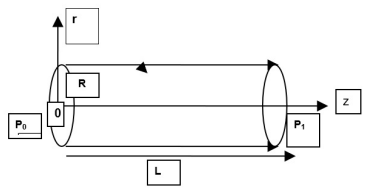

Figure 1: Blood flow in straight tube

For the initial calculation of velocity, flow rate (Q), pressure gradient and body acceleration are assumed to be of the form [Ref.(8)].

$$-\frac{\partial p}{\partial z} = A_0 + \ A_1\cos(\omega t) \quad , \qquad t \geq 0 \tag{4}$$

$$G = a_0\cos\left(\omega_1 t + \varnothing\ \right) \qquad t \geq 0 \tag{5}$$

Where A_0 the steady-state part of pressure gradient, A_1 is the amplitude of the oscillatory part,$\omega = 2\pi f$ and f is the heart pulse frequency, a_0 is the amplitude of body acceleration,$\omega_1 = 2\pi f_1$ *and* f_1 is body acceleration frequency, $\varnothing$ is the phase difference, z is the axial distance and t is time. Flow variables have been normalized by using following relations:

$$u^* \ = \ \frac{u}{\omega R} \ , \ r^* = \ \frac{r}{R} \ , \ A_0^* = \ \frac{R}{\mu\omega}A_0 \ , \ A_1^* = \ \frac{R}{\mu\omega}A_1 \ , \ a_0^* = \ \frac{\rho R}{\mu\omega}a_0 \ , \ z^* = \ \frac{z}{R} \tag{6}$$

Equation (2) simplifies to [after dropping stars]

$$\overline{\alpha}^2 a^2\frac{\partial u}{\partial t} = \overline{\alpha}^2 A_0 + \overline{\alpha}^2 A_1 cost + \overline{\alpha}^2 a_0\cos(bt+\varnothing) + \overline{\alpha}^2\left(\frac{1}{r}\frac{\partial}{\partial r}\left(r\frac{\partial u}{\partial r}\right)\right)$$
$$-\left(\frac{1}{r}\frac{\partial}{\partial r}\left(r\frac{\partial u}{\partial r}\right)\right)\left(\frac{1}{r}\frac{\partial}{\partial r}\left(r\frac{\partial u}{\partial r}\right)\right) - \overline{\alpha}^2 H^2 u \tag{7}$$

Where $\overline{\alpha}^2 = \overline{a}^{*^2}\frac{\mu}{\mu 1}$, couple stress parameter, $a = a^*$ Womersley parameter, $H = H^*\sqrt{\frac{\mu}{\mu 1}}$ is the Hartmann number, and R is the radius of the pipe.

$$\overline{a}^{*^2} = \ \frac{R^2\mu_1}{\eta} \quad , \qquad H^* = \ B_0 R\sqrt{\frac{\sigma}{\mu 1}} \quad , \quad a^* = R\sqrt{\frac{\omega\rho}{\mu_1}} \quad , \quad b = \frac{\omega_1}{\omega} \tag{8}$$

Shear Stress

Shear stress τ_{rz} which is one of the physiological importance parameters has been computed by using following relation

$$\tau_{rz} = -\mu \frac{\partial u(r)}{\partial r} \tag{9}$$

Using Equation (12), Shear stress simplifies to

RESULTS AND DISCUSSIONS

In order to compute shear stress to flow, the data on viscosity μ for various blood diseases are required and the same has been taken from [7] and shown in table one. The remaining data on $\overline{\alpha}^*,\ A_1,\ A_0\ ,\ H^*,\ a_0,\ \varnothing,\ t,\ b\ and\ a$ have been taken from Shakera [7]. The variation of shear stress to flow for various set of data has been computed and shown in figure 2-3. The comparison of the present model to that of time-independent model [8] has been indicated by solid lines in the figure.

The results of present findings have also been compared to that of Newtonian results by computing the model for $\overline{\alpha}^* = 20\ t0\ 80]$. The results indicate that, the time dependent values are in comparison time independent lower results. Also a reversible trend that of resistance to flow has been observed here also like that of previous observations.

Table 1: Viscosity Data [Ref.7]

Diseases	μ, cP	$\mu_1,\ cP$
Normal Blood	3.81	1.2
Polycythemia	6.75	1.2
Plasma cell Dyscrasis	4.99	1.2
Hb.ss	3.29	1.2

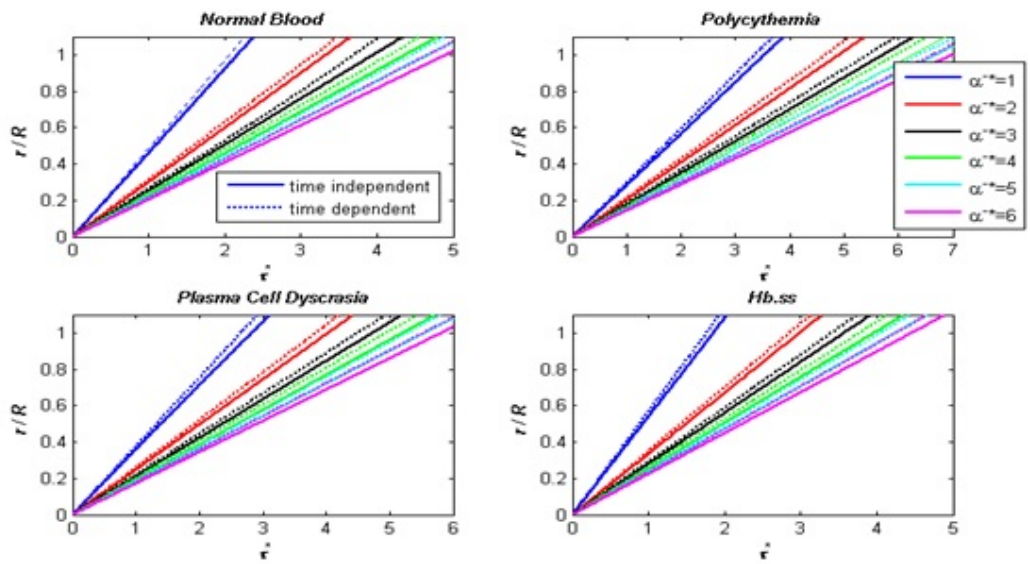

Figure 2: Shear Stress for straight tube, different $\overline{\alpha}^*$'s [H^*=2, A_0=2, A_1=4,$a_0 = 3,\ \phi =\ 15^0,\ t = 0.5,\ \ b = 0, a = 1$].

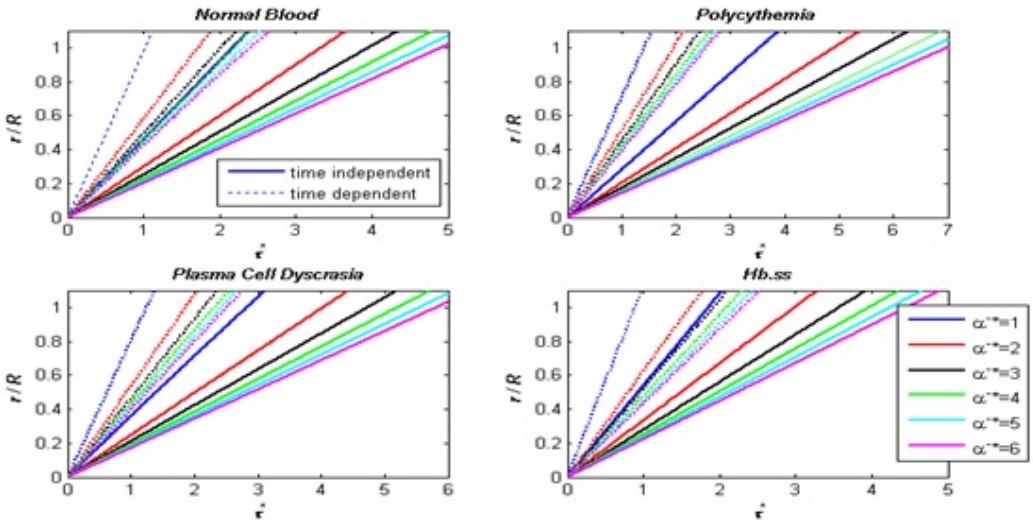

Figure 3: Shear Stress for straight tube,different $\overline{\alpha}^*$'s [H^*=2, A_0=2, A_1=4,$a_0 = 3$, $\varnothing = 15^0$, $t = 1.5$, $b = 1.5, a = 5$].

CONCLUSIONS

Size effects in blood flow have been studied in the present studies. One of the main thrust in the modeling approach is to include effects of blood cells (mainly Red Blood Cells) on the flow situations under the influence of periodic and body accelerations. Effects of body accelerations and magnetic have also observed to influence significantly. The utility of model has also been explored by applying it for various blood diseases and comparing it with normal case. The results indicate that shear stress to flow have significant variations with applications of body acceleration and magnetic induction.

References

[1] W.A. Hyman, *the role of slip in the rheology of blood, Biorheology (1973) 10,57.*

[2] L.Dintenfass, *Inversion of the Fahraeus-Lindqvist phenomenon in blood flow through capillaries of diminishing radius, Nature 215(5105)(1099)(1967).*,

[3] k.Halder, *Oscillatory flow of bllod in a stenosed artery. Bull.Math. Biol.49,3(1987)279-287.*

[4] D.F. Young, *effect of a time dependent stenosis of flow through a tube. J.Engnj Ind.90(1968)248-254.*

[5] D.A. McDonald, *Blood Flow in arteries 2th Education Edward Arnold, London (1974) 496.*

[6] S.C.Cowin, *The theory of polar fluids. Adv. In Appl. Mech. 14 (1974) 279-347.*

[7] S.Tanveer, *Blood flow through narrow tubes with periodic body acceleration in presence of magnetic field and its application to cardiovascular diseases, Ph.D, Thesis Gulbarga University (2005).*

[8] A. R.Haghighi, M. S. Asl and M. Kiyasatfar. *Mathematical modeling of unsteady blood flow through elastic tapered artery with overlapping stenosed,* Journal of the Braziliam Society of Mechanical Sciences and Engineering. *Vol.37,pp(2015)571–583.*

[9] M.Asif Ikbal,P. Mandal, *Mathematical Studies of non-Newtonian Blood Flow through a Patient-Specific Atherosclerotic Artery,* Journal of Applied Nonlinear Dynamics, Vol.12, No.3, pp (2023) 441-451

e-mail: ah.haghighi@gmail.com

Mathematical model of cystic fibrosis pulmonary disease and air flow in the lung

Fatemeh Hasanzadeh[1]
Zahra Hasanzadeh[2]
Hamidreza Marasi
Faculity of Mathematics, statistics and computer science, University of Tabriz, Tabriz, Iran

Abstract

In this article, we write the EIR mathematical model of cystic fibrosis and derive the equations related to this model. Also, by using the definition of Reynolds number and its application in fluid mechanics, we investigate the types of air flow and specify the type of each of them. This number includes 2 quiet and disturbed intervals. According to this information, the result obtained is that the Reynolds number of the person suffering from this disease will be in the disordered category.

Keywords: EIR model, Reynolds number, types of air flow, cystic fibrosis, Turbulent

AMS Mathematical Subject Classification [2010]: 13D45, 39B42

1 Introduction

In certain disorders, a measurement that serves as a reliable indicator of the patient's prognosis can be used, such as: 1. PSA, or prostate specific antigen 2. The kidney's Glomerular Filtration Amount[2] 3. The quantity of HIV-positive CD4 T lymphocytes[3]. Precise mathematical models ought to encompass the shared phenomenon of longitudinal alterations in this assessment and death, which may be linked to shifts between discrete patient conditions, like obtaining or losing a pathogen[5].

In this article, we primarily aim to provide a model of the progressive, genetic lung condition known as cystic fibrosis. The forced expiratory volume in one second (FEV1) is typically used to measure this disease, which is brought on by a mutation in the CFTR gene[5].

The interplay between long-term bacterial infections and the inflammatory immune response generated to combat them is primarily responsible for the decline in FEV1. The Reynolds number and how to use it to determine the kind of airflow are covered in the following.

[1] hstyhsnzadh5@gmail.com
[2] zhsnzadh49@gmail.com

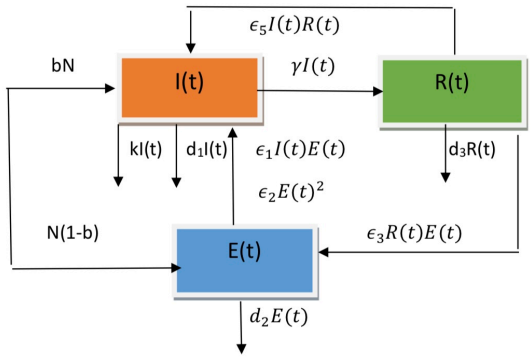

Figure 1: .

2 Mathematical model of cystic fibrosis transmission

The genetic illness known as cystic fibrosis is brought on by the introduction of two faulty genes into an individual's body at birth. In actuality, the majority of people are usually unaware that they are carriers. It should be mentioned that family weddings might sometimes be the cause of this illness. The EIR mathematical model of cystic fibrosis is introduced for the first time in this article. Three compartments are included in this model: Babies with two faulty genes who can spread the disease are included in the first compartment, I(t). Babies in the second compartment, E(t), have a faulty gene and are regarded as carriers but are not contagious. Those who are healthy or who can only be healed by lung transplantation are included in the third compartment R(t). The equations related to this model are as follows:

$$
\begin{aligned}
I'(t) &= bN + \epsilon_1 I(t)E(t) + \epsilon_2 E(t)^2 + \epsilon_5 I(t)R(t) - d_1 I(t) - kI(t) - \gamma I(t) \\
E'(t) &= N(1-b) + \epsilon_3 R(t)E(t) - \epsilon_1 I(t)E(t) - d_2 E(t) - \epsilon_2 E(t)^2 \\
R'(t) &= \epsilon_4 R(t)^2 - \epsilon_5 I(t)R(t) - \epsilon_3 R(t)E(t) + \gamma I(t) - d_3 R(t)
\end{aligned}
$$

3 Determining the types of air flow in the lung using Reynolds number

Reynolds number, which is a dimensionless quantity in fluid mechanics and one of the most important parameters in determining whether the flow is calm or turbulent, is used to predict the flow pattern. This number is the result of the ratio of inertial force to viscosity. If the flow moves in a closed channel or in a pipe, the Reynolds number depends on the hydraulic diameter of the pipe (d_h) and its length L, and in the case that if the pipe is cylindrical, its hydraulic diameter is actually the same diameter. It will be a pipe. The respiratory system is a biological system whose task is to supply oxygen to body cells and remove carbon dioxide resulting from metabolism. The organs of this system are the nose, pharynx, larynx, trachea and lungs. In this article, we will examine air flow and its types in the lungs. The respiratory system is like a tree that starts from the trachea and branches 23 times before reaching the alveolar sacs[7, 8]. According to the mentioned cases, the mathematical definition of this number for the flow through a pipe of diameter d is as follows

$$
R_e = \frac{F_{\text{inertia}}}{F_{\text{viscous}}} = \frac{\rho V L}{\mu} = \frac{VL}{v} \tag{1}
$$

So the terms used are as follows:

ρ fluid density in $\left(\mathrm{kg/m^3}\right)$

V fluid velocity in (m/s)

L is the characteristic length of the fluid in (m)

v kinematic viscosity of fluid $\left(\mathrm{m^2/s}\right)$

The volumetric velocity of the phase flow is obtained through the following equation

$$\varphi = V.A \tag{2}$$

The Reynolds number is recast in terms of flow rate using equations (2) and (1) since A is the pipe's cross-sectional area and V is the fluid velocity.

$$d = 2r, \quad V = \frac{\varphi}{A}, \quad v = \frac{\mu}{\rho}$$

By inserting the values mentioned in equation (1), we will have

$R_e = \frac{Vd}{v} = \frac{\frac{\varphi}{A}\times 2r}{\frac{\mu}{\rho}} = \frac{\frac{\varphi}{\pi r^2}\times 2r}{\frac{\mu}{\rho}}$

So $\quad R_e = \frac{2\rho\varphi}{\pi r\mu}$

The average Reynolds number has been determined by applying equation (3). Based on the kind of flow, several lung generations have been categorized using the following ranges of Reynolds numbers[6]. The Reynolds number is represented by the numbers 0, 2300, 4000, and infinite. The ranges for laminar, transitional, and turbulent flow are defined differently in experiments, and these definitions are given above. There are two types of flows: calm and turbulent. The criterion for identifying a smooth or turbulent flow is the Reynolds number. A laminar flow is one in which the fluid follows predetermined routes and travels in an ordered fashion. However, the fluid is susceptible to strong mixing processes and flow variations in its

turbulent flow. Three-dimensionality, periodicity, temporal and spatial fluctuations, as well as random and unexpected behavior, are some of the most significant characteristics of turbulent flow. Turbulent flows have a variety of durations and times, and they happen at elevated Reynolds numbers. These streams comprise an ever-changing environment. Furthermore, mixing is the primary distinction between this kind of flow and slow flow.

Table 1. Reynolds number result.

GENERATION	REYNOLDS	AIR FLOW TYPE
1	17706	Turbulent
2	13061	Turbulent
3	9599	Turbulent
4	7114	Turbulent
5	4426	Turbulent
6	2845	Transitional
7	1778	Laminar
8	1082	Laminar
$\ldots, 23$	< 1000	Laminar

4 Conclusion and Results

It is clear from the diagram that there is an inverse relationship between viscosity forces and the Reynolds number and that the Reynolds number is directly related to inertial forces. Determining if the flow is calm or turbulent is a crucial usage of this value. For instance, the flow will be smooth if the Reynolds number is less than a given value and turbulent if it is larger. In actuality, the crucial Reynolds number is the value at which the fluid flow starts to become turbulent, and this specific value is known as such. orange This article examines the IER model of cystic fibrosis disease and reveals that it is transmissible and does not affect any susceptible individuals. to the infant only through two faulty genes from the parents, and to use this information to further research the Reynolds number and identify the kind of air flow. The number was paid for by us. Lastly, it should be noted that the data obtained indicate that lung airflow in individuals with cystic fibrosis is consistently disrupted. The next articles will look at FEV1 and how it relates to the affected person's lung, the kind of flow, and Reynolds number.

References

[1] Dayananda, P., J.T. Kemper, and M.M. Shvartsman, A stochastic model for prostate-specific antigen levels. Mathematical biosciences, 2004

[2] Imai, E., et al., Slower decline of glomerular filtration rate in the Japanese general population: a longitudinal 10-year follow-up study. Hypertension Research, 2008.

[3] Madec, Y. and C. Japhet, First passage time problem for a drifted OrnsteinUhlenbeck process. Mathematical biosciences, 2004

[4] Zarei, Sara, et al. "Modeling the airflow in a lung with cystic fibrosis." Journal of Non-Equilibrium Thermodynamics 38.2 (2013)

[5] . Adler, Frederick R., and Theodore G. Liou. "The dynamics of disease progression in cystic fibrosis." PLoS One 11.6 (2016)

[6] Mikhailov, M. D. "Basic heat transfer: McGraw-Hill, New York (1977), 572 pp." (1979)

[7] Weibel, E. R., Design of airways and blood vessels considered as branching trees, in: The Lung: Scientific Foundations, pp. 711720, Raven, New York, 1991.

[8] . Kulish, V. V., Lage, J. L., Hsia, C. C. W. and Johnson, R. L., A porous medium model of alveolar gas diffusion, J. Porous Media, 2 (2002)

Dynamic Behaviour of a Cancer Tumor

Zahra Hasanzadeh[1]
Fatemeh Hasanzadeh
Hossein Kheiri
Faculity of Mathematics, statistics and computer science, University of Tabriz, Tabriz, Iran

Abstract

Kheiri This research develops a dynamic model of cancer formation that includes interactions between activated immune system cells, tumor cells, and healthy tissue cells, obviously resulting in chaotic behavior. In reality, the conditions under which the dynamics of chaos can be observed, as well as the ways in which this model differs from the others, have all been examined. Furthermore, the existence of chaos has been reliably proven by computing the Lyapunov power and system dimension.

Keywords: chaotic dynamics, tumor growth, Lyapunov exponent, Lyapunov dimension, and cancer model

AMS Mathematical Subject Classification [2010]: 13D45, 39B42

1 Introduction

It should be noted that the primary components of mathematical models for tumor growth are immune system and host cells, and that these interactions may produce different outcomes. These models have been extensively researched in the literature to comprehend the mechanism underlying the disease and forecast its future behavior. An ordinary differential equation (ODE) -based second-order model that encompasses the tumor cell and effective immune cell populations was presented by Kuznetsov et al. Depending on the system parameters, these models can provide quite interesting dynamics even with two cell populations. and clarify a few crucial elements of the development of cancer [1]. Depilis and Radonskaya used optimal control theory to study the impact of chemotherapy treatment, added normal tissue cells in their model, and carried out fuzzy space analysis [2]. Kirschner and Panetta also looked into how tumor cells proliferate when immune cells are present. Tumor cell antigen is critical for the immune system to recognize tumor cells, as evidenced by the effectiveness of the cytokine IL- 2, which is crucial for immune system activation and stimulation [3]. The majority of the intriguing dynamics have been found to revolve on symbiotic equilibria, which may lead to variations in cell populations. Conversely, models of tumor formation that incorporate interactions across cell populations mostly rely on population dynamics, which are inspired by predator-prey models. Although a Hunter derivative that can also display chaos has been developed, it is yet unknown

[1]Speaker

whether dynamic chaos exists in cancer models [4]. Actually, this study constructed and examined a very basic tumor growth model. This displays the interest disturbance parameter's range [5]. Furthermore, the three cell types in this model are T(t) tumor cells, $H(t)$ healthy host cells, and $E(t)$ effective immune cells. Even while the model in question shares terminology with other cancer models, it nonetheless illustrates chaotic dynamics, one of the most important issues for nonlinear systems. It's been verified. This article's goals are to present the biological model and its relationship, normalize the system states and minimize the number of parameters in order to streamline the analysis, which then goes on to examine the stability and balance of the system and displays the turbulent absorber in a matter of seconds. Lastly, the article addresses the range of parameters. The system's Lyapunov dimension and power calculations have reached the required result [4].

2 Mathematical model of cancer

Three cell populations are included in this model: $T(t)$ represents the number of tumor cells at time t, $H(t)$ represents the number of healthy host cells, and $E(t)$ represents the number of immune cells that are active at the same time. Additionally, the goal of this model is to describe the interaction and competition between these cells [4].

$$\frac{dT}{dt} = r_1 T\left(1 - \frac{T}{k_1}\right) - a_{12}TH - a_{13}TE, \tag{1}$$

$$\frac{dH}{dt} = r_2 H\left(1 - \frac{H}{k_2}\right) - a_{21}TH, \tag{2}$$

$$\frac{dE}{dt} = \frac{r_3 TE}{T + k_2} - a_{31}TE - d_3 E, \tag{3}$$

By assuming

$$\frac{T}{k_1} = x_1, \quad \frac{H}{k_2} = x_2, \quad \frac{E}{k_3} = x_3,$$

The equations (1)-(3) are converted into [4]

$$\frac{dx_1}{dt} = x_1(1 - x_1) - a_{12}x_1x_2 - a_{13}x_1x_3, \tag{4}$$

$$\frac{dx_2}{dt} = r_2x_2(1 - x_2) - a_{21}x_1x_2, \tag{5}$$

$$\frac{dx_3}{dt} = \frac{r_3x_1x_3}{x_1 + k_3} - a_{31}x_1x_3 - d_3x_3. \tag{6}$$

3 Equilibrium points of the system

Because the aim of this article is to find system dynamic chaos, the authors focused on balance and parameter range to achieve system chaos. More intriguingly, they were able to obtain the system's local behavior by linearizing the system and calculating the Jacopin matrix. The system has eight equilibrium points, designated $E_1 - E_8$, according to the aforementioned Jacopin matrix. E_1 is a saddle point, whereas E_2 and E6 is stability and instability depend on the value of a_{12} . For this reason, the eigenvalues are unstable if $a_{12} > 1$ and stable if $a_{12} < 1$. Point E_2 will serve as a saddle. Furthermore, E_2 will be a destroyed point if $a_{12} = 1$. The computed results indicate that point E_3 is a saddle point and point E_4 and E_7 are not chosen

because of their mixed specific values; point E_5 is unsuitable since of its biological attributes; and E_8 is unsuitable for examination because of its non-positive value [4].

$$J = \begin{bmatrix} 1 - 2x_1 - a_{12}x_2 - a_{13}x_3 & -a_{12}x_1 & -a_{13}x_1 \\ -a_{21}x_2 & r_2 - 2r_2x_2 - a_{21}x_1 & 0 \\ \frac{r_3x_3}{x_1+k_3} - a_{31}x_3 & 0 & \frac{r_3x_1}{x_1+k_3} - a_{31}x_1 - d_3 \end{bmatrix}.$$

The following are the equilibrium points:

Table 1: Equilibrium points [4].

E_1	E_2	E_3	E_4	E_5	E_6
$(0,0,0)$	$(0,1,0)$	$(1,0,0)$	$(0.132,0,0.347)$	$(0,1,0)$	$(0.13,0.66,0.079)$
$\lambda_1 = 1$	$\lambda_1 = 0.6$	$\lambda_1 = -1$	$\lambda_1 = -0.066 + 0.61i$	$\lambda_1 = 0.6$	$\lambda_1 = 0.06143$
$\lambda_2 = 0.6$	$\lambda_2 = 0$	$\lambda_2 = -0.9$	$\lambda_2 = -0.066 - 0.61i$	$\lambda_2 = -0.9$	$\lambda_2 = 0.403 + 0.2351i$
$\lambda_3 = -0.5$	$\lambda_3 = -0.5$	$\lambda_3 = 1.55$	$\lambda_3 = 0.4012$	$\lambda_3 = 1.55$	$\lambda_3 = 0.403 - 0.235i$
saddle		*saddle*	*Snail*		*Snail*

4 Chaotic dynamics

The set of chosen parameters of a chaotic system with Shilnikov-like connections is displayed in this section, along with the calculation of the Lyapunov's power and dimension. Specifically, n orthogonal tangent vectors $v_1, \cdots, v_n$ are chosen as initial conditions such that $\dot{\rho} = J\rho$, which is solved by each of $V_1 - V_n$, and $V(t)$ is obtained for $0 \ll t \ll t_1$, so m, τ are defined as follows [4]:

$$m = \frac{t_f - t_0}{\tau}, \quad \tau = t_{i+1} - t_i, \ \forall i = 0, \cdots, m.$$

The following formula is used to calculate orthogonal vectors.

$$v'_n = \frac{v_n - < v_n, v'_{n-1} > v'_{n-1} - \cdots - < v_n, v'_1 > v'_1}{\|v_n - < v_n, v'_{n-1} > v'_{n-1} - \cdots - < v_n, v'_1 > v'_1\|},$$
$$N_p(i) = \|v_n - < v_n, v'_{n-1} > v'_{n-1} - \cdots - < v_n, v'_1 > v'_1\|,$$

Finally, the following equation gives the Lyapunov dimension.

$$\mu_p = \lim_{m\to\infty} \frac{\sum_{i=1}^{m} \ln N_p(i)}{m\tau}, \qquad d_l = j + \frac{\sum_{p=1}^{j} \mu_p}{|\mu_j + 1|}.$$

Additionally, the Lyapunov exponent is produced using the same method as previously, and the following set of parameters for the Lyapunov exponent will result.

$$\mu_1 = 0.021468, \ \ \mu_2 = -0.0055424, \ \ \mu_3 = -0.540526.$$

5 Results

This work constructed and analyzed a new population dynamics-inspired model for the evolution of cancer cells, which includes terminology to characterize the competition and interaction between tumor cells and other body cells, such as immune cells. It shows functional and sound tissue cells. Furthermore, by displaying Shilnikov-like connections, this model demonstrated chaotic dynamics. It further demonstrated chaotic dynamics by determining Lyapunov's power and dimension and fractal parameters. possesses it. While some research suggest that some cancer-like models might show chaos, they haven't shown it to be present. It's heartening [4].

References

[1] Kuznetsov, V.A., et al., Nonlinear dynamics of immunogenic tumors: parameter estimation and global bifurcation analysis. Bulletin of mathematical biology, .1994

[2] De Pillis, L.G. and A. Radunskaya, The dynamics of an optimally controlled tumor model: A case study. Mathematical and computer modelling, 2003

[3] Kirschner, D. and J.C. Panetta, Modeling immunotherapy of the tumor-immune interaction. Journal of mathematical biology, 1998

[4] S.P. Banks, Chaos in a three-dimensional cancer model.Itik, M International Journal of Bifurcation and Chaos, 2010

[5] Ahmed, E., Fractals and chaos in cancer models. International journal of theoretical physics, 1993

Generating pharmaceutical molecules using deep Learning

Sanaz Hashemipour[1]
Department of Computer Science, Faculty of Mathematics, Statistics, and Computer Science, University of Tabriz, Tabriz, Iran.

Habib Izadkhah
Department of Computer Science, Faculty of Mathematics, Statistics, and Computer Science, University of Tabriz, Tabriz, Iran.

Abolfazl Barzegar
Research Institute for Fundamental Sciences (RIFS), University of Tabriz, Tabriz, Iran.

Abstract

The traditional drug design process is highly expensive, often causing delays in the availability of life-saving treatments for patients. This presents a major challenge for developing new medications. In contrast, deep learning has greatly accelerated the development of new therapies. This study explores the potential of a recurrent neural network, specifically using bidirectional long short-term memory (Bi-LSTM) cells, to learn and infer meaningful chemical rules. This network is trained using existing compounds represented by SMILES strings (Simplified Molecular Input Line Entry System) and can generate new drug molecules with desirable properties. The properties of these molecules are fine-tuned using a dataset of drug-like molecules. The generated compounds and the training data set show a similar distribution in terms of predicted logP, molecular weight, hydrogen bond acceptors and donors, topological polar surface area, and rotatable bonds. As assessed by SwissADME, some of these compounds can be synthesized.

Keywords: Deep Learning, Drug Design, Recurrent Neural Network, Bi-LSTM, SMILES Strings
AMS Mathematical Subject Classification [2010]: 13D45, 39B42

1 Introduction

In recent years, the merging of artificial intelligence (AI) with drug discovery has sparked a revolutionary approach to designing molecules. At the heart of this transformation are deep learning techniques, particularly recurrent neural networks (RNNs) [1] like bidirectional long short-term memory (Bi-LSTM) networks [1]. These innovations promise to overhaul drug development by integrating computational creativity and efficiency, thereby complementing traditional, labor-intensive methods.

Deep learning offers an exciting frontier in pharmaceutical research for generating novel drug molecules. By leveraging the extensive data stored in molecular structures, often represented as simplified molecular-input line-entry system (SMILES) [2] strings, researchers can train neural networks to understand the

[1]Speaker

intricate connections between chemical structures and their properties. This method not only speeds up the discovery of potential drug candidates but also broadens the exploration of chemical space beyond traditional methods.

Recent studies have highlighted the effectiveness of Bi-LSTM networks in capturing the sequential dependencies found in SMILES strings [3]. This capability enables the generation of diverse molecular structures that are pharmacologically relevant. The ability to create molecules with desired biological activities, while also meeting physicochemical constraints, represents a notable advancement in computational drug discovery.

This paper delves into the significant impact of deep learning methods, specifically Bi-LSTM networks, in the creation of drug molecules. By training on datasets tailored for drug-like compounds, which include annotated SMILES representations, researchers can harness these models to navigate the intricate realm of molecular design with precision. Through this perspective, the study seeks to highlight the potential of AI-driven approaches in expediting the discovery and advancement of therapeutic agents.

2 Main results

The clean drug-like dataset (p13) was downloaded in SMILES format from the Zinc12 [4] [5] website. After extracting the data from its compressed format, it was converted into a data frame using Python 3.1 [6] and Pandas [7]. The resulting data frame contained two columns: ”smiles” and ”name” with columns separated by spaces.

Next, the data frame was saved as a CSV file, including the column names and excluding row numbers. Using Pandas, the information from the ”smiles” column was then aggregated into a single text string.

First, the 35 unique characters present in the ”SMILES” text were identified. Each of these characters was mapped to a unique integer, resulting in a dictionary where each unique character was associated with its corresponding integer value. Subsequently, the total number of characters and unique words in the dataset were counted, yielding 7,825,572 characters and 36 unique vocabularies.

The data was then segmented into smaller sequences, each with a fixed length. For each sequence, an input vector and a corresponding output value were generated for model training. A total of 7,825,562 sequences were produced for training purposes.

The shape of the input array was then transformed into a three-dimensional array with dimensions (number of sequences, sequence length, 1). The data was normalized, and the output values were encoded using one-hot encoding.

A Recurrent Neural Network (RNN) was developed using Keras [8] with TensorFlow [9] as the backend, consisting of six layers. The first layer is a bidirectional LSTM with 64 units, processing data in both forward and backward directions, enabling the model to capture temporal dependencies in both directions. The input shape for this layer was specified. The second layer is another bidirectional LSTM, but with 128 units, followed by a third bidirectional LSTM with 256 units, continuing the sequence processing. The fourth layer mirrors the second, also being a bidirectional LSTM with 128 units. Layers one through four return full sequences to the next layer, maintaining the flow of data across the network. The fifth layer, similar to the first, is a bidirectional LSTM with 64 units, but it only returns the last output instead of the full sequence, passing only the final output to the next layer. The sixth layer was a fully connected layer with 64 units, corresponding to the number of output classes. This layer used the softmax activation

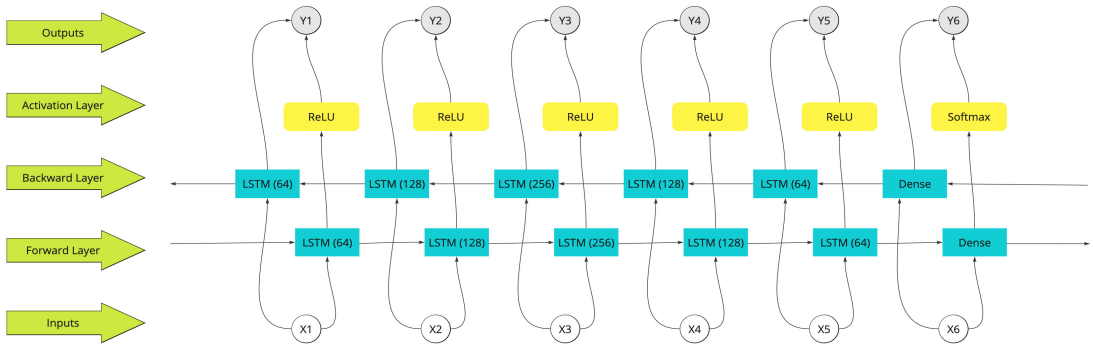

Figure 1: Architecture of Bidirectional Long Short-Term Memory (Bi-LSTM) Cells.

function, which is suitable for classification tasks as it produces output values that sum up to 1 (Figure 1). The model was compiled using categorical_crossentropy as the loss function and Adam as the optimizer, with accuracy as the evaluation metric. During training, the best model weights were saved based on the lowest loss value.

The neural network was trained on 200,000 SMILES strings for 10 epochs with a batch size of 64. Subsequently, the saved model weights were loaded, the model was compiled again, and a random string of SMILES data was selected. Finally, a sequence of strings was generated. The model produced 152 SMILES strings, one of which lacked molecular properties, and two molecules with desirable properties were repeatedly generated (Figure 2).

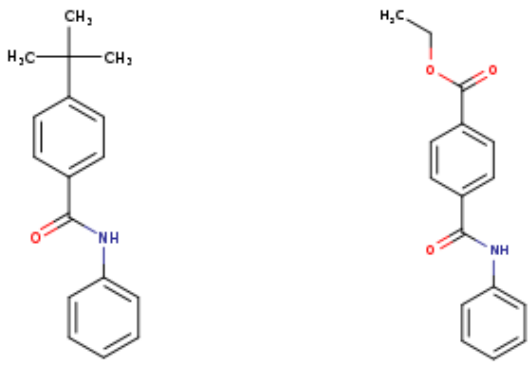

Figure 2: Molecules generated by our model.

Drug-like compounds are defined by the following properties: $logP \leq 3.83$, $molecularweight(MWT) \leq 269.30$, $numberofrotatablebonds \leq 6$, $topologicalpolarsurfacearea(TPSA) \leq 55.40$, $hydrogenbonddonors \leq 1$, and $hydrogenbondacceptors \leq 3$. According to Lipinski's Rule of Five, drug-like molecules generally adhere to no more than one of the following criteria being violated [10]:

1. No more than 5 hydrogen bond donors (total of nitrogen-hydrogen and oxygen-hydrogen bonds).
2. No more than 10 hydrogen bond acceptors (total number of nitrogen and oxygen atoms).
3. Molecular weight less than 500 Daltons.
4. Calculated octanol-water partition coefficient (Clog P) not greater than 5.

Figure 3 shows the molecules evaluated using SwissADME [11]. One of the crucial aspects considered for pharmaceutical compounds is pharmacokinetics, which relates to the movement of drugs within the body.

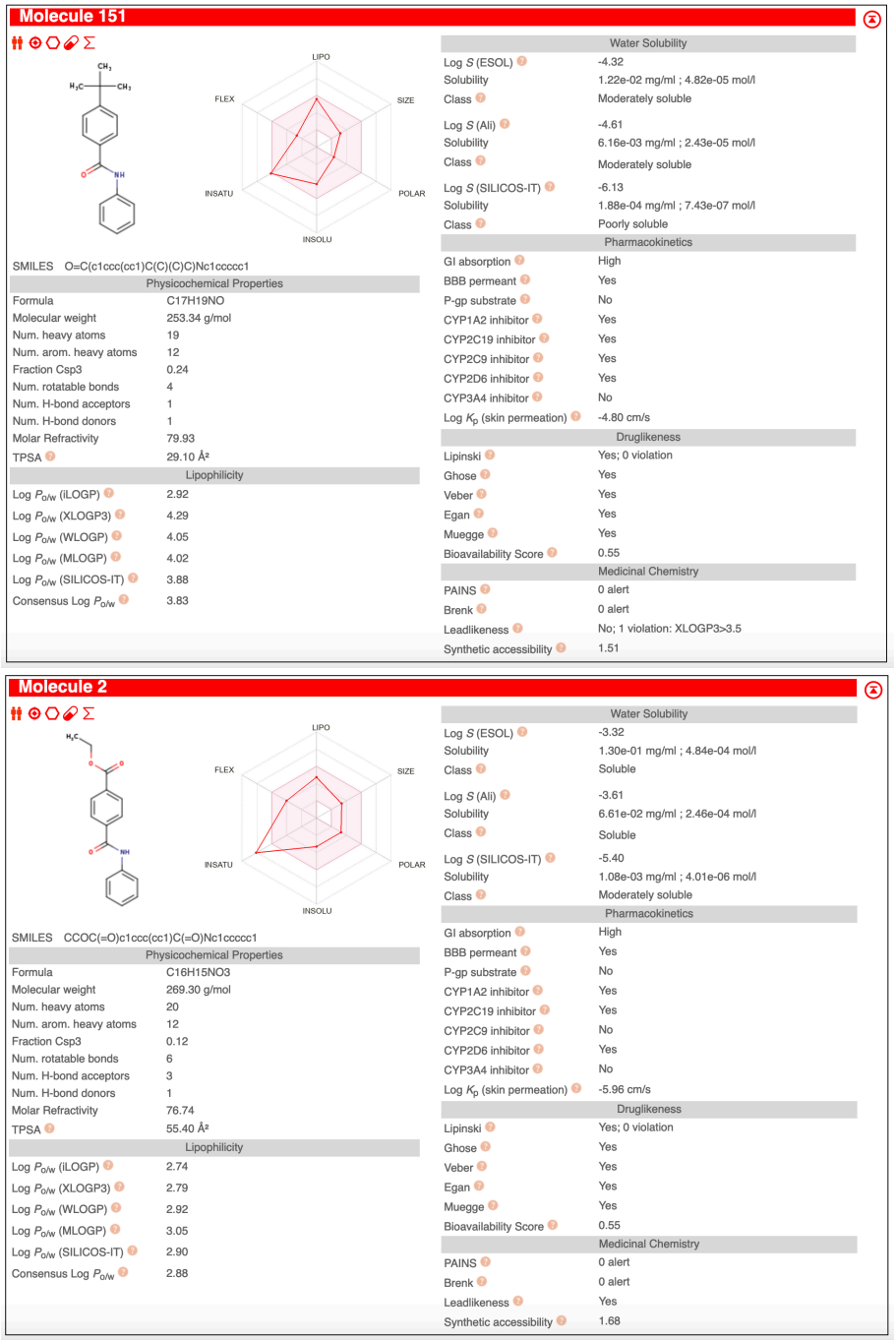

Figure 3: Properties of the resulting molecules.

It examines how the body affects a specific drug after administration through mechanisms of absorption, distribution, metabolism, and excretion (ADME). The primary goals of pharmacokinetics are to determine the onset, duration, and intensity of a drug's effect [12].

Consequently, recurrent neural networks with Bi-LSTM cells can be trained to generate new, chemically acceptable molecules, as evaluated by SwissADME.

References

[1] Izadkhah, H. (2022). Deep learning in bioinformatics: techniques and applications in practice. Academic Press.

[2] Weininger, D. (1988). SMILES, a chemical language and information system. 1. Introduction to methodology and encoding rules. Journal of chemical information and computer sciences, 28(1), 31-36.

[3] D'Souza, S., Kv, P., & Balaji, S. (2022). Training recurrent neural networks as generative neural networks for molecular structures: how does it impact drug discovery?. Expert Opinion on Drug Discovery, 17(10), 1071-1079.

[4] Irwin, J. J., & Shoichet, B. K. (2005). ZINC− a free database of commercially available compounds for virtual screening. Journal of chemical information and modeling, 45(1), 177-182.

[5] Irwin, J. J., Sterling, T., Mysinger, M. M., Bolstad, E. S., & Coleman, R. G. (2012). ZINC: a free tool to discover chemistry for biology. Journal of chemical information and modeling, 52(7), 1757-1768.

[6] Van Rossum, G., & Drake Jr, F. L. (1995). Python reference manual. Centrum voor Wiskunde en Informatica Amsterdam, 111, 1-52.

[7] Heydt, M. (2017). Learning pandas. Packt Publishing Ltd.

[8] Moolayil, J., Moolayil, J., & John, S. (2019). Learn Keras for deep neural networks (pp. 33-35). Birmingham: Apress.

[9] Singh, P., Manure, A., Singh, P., & Manure, A. (2020). Introduction to tensorflow 2.0. Learn TensorFlow 2.0: Implement Machine Learning and Deep Learning Models with Python, 1-24.

[10] Lipinski CA, Lombardo F, Dominy BW, Feeney PJ (March 2001). "Experimental and computational approaches to estimate solubility and permeability in drug discovery and development settings". Advanced Drug Delivery Reviews. 46 (1–3): 3–26.

[11] Daina, A., Michielin, O., & Zoete, V. (2017). SwissADME: a free web tool to evaluate pharmacokinetics, drug-likeness and medicinal chemistry friendliness of small molecules. Scientific reports, 7(1), 42717.

[12] Rowland, M., & Tozer, T. N. (2011). Clinical Pharmacokinetics and Pharmacodynamics: Concepts and Applications (4th ed.). Philadelphia: Wolters Kluwer Health/Lippincott Williams & Wilkins.

e-mail: `s.hashemi1400@ms.tabrizu.ac.ir`
e-mail: `izadkhah@tabrizu.ac.ir`
e-mail: `barzegar@tabrizu.ac.ir`

سومین همایش بین‌المللی و پنجمین همایش ملّی ریاضیات زیستی
Third International and Fifth National Biomath Conference
مردادماه ۱۴۰۳

Modeling and forecasting of rainfall from satellite data using radial base and generalized regression neural networks

Nahideh Hossein Babazadeh[1]
University of Tabriz, Tabriz, Iran

Gholam Reza Zaki
University of Tabriz, Tabriz, Iran

Abstract

In this article, the precipitation forecast in the west of Sahand Mountain in East Azarbaijan Province has been investigated. Satellite data and these algorithms, often do not match the measured data at weather stations. Contradictory forecasts by these algorithms, confuse meteorologists. To overcome this problem, we propose two special case of artificial neural network to modelling the 8 algorithms together. The neural network receives the satellite data of previous years and compares them with the data measured in weather stations. After training, the neural network predicts the rainfall from the data of the above satellites algorithms with admirable accuracy.

Keywords: Weather satellites, climate data records, radial basis neural network, Generalized regression neural network.

Mathematics Subject Classification [2010]: 13D45, 39B42

1 Introduction

Today, artificial intelligence has conquered many branches of science. The ability to learn artificial neural networks, as one of the important branches of artificial intelligence, has turned it into an important tool in identifying the behavior of a system and consequently predicting the future of that system. The weather condition is one of the fields whose prediction is very important. The use of neural networks in rainfall forecasting goes back decades. In the 1997, Chuan, use the artificial neural network to Weather prediction.[1] In the 1999, Hall, use the neural network for Precipitation forecasting.[3] In 2001, Luk, presented an application of neural networks for rainfall forecasting.[4] In 2005, ferreira, introduced the neural network technique to predict rainfall in City *São* Paulo region in Brazil.[2]

Today, weather forecasting is usually done with the help of satellites. Satellites measure parameters of atmospheric conditions and predict the amount of rainfall in a region. Often, the predictions of satellites do not agree with the data measured by meteorological stations, or the predictions of satellites are contradictory. To overcome this problem, we have used radial base artificial neural networks. The proposed neural network receives the forecasts of 8 satellites and provides a more accurate forecast from their combination.

[1] Gholam Reza Zaki

2 Preliminary

In this section, we introduce the satellites and the parameters measured by them. Eight groups of data obtained from satellites and related algorithms are: $CCSCDR$, CCS, $PDIR$, $PERSIANN$, CDR, $EARLY$, $LATE$, $FINAL$. They measure several atmospheric parameters and predict the amount of rainfall in a region with the help of their own algorithms. We have the amount of rainfall predicted by these eight satellites for 19 meteorological stations in west of Sahand Mountain (East Azarbaijan province) for 13 years. On the other hand, the amount of rainfall measured every day has been recorded in each of the stations of the province. In most cases, satellite forecasts are contradictory and do not correspond to the amount of precipitation recorded in the stations. For example, on 13/04/17,14/04/17 and 15/04/17 we see the forecast of these eight algorithms for Azarshahr station in Table 1. This is despite the fact that 49 mm of rainfall has been recorded for the above station in date 14/04/17. This rain caused floods and many human and financial losses. To focus more on the subject, we only examine Azarshahr station. Table 2, shows

Table 1: Rainfall forecast by each of the eight algoritms for Azarshahr station in three consecutive days.

Date	CCSCDR	CCS	PDIR	PERSIANN	CDR	EARLY	LATE	FINAL
13/04/17	12	26	11	12.07	8	0.624.4	0.458	1.902
14/04/17	4	9	5	9.34	14	8.835	9.184	14.758
15/04/17	0	0	0	1	0	0	0	0

three types of errors for Azarshahr station during 4746 days (13 years). The first row is the mean squared error(MSE), the second row is the maximum absolute error(MAE) and the third row is the norm 2 for error($Norm_2$). The prediction of the $PERSIANN$ data is better than the prediction of the other algorithms.

Table 2: Errors of prediction of each algoritms.

Error	CCSCDR	CCS	PDIR	PERSIANN	CDR	EARLY	LATE	FINAL
MSE	27.9	56.9	12.5	8.4	10.6	15.4	16.4	11.9
MAE	89.0	275.0	74.0	39.7	35.0	58.4	77.0	40.0
$Norm_2$	364.1	519.7	243.9	199.4	224.1	270.8	279.2	237.5

3 Proposed method

In order to make better predictions, we propose the use of artificial neural networks. Two types of neural networks have performed better than other networks. These two types of networks are: radial basis neural network(Net_{rb}) and Generalized regression neural network(Net_{grnn}). Table 3 shows the types of errors of these two networks for Azarshahr station.

Table 3: Three types of errors for predictions of two types of neural networks.

Error	Net_{rb}	Net_{grnn}
MSE	2.9893	2.3808
MAE	22.5735	22.7705
$Norm_2$	119.1354	106.3207

As can be seen, each of the networks was able to reduce the error MSE by at least three times. Figure 1 compares the amount of rainfall predicted by the $PERSIANN$ with the amount recorded at the station for 4746 days.

Figure 2, predictions of network Net_{rb} and Figure 3, predictions of network Net_{grnn} compare with the amount recorded at the station for 4746 days. As can be seen, each of the two neural networks have predicted the amount of rainfall of 49 mm in day 14/04/17, while the $PERSIAN$ algorithm has predicted it to a much lesser extent.

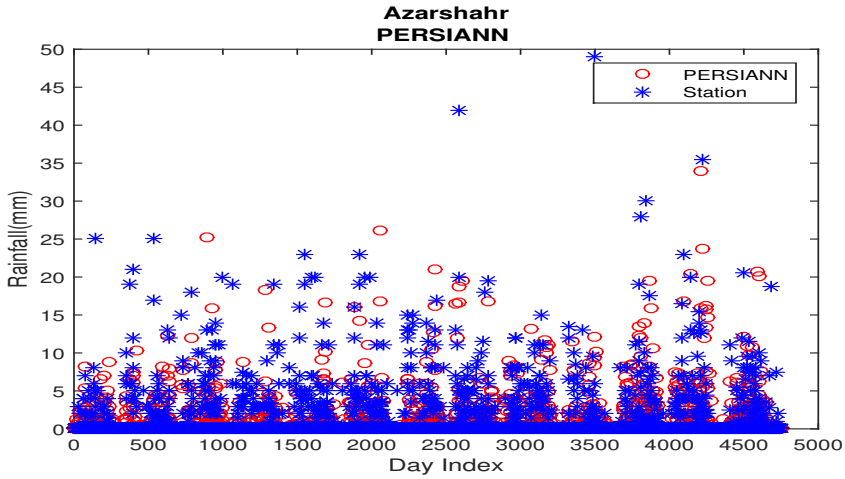

Figure 1: Comparing the amount of rainfall predicted by the Persian satellite with the data recorded by the Azarshahr station for 4746 days.

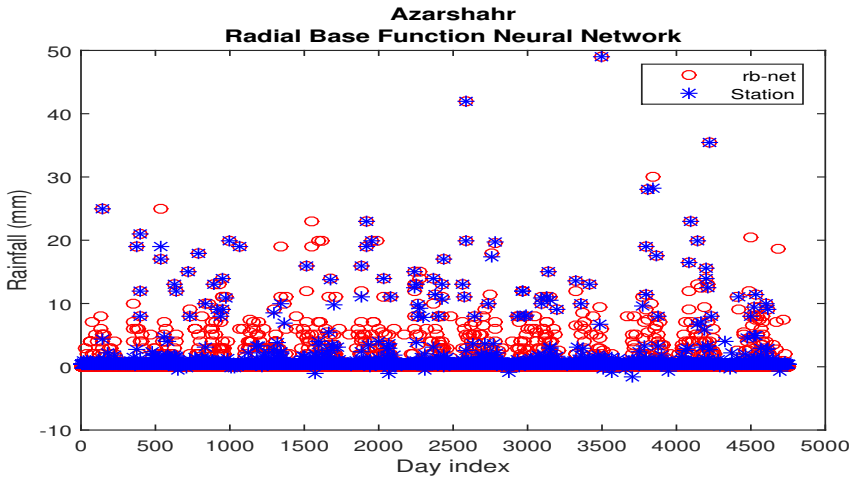

Figure 2: Comparing the amount of rainfall predicted by the Net_{rb} with the data recorded by the Azarshahr station for 4746 days.

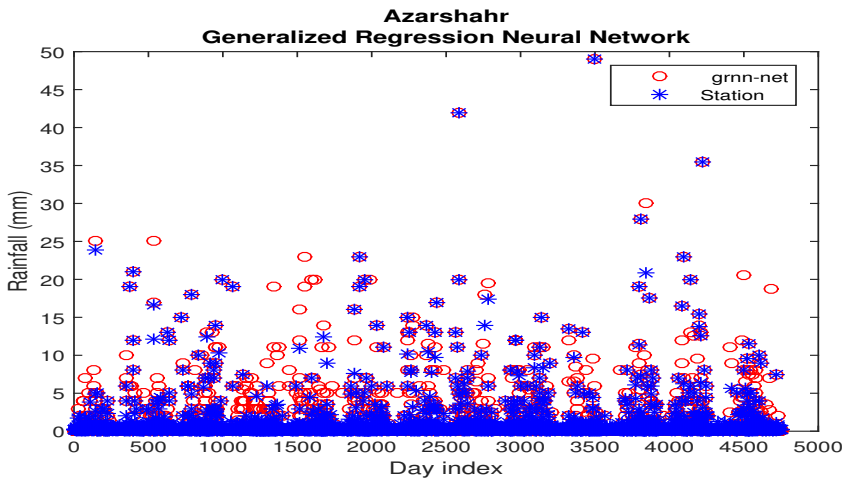

Figure 3: Comparing the amount of rainfall predicted by the Net_{grnn} with the data recorded by the Azarshahr station for 4746 days.

4 Conclusion

It is very valuable to use appropriate neural networks that take the predictions of 8 algorithms and provide better predictions. In this paper, two types of neural networks were proposed, which reduced the MSE error by three times. Needless to say, the author did not get favorable results from using feed-forward backpropagation neural networks.

Acknowledgment

We are very grateful to the Meteorological Organization for providing the measured data of meteorological stations located in East Azarbaijan province.

References

[1] Chuan, C.S. (1997) *Weather prediction using artificial neural network*, Journal of Hydrology, 230: 101–119.

[2] Ferreira, N.J., Velho, H.F. and Ramirez, M.C.V. (2005), *Artificial neural network technique for rainfall forecasting applied to the Sa˜o Paulo region*, Journal of Hydrology, 301: 146–162.

[3] Hall, T., Brooks, H.E. and Doswell, C.A. (1999) *Precipitation forecasting use a neural network* , Weather and Forecasting Journal, 14: 338-345.

[4] Luk, K.C., (2001) *An application of artificial neural networks for rainfall Forecasting*, Mathematical and Computer Modeling Journal, 33: 883-699.

Email: babazadeh9@gmail.com
Email: GhRezaZaki@gmail.com

Influence of Backward Bifurcation in a Model of Tuberculosis

Azizeh Jabbari[1]
Marand Faculty of Engineering, University of Tabriz, Tabriz, Iran

Abstract

This study presents a two-patch model of a tuberculosis (TB) epidemic, where individuals can freely move between the regions, but only the susceptible population is able to do so. We determine the conditions under which a backward bifurcation can occur, leading to the existence of multiple boundary equilibria. Additionally, we show that a TB model with incomplete treatment, where treated individuals can return to either the latent or infectious compartments, can exhibit exogenous reinfection without displaying a backward bifurcation. In this case, the disease-free equilibrium of the model is globally asymptotically stable when the associated reproduction number is less than one. In the absence of reinfection, the model can exhibit up to four distinct equilibria.

Keywords: TB, Backward bifurcation, Basic reproduction number, Stability analysis.
Mathematics Subject Classification [2010]: 92D30, 37N25

1 Introduction

TB is a serious infectious disease caused by a bacteria known as Mycobacterium TB, which primarily affects the lungs. In TB models, the treated individuals have the potential to leave the treatment compartment and subsequently enter either the latent or infectious compartment, due to the persistence of Mycobacterium TB or treatment failure, respectively.

Many TB models that account for the phenomenon of exogenous reinfection have been observed to exhibit a specific type of bifurcation known as a backward bifurcation, where a stable endemic equilibrium coexists with a stable disease-free equilibrium [1].

This study considers a model where only the susceptible individuals are able to migrate between the two regions. We determine the conditions under which a backward bifurcation can occur, leading to the existence of multiple boundary equilibria. Furthermore, we show that a TB model with incomplete treatment, where treated individuals can transition to the latent or infectious compartments, can exhibit exogenous reinfection without displaying a backward bifurcation.

2 Model Description

We assume that only the susceptible population is able to migrate between the two patches. The total population in patch i, where $i = 1, 2$, is divided into four compartments: Susceptible individuals, S_i; Latent individuals, L_i, who have been infected but are not infectious; Infectious individuals, I_i, who have active TB and can transmit the infection but are not undergoing treatment; and Treated individuals, T_i. In this model, the treated individuals can leave the treatment compartment and transition to either the latent

[1]Speaker

compartment due to the persistence of Mycobacterium TB, or the infectious compartment due to treatment failure. This leads to the following system of fractional differential equations:

$$\begin{aligned}
\frac{dS_1}{dt} =& \Lambda_1 - \beta_1 I_1 S_1 - \mu_1 S_1 + q_{12} S_2 - q_{21} S_1, \\
\frac{dL_1}{dt} =& \beta_1 I_1 S_1 + (1-k_1)\delta_1 T_1 + (1-p_1)\theta_1 \beta_1 I_1 T_1 - (\epsilon_1 + \mu_1) L_1, \\
\frac{dI_1}{dt} =& \epsilon_1 L_1 + k_1 \delta_1 T_1 + p_1 \theta_1 \beta_1 I_1 T_1 - (\mu_1 + \gamma_1 + \alpha_1) I_1, \\
\frac{dT_1}{dt} =& \gamma_1 I_1 - \theta_1 \beta_1 I_1 T_1 - (\delta_1 + \alpha_2 + \mu_1) T_1, \\
\frac{dS_2}{dt} =& \Lambda_2 - \beta_2 I_2 S_2 - \mu_2 S_2 + q_{21} S_1 - q_{12} S_2, \\
\frac{dL_2}{dt} =& \beta_2 I_2 S_2 + (1-k_2)\delta_2 T_2 + (1-p_2)\theta_2 \beta_2 I_2 T_2 - (\epsilon_2 + \mu_2) L_2, \\
\frac{dI_2}{dt} =& \epsilon_2 L_2 + k_2 \delta_2 T_2 + p_2 \theta_2 \beta_2 I_2 T_2 - (\gamma_2 + \omega_1 + \mu_2) I_2, \\
\frac{dT_2}{dt} =& \gamma_2 I_2 - \theta_2 \beta_2 I_2 T_2 - (\delta_2 + \omega_2 + \mu_2) T_2,
\end{aligned} \tag{1}$$

3 Model Properties and Characteristics

In this part of the study, we examine the fundamental properties and characteristics of the TB model under consideration.

3.1 Analyzing the Disease Free Equilibrium (DFE)

Substituting $L_1 = I_1 = T_1 = L_2 = I_2 = T_2 = 0$ into the system of equations (1) yields the following simplified expressions:

$$\begin{aligned}
\Lambda_1 - \mu_1 S_1 + q_{12} S_2 - q_{21} S_1 = 0, \\
\Lambda_2 - \mu_2 S_2 + q_{21} S_1 - q_{12} S_2 = 0,
\end{aligned}$$

or $AS = \Lambda$, where $A = \begin{pmatrix} \mu_1 + q_{21} & -q_{12} \\ -q_{21} & \mu_2 + q_{12} \end{pmatrix}$, $S = (S_1, S_2)^T$ and $\Lambda = (\Lambda_1, \Lambda_2)^T$. Linear system $AS = \Lambda$, has a unique positive solution $S^0 = (S_1^0, S_2^0)^T = A^{-1}\Lambda$, where the individual components are expressed as:

$$S_1^0 = \frac{q_{12}\Lambda_2 + (\mu_2 + q_{12})\Lambda_1}{\mu_1\mu_2 + \mu_1 q_{12} + \mu_2 q_{21}}, \; S_2^0 = \frac{q_{21}\Lambda_1 + (\mu_1 + q_{21})\Lambda_2}{\mu_1\mu_2 + \mu_1 q_{12} + \mu_2 q_{21}}. \tag{2}$$

Hence, As a consequence, system $AS = \Lambda$, has a unique DFE

$$E_0 = (S_1^0, 0, 0, 0, S_2^0, 0, 0, 0). \tag{3}$$

Through the analysis conducted thus far, we have been able to establish the following result:

Proposition 3.1. *System* (1) *has the unique DFE,* $E_0 = (S_1^0, 0, 0, 0, 0, S_2^0, 0, 0, 0, 0, 0)$.

3.2 Biologically Feasible Region

Let us define the total population size N as the sum of the susceptible, latent, infectious, and treated individuals across the two patches, i.e., $N = \sum_{i=1}^{2} (S_i + L_i + I_i + T_i)$, $\mu = min\{\mu_1, \mu_2\}$, $\bar{\Lambda} = \sum_{i=1}^{2} \Lambda_i$ and $\bar{N} = max\{N_0, \frac{\bar{\Lambda}}{\mu}\}$, where $N_0 = N(0)$. We can establish the following important result regarding the biologically feasible region for the TB model:

Proposition 3.2. *The feasible region Ω is defined as:*

$$\Omega = \{(S_1, L_1, I_1, T_1, S_2, L_2, I_2, T_2) \in R_+^8 : S_i \leq S_i^0,\ N \leq \bar{N}\}$$

is positively invariant and attracting with respect to the TB model described by the system of equations (1).

3.3 Epidemiological Threshold Quantity

Define $F = \left[\begin{array}{c|c} 0 & F_{12} \\ \hline 0 & 0 \end{array}\right]$, where $F_{12} = \begin{bmatrix} 0 & \beta_1 S_1^0 & 0 \\ 0 & 0 & \beta_2 S_2^0 \\ 0 & 0 & 0 \end{bmatrix}$ and $V = \left[\begin{array}{c|c} V_{11} & V_{12} \\ \hline V_{21} & V_{22} \end{array}\right]$, where

$$V_{11} = \begin{bmatrix} \mu_1 + \varepsilon_1 & 0 & -(1-k_1)\delta_1 \\ 0 & \mu_2 + \varepsilon_2 & 0 \\ 0 & 0 & \mu_1 + \delta_1 + \alpha_2 \end{bmatrix},\ V_{12} = \begin{bmatrix} 0 & 0 & 0 \\ -(1-k_2)\delta_2 & 0 & 0 \\ 0 & -\gamma_1 & 0 \end{bmatrix},$$

$$V_{21} = \begin{bmatrix} 0 & 0 & 0 \\ -\varepsilon_1 & 0 & -k_1\delta_1 \\ 0 & -\varepsilon_2 & 0 \end{bmatrix},\ V_{22} = \begin{bmatrix} \mu_2 + \delta_2 + \omega_2 & 0 & -\gamma_2 \\ 0 & \mu_1 + \gamma_1 + \alpha_1 & 0 \\ -k_2\delta_2 & 0 & \mu_2 + \gamma_2 + \omega_1 \end{bmatrix}.$$

The first matrix, denoted as F, represents the rate at which new infections are generated in each patch. The second matrix, denoted as V, represents the transfer rates of infected individuals among the different patches. The next generation matrix of system (1) is

$$\begin{aligned} FV^{-1} &= \left[\begin{array}{c|c} 0 & F_{12} \\ \hline 0 & 0 \end{array}\right] \left[\begin{array}{c|c} V_{11} & V_{12} \\ \hline V_{21} & V_{22} \end{array}\right]^{-1} = \left[\begin{array}{c|c} 0 & F_{12} \\ \hline 0 & 0 \end{array}\right] \left[\begin{array}{c|c} X & Y \\ \hline Z & W \end{array}\right] \\ &= \left[\begin{array}{c|c} F_{12}Z & F_{12}W \\ \hline 0 & 0 \end{array}\right]. \end{aligned}$$

To determine the basic reproduction number, $\mathcal{R}_0$, for the TB model described by the system of equations (1), we can employ the well-established method proposed by van den Driessche and Watmough [3]. we have:

$$\begin{aligned} R_0 =& \rho\{FV^{-1}\} = \rho\{F_{12}Z\} = \rho\{F_{12}{V_{22}}^{-1}V_{21}(V_{12}{V_{22}}^{-1}V_{21} - V_{11})^{-1}\} \\ =& \rho\{\begin{bmatrix} R_0^1 & 0 & * \\ 0 & R_0^2 & 0 \\ 0 & 0 & 0 \end{bmatrix}\} = max\{R_0^1, R_0^2\}, \end{aligned} \tag{4}$$

where

$$\begin{aligned} R_0^1 &= \frac{\beta_1 \varepsilon_1 S_1^0 b_3}{b_1 b_2 b_3 - \delta_1\gamma_1[b_1 k_1 + \varepsilon_1(1-k_1)]}, \\ R_0^2 &= \frac{\beta_2 \varepsilon_2 S_2^0 a_3}{a_1 a_2 a_3 - \delta_2\gamma_2[a_1 k_2 + \varepsilon_2(1-k_2)]}, \end{aligned} \tag{5}$$

$b_1 = \mu_1 + \varepsilon_1,\ b_2 = \mu_1 + \gamma_1 + \alpha_1,\ b_3 = \mu_1 + \delta_1 + \alpha_2,\ a_1 = \mu_2 + \varepsilon_2,\ a_2 = \mu_2 + \gamma_2 + \omega_1,\ a_3 = \mu_2 + \delta_2 + \omega_2.$ R_0^1 and R_0^2 are the basic reproduction numbers in patches 1 and 2 in isolation, respectively, when there is no travel between patches.

4 Backward Bifurcation Analysis

In the analysis of the TB model described by the system of equations (1), we investigate the phenomenon of backward bifurcation, which can lead to the coexistence of a stable disease-free equilibrium and a stable endemic equilibrium, even when the basic reproduction number, $\mathcal{R}_0$, is less than 1. This unexpected behavior, where the disease can persist in the population despite $\mathcal{R}_0 < 1$, is an important consideration in understanding the long-term dynamics and potential control strategies for the TB model. To study the

backward bifurcation, we follow the approach outlined by Castillo-Chavez and Song [2]. We first make the following change of variables to simplify the analysis:

$$x_1 = L_1,\ x_2 = L_2,\ x_3 = I_1,\ x_4 = I_2,\ x_5 = T_1,\ x_6 = T_2,\ x_7 = S_1,\ x_8 = S_2.$$

By setting $X = (x_1, x_2, x_3, x_4, x_5, x_6, x_7, x_8)^T$,the model (1) can be re-written in the form ${}_0^cD_t^\alpha X = F(X)$, with $F = (f_1, f_2, f_3, f_4, f_5, f_6, f_7, f_8)^T$. The Jacobian matrix evaluated at the DFE, E_0, is given by $J^0 = \begin{bmatrix} F-V & 0 \\ D & -A \end{bmatrix}$, where $D = \begin{bmatrix} 0 & 0 & 0 & 0 & -\beta_1 S_1^0 & 0 \\ 0 & 0 & 0 & 0 & 0 & -\beta_2 S_2^0 \end{bmatrix}$.
If $R_0^1 \geq R_0^2$, then $R_0 = R_0^1 = \frac{\beta_1 \varepsilon_1 S_1^0 b_3}{b_1 b_2 b_3 - \delta_1 \gamma_1 [b_1 k_1 + \varepsilon_1 (1-k_1)]}$. We choose the transmission rate β_1 as the bifurcation parameter. The condition $\mathcal{R}_0 = 1$ is satisfied when the bifurcation parameter takes the value: $\beta_1^* = \frac{b_1 b_2 b_3 - \delta_1 \gamma_1 [b_1 k_1 + \varepsilon_1 (1-k_1)]}{\varepsilon_1 S_1^0 b_3}$ At the bifurcation point $\beta_1 = \beta_1^*$, the Jacobian matrix $\mathbf{J}^0$ has a simple zero eigenvalue, and the corresponding right and left eigenvectors are denoted as $\mathbf{W} = (w_1, w_2, w_3, w_4, w_5, w_6, w_7, w_8)^T$ and $\mathbf{V} = (v_1, v_2, v_3, v_4, v_5, v_6, v_7, v_8)^T$, respectively, where

$$w_1 = \frac{b_2 b_3}{\gamma_1 \varepsilon_1} - \frac{k_1 \delta_1}{\varepsilon_1},\ w_2 = 0,\ w_3 = 1,\ w_4 = 0,\ w_5 = \frac{b_3}{\gamma_1},\ w_6 = 0, w_7 = -\frac{(\mu_2 + q_{12})}{\mu_1 \mu_2 + \mu_1 q_{12} + \mu_2 q_{21}} \beta_1 S_1^0 w_5,$$

$$w_8 = \frac{q_{21}}{\mu_2 + q_{12}} w_7, v_1 = 1,\ v_2 = 0,\ v_3 = \frac{\delta_1 [b_1 k_1 + \varepsilon_1 (1-k_1)]}{\varepsilon_1 b_3},\ v_4 = 0,\ v_5 = \frac{b_1}{\varepsilon_1},\ v_6 = v_7 = v_8 = 0.$$

The associated backward bifurcation coefficients denoted by a and b, as defned in Theorem 4.1 of [2], are given by

$$\begin{aligned} a =& \sum_{k,i,j=1}^{8} v_k w_i w_j \frac{\partial^2 f_k}{\partial x_i \partial x_j}(E_0, \beta_1{}^*) \\ =& 2 v_1 w_5 w_7 \beta_1{}^* + 2 v_1 w_3 w_5 (1-p_1) \theta_1 \beta_1{}^* + 2 v_3 w_5 w_3 (-\theta_1 \beta_1{}^*) + 2 v_5 w_5 w_3 p_1 \theta_1 \beta_1{}^* \\ =& 2 w_5 \beta_1{}^* \left[w_7 + \left((1-p_1) - v_3 + v_5 p_1 \right) \theta_1 \right] \\ =& 2 w_5 \beta_1{}^* \left[w_7 + \left(\frac{b_3 [\varepsilon_1 (1-p_1) + b_1 p_1] - \delta_1 [\varepsilon_1 (1-k_1) + b_1 k_1]}{\varepsilon_1 b_3} \right) \theta_1 \right], \end{aligned} \tag{6}$$

$$b = \sum_{k,i=1}^{8} v_k w_i \frac{\partial^2 f_k}{\partial x_i \partial \beta_1}(E_0, \beta_1{}^*) = v_1 w_5 S_1^0 = \frac{b_3}{\gamma_1} S_1^0 > 0. \tag{7}$$

Set $R_1^* = \frac{b_3 [\varepsilon_1 (1-p_1) + b_1 p_1]}{\delta_1 [\varepsilon_1 (1-k_1) + b_1 k_1]}$. It can be checked that $w_7 < 0$, and for $R_1^* > 1$ the term between the larger parentheses is positive. Due to Theorem 4.1 of [2], if both the bifurcation coefficients a_1 and b_1 are positive, then the system (1) exhibits backward bifurcation. Thus, we have proved the following theorem.

Theorem 4.1. *Suppose that $R_0^1 \geq R_0^2$ and $R_1^* = \frac{b_3 [\varepsilon_1 (1-p_1) + b_1 p_1]}{\delta_1 [\varepsilon_1 (1-k_1) + b_1 k_1]} > 1$.*
If

$$\theta_1 > \frac{(\mu_2 + q_{12}) \varepsilon_1 b_3{}^2 \beta_1{}^* S_1^0}{\gamma_1 (\mu_1 \mu_2 + \mu_1 q_{12} + \mu_2 q_{21}) \left(b_3 [(1-p_1) \varepsilon_1 + b_1 p_1] - \delta_1 [\varepsilon_1 (1-k_1) + b_1 k_1] \right)},$$

then the system (1) *undergoes a backward bifurcation at $R_0 = 1$.*

Similarly, if $R_0^2 \geq R_0^1$, the backward bifurcation coefficients are given by

$$a = 2 w_5' \beta_2{}^* \left[w_7' + \left(\frac{a_3 [\varepsilon_2 (1-p_2) + a_1 p_2] - \delta_2 [\varepsilon_2 (1-k_2) + a_1 k_2]}{\varepsilon_2 a_3} \right) \theta_2 \right], \tag{8}$$

$$b = \frac{a_3}{\gamma_2} S_2^0 > 0, \tag{9}$$

where

$$w_5' = \frac{a_3}{\gamma_2},\ w_7' = -\frac{(\mu_1 + q_{21})}{\mu_1 \mu_2 + \mu_1 q_{12} + \mu_2 q_{21}} \beta_2 S_2^0 w_5'.$$

Similar to Theorem 4.1, we can prove the following result.

Theorem 4.2. *Suppose that* $R_0^2 \geq R_0^1$ *and* $R_2^* = \frac{a_3[\varepsilon_2(1-p_2)+a_1p_2]}{\delta_2[\varepsilon_2(1-k_2)+a_1k_2]} > 1$.
If

$$\theta_2 > \frac{(\mu_1 + q_{21})\varepsilon_2 {a_3}^2 {\beta_2}^* S_2^0}{\gamma_2(\mu_1\mu_2 + \mu_1 q_{12} + \mu_2 q_{21})\left(a_3[(1-p_2)\varepsilon_2 + a_1p_2] - \delta_2[\varepsilon_2(1-k_2) + a_1k_2]\right)},$$

then the system (1) *undergoes a backward bifurcation at* $R_0 = 1$.

Therefore, only reducing R_0 to less than one can not eradicate the disease from the population.

It is observed from (6)-(9) that for $R_1^* < 1$ and $R_2^* < 1$ the bifurcation coefficient a is negative and b is positive. Thus, it follows from item (iv) of Theorem 4.1 of [2] that the system (1) will not undergo backward bifurcation. Thus, the following result is established.

Theorem 4.3. *(i) If* $R_0^1 > R_0^2$ *and* $R_1^* < 1$, *then the system* (1) *does not exhibit backward bifurcation.*
(i) If $R_0^1 < R_0^2$ *and* $R_2^* < 1$, *then the system* (1) *does not exhibit backward bifurcation.*

Theorem 4.3 establishes that the system (1) will not exhibit the phenomenon of backward bifurcation, provided that the patch-specific reproduction numbers, denoted as $\mathcal{R}_0^1$ and $\mathcal{R}_0^2$, are both less than unity. It is important to note that the parameters $\mathcal{R}_i^*$, where $i \in 1, 2$, depend on several other model parameters, namely δ_i, k_i, and p_i. In other words, the TB model that captures the dynamics of exogenous reinfection, along with the relapse of the disease, will not display the coexistence of a stable disease-free equilibrium and a stable endemic equilibrium, under the specified conditions. This is an important finding, as the occurrence of backward bifurcation can complicate the disease control and eradication efforts. The lack of backward bifurcation in this TB modeling framework suggests that the disease dynamics may be more amenable to interventions aimed at reducing the reproduction numbers below the critical threshold of unity, leading to the elimination of the disease in the long run.

5 Conclusion

In this study, we have developed a two-patch mathematical model to capture the dynamics of a TB epidemic, where the key feature is the incorporation of exogenous reinfection among the treated individuals. The model assumes that only the susceptible population can freely migrate between the two distinct geographical regions or patches. In this work, we have derived the necessary conditions that lead to the occurrence of backward bifurcation in the proposed two-patch TB model. These conditions involve the model parameters and the patch-specific reproduction numbers, which ultimately determine the stability and multiplicity of the equilibrium states. Identifying the conditions for backward bifurcation is crucial, as it reveals the potential for the persistent presence of the disease even when the epidemiological threshold appears to be met at the population level.

References

[1] A. Jabbari, M. Lotfi, H. Kheiri, S. Khajanchi, Mathematical analysis of the dynamics of a fractional-order TB epidemic in a patchy environment under the influence of re-infection, Math. Methods Appl. Sci. 46 (17) (2023) 17798–17817.

[2] C. Castillo-Chavez, B. Song, Dynamical models of TB and their applications, Math. Biosci. Eng. 2 (1) (2004) 361–404.

[3] P. van den Driessche and J. Watmough, Reproduction numbers and sub-threshhold endemic equilibria for compartmental models of disease transmission, Math. Biosci. 180 (2002) 29–48.

Email: a_jabari@tabrizu.ac.ir

Real Data Feedback to Control Thyroid Behavior

Arta A. Jamshidi[1]

Gholam Reza Rokni Lamouki

Advanced Systems Biology and Cancer Research Lab,

School of Mathematics, Statistics, and Computer Science, College of Science, University of Tehran.

Abstract

We present a real data, computationally low-cost feedback control to regulate a perturbed biological system which has a cyclic invariant object. We provide an overview of the limit cycle detection in the thyroid real hormone data (T_3, T_4), and design a data feedback mechanism using TSH. We apply real TSH data feedback to compensate thyroid deficiency due to lack of adequate production of T_3 and T_4 and reinstate its normal functionality on a limit cycle. Although in this work we focus on thyroid control, the proposed method could be used for other perturbed biological systems that have a cyclic invariant object.

Keywords: Real Data Feedback, Control, Cybernetics, Dynamical Systems, Biological Systems.

AMS Mathematical Subject Classification [2010]: 37N25, 92B05.

1 Introduction

Thyroid as a complex system, serves a major rule in the proper development and functionality of a wide range of species. Thyroid produces Triiodothyronine (T_3) and Tetraiodothyronine (T_4, known as Thyroxin), which are vital for cell differentiation at early stages of life formation, various growth stages, and metabolism. Thyroid is regulated by the Thyroid Stimulating Hormone (TSH) via a feedback system in the HPT-axis as shown in Figure 1. The performance of thyroid greatly affects the behavior of every organ in the human body. Various illnesses such as sepsis, could perturb the biological behavior of thyroid. When a biological system suffers perturbation due to an environmental or internal source, it takes a considerable time to recover and return to its normal behavior. A healing regulator is needed to keep the operation of the biological system around its normal behavior until the source of perturbation vanishes.

In this paper, we focus on designing an auxiliary data feedback control system to regulate a perturbed thyroid from its normal operation. We assume that the source of perturbation that deviates thyroid from its normal operation persists and there is no direct clinical intervention to cure the perturbation source at time scale that we run the control system. To reach this goal we first illustrate the invariant cyclic behavior in thyroid that is revealed by studying a 23-dimensional system of dynamical equations in [1]. The geometry of this limit cycle is studied by [2] and [3]. The high-dimensional thyroid model that is derived using reaction

[1]Speaker

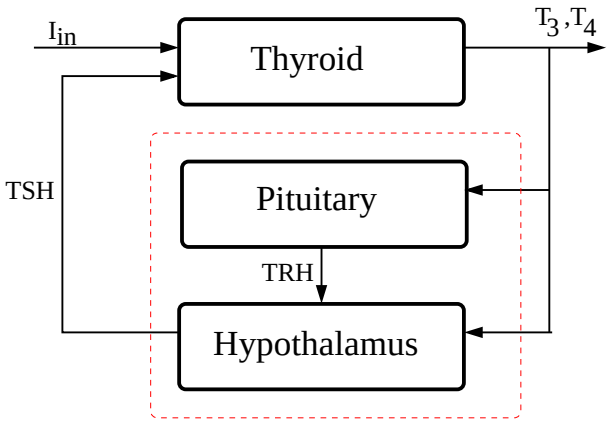

Figure 1: The HPT-axis axis with its internal feedback control.

kinetics and the bio-synthetic processes that reveal the normal limit cyclic behavior of thyroid, is presented below, [1]:

$$\dot{x} = \epsilon X(x, y, \alpha, a) + \epsilon I_{in}, \tag{1}$$

$$\dot{y} = \epsilon Y(x, y, \alpha, a), \tag{2}$$

$$\dot{\alpha} = \epsilon A(x, y, \alpha, a), \tag{3}$$

$$\dot{u} = \epsilon v_1(x_6) + \epsilon v_2(x_7) - \epsilon \delta u. \tag{4}$$

Here, the vector fields X, Y, A, and the input I represent the time evolution of seven main chemicals, ten intermediate chemicals, and five main thyroid enzymes, respectively. ϵ and δ represent the time scales, while v_1 and v_2 are Hill function type decreasing functions representing the negative feedbacks used in the controller u. According to the standard lab examination of thyroid, we consider a three dimensional subsystem (x_6, x_7, u), derived from Equations (1)-(4) which represents the three major chemicals T_3, T_4, and TSH. The projection of a typical solution in the two-dimensional (x_6, x_7), or (T_3, T_4)-plane, is illustrated in Figure 2(**a**). The real scattered data of clinical measurements are shown in Figure 2(**b**). For details about the data specification, see [4, 5]. The elliptical limit cycle Γ, that represents the overall normal thyroid behavior of this data set is presented in [2] and is shown in Figure 2(**c**). The location of the ellipse center, its major and minor axis in this figure are also provided in [2]. In this figure the horizontal axis is x_6 which represents the concentration of T_3 in blood and the vertical axis x_7, shows the T_4 concentration in blood.

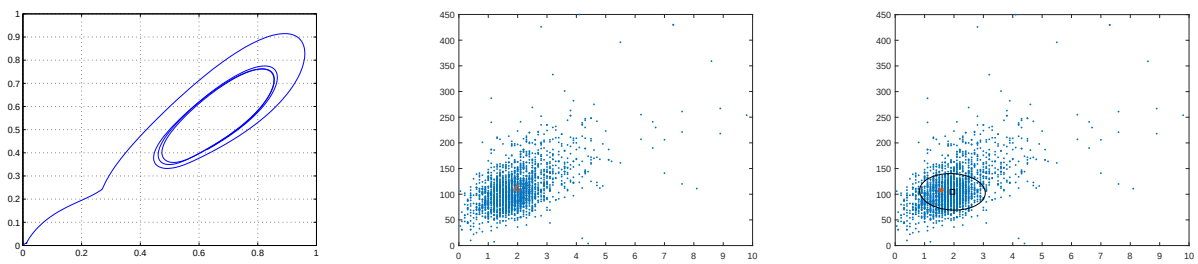

(a) The simulated Limit Cycle. (b) The real scatered data. (c) The normal limit cycle.

Figure 2: The geometric properties of the thyroid normal limit cycle from simulation and real data.

Having the target limit cycle Γ, in the next section we design a low cost data feedback system that could compensate the malfunctioning of thyroid due to a systemic perturbation.

2 Data feedback control strategy

In this work we focus on a data feedback control scheme that intervenes with the TSH degradation rate. As mentioned in the previous section, we assume the malfunctioning source of thyroid persists and there is no direct clinical intervention for its cure while the external data feedback is applied. In terms of the dynamical model in Equations (1)-(4), we focus on the external feedback control by intervention into the rate of TSH degradation, δ. $\delta(t)$ could in fact be used as a gate for continuous-time control, piece-wise constant control, or hybrid discrete time control. In this context, $\delta(t) = \Delta(s, \delta_0(t))$ where $s \in [0,\ 1]$ is the rate change and δ_0 is the initial rate value. In this setting, we are required to run the full model at each feedback iteration, which is computationally intense. To overcome this complexity we propose a data feedback strategy that uses real TSH data that replaces the model output. In this view, we use the actual thyroid machinery as a real simulator to get the TSH output values. The dataset that we use in this work is the aggregated data of many people which provides us with a rich data source in the context of poly-body or multi-body. We consider the 3−dimensional data (T_3, T_4, TSH) in [5] and denote this as an $N \times 3$ table $\mathcal{T}$, where N is the total number of available data points.

In our data feedback design we choose an arbitrary pair (T_3, T_4) from the table $\mathcal{T}$ and assign a time label τ_0. We denote the associated point on the normal limit cycle Γ as presented in the previous section, as Γ_{τ_0}. Note that one full cycle of the limit cycle Γ is associated to a 24-hour period. The associated TSH value to time τ is read from table $\mathcal{T}$, TSH_{τ_0}. We define a feedback value as the distance between $(T_3, T_4)_{\tau_0}$ and its associated normal point on the limit cycle, Γ_{τ_0}, that is: $F = ||(T_3, T_4)_{\tau_0} - \Gamma_{\tau_0}||$. The new value of TSH is computed via its previous value multiplied by $(1 + \epsilon F)$, where ϵ is a constant coefficient, that is $TSH_\tau = (1 + \epsilon F)TSH_{\tau_0}$. The new TSH value, TSH_τ, is used to find a new (T_3, T_4) entry in table $\mathcal{T}$, $(T_3, T_4)_\tau$. This process is repeated until the feedback value F gets small and $(T_3, T_4)_\tau$ gets close enough to the Γ_τ. Figure 3 shows a conceptual diagram for our external data feedback control. The results that we obtained using this procedure are shown Figure 4. In Figure 4 (a), $(T_3, T_4)_\tau$'s are shown with stars and the Γ_τ's are shown with squares. Figure 4 (b) shows the time series associated to TSH_τ, $T_{3\tau}$ and $T_{4\tau}$. We observe that the $(T_3, T_4)_\tau$'s that are shown with stars, successfully reach the limit cycle Γ.

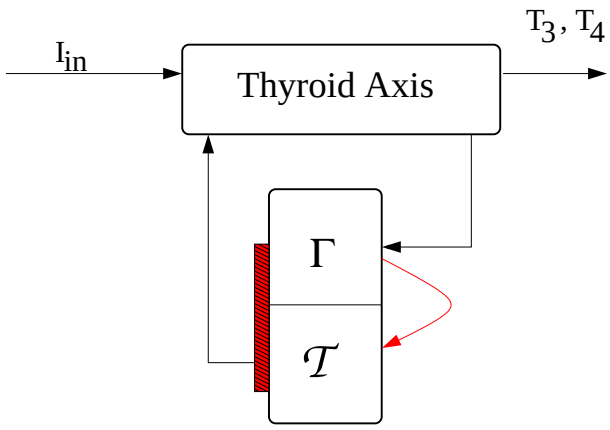

Figure 3: A conceptual diagram for our external data feedback control.

In this design we have the following limitations: (1) At each step, the body can bear a bounded level of intervention. (2) The number of steps are bounded to a plausible level that body can tolerate. (3)

Convergence to the normal limit cycle is gradual. (4) The channel to intervene in TSH degradation is open. This assumptions imply that the thyroid has no problem in using the prescribed TSH by applying it to its internal system.

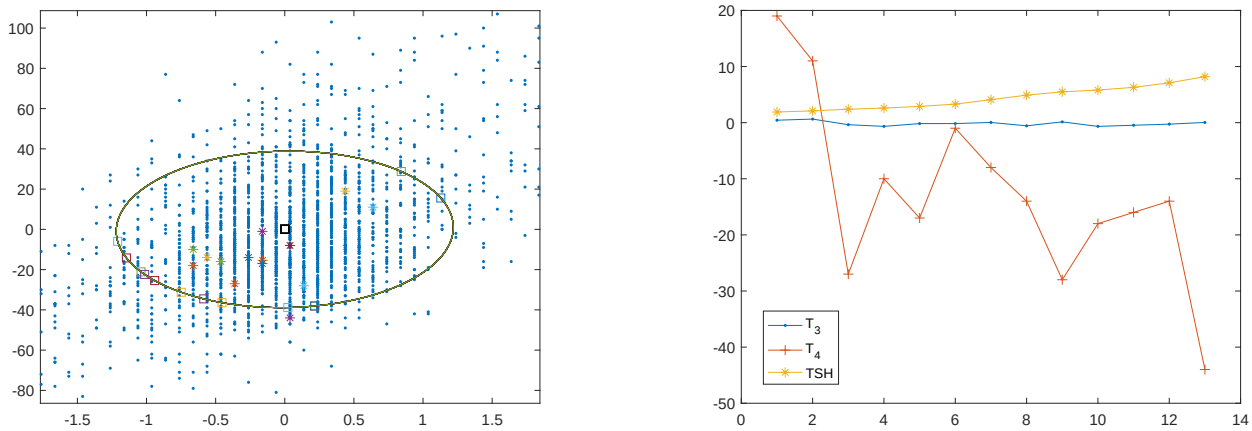

(a) Phase portrate.

(b) Hormone time series.

Figure 4: The time series' of T_3, T_4, TSH, and the associated phase portrait.

3 Concluding Remarks

In this paper, we aim at designing a fast, non-invasive data feedback control strategy to provide a compensation mechanism for a systematic cause of thyroid perturbation. We utilized the real clinical thyroid TSH data to control the (T_3, T_4) thyroid behavior to compensate for a general perturbation caused by various conditions, such as sepsis. Our effective and low cost method, benefits from a rigorous geometric analysis of thyroid model and data analysis tools. Our computational experiments show the promise of this data driven method to control various thyroid's hormonal perturbations.

References

[1] G. R. Rokni Lamouki, A. H. Shirazi and A. R. Mani, *Dynamical model for thyroid*, Commun Nonlinear Sci Numer Simulat, 22, 297-313, 2015.

[2] Jamshidi A. A. and Rokni Lamouki, G. R., *A data driven diagnosis tool for thyroid hormones*, Computers in biology and medicine, 103, 301-311, 2018.

[3] Jamshidi A. A. and Rokni Lamouki, G. R., *An algorithmic treatment strategy for the inhibition of type-II deiodinase enzyme on thyroid secretion hormones*, Biomedical Signal Processing and Control, 66, 102473, 2021.

[4] J. R. Quinlan. Induction of decision trees. Machine Learning, 1:81–106, 1986.

[5] J. R. Quinlan. Thyroid disease records supplied by the Garavan Institute. New South Wales Institute, Sydney, Australia, 1987.

e-mail: `arta.jamshidi@ut.ac.ir`
e-mail: `rokni@ut.ac.ir`

Global dynamic of generalized viral infection model with two transmission mode, cure rate, latently infected cells, cellular immunity and humoral immunity

Tohid Kasbi Gharahasanlou[1]
Department of Mathematics and Statistics, Imam Hossein University, Tehran, Iran

Behnam Mohammadaliee
Department of Mathematics, Azarbaijan Shahid Madani University, Tabriz, Iran

Vahid Roomi
Department of Mathematics, Azarbaijan Shahid Madani University, Tabriz, Iran
Insurance Reserach Center, Tehran, Iran

Abstract

In this paper, Global dynamic of generalized viral infection model will be presented. By the values of five threshold number and conditions on the parameters of model, the global stability of equilibria will be given by using Lyapunov's second method and LaSalle's invariance principle. Also, Numerical simulation of model will be presented in the last section.

Keywords: Viral infection, Cellular immunity, Humoral immunity, Stability

Mathematics Subject Classification [2010]: 34D23, 37B25

1 Introduction

In past decades, research in mathematical biology has been increased. In [1, 2, 3, 4], some viral infection model have been studied. In this work, we consider the following system

$$\begin{aligned}
\dot{x} &= \lambda - dx - vf(x,v) - yg(x,y) + \rho y,\\
\dot{s} &= (1-m)[vf(x,v) + yg(x,y)] - (e+\delta)s,\\
\dot{y} &= m[vf(x,v) + yg(x,y)] + \delta s - (a+\rho)y - pyz,\\
\dot{v} &= ky - uv - qvw,\\
\dot{w} &= gvw - hw,\\
\dot{z} &= cyz - bz.
\end{aligned} \tag{1}$$

where $x(t)$, $s(t)$, $y(t)$, $v(t)$, $w(t)$ and $z(t)$ show the density of susceptible cells, the number of latently infected cells, actively infected cells, the virus, Cytotoxic T cells and B lymphocyte cells, respectively. The fractions $(1-m)$ and m with $0 < m < 1$ are the probabilities that upon infection, an uninfected cell will become either latently infected or actively infected. The functions $f(x,v)$ and $g(x,y)$ describing the virus to cell

[1]Speaker

and the cell to cell transmission, respectively. Furthermore, the function $f(x,v)$ and $g(x,y)$ are assumed to satisfy the following properties:

$$
\begin{aligned}
&(\mathbf{A_1})\ \ f(0,v)=0,\ \ for\ \ all\ \ v\geq 0\ \ and\ \ g(0,y)=0,\ \ for\ \ all\ \ y\geq 0,\\
&(\mathbf{A_2})\ \ \frac{\partial f}{\partial x}(x,v)>0\ \ and\ \ \frac{\partial g}{\partial x}(x,y)>0,\ \ for\ \ all\ \ x>0,\ \ y\geq 0\ \ and\ \ v\geq 0,\\
&(\mathbf{A_3})\ \ \frac{\partial f}{\partial v}(x,v)\leq 0\ \ and\ \ \frac{\partial g}{\partial y}(x,y)\leq 0,\ \ for\ \ all\ \ x\geq 0,\ \ y\geq 0\ \ and\ \ v\geq 0.
\end{aligned}
$$

This paper is organized as follows. In Section 2, some basic properties of solutions such as positivity and boundedness wii be given. In Section 3, the definition of five threshold number and the form of equilibrium points of system 1 will be presented. The global stability of the rest points will be considered in Section 3. Finally the numerical simulation of system 1 will be shown in Section 4.

2 Basic Results

System (1) represent the interaction between the cells in the body. Hence, the number of these cells must be bounded and positive. By the same arguments in [1], the following proposition can be proven.

Proposition 2.1. *All solutions of system* (1) *with non-negative initial conditions exist for all* $t>0$ *and remain bounded and non-negative.*

3 Global Stability

In this section, the global stability analysis of model (1) will be shown. System (1) has five rest points in the following form:
1) Infection-free equilibrium $\mathbf{E_0}=(x_0,0,0,0,0,0)$,
2) Immune-free equilibrium $\mathbf{E_1}=(x_1,s_1,y_1,v_1,0,0)$,
3) humoral immune-free equilibrium $\mathbf{E_2}=(x_2,s_2,y_2,v_2,0,z_2)$,
4) CTL immune-free equilibrium $\mathbf{E_3}=(x_3,s_3,y_3,v_3,w_3,0)$,
5) chronic equilibrium $\mathbf{E_4}=(x_4,s_4,y_4,v_4,w_4,z_4)$.
As in [2, 3], the basic reproduction number ($\mathbf{R_0}$) of system (1) is as follows:

$$
\mathbf{R_0}=\frac{k(em+\delta)f(x_0,0)}{(a+\rho)(e+\delta)u}+\frac{(em+\delta)g(x_0,0)}{(a+\rho)(e+\delta)}. \tag{2}
$$

In addition to $\mathbf{R_0}$, we need the another immune response reproduction rates. As in [1], these threshold numbers have the following form:

$$
\begin{aligned}
\mathbf{R_{CTL}}&=\frac{cy_1}{b},\\
\mathbf{R_{Hom}}&=\frac{gv_1}{h},\\
\mathbf{R_{CTLC}}&=\frac{cy_3}{b},\\
\mathbf{R_{HomC}}&=\frac{gv_2}{h}.
\end{aligned} \tag{3}
$$

In the following, theorems about the global stability of equilibria will be presented.

Theorem 3.1. *If* $\mathbf{R_0}\leq 1$, *then Infection-free equilibrium* $\mathbf{E_0}$ *is globally asymptotically stable.*

Theorem 3.2. *If* $\mathbf{R_0}>1$, $\mathbf{R_{CTL}}\leq 1$, $\mathbf{R_{Hom}}\leq 1$ *and* $dx_1-\rho y_1\geq 0$, *then Immune-free equilibrium* $\mathbf{E_1}$ *is globally asymptotically stable.*

Theorem 3.3. *If* $\mathbf{R_{CTL}}>1$, $\mathbf{R_{HomC}}\leq 1$, $\mathbf{R_{CTLC}}>1$ *and* $dx_2-\rho y_2\geq 0$, *then humoral immune-free equilibrium* $\mathbf{E_2}$ *is globally asymptotically stable.*

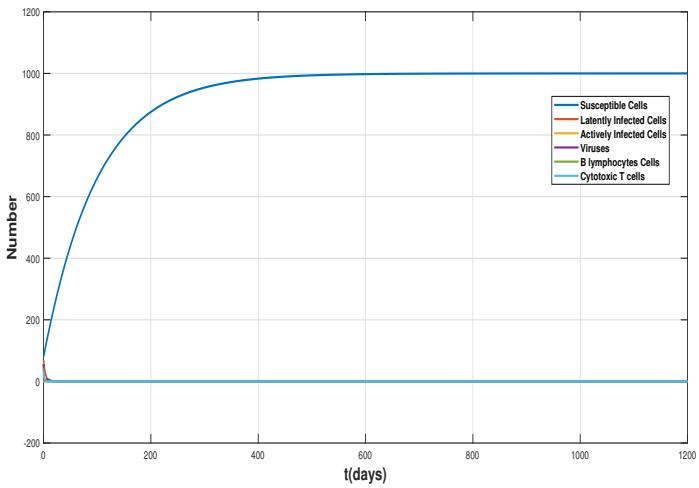

Figure 1: Global Stability of infection-free equilibrium $\mathbf{E_0}$ with $\beta_1 = 0.0002$, $\beta_2 = 0.0003$, $g = 0.04$ and $c = 0.03$ ($\mathbf{R_0} = 0.9945$)

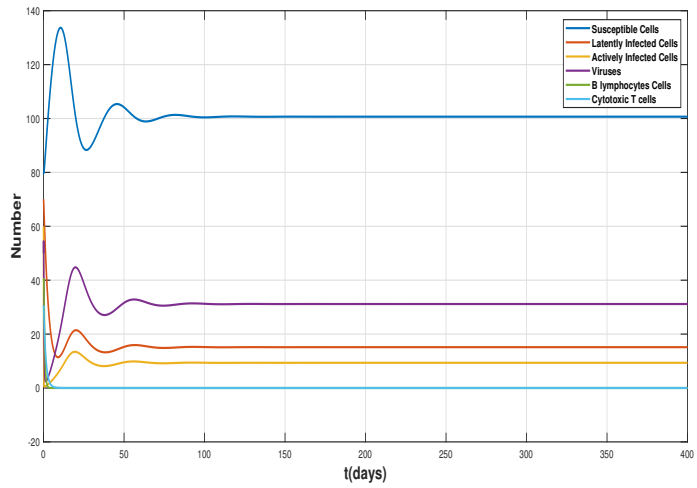

Figure 2: Global Stability of immune-free equilibrium $\mathbf{E_1}$ with $\beta_1 = 0.002$, $\beta_2 = 0.003$, $g = 0.04$ and $c = 0.03$ ($\mathbf{R_0} = 9.9451$, $\mathbf{R_{CTL}} = 0.3714$ and $\mathbf{R_{Hom}} = 0.6232$)

Theorem 3.4. *If* $\mathbf{R_{Hom}} > 1$, $\mathbf{R_{CTLC}} \leq 1$, $\mathbf{R_{HomC}}\mathbf{R_{CTLC}} > 1$ *and* $dx_3 - \rho y_3 \geq 0$, *then CTL Immune-free equilibrium* $\mathbf{E_3}$ *is globally asymptotically stable.*

Theorem 3.5. *If* $\mathbf{R_{HomC}} > 1$, $\mathbf{R_{CTLC}} > 1$ *and* $dx_4 - \rho y_4 \geq 0$, *then chronic equilibrium* $\mathbf{E_4}$ *is globally asymptotically stable.*

4 Numerical Simulation

In this section, to illustrate the theoretical results, applying MATLAB with ODE45 method, some numerical simulation of system 1 will be presented. We put $f(x, v) = \dfrac{\beta_1 x}{1 + \eta_1 v}$ and $g(x, y) = \dfrac{\beta_2 x}{1 + \eta_2 y}$, which are saturated mass action functional response. For simulation, we consider a set of parameters

$$\lambda = 10,\ d = 0.01,\ \eta_1 = 0.00005,\ \eta_2 = 0.00005,\ \rho = 0.01,\ m = 0.5,\ e = 0.1,$$
$$\rho = 0.01,\ \delta = 0.2,\ a = 0.8,\ p = 0.9,\ k = 10,\ u = 3,\ q = 0.01,\ h = 2,\ b = 0.755$$

and different values of β_1, β_2, g and c (See Figures 1-5).

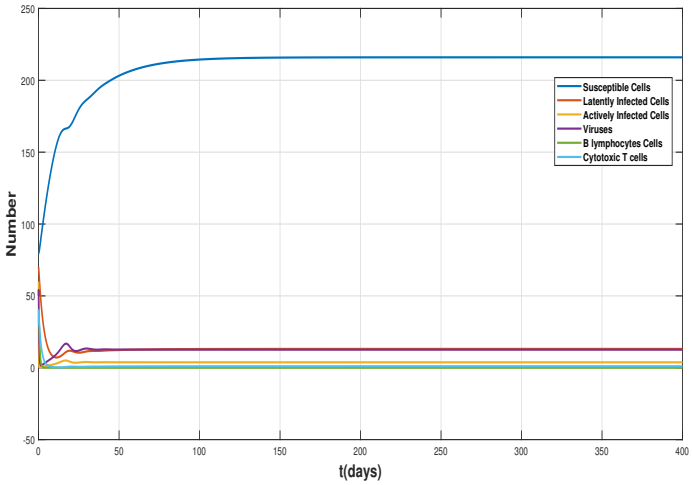

Figure 3: Global Stability of homoral immune-free equilibrium $\mathbf{E_2}$ with $\beta_1 = 0.002$, $\beta_2 = 0.003$, $g = 0.04$ and $c = 0.2$ ($\mathbf{R_0} = 9.9451$, $\mathbf{R_{CTL}} = 2.4763$, $\mathbf{R_{CTLC}} = 2.1746$ and $\mathbf{R_{HomC}} = 0.3356$)

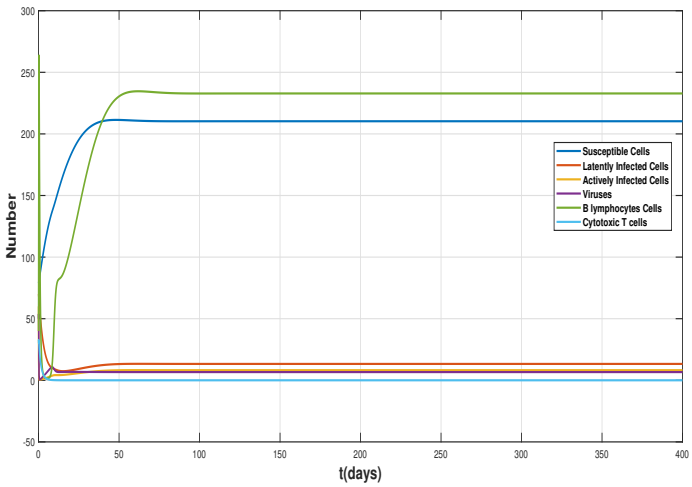

Figure 4: Global Stability of CTL immune-free equilibrium $\mathbf{E_3}$ with $\beta_1 = 0.002$, $\beta_2 = 0.003$, $g = 0.3$ and $c = 0.08$ ($\mathbf{R_0} = 9.9451$, $\mathbf{R_{Hom}} = 4.6745$, $\mathbf{R_{HomC}} = 1.8875$ and $\mathbf{R_{CTLC}} = 0.8698$)

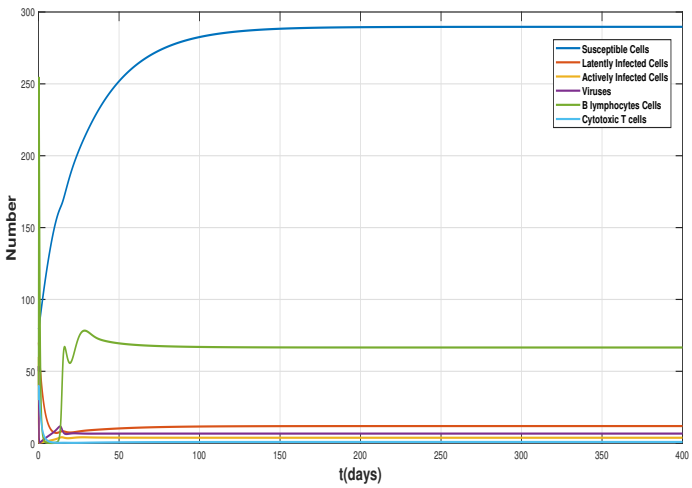

Figure 5: Global Stability of chronic equilibrium $\mathbf{E_4}$ with $\beta_1 = 0.002$, $\beta_2 = 0.003$, $g = 0.3$ and $c = 0.2$ ($\mathbf{R_0} = 9.9451$, $\mathbf{R_{HomC}} = 1.8875$ and $\mathbf{R_{CTLC}} = 2.1746$)

References

[1] Z. Hemmatzadeh, V. Rommi and T. K. Gharahasanlou, *Stability, Hopf Bifurcation and Numerical Simulation of an HIV Model with Two Modes of Transmission and with Cellular and Humoral Immunity,* International Journal of Bifurcation and Chaos. 33 (14) (2023).

[2] F. Li, J. Wang, *Analysis of an HIV infection model with logistic target-cell growth and cell-to-cell transmission*, Chaos, Solitons and Fractals., 81, Part A (2015), 136–145.

[3] S. Pan and Siddhartha P. Chakrabarty, *Threshold dynamics of HCV model with cell-to-cell transmission and a non-cytolytic cure in the presence of humoral immunity,*, Communications in Nonlinear Science and Numerical Simulation., 61 (2018), 180–197.

[4] Y. Yang, L. Zou, S. Ruanet, *Global dynamics of a delayed within-host viral infection model with both virus-to-cell and cell-to-cell transmissions*, Mathematical Biosciences., 270 (2015) 183–191.

Email: `t.kasbi@ihu.ac.ir`
Email: `behnam.mohammadaliee@azaruniv.ac.ir`
Email: `Roomi@azaruniv.ac.ir`

Machine learning model for classifying BRCA1 missense variants

Hamed KA[1]
Department of Computer Science, Faculty of Mathematics, Statistics, and Computer Science, University of Tabriz, Tabriz, Iran

Maryam Naghinejad
Department of Medical Genetics, Faculty of Medicine, Tabriz University of Medical Genetics, Tabriz, Iran

Akbar Amirfiroozy
Department of Medical Genetics, Faculty of Medicine, Tabriz University of Medical Genetics, Tabriz, Iran

Jafar Razmara
Department of Computer Science, Faculty of Mathematics, Statistics, and Computer Science, University of Tabriz, Tabriz, Iran

Sepideh Parvizpour
Research Center for Pharmaceutical Nanotechnology, Biomedicine Institute, Tabriz University of Medical Sciences, Tabriz, Iran

Abstract

The right classification of BRCA1 variants is the key to pre-symptomatic detection of breast and ovarian cancers to conduct preventive actions. Since BRCA1 has a high incidence and penetrance in these kinds of cancer, a high-performance predictive tool can be employed to classify the clinical significance of its variants. Several tools have previously been developed for this purpose which poorly classify the significance in specific cases. In this study, an ensemble classifier is proposed as a predictive model with high specificity and sensitivity in variants classification.

Keywords: BRCA1, Breast cancer, VUS, Predictive model, Machine learningArticle
Mathematics Subject Classification [2010]: 13D45, 39B42

1 Introduction

Breast cancer has become one of the most prevalent malignancies among women worldwide. The increasing rate of mortality and morbidity caused by breast cancer has led researchers to explore novel preventive and therapeutic ways against malignancy. Breast cancer incidence is majorly sporadic. However, individuals at early ages are more likely to be associated with an increased familial risk of breast cancer. This hereditary predisposition includes approximately 5-10% of the patients [1]. The germline mutations in the BRCA1 and BRCA2 genes are the origin of nearly 50% of hereditary breast cancers [2]. The BRCA1 gene with an autosomal dominant inheritance pattern in 17q21 involves DNA repair, genomic stability, transcription regulation, RNA processing, and cell cycle checkpoints (S and G2). This gene acts as a tumor suppressor, and its mutations mostly lead to loss of function [3, 4, 5]. BRCA1 (NM_007294.4) has 24 exons, of which 22 of them are coding exons and translates to 1863 amino acids [6]. Ring finger domain and BRCT repeats are remarked as BRCA1 domains and also are considered more to be pathogenic [7]. The protein of this

[1]Speaker

gene, with its ligase properties, facilitates the calling of molecules involved in the DNA repairment and also plays its role by binding to small molecules or proteins such as BARD1 small molecules or PALB2 protein [8, 9, 10]. Indeed BRCA1 due to its significant prevalence and incidence is one of the most well-known genes in hereditary breast and ovarian cancers, which are somewhat screenable and treatable [3]. The emergence of next-generation sequencing (NGS) technology has made a revolution in the early detection of BRCA1 mutations. The variants obtained from NGS can be classified based on the guidelines provided by the American College of Medical Genetics and Genomics (ACMG) [11]. One of the most problematic decisions in reporting NGS data interpretation is concluding about variants of unknown significance (VUS) [12].

Recent advances in developing computational tools for analyzing biological data have increased the impact of bioinformatics in ACMG guidelines. These computational methods can be a step towards improving the classification of the variants [13]. For instance, Sorting Intolerant from Tolerant (SIFT) [14], Polymorphism Phenotyping v2 (PolyPhen2) [15], Deep Neural Network (DNN), [16] and Combined Annotation-Dependent Depletion (CADD) [17] are four well-known in silico predictors in NGS annotation analysis, which have special thresholds to distinguish pathogenic variants from benign variants. Unfortunately, the available in silico tools can confidently identify a very small number of disease-related variants [18]. Recently, several methods have been developed with a high degree of confidence based on machine learning approaches to build predictive models using post-mutation differences [19, 20]. The proposed method investigate the effects of benign and pathogenic missense variants on the protein structure based on the changes in its physiochemical properties.

2 Method

The missense variants of BRCA1 were downloaded from the ClinVar database [18]. Among these variants, the variants with the clinical significance of the benign and pathogenic were selected. The clinical significance of the selected variants was further checked using the ACMG guidelines provided by the VarSome web server [19]. Next, the list of variants was enriched by adding physicochemical properties of amino acids in the protein.

To classify the variants of the BRCA1 gene, the Random Forest (RF) ensemble classifier was used. The most important parameters of the designed RF in this study are represented in Table 1, while other parameters were set to their default values. The parameters in Table 1 were fine-tuned using grid search as a search strategy and the optimal values were determined. Each possible setting of parameters was evaluated using the Area Under the Curve (AUC) of the Receiver Operating Curve (ROC) score resulting from ten-fold cross-validation. Before fine-tuning the model, the dataset was split into training (80%) and test sets (20%). The training set was used in fine-tuning RF and the test set was utilized to evaluate the best model resulting from the grid search. Data split and fine-tuning of the model were performed using the scikit-learn library.

Table 1: Selected parameters of RF and their optimal values results from grid search.

Parameter	**Optimal value**
Bagging fraction	0.7
Feature fraction	0.8
Learning rate	0.01
Max depth	-1
Min data in the leaf	10
Number of estimators	150
Number of leaves	4

3 Experimental Results

In this section, we first determine the optimal threshold for the proposed model. Subsequently, we evaluate the model's performance using this optimal threshold. Next, we compare the proposed model with other state-of-the-art tools from the literature. The performance of the proposed model was investigated using three evaluation metrics including Recall, Precision, and AUC-ROC. To evaluate the Recall and Precision scores of the model, it is necessary to obtain the predicted class labels of each pattern. To convert the probabilities of the proposed model to the class labels, the optimal threshold of the model was estimated using the test set. There are several techniques to find the optimal threshold of a probabilistic model. In this work, the optimal threshold was calculated using the index of Younden [20] which is defined as:

$$J = TPR - FPR$$

where TPR and FPR are True Positive Rate and False Positive Rate, respectively. Table 2 illustrates results obtained for above mentioned metrics. Finally, the performance of the proposed method and each of state-of-the-art tools is summarized in Table 3. Besides, the AUC-ROC and AUC-PR curves were plotted to specify the performance of the tools at different threshold settings, as shown in figures 1 and 2.

Table 2: The performance of the proposed model using the single train-test split

Single Train-Test	**Optimal threshold**	**Recall**	**Precision**	**AUC-ROC**
Training data	0.344	0.977	0.924	0.953
Testing data		1.0	0.916	0.960

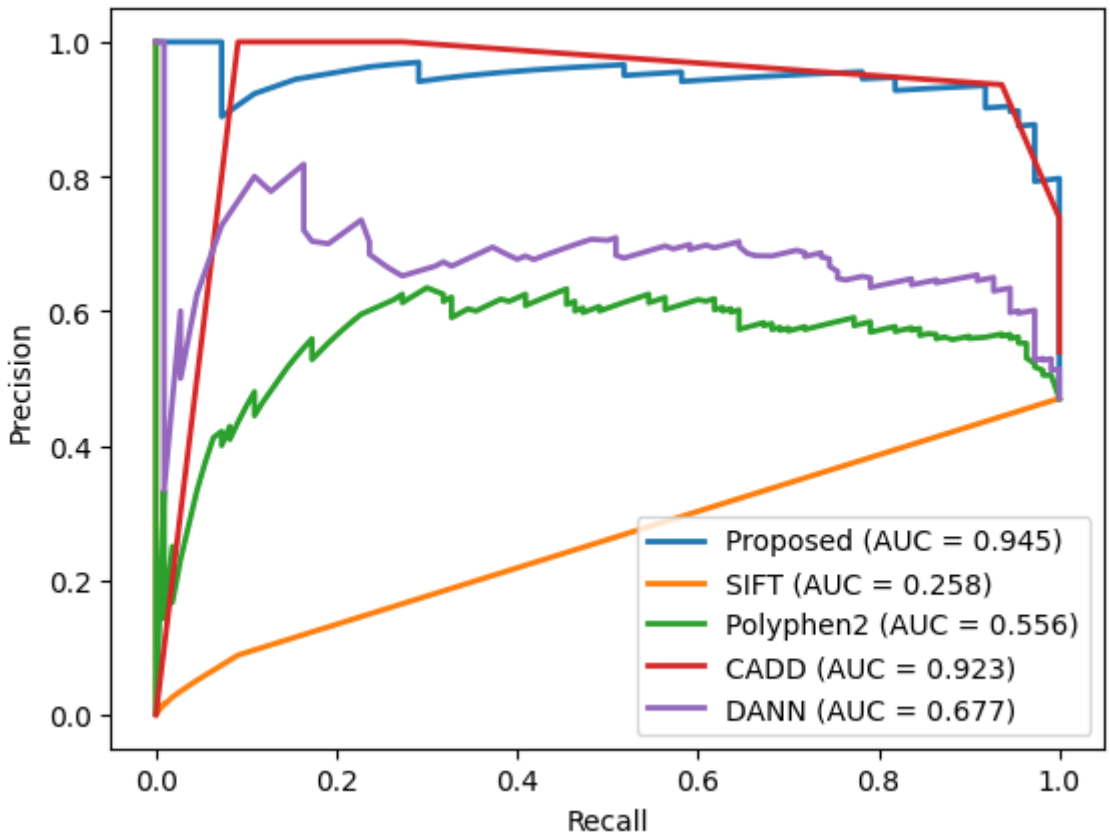

Figure 1: The AUC-PR curve of the proposed model and other tools

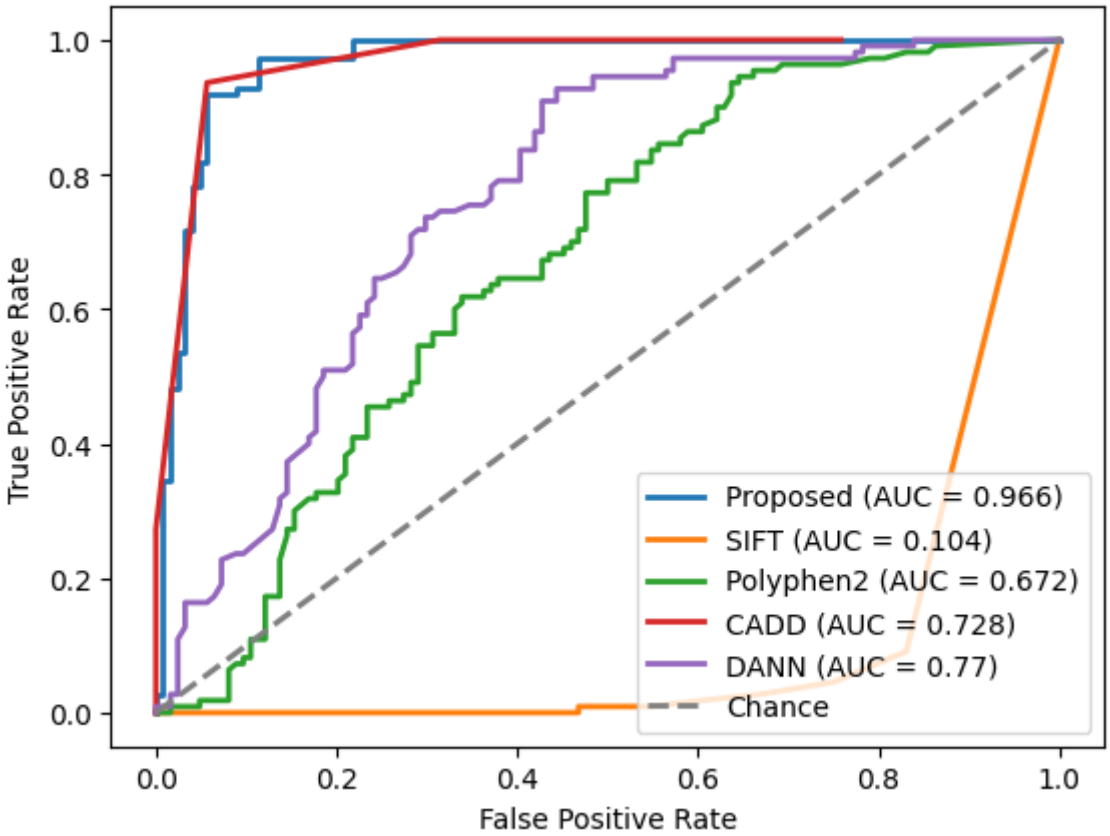

Figure 2: The AUC-ROC curve of the proposed model and other tools

Table 3: Comparing the proposed model with other tools

Tool	Threshold	Recall	FPR	Precision	AUC-ROC
SIFT	0.05	0.991	0.548	0.661	0.104
CADD	15	1.0	0.508	0.636	0.728
DANN	0.96	0.945	0.564	0.598	0.770
Proposed	0.604	0.918	0.066	0.935	0.966

4 Conclusion

The main purpose of this study was to develop an accurate predictive model for classifying BRCA1 missense variants. The proposed model works based on random forest approach as a powerful machine learning tool for evaluating the missense mutations effect based on a set of physicochemical properties. The model can be used to evaluate variants before conducting further functional studies in the laboratory.

References

[1] Rhei, E., et al., *Molecular genetic characterization of BRCA1-and BRCA2-linked hereditary ovarian cancers*, Cancer research, 1998. 58(15): p. 3193-3196.

[2] Kuchenbaecker, K.B., et al., *Risks of breast, ovarian, and contralateral breast cancer for BRCA1 and BRCA2 mutation carriers*, Jama, 2017. 317(23): p. 2402-2416.

[3] Deng, C.-X., *BRCA1: cell cycle checkpoint, genetic instability, DNA damage response and cancer evolution*, Nucleic acids research, 2006. 34(5): p. 1416-1426.

[4] Venkitaraman, A.R., *How do mutations affecting the breast cancer genes BRCA1 and BRCA2 cause cancer susceptibility?*, DNA repair, 2019. 81: p. 102668.

[5] Xu, B., et al., *Phosphorylation of serine 1387 in Brca1 is specifically required for the Atm-mediated S-phase checkpoint after ionizing irradiation*, Cancer research, 2002. 62(16): p. 4588-4591.

[6] UniProt, *The universal protein knowledgebase in 2023*, Nucleic Acids Research, 2023. 51(D1): p. D523-D531.

[7] Dines, J.N., et al., *Systematic misclassification of missense variants in BRCA1 and BRCA2 "coldspots"*, Genetics in Medicine, 2020. 22(5): p. 825-830.

[8] Hengel, S.R., M.A. Spies, and M. Spies, *Small-molecule inhibitors targeting DNA repair and DNA repair deficiency in research and cancer therapy*, Cell chemical biology, 2017. 24(9): p. 1101-1119.

[9] Sy, S.M., M.S. Huen, and J. Chen, *PALB2 is an integral component of the BRCA complex required for homologous recombination repair*, Proceedings of the National Academy of Sciences, 2009. 106(17): p. 7155-7160.

[10] Wu-Baer, F., et al., *The BRCA1/BARD1 heterodimer assembles polyubiquitin chains through an unconventional linkage involving lysine residue K6 of ubiquitin*, Journal of Biological Chemistry, 2003. 278(37): p. 34743-34746.

[11] D'Argenio, V., et al., *The molecular analysis of BRCA1 and BRCA2: Next-generation sequencing supersedes conventional approaches*, Clinica Chimica Acta, 2015. 446: p. 221-225.

[12] Vears, D., et al., *Points to consider for laboratories reporting results from diagnostic genomic sequencing*, European journal of human genetics, 2018. 26(1): p. 36-43.

[13] Richards, S., et al., *Standards and guidelines for the interpretation of sequence variants: a joint consensus recommendation of the American College of Medical Genetics and Genomics and the Association for Molecular Pathology*, Genetics in medicine, 2015. 17(5): p. 405-423.

[14] Ng, P.C. and S. Henikoff, *SIFT: Predicting amino acid changes that affect protein function*, Nucleic acids research, 2003. 31(13): p. 3812-3814.

[15] Adzhubei, I.A., et al., *A method and server for predicting damaging missense mutations*, Nature methods, 2010. 7(4): p. 248-249.

[16] Quang, D., Y. Chen, and X. Xie, *DANN: a deep learning approach for annotating the pathogenicity of genetic variants*, Bioinformatics, 2014. 31(5): p. 761-763.

[17] Kircher, M., et al., *A general framework for estimating the relative pathogenicity of human genetic variants*, Nature genetics, 2014. 46(3): p. 310-315.

[18] Landrum, M.J., et al., *ClinVar: public archive of interpretations of clinically relevant variants*, Nucleic acids research, 2016. 44(D1): p. D862-D868.

[19] Kopanos, C., et al., *VarSome: the human genomic variant search engine*, Bioinformatics, 2019. 35(11): p. 1978.

[20] Youden, W.J., *Index for rating diagnostic tests*, Cancer, 1950. 3(1): p. 32-35.

A new gene selection approach for Alzheimer's disease

Hamed KA[1]
Department of Computer Science, Faculty of Mathematics, Statistics, and Computer Science, University of Tabriz, Tabriz, Iran

Jafar Razmara
Department of Computer Science, Faculty of Mathematics, Statistics, and Computer Science, University of Tabriz, Tabriz, Iran

Sepideh Parvizpour
Research Center for Pharmaceutical Nanotechnology, Biomedicine Institute, Tabriz University of Medical Sciences, Tabriz, Iran

Morteza Hadizadeh
Physiology Research Center, Institute of Neuropharmacology, Kerman University of Medical Sciences, Kerman, Iran

Abstract

Diagnosing a disease based on gene expression data extracted from microarrays is still an open field of research. Due to the availability of whole-genome data through microarrays technology, diagnosis accuracy is expected to be improved. Despite the high potential of the data prepared by the technology, their analysis on different platforms shows that they may differ for different samples concerning biomarker status. This affects the diagnosis accuracy because of the existing bias between two different experimental conditions. To address this problem, we propose a new approach using statistical analysis of biological data combined with artificial intelligence techniques.

Keywords: Alzheimer's disease, disease diagnosis, gene expression, machine learning
Mathematics Subject Classification [2010]: 13D45, 39B42

1 Introduction

A disruption in thinking, remembering, and behaving in doing daily work is called Dementia. Alzheimer's disease (AD) is the most prevalent kind of Dementia that begins silently with mild cognitive impairment (MCI) and progresses gradually. AD is a chronic neurodegenerative brain disorder in which neurons decline irremediably [1]. The pathogenesis of AD has not been identified as its reliable biomarkers are unknown. No effective and reliable therapy exists for AD and the existing medicines can only relieve or slow its progression [2, 3]. The previous facts reveal the importance and necessity for the early detection of AD [4, 5, 6]. With the advances in technology, recent works use computer-aided diagnosis (CAD) tools to predict AD through artificial intelligence (AI) approaches. Researchers take advantage of AI to diagnose AD from different perspectives. Generally, from the biological point of view, AI is used with phenotypic or genotypic data [7, 8]. A common example of the phenotypic approach is diagnosing AD using brain images. For instance, Sarraf and Tofighi [9] used functional Magnetic Resonance Imaging (fMRI) data with LeNet as the state-of-the-art Convolutional Neural Network (CNN) to diagnose AD. Ramazan et al. [10] employed ResNet-18

[1]Speaker

along with transfer learning to diagnose different stages of AD using fMRI data. Farooq et al. [11] employed GoogLeNet, ResNet-18, and ResNet-152 and used data augmentation on MRI images. These models were trained from scratch to predict different cases of AD, including mild cognitive impairment (MCI), late mild cognitive impairment (LMCI), and normal. Wang et al. [12] introduced an eight-layer CNN to diagnose AD and normal cases using MRI data. The methods based on this approach are accompanied by low-accurate outcomes which cause late remedies against AD. Such deficiencies motivate researchers to employ a genotypic approach for the treatment of the disease [13]. Various studies have been conducted to diagnose AD using genotypic data such as gene expression (GE) profile data. The key step in diagnosing diseases using GE data is to find differentially expressed genes (DEGs). The GE datasets are generally vast, and thus, researchers have been motivated to employ machine learning (ML) techniques along with statistical methods to analyze GE data and find DEGs. In this regard, Sahu et al. [14] proposed a framework to identify highly specific genes to AD based on a statistical analysis of gene ontology and ML. Liu et al. [15] used graph Laplacian regularization to include protein-protein interaction network information as well as GE data for diagnosing AD. In another study, Sharma and Dey [16] proposed an ensemble feature selection method to identify potential biomarkers related to AD. El-Gawady et al. [17] introduced a four-staged ML-based framework for AD diagnosis. The main stage of the framework deals with gene selection where they used filter-based metrics to score the importance of each gene in AD diagnosis, and then, they incrementally assessed the rest of genes using ML techniques. Park et al. [18] combined GE data with DNA methylation data for AD diagnosis. After feature selection, they used a Deep Neural Network to predict AD based on the integrated data. The incidence of AD, similar to other complex diseases, involves the interaction between multiple genes. Univariate analysis of associations enables us to identify risk genes at the expense of ignoring biomarkers with weak associations. Accordingly, scientists paid more attention to the role of biological networks such as protein interaction network (PIN) and gene interaction network (GIN) besides GE data in the occurrence and development of a disease. In this regard, several works have been conducted to identify disease-related genetic networks [19, 20]. These studies have opened a new way for investigating the pathogenic origin of diseases. In this paper, our focus is to introduce a novel approach for diagnosing AD by integrating GE and GIN data. The effectiveness of the proposed framework was illustrated via several experimental studies.

2 Method

The Gene Expression Omnibus (GEO) web server was used to download the GE profile dataset, with accession number GSE5281 [21]. The dataset contains 54,675 gene expressions of 161 samples including 87 AD and 74 normal aged brain cases. The expressions have been measured from six different regions of the brain including the entorhinal cortex (EC), the hippocampus (HIP), the medial temporal gyrus (MTG), the posterior cingulate (PC), the superior frontal gyrus (SFG), and the primary visual cortex (VCX). The GE dataset faces the problem of skewed distribution. In this regard, all data within the dataset was transformed using the log2 function. Next, All the available genes in the platform of the GE dataset were extracted and submitted to the STRING online server to obtain the corresponding GIN.

After data preparation, the B-statistics and a new score based on a gene interaction network are used to evaluate genes. The B-statistics helps us to find differentially expressed genes. The new score, called the evidence score, measures the compliance level of the differentially expressed genes with past biological evidence. The evidence score for each gene is defined via the formula:

$$ES(g_i) = \frac{N_{\text{DEGs}}}{N_{\text{All}}}$$

where N_{DEGs} indicates the number of neighbors of the gene g_i in the co-expression network which is in the DEGs list and N_{All} is the total number of g_i's neighbors in the network.

3 Experimental Results

The performance of the proposed approach for identifying the potential candidate genes for AD was assessed based on the classification performance of different classifiers. Along with the proposed method, three different gene selection methods were used including PCA, ANOVA, and MI. The results are summarized in Table 1.

Table 1: The accuracy (A), precision (P), recall (R), and F1-score (F) obtained by different classifiers using four different gene selection methods besides the proposed method

	Metric	KNN	SVM	RF	MLP	NB	LDA
PCA	A	88.19	90.68	86.33	93.78	81.36	91.3
	P	91.04	96.82	91.93	94.44	97.82	92.85
	R	82.43	82.43	77.02	91.89	60.81	87.83
	F	86.52	89.05	83.82	93.15	75	90.27
ANOVA	A	83.85	85.71	82.6	82.6	86.33	85.09
	P	84.28	86.95	82.85	83.82	88.23	86.76
	R	79.72	81.08	78.37	77.02	81.08	79.72
	F	81.94	83.91	80.55	80.28	84.5	83.09
MI	A	88.19	89.44	85.71	90.68	86.33	87.57
	P	93.65	92.53	84.93	91.54	87.14	90.90
	R	79.72	83.78	83.78	87.83	82.43	81.08
	F	86.13	87.94	84.35	89.65	84.72	85.71
Proposed	A	96.89	93.16	91.3	95.03	90.06	90.68
	P	98.59	94.36	92.85	95.4	90.27	92.75
	R	94.59	90.54	87.83	95.4	87.83	86.48
	F	96.55	92.41	90.27	95.4	89.04	89.51

4 Conclusion

For diagnosing AD, we aimed to take advantage of all the available tools and information from bioinformatics and artificial intelligence. As a result, we introduced the new approach. A focal point of this approach is the third step, in which we define the evidence score based on the GIN. Through this score, we complement past experiences with the results of statistical analysis from the previous step to further filter out genes. The performance of the propsed method was approximately the same or better than the state-of-the-art feature selection methods.

References

[1] Nussbaum, R.L. and C.E. Ellis, *Alzheimer's disease and Parkinson's disease*, New england journal of medicine, 2003. 348(14): p. 1356-1364.

[2] Pulido, M.L.B., et al, *Alzheimer's disease and automatic speech analysis: a review*, Expert systems with applications, 2020. 150: p. 113213.

[3] Irankhah, E, *Evaluation of early detection methods for Alzheimer's*, Bioprocess Eng, 2020. 4(1): p. 17-22.

[4] He, Y., et al, *Regional coherence changes in the early stages of Alzheimer's disease: a combined structural and resting-state functional MRI study*, Neuroimage, 2007. 35(2): p. 488-500.

[5] Vemuri, P., D.T. Jones, and C.R. Jack, *Resting state functional MRI in Alzheimer's Disease*, Alzheimer's research therapy, 2012. 4(1): p. 1-9.

[6] Helaly, H.A., M. Badawy, and A.Y. Haikal, *Deep learning approach for early detection of Alzheimer's disease*, Cognitive computation, 2021: p. 1-17.

[7] Razmara, J., M.H. Zaboli, and H. Hassankhani, *Elderly fall risk prediction based on a physiological profile approach using artificial neural networks*, Health informatics journal, 2018. 24(4): p. 410-418.

[8] Salehi, M., J. Razmara, and S. Lotfi, *Development of an ensemble multi-stage machine for prediction of breast cancer survivability*, J. AI Data Min. 8 (3)(2020) 371–378. 1978.

[9] Sarraf, S. and G. Tofighi, *Deep learning-based pipeline to recognize Alzheimer's disease using fMRI data*, 2016 future technologies conference (FTC). 2016. IEEE.

[10] Ramzan, F., et al, *A deep learning approach for automated diagnosis and multi-class classification of Alzheimer's disease stages using resting-state fMRI and residual neural networks*, Journal of medical systems, 2020. 44: p. 1-16.

[11] Farooq, A., et al, *A deep CNN based multi-class classification of Alzheimer's disease using MRI*, in 2017 IEEE International Conference on Imaging systems and techniques (IST). 2017. IEEE.

[12] Wang, S.-H., et al, *Classification of Alzheimer's disease based on eight-layer convolutional neural network with leaky rectified linear unit and max pooling*, Journal of medical systems, 2018. 42: p. 1-11.

[13] Mahendran, N., et al, *Improving the classification of alzheimer's disease using hybrid gene selection pipeline and deep learning*, Frontiers in Genetics, 2021. 12: p. 784814.

[14] Sahu, S., P.S. Dholaniya, and T.S. Rani, *Identifying the candidate genes using co-expression, GO, and machine learning techniques for Alzheimer's disease*, Network Modeling Analysis in Health Informatics and Bioinformatics, 2022. 11(1): p. 10.

[15] Liu, L., et al, *An improved graph Laplacian regularization method for identifying biomarkers of Alzheimer's disease*, Journal of Theoretical Biology, 2022. 543: p. 111121.

[16] Sharma, A. and P. Dey, *A machine learning approach to unmask novel gene signatures and prediction of Alzheimer's disease within different brain regions*, Genomics, 2021. 113(4): p. 1778-1789.

[17] El-Gawady, A., et al, *Machine Learning Framework for the Prediction of Alzheimer's Disease Using Gene Expression Data Based on Efficient Gene Selection*, Symmetry, 2022. 14(3): p. 491.

[18] Park, C., J. Ha, and S. Park, *Prediction of Alzheimer's disease based on deep neural network by integrating gene expression and DNA methylation dataset*, Expert Systems with Applications, 2020. 140: p. 112873.

[19] Lanke, V., et al, *Integrative analysis of hippocampus gene expression profiles identifies network alterations in aging and Alzheimer's disease*, Frontiers in Aging Neuroscience, 2018. 10: p. 153.

[20] Aubry, S., et al, *Assembly and interrogation of Alzheimer's disease genetic networks reveal novel regulators of progression*, PloS one, 2015. 10(3): p. e0120352.

[21] Liang, W.S., et al, *Gene expression profiles in anatomically and functionally distinct regions of the normal aged human brain*, Physiological genomics, 2007. 28(3): p. 311-322.

SEAICR model for Covid-19 via Caputo derivative

Behnam Mohammadaliee[1]
Department of Mathematics, Azarbaijan Shahid Madani University, Tabriz, Iran

Tohid Kasbi Gharahasanlou
Department of Mathematics and Statistics, Imam Hossein University, Tehran, Iran

Abstract

In this paper, a model for the transmission of Covid-19 is analyzed using Caputo derivative. A numerical method for the model is obtained by applying the fractional Euler method. To forecast the spread of Covid-19 in the world, a numerical simulation based on real data is presented. These simulations focus on investigating the impact of different fractional orders on the transmission dynamics.

Keywords: Epidemic Model, Caputo Derivative, Numerical Simulation
AMS Mathematical Subject Classification [2010]: 26A33, 34A08, 74H15

1 Introduction

The first instances of the novel coronavirus (nCoV) were discovered in China in December 2019. The virus rapidly spread to various countries worldwide, leading to a significant amount of deaths. The largest peak of Covid-19 in the world happened in January 2022, here we are going to simulate it. We consider active infected cases reported worldwide in the period of time T , from December 3, 2021 to February 11, 2022. New mathematical models of fractional order have been developed to help predict and control disease outbreaks ([1, 2, 3]).

2 Preliminary Definitions

Here, we start by introducing the fundamental definitions of fractional calculus that are relevant to the present manuscript.

Definition 2.1. ([4]) For a function $\mathcal{M}$, the Caputo fractional derivative of order $\alpha \in (0,1)$ is given by

$$^{C}\mathcal{D}_{\mathfrak{t}}^{\alpha}[\mathcal{M}(\mathfrak{t})] = \frac{1}{\Gamma(\ell-\alpha)} \int_0^{\mathfrak{t}} \frac{\mathcal{M}^{(\ell)}(\zeta)}{(\mathfrak{t}-\zeta)^{(\alpha-\ell+1)}}\, \mathrm{d}\zeta, \qquad \ell = [\alpha]+1.$$

Also, fractional integral of order α with $\alpha \in \mathbb{R}^+$ is defined as

$$^{C}\mathcal{I}_{\mathfrak{t}}^{\alpha}[\mathcal{M}(\mathfrak{t})] = \frac{1}{\Gamma(\alpha)} \int_0^{\mathfrak{t}} (\mathfrak{t}-\zeta)^{\alpha-1}\mathcal{M}(\zeta)\, \mathrm{d}\zeta.$$

[1]Speaker

3 Model Formulation

In this section, a model is developed where the population is divided into six distinct classes; namely: Susceptible ($\mathcal{S}$), Exposed ($\mathcal{E}$), Asymptomatic infected ($\mathcal{A}$), Symptomatic infected ($\mathcal{I}$), Critical infected ($\mathcal{C}$) and Recovered ($\mathcal{R}$). The system is as

$$\begin{cases} \Xi^{\alpha-1}\mathcal{D}_{\mathfrak{t}}^{\alpha}[\mathcal{S}(\mathfrak{t})] = \Psi - \lambda^*(\mathfrak{t}) - \hbar_{\mathbf{d}}\mathcal{S}(\mathfrak{t}), \\ \Xi^{\alpha-1}\mathcal{D}_{\mathfrak{t}}^{\alpha}[\mathcal{E}(\mathfrak{t})] = \lambda^*(\mathfrak{t}) - (\xi + \hbar_{\mathbf{d}})\mathcal{E}(\mathfrak{t}), \\ \Xi^{\alpha-1}\mathcal{D}_{\mathfrak{t}}^{\alpha}[\mathcal{A}(\mathfrak{t})] = p\xi\mathcal{E}(\mathfrak{t}) - (\rho + \hbar_{\mathbf{d}})\mathcal{A}(\mathfrak{t}), \\ \Xi^{\alpha-1}\mathcal{D}_{\mathfrak{t}}^{\alpha}[\mathcal{I}(\mathfrak{t})] = (1-p)\xi\mathcal{E}(\mathfrak{t}) - (\pi + \tau + \nu + \hbar_{\mathbf{d}})\mathcal{I}(\mathfrak{t}), \\ \Xi^{\alpha-1}\mathcal{D}_{\mathfrak{t}}^{\alpha}[\mathcal{C}(\mathfrak{t})] = \pi\mathcal{I}(\mathfrak{t}) - (\sigma + \delta + \hbar_{\mathbf{d}})\mathcal{C}(\mathfrak{t}), \\ \Xi^{\alpha-1}\mathcal{D}_{\mathfrak{t}}^{\alpha}[\mathcal{R}(\mathfrak{t})] = \rho\mathcal{A}(\mathfrak{t}) + \tau\mathcal{I}(\mathfrak{t}) + \sigma\mathcal{C}(\mathfrak{t}) - \hbar_{\mathbf{d}}\mathcal{R}(\mathfrak{t}), \end{cases} \tag{1}$$

where

$$\lambda^*(\mathfrak{t}) = \frac{(\zeta_1\mathcal{E}(\mathfrak{t}) + \zeta_2\mathcal{A}(\mathfrak{t}) + \zeta_3\mathcal{I}(\mathfrak{t}) + \zeta_4\mathcal{C}(\mathfrak{t}))\mathcal{S}(\mathfrak{t})}{\aleph},$$

for time $\mathfrak{t} \in [0, T]$ where the initial conditions are

$$\mathcal{S}(0) > 0, \quad \mathcal{E}(0) > 0, \quad \mathcal{A}(0) > 0, \quad \mathcal{I}(0) > 0, \quad \mathcal{C}(0) > 0, \quad \mathcal{R}(0) > 0.$$

The positively invariant region of system (1) with the initial conditions is as

$$\Phi = \left\{ (\mathcal{S}, \mathcal{E}, \mathcal{A}, \mathcal{I}, \mathcal{C}, \mathcal{R}) \in \mathbb{R}_6^+ \, : \, \aleph \leq \frac{\Psi}{\hbar_{\mathbf{d}}} \right\}.$$

The disease-free equilibrium point is

$$\breve{E}^0 = (\mathcal{S}^0, \mathcal{E}^0, \mathcal{A}^0, \mathcal{I}^0, \mathcal{C}^0, \mathcal{R}^0) = \left(\frac{\Psi}{\hbar_{\mathbf{d}}}, 0, 0, 0, 0, 0 \right).$$

Also, the endemic equilibrium point is acquired as $\breve{E}^{\circledast} = (\mathcal{S}^{\circledast}, \mathcal{E}^{\circledast}, \mathcal{A}^{\circledast}, \mathcal{I}^{\circledast}, \mathcal{C}^{\circledast}, \mathcal{R}^{\circledast})$, where

$$\begin{aligned} \mathcal{S}^{\circledast} &= \frac{\Psi\aleph}{\zeta_1\mathcal{E}^{\circledast} + \zeta_2\mathcal{A}^{\circledast} + \zeta_3\mathcal{I}^{\circledast} + \zeta_4\mathcal{C}^{\circledast} + \aleph\hbar_{\mathbf{d}}}, \\ \mathcal{E}^{\circledast} &= \frac{(\zeta_2\mathcal{A}^{\circledast} + \zeta_3\mathcal{I}^{\circledast} + \zeta_4\mathcal{C}^{\circledast})\mathcal{S}^{\circledast}}{\aleph(\xi + \hbar_{\mathbf{d}}) - \zeta_1\mathcal{S}^{\circledast}}, \\ \mathcal{A}^{\circledast} &= \frac{p\xi\mathcal{E}^{\circledast}}{\rho + \hbar_{\mathbf{d}}}, \\ \mathcal{I}^{\circledast} &= \frac{(1-p)\xi\mathcal{E}^{\circledast}}{\pi + \tau + \nu + \hbar_{\mathbf{d}}}, \\ \mathcal{C}^{\circledast} &= \frac{\pi\mathcal{I}^{\circledast}}{\sigma + \delta + \hbar_{\mathbf{d}}}, \\ \mathcal{R}^{\circledast} &= \frac{\rho\mathcal{A}^{\circledast} + \tau\mathcal{I}^{\circledast} + \sigma\mathcal{C}^{\circledast}}{\hbar_{\mathbf{d}}}. \end{aligned}$$

The basic reproduction number is as

$$\mathfrak{R}_0 = \frac{\zeta_1}{\xi + \hbar_{\mathbf{d}}} + \frac{\zeta_2 p\xi}{(\xi + \hbar_{\mathbf{d}})(\rho + \hbar_{\mathbf{d}})} + \frac{\zeta_3(1-p)\xi}{(\xi + \hbar_{\mathbf{d}})(\pi + \tau + \nu + \hbar_{\mathbf{d}})} + \frac{\zeta_4(1-p)\xi\pi}{(\xi + \hbar_{\mathbf{d}})(\pi + \tau + \nu + \hbar_{\mathbf{d}})(\sigma + \delta + \hbar_{\mathbf{d}})}.$$

Theorem 3.1. *The disease-free equilibrium point* $\breve{E}^0$ *of* (1) *is locally asymptotically stable if* $\mathfrak{R}_0 < 1$.

Theorem 3.2. *The disease-free equilibrium point* $\breve{E}^0$ *of* (1) *is globally asymptotically stable if* $\mathfrak{R}_0 \leq 1$.

4 Numerical Method and Simulation

Consider system (1) in a compact form as follows:

$$\Xi^{\alpha-1C}\mathcal{D}_{\mathfrak{t}}^{\alpha}\omega(\mathfrak{t}) = \mathcal{M}(\mathfrak{t},\omega(\mathfrak{t})), \qquad \omega(0) = \omega_0,\ 0 \leq \mathfrak{t} \leq T < \infty, \tag{2}$$

where $\omega = (\mathcal{S},\mathcal{E},\mathcal{A},\mathcal{I},\mathcal{C},\mathcal{R}) \in \mathbb{R}_+^6$, $\omega_0 = (\mathcal{S}_0,\mathcal{E}_0,\mathcal{A}_0,\mathcal{I}_0,\mathcal{C}_0,\mathcal{R}_0)$ is the initial vector, and $\mathcal{M}(\mathfrak{t}) \in \mathbb{R}$ is a continuous vector function satisfying Lipschitz condition

$$||\mathcal{M}(\omega_1(\mathfrak{t})) - \mathcal{M}(\omega_2(\mathfrak{t}))|| \leq c||\omega_1(\mathfrak{t}) - \omega_2(\mathfrak{t})||, \qquad c > 0.$$

Applying a fractional integral operator corresponding to the Caputo derivative to equation (2), we obtain

$$\omega(\mathfrak{t}) = \Xi^{1-\alpha}[\omega_0 + \mathcal{I}^{\alpha}\mathcal{M}(\omega(\mathfrak{t}))], \qquad 0 \leq \mathfrak{t} \leq T < \infty.$$

Set $k = \frac{T-0}{N}$ and $\mathfrak{t}_{\mathfrak{n}} = \mathfrak{n}k$, where $\mathfrak{t} \in [0,T]$ and N is a natural number and $\mathfrak{n} = 0,1,2,...,N$.
Let $\omega_{\mathfrak{t}}$ be the approximation of $\omega(\mathfrak{t})$ at $\mathfrak{t} = \mathfrak{t}_{\mathfrak{n}}$. Using the fractional Euler method in [5], we get

$$\omega_{\mathfrak{n}+1} = \Xi^{1-\alpha}[\omega_0 + \frac{k^{\alpha}}{\Gamma(\alpha+1)}\sum_{i=0}^{\mathfrak{n}}\mathfrak{u}_{\mathfrak{n}+1,i}\mathcal{M}(\mathfrak{t}_i,\omega_i)], \qquad i = 0,1,2,...,N-1,$$

where

$$\mathfrak{u}_{\mathfrak{n}+1,i} = (\mathfrak{n}+1-i)^{\alpha} - (\mathfrak{n}-i)^{\alpha}, \qquad i = 0,1,2,...,\mathfrak{n}.$$

In simulation of model (1), we utilize the numerical values provided in Table 1. The real data for active

Table 1: Details of the model parameters and their numerical value.

Parameter explanation	Parameter	Value	Ref
Susceptible individuals	$\mathcal{S}(0)$	7910775988	Estimated
Exposed individuals	$\mathcal{E}(0)$	43367979	Estimated
Asymptomatic infected individuals	$\mathcal{A}(0)$	3613998	Estimated
Symptomatic infected individuals	$\mathcal{I}(0)$	14455993	[6]
Critical infected individuals	$\mathcal{C}(0)$	2891198	Estimated
Recovered individuals	$\mathcal{R}(0)$	0	Hypothetical
Birth rate of population	Ψ	386038.78	Estimated
Natural death rate	$\hbar_{\mathbf{d}}$	2.10356×10^{-5}	Estimated
Transmission rate of infection from $\mathcal{E}$ to $\mathcal{S}$	ζ_1	4.78×10^{-11}	Fitted
Transmission rate of infection from $\mathcal{A}$ to $\mathcal{S}$	ζ_2	2.17×10^{-11}	Fitted
Transmission rate of infection from $\mathcal{I}$ to $\mathcal{S}$	ζ_3	3.41×10^{-11}	Fitted
Transmission rate of infection from $\mathcal{C}$ to $\mathcal{S}$	ζ_4	1.69×10^{-11}	Fitted
Rate at which exposed become infectious	ξ	0.5	Fitted
Isolation rate of symptomatic infected people	π	0.34	Fitted
Recovery rate of $\mathcal{A}$	ρ	0.36	Fitted
Recovery rate of $\mathcal{I}$	τ	0.34	Fitted
Recovery rate of $\mathcal{C}$	σ	0.15	Fitted
Death rate due to disease in class $\mathcal{I}$	ν	0.05	Fitted
Death rate due to disease in class $\mathcal{C}$	δ	0.1	Fitted
Population progress to $\mathcal{A}$	p	0.5	Hypothetical

infected cases, also the results of model (1) for $\alpha \in \{0.90, 1\}$ on periode T can be seen in Fig. 1. Clearly, the model has very well support from the data and the advantage of using the derivative of the fractional order instead of the derivative of the integer order can be seen. The changes of classes $\mathcal{S},\mathcal{E},\mathcal{A},\mathcal{I},\mathcal{C}$ and $\mathcal{R}$ with $\alpha \in \{0.70, 0.80, 0.90\}$ frome December 3, 2021 to September 28, 2022 are shown in Fig. 2.

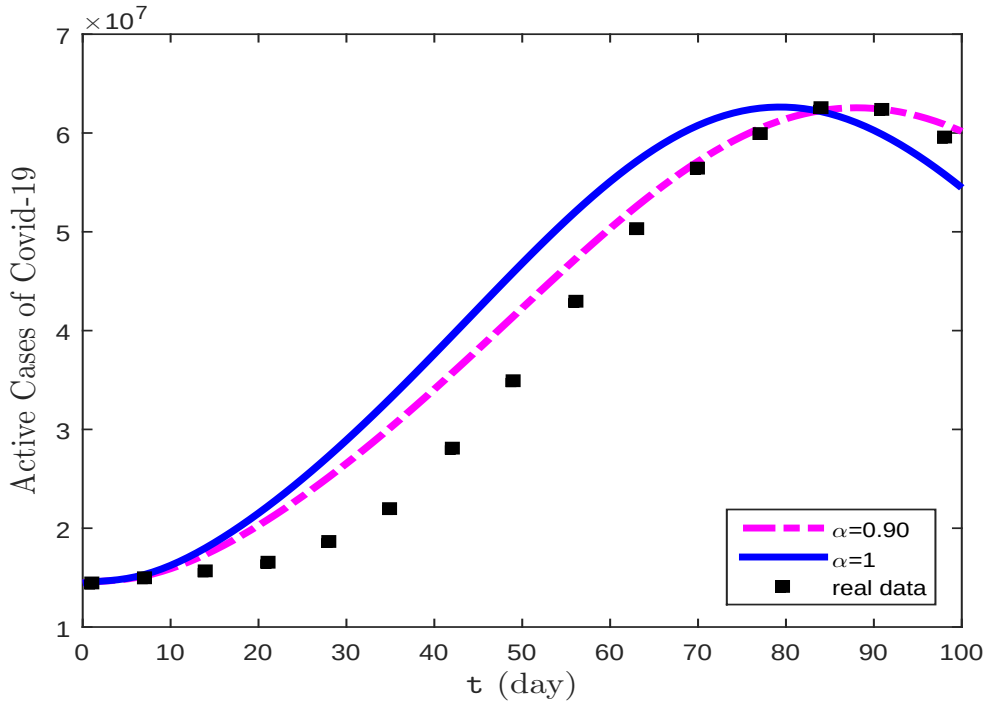

Figure 1: Active cases of Covid-19 on periode T.

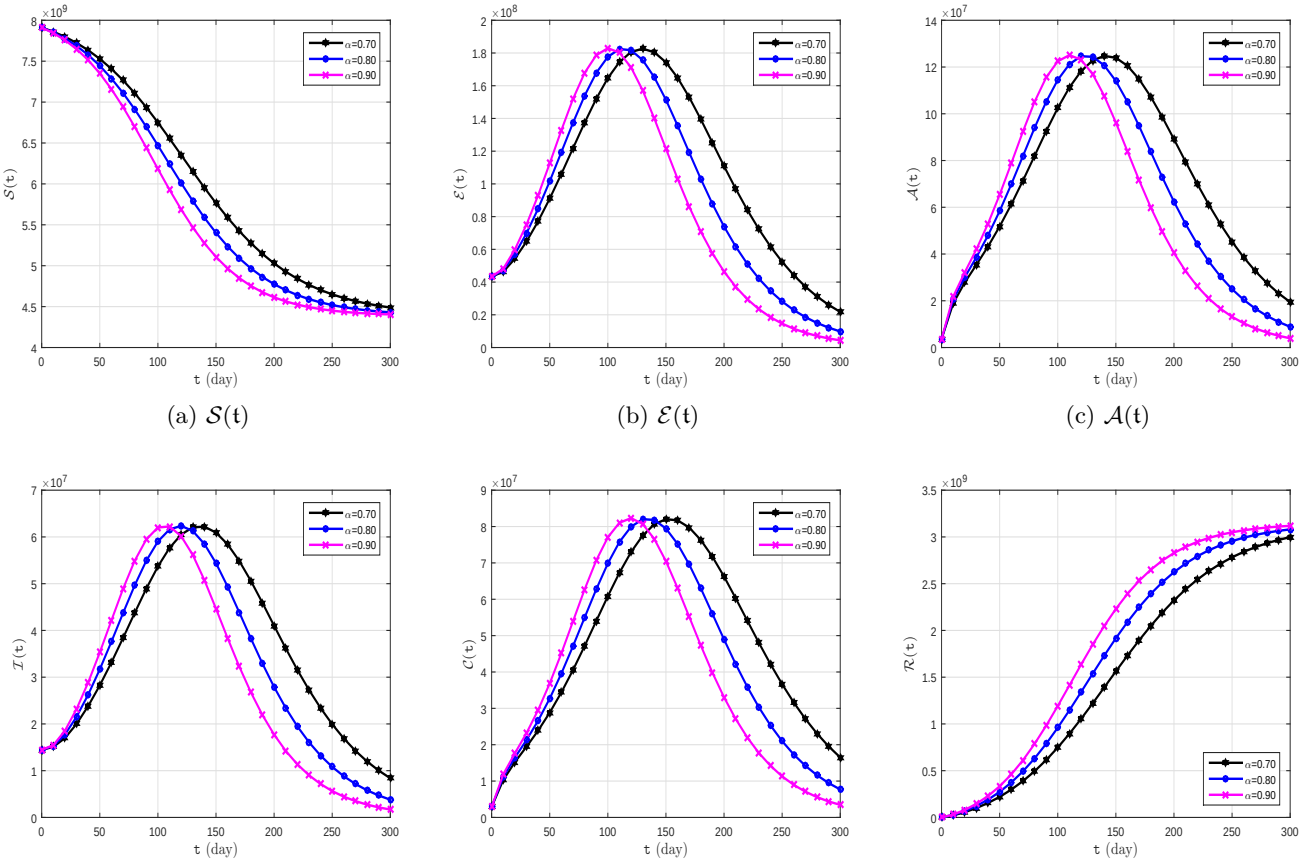

(a) $\mathcal{S}(t)$ (b) $\mathcal{E}(t)$ (c) $\mathcal{A}(t)$

(d) $\mathcal{I}(t)$ (e) $\mathcal{C}(t)$ (f) $\mathcal{R}(t)$

Figure 2: Dynamics of $\mathcal{S}(t), \mathcal{E}(t), \mathcal{A}(t), \mathcal{I}(t), \mathcal{C}(t)$ and $\mathcal{R}(t)$ with Caputo derivative whenever $\alpha \in \{0.70, 0.80, 0.90\}$.

References

[1] B. Mohammadaliee, V. Roomi, and M.E. Samei, *SEIARS model for analyzing COVID-19 pandemic process via ψ-Caputo fractional derivative and numerical simulation*, Scientific Reports, 14 (2024) 723

[2] S. Ahmad, A. Ullah, Q. M. Al-Mdallal, H. Khan, K. Shah, and A. Khan, *Fractional order mathematical modeling of COVID-19 transmission*, Chaos, Solitons & Fractals, 139 (2020) 110256

[3] K. Rajagopal, N. Hasanzadeh, F. Parastesh, I.I. Hamarash, S. Jafari, and I. Hussain, *A fractional-order model for the novel coronavirus (COVID-19) outbreak*, Nonlinear Dynamics, 101 (2020) 711-718

[4] S.G. Samko, A.A. Kilbas and O.I. Marichev, *Fractional Integrals and Derivatives: Theory and Applications*, Gordon and Breach Science Publishers, Switzerland, (1993)

[5] C. Li, F. Zeng, *The finite difference methods for fractional ordinary differential equations*, Numer. Funct. Anal. Optim, 34 (2013) 149–179

[6] World Health Organization, Coronavirus (COVID-19), *https://covid19.who.int/, accessed April 17*, (2022)

e-mail: `behnam.mohammadaliee@azaruniv.ac.ir`
e-mail: `t.kasbi@ihu.ac.ir`

Modeling the Dynamics of Cancer Stem Cells Using Nonlinear Integro-Differential Equations

S. Mohammadi[1]
Department of Applied Mathematics, Faculty of Mathematical Sciences,
Shahid Beheshti University, Tehran, Iran.

M.S. Shahrokhi-Dehkordi
Department of Applied Mathematics, Faculty of Mathematical Sciences,
Shahid Beheshti University, Tehran, Iran.

Abstract

In this article, a nonlinear model of integro-differential equations for the evolution of a heterogeneous population of cancer stem cells (CSCs) and cancer cells (CCs) is presented. We will prove the existence of the solution and uniqueness for the model using a suitable iterative scheme that converges to the solution.

Keywords: Cancer modelling, Integro-differential systems, Upper and lower solutions, Numerical integration.

1 Introduction

Recent studies have shown that cancer stem cells (CSCs), which are known as tumor-initiating cells, are the primary mediators of resistance to chemotherapy, radiotherapy and are also responsible for tumor recurrence after treatment [6]. A cancer stem cells (CSCs) has been defined as a small subpopulation of cells within a tumor that possesses the capability to renew itself and give rise to heterogeneous cell lineages of cancer cells that, in turn, comprise the tumor [5, 2].

2 Mathematical model

In 2009, Enderling proposed an individual-based cellular automaton model, in which individual cells are described by elements of a square grid, to simulate the dynamics of CSC, CC and their competition for developed an in silico environment. In the case, the mortality rate for CCs increases, for example due to treatment, CCs finds open space to grow. They generate more CSCs through occasional symmetric divisions, resulting in larger tumors.

Definition 2.1. The effect that increased CCs death can lead to a larger tumor is called the tumor growth paradox.

They noted that their result required some movability of CSC stimulation, otherwise the tumor growth paradox would not occur [1].

In 2013, Hillen rewrote Enderling's cellular automata dynamics model as a system of integral partial differential equations (iPDEs) for continuous CSCs and CCs population densities.
The simulation of the model based on the Enderling factor shows the paradox of tumor growth, which increases with the increase of cell death in the CCs compartment of tumor growth. This paradox is defined in the mathematical model as follows:

[1]Speaker

Definition 2.2. Let $p_\alpha(t)$ show the total tumor size at time $t \geq 0$ and $\alpha \geq 0$ represents the death rate of non-cancer stem cells CCs. If the death rate $\alpha_1 < \alpha_2$ and there are times t_1,t_2 and $T > 0$ then the tumor growth paradox model shows that

$$p_{\alpha_1}(t_1) = p_{\alpha_2}(t_2), \quad p_{\alpha_1}(t_1 + T) < p_{\alpha_2}(t_2 + T),$$

for $0 < T < T_0$.

Let $u(x,t)$ and $v(x,t)$ denote the density of cancer stem cells (CSCs) and non-cancer stem cells (CCs) at time t and place x respectively. Also, the total density of the tumor can be represented by $p(x,t) = u(x,t) + v(x,t)$. In the following we assume that cells cannot be stacked on top of each other, so there is a maximum density of one cell per unit cell area. This means $p(x,t) \leq 1$. Cells can reproduce only when there is room for the cell to accommodate the daughter cell, otherwise reproduction is prevented. To model the spatial search, they defined a nonlinear integral expression. According to the model based on the Enderling factor, they assumed that all cells can migrate randomly. These assumptions led to the following system of coupled equations that describe the dynamics of CSCs and CCs

$$\begin{cases} \dfrac{\partial u(x,t)}{\partial t} = D_u \triangle u(x,t) + \delta\gamma \displaystyle\int_\Omega k(x,y,p(x,t))u(y,t)dy, \\ \dfrac{\partial v(x,t)}{\partial t} = D_v \triangle v(x,t) + (1-\delta)\gamma \displaystyle\int_\Omega k(x,y,p(x,t))u(y,t)dy, \\ \qquad\qquad + \rho \displaystyle\int_\Omega k(x,y,p(x,t))v(y,t)dy - \alpha v(x,t) \end{cases} \tag{1}$$

Where, γ and ρ represent the number of cell cycle times of cancer stem cells and non-cancer stem cells per unit of time, respectively. Also, $\delta(0 < \delta < 1)$, the average ratio of symmetric division of cancer stem cells and $\alpha > 0$ shows the death rate of non-cancer stem cells and the diffusion coefficient for cancer stem cells and non-cancer stem cells respectively with D_u, D_v is shown. Also Ω is the spatial domain and $k(x,y,p(x,t))$ is the probability density that a cell located at y produces a cell located at x [3].

Remark 2.3. Let $k(x,y,p(x,t)) = k(x,y)F(p(x,t))$ where

A) The domain of $F(p)$ is in the interval $[0,1]$ and is a non-negative non-increasing continuous Lipschitz function such that

1. $F(0) = 1, \quad F(1) = 0,$
2. $\forall p \in (0,1) \quad F(p) > 0$,
3. $\forall p > 1, \quad F(p) = 0.$

B) $K \geq 0, \quad K \in C(\bar{\Omega}, \bar{\Omega}), \quad \int_\Omega K(x,y)dy \leq 1.$

3 Existence and uniqueness

Assume that initial values u_0, v_0, are smooth, $u_0, v_0 \in C^2(\Omega)$ and at every point $x \in \Omega$ boundary conditions

$$0 \leq u_0(x), v_0(x) \leq 1, \tag{2}$$

is established. First, we will start with uniform functions. Suppose

$$\check{u}_0(x,t) \equiv 0, \quad \check{v}_0(x,t) \equiv 1, \quad \hat{u}_0(x,t) \equiv 1, \quad \hat{v}_0(x,t) \equiv 0,$$

then, $\check{u}_h(x,t), \check{v}_h(x,t), \hat{u}_h(x,t), \hat{v}_h(x,t)$ for $h = 1, 2, \ldots$ are defined by the following iterative scheme

$$\frac{\partial \check{u}_h}{\partial t} = D_u \Delta \check{u}_h + \delta\gamma \int_\Omega k(x,y,\check{u}_h(x,t) + \check{v}_{h-1}(x,t))\check{u}_h(y,t)dy, \tag{3}$$

$$\frac{\partial \check{v}_h}{\partial t} = D_v \Delta \check{v}_h + (1-\delta)\gamma \int_\Omega k(x,y,\check{u}_{h-1}(x,t) + \check{v}_h(x,t))\hat{u}_{h-1}(y,t)dy + \rho \int_\Omega k(x,y,\check{u}_{h-1}(x,t) + \check{v}_h(x,t))\check{v}_h(y,t)dy - \alpha \check{v}_h \tag{4}$$

and

$$\frac{\partial \hat{u}_h}{\partial t} = D_u \Delta \hat{u}_h + \delta\gamma \int_\Omega k(x,y,\hat{u}_h(x,t)+\hat{v}_{h-1}(x,t))\hat{u}_h(y,t)dy, \tag{5}$$

$$\frac{\partial \hat{v}_h}{\partial t} = D_v \Delta \hat{v}_h + (1-\delta)\gamma \int_\Omega k(x,y,\hat{u}_{h-1}(x,t)+\hat{v}_h(x,t))\check{u}_{h-1}(y,t)dy+$$
$$\rho \int_\Omega k(x,y,\hat{u}_{h-1}(x,t)+\hat{v}_h(x,t))\hat{v}_h(y,t)dy - \alpha\hat{v}_h, \tag{6}$$

with boundry conditions

$$\frac{\partial \check{u}_h}{\partial n} = \frac{\partial \check{v}_h}{\partial n} = 0 = \frac{\partial \hat{u}_h}{\partial n} = \frac{\partial \hat{v}_h}{\partial n}, \qquad in\ \ \partial\Omega \times [0,T]$$

and

$$\check{u}_h(x,0) = u_0(x) = \hat{u}_h(x,0),\ \check{v}_h(x,0) = v_0(x) = \hat{v}_h(x,0),$$

$in\ \ \Omega$. keep in your mind that $u_0(x), v_0(x)$ show the same initial values in the original model. Note that in equation (3), the time evolution for the function $\check{u}_h(x,t)$ using the previous value of $\check{v}_{h-1}(x,t)$ calculated in the previous step is obtained. In this way, $\check{u}_h(x,t)$ remains the only unknown variable in this equation. Similar to the process above, we will have (4),(5) and (6) for three equations. The benefit obtained in the scheme is that the differential system consists of non-coupled equations whose analysis can be done with classical and well-known arguments based on the existence of upper and lower solutions. For the iterative schemes (3),(4),(5) and (6) we assume that the kernel $k(x,y,\cdot)$ for each $p \in [0,1]$ is C^1 and we define the uniform functions

$$\varphi(x,t) \equiv 0, \psi(x,t) \equiv 1.$$

According to the relation (2), on the whole domain Ω, we can write

$$\varphi(x,0) \leq u_0(x), v_0(x) \leq \psi(x,0).$$

In addition, $\varphi(x,t)$ and $\psi(x,t)$ satisfy the Neumann boundary conditions. In the proof process, we put $\varphi(x,t)$ and $\psi(x,t)$ in the equations (3), (4),(5) and (6) respectively.
We notice that $\varphi(x,t)$ solves the previous equations (3) and (5); on the other hand, as what concerns (4),(6), we have

$$D_v\Delta\varphi(x,t) + (1-\delta)\gamma \int_\Omega k(x,y,\check{u}_{h-1}(x,t)+\varphi(x,t))\hat{u}_{h-1}(y,t)dy+$$
$$\rho \int_\Omega k(x,y,\check{u}_{h-1}(x,t)+\varphi(x,t))\varphi(y,t)dy - \alpha\varphi(x,t) - \frac{\partial\varphi(x,t)}{\partial t} =$$
$$(1-\delta)\gamma \int_\Omega k(x,y,\check{u}_{h-1}(x,t))\hat{u}_{h-1}(y,t)dy \geq 0$$

and

$$D_v\Delta\varphi(x,t) + (1-\delta)\gamma \int_\Omega k(x,y,\hat{u}_{h-1}(x,t)+\varphi(x,t))\check{u}_{h-1}(y,t)dy+$$
$$\rho \int_\Omega k(x,y,\hat{u}_{h-1}(x,t)+\varphi(x,t))\varphi(y,t)dy - \alpha\varphi(x,t) - \frac{\partial\varphi(x,t)}{\partial t} =$$
$$(1-\delta)\gamma \int_\Omega k(x,y,\hat{u}_{h-1}(x,t))\check{u}_{h-1}(y,t)dy \geq 0.$$

According to the above relations, it follows that $\psi(x,t)$ is a lower solution for each of the equations (3), (4), (5) and (6). Moreover we notice that $\psi(x,t)$ solves the previous equations (3) and (5); on the other hand, as what concerns (4) and (6), we have

$$D_v\Delta\psi(x,t) + (1-\delta)\gamma \int_\Omega k(x,y,\hat{u}_{h-1}(x,t)+\psi(x,t))\check{u}_{h-1}(y,t)dy+$$
$$\rho \int_\Omega k(x,y,\hat{u}_{h-1}(x,t)+\psi(x,t))\psi(y,t)dy - \alpha\psi(x,t) - \frac{\partial\psi(x,t)}{\partial t} = -\alpha \geq 0$$

and

$$D_v\Delta\psi(x,t)+(1-\delta)\gamma\int_\Omega k(x,y,\check{u}_{h-1}(x,t)+\psi(x,t))\hat{u}_{h-1}(y,t)dy+$$
$$\rho\int_\Omega k(x,y,\check{u}_{h-1}(x,t)+\psi(x,t))\psi(y,t)dy-\alpha\psi(x,t)(x,t)-\frac{\partial\psi(x,t)}{\partial t}=-\alpha\geq 0.$$

According to the relations obtained above, it follows that $\psi(x,t)$ is an upper solution for each of the equations (3),(4),(5) and (6) will be So it allows us to apply Stinger's results to the given problem. It follows that the equation (3) will have a strong solution $\check{u}_h$ with $\varphi\leq\check{u}_h\leq\psi$. Similar to the above argument, it can be proved that the equations (4), (5) and (6) have strong solutions whose values are between φ and ψ. Hence, the following relation holds for $h=1,2,\ldots$

$$0\leq\check{u}_h(x,t),\hat{u}_h(x,t),\check{v}_h(x,t),\hat{v}_h(x,t)\leq 1, \tag{7}$$

for any $(x,t)\in\Omega\times[0,T]$.

Lemma 3.1. *For each $h=1,2,\ldots,$ the following statement is true on the entire domain:*

$$\check{u}_{h-1}(x,t)\leq\check{u}_h(x,t)\leq\hat{u}_h(x,t)\leq\hat{u}_{h-1}(x,t), \tag{8}$$
$$\hat{v}_{h-1}(x,t)\leq\hat{v}_h(x,t)\leq\check{v}_h(x,t)\leq\check{v}_{h-1}(x,t), \tag{9}$$

Theorem 3.2. *Suppose $u_0,v_0\in C(\Omega)$, $k(x,y,\cdot)\in C^1([0,p])$ and also the boundary conditions (2) is established. Then the sequences $\{(\check{u}_h(x,t),\check{v}_h(x,t))\}_h$, $\{(\hat{u}_h(x,t),\hat{v}_h(x,t))\}_h$ obtained using the previous scheme , monotonically to a regular solution (u,v) of the problem (1) such that*

$$0\leq u(x,t),v(x,t)\leq 1,$$

over $\Omega\times[0,T]$.

Proof. In the general, since

$$0\leq\check{u}_h(x,t),\hat{u}_h(x,t),\check{v}_h(x,t),\hat{v}_h(x,t)\leq 1$$

and on the other hand according to the lemma 3.1

$$\check{u}_h(x,t)\leq\hat{u}_h(x,t),\quad \hat{v}_h(x,t)\leq\check{v}_h(x,t),$$

by setting h to infinity, we will have over the entire domain

$$0\leq\check{u}(x,t)\leq\hat{u}(x,t)\leq 1,\qquad 0\leq\hat{v}(x,t)\leq\check{v}(x,t)\leq 1.$$

Next, we consider the functions $z(x,t)=\hat{u}(x,t)-\check{u}(x,t)\geq 0$ and $w(x,t)=\check{v}(x,t)-\hat{v}(x,t)\geq 0$, then we define the following functions

$$F_1(x,t)=\int_\Omega[k(x,y,\hat{u}(x,t)+\hat{v}(x,t))\hat{u}(y,t)-k(x,y,\check{u}(x,t)+\check{v}(x,t))\check{u}(y,t)]dy, \tag{10}$$
$$F_2(x,t)=\int_\Omega[k(x,y,\check{u}(x,t)+\check{v}(x,t))\hat{u}(y,t)-k(x,y,\hat{u}(x,t)+\hat{v}(x,t))\check{u}(y,t)]dy, \tag{11}$$
$$F_3(x,t)=\int_\Omega[k(x,y,\check{u}(x,t)+\check{v}(x,t))\check{v}(y,t)-k(x,y,\hat{u}(x,t)+\hat{v}(x,t))\hat{v}(y,t)]dy. \tag{12}$$

By subtracting $\hat{u}-\check{u}$ and $\check{v}-\hat{v}$, the system of the following equations is obtained

$$\frac{\partial z}{\partial t}=D_u\Delta z+\delta\gamma F_1(x,t), \tag{13}$$
$$\frac{\partial w}{\partial t}=D_v\Delta w+(1-\delta)\gamma F_2(x,t)+\rho F_3(x,t)-\alpha w, \tag{14}$$

with conditions

$$\frac{\partial z}{\partial n} = \frac{\partial w}{\partial n} = 0,$$

in $\partial\Omega \times [0,T]$ and

$$z(x,0) = w(x,0) = 0,$$

in Ω. By adding and subtracting the phrase

$$\int_\Omega k(x,y,\check{u}(x,t) + \hat{v}(x,t))z(y,t)dy,$$

to the relationship (10), (11) and also by adding and subtracting the phrase

$$\int_\Omega k(x,y,\check{u}(x,t) + \hat{v}(x,t))w(y,t)dy,$$

to the relationship (12), we will have

$$F_1(x,t) \leq |\Omega| C w(x,t) + \|z(\cdot,t)\|_{L^1(\Omega)},$$

$$F_2(x,t) \leq |\Omega| C z(x,t) + \|z(\cdot,t)\|_{L^1(\Omega)},$$

$$F_3(x,t) \leq |\Omega| C z(x,t) + \|w(\cdot,t)\|_{L^1(\Omega)}.$$

Finally, by multiplying z in the equation (13) and also by multiplying w in the equation (14) Using Holder's inequality for every $t \in [0,T]$ we have

$$\frac{d}{dt}\int_\Omega (\|w\|^2 + \|z\|^2)dx \leq (\gamma+\rho)|\Omega|(C+2)\int_\Omega (\|w\|^2 + \|z\|^2)dx,$$

we conclude that for arbitrary $x \in \Omega$, $z(x,0) = w(x,0) = 0$.
Then the granular inequality implies $\|w\|^2 + \|z\|^2 = 0$ which means $z(x,t) = w(x,t) = 0$ almost is everywhere in $\Omega \times [0,T]$. The result is that $\check{u} = \hat{u} = u$ and $\check{v} = \hat{v} = v$ solve the equation (1). □

Theorem 3.3. *Under the assumptions of Theorem 3.2, problem* (1) *has a unique regular solution which satisfies the condition* $0 \leq u(x,t), v(x,t) \leq 1$ *over* $\Omega \times [0,T]$ *and depends continuously on the initial values.*

References

[1] I. Borsi, A. Fasano, M. Primicerio and T. Hillen, A non-local model for cancer stem cells and the tumour growth paradox. Mathematical Medicine and Biology: IMA J. (2017) Mar 1;34(1):59-75.

[2] K. Chen, Y.H. Huang and J.L. Chen, Understanding and targeting cancer stem cells: therapeutic implications and challenges. Acta Pharmacol. Sin.a. (2013) Jun;34(6):732-40.

[3] T. Hillen, H. Enderling and P. Hahnfeldt, The tumor growth paradox and immune system-mediated selection for cancer stem cells. Bull. Math. Biol. (2013) Jan; 75:161-84.

[4] L. Maddalena and S. Ragni , Existence of solutions and numerical approximation of a non-local tumor growth model. Mathematical Medicine and Biology: IMA J. (2020) Feb 28;37(1):58-82.

[5] B. Malik and D. Nie, Cancer stem cells and resistance to chemo and radio therapy. FBE. (2012) Jan 1;4(6):2142-9.

[6] T. Yamashita and X.W Wang, Cancer stem cells in the development of liver cancer. JCI. 2013 May 1;123(5):1911-8.

Email: `saeideh.mohammadi.5.19@gmail.com`
Email: `shahrokhi@ipm.ir`

Find New Hypergraph for Polynomials Modeling

Marzieh Moradi Daleni[1]
Department of Mathematics Neyriz Branch, Islamic Azad University

Abstract

In this paper we consider the minimization of two classes of polynomials over the standard simplex. These polynomials have their variables labeled by the edges of a complete uniform hypergraph and their coefficients are defined in terms of some cardinality patterns of unions of edges. Data envelopment Analysis (DEA) is a nonparametric method that aims to use scientific methods in order to investigate the performance of Decision-Making Unit (DMU). One of the interesting subjects in DEA is the minimization of the empirical error, satisfying, at the same time, some shape constraints (convexity and free disposability). Unfortunately, by construction, DEA is a descriptive approach that is not concerned about preventing overfitting. In this research, the question is whether these polynomials attain their minimum value at the barycenter of the standard simplex, which corresponds to showing optimality of the uniform distribution for the underlying queuing problem.

Keywords: Polynomials, Data Envelopment Analysis, optimization model, hypergraph, symmetric

AMS Mathematical Subject Classification [2010]: 13D45, 39B42

1 Introduction

Optimizing Hypergraph-Based Polynomials Modeling Job-Occupancy in Queuing with Redundancy Scheduling. In this paper we consider a question posed in [1] coming from redundancy scheduling in queuing theory. Redundancy scheduling is based on the idea that sending the same job to multiple distinct servers can be advantageous, if balanced against the risk of wasted capacity. Here one wants to determine the optimal policy of choosing which subset of servers one should send the copies of the job to, and it is conjectured that the uniform probability distribution is optimal. This can be formulated as saying that a certain highly symmetric polynomial attains its minimum at the normalized all-one vector. While we do not manage to prove the general case, we prove a similar result for a simplification of the family of polynomials by exploiting its symmetries, as well as some special cases of the original problem. Symmetry is used more generally to give tractable reformulations for the semidefinite bounds arising from the next levels of Lasserre's hierarchy in [2] For more examples and a broad exposition about the use of symmetry in semidefinite programming we refer to [3] and further references therein. In the other hand Data Envelopment Analysis (DEA) (Charnes et al. [4]) is one of the existing techniques for estimating production functions and measuring efficiency. DEA relies on the construction of a polyhedral technology in the space of inputs and outputs that satisfies certain

[1]Speaker

classical axioms of production theory (e.g., monotonicity and convexity). It is a non-parametric data-driven approach with many advantages from a benchmarking point of view. Additionally, the treatment of the multi-output multi-input framework is relatively straightforward with DEA, in comparison with other methods available. However, Data Envelopment Analysis has been criticized for its non-statistical nature, even being labeled as a pure descriptive tool of the data sample at a frontier level with little inferential power. In this paper, our main objective is to use DEA for polynomial optimization.

2 Methods

2.1 DEA

DEA method introduced by Charnes et al (1978), DEA model can estimate an efficiency frontier by considering the best performance observations (extreme points) which "envelop" the remaining observations using mathematical programming techniques. The concept of efficiency can be defined as a ratio of produced outputs to the used inputs:

$$efficiency = \frac{outputs}{inputs} \tag{1}$$

So that an inefficient unit can become efficient by expanding products (output) keeping the same level of used resources, or by reducing the used resources keep the same production level, or by a combination of both. Considering $j = 1, \ldots, m$ Decision Making Units (DMUs) using $x_i (i = 1, \ldots, n)$ inputs to produce $y_r (r = 1, \ldots, s)$ outputs and prices (multipliers) v_i and u_r associated with those inputs and outputs, we can also formalize the efficiency expression in (1) as the ratio of weighted outputs to weighted inputs:

$$efficiency = \frac{\sum_{r=1}^{s} u_r y_{rj}}{\sum_{i=1}^{n} v_i x_{ij}} \tag{2}$$

$$\max \frac{\sum_{r=1}^{s} u_r y_{ro}}{\sum_{i=1}^{n} v_i x_{io}} \quad \sum_{r=1}^{s} u_r y_{rj} - \sum_{i=1}^{n} v_i x_{ij} \leq 0 \quad \forall i, r, j \; ; \quad v_i, u_r \geq 0 \tag{3}$$

This problem is denominated the CCR constant return to scale input-oriented model, which by duality is equivalent to solving the following linear programming

$$\begin{aligned} &\text{Min}(\theta) \\ &\sum_{j=1}^{m} z_j x_{ij} \leq \theta x_{io}, \\ &\sum_{j=1}^{m} z_j y_{rj} \leq \theta x_{io}, \\ &\sum_{j=1}^{m} z_j = 1 \quad (z_j \geq 0) \end{aligned} \tag{4}$$

As a result, we have an efficiency score which varies from 0 to 1 designating the efficiency for each decision-making unit. We can obtain the marginal contribution of each input and output in the multiplier model of (2), the peers of efficiency and respective weights in the primal (or envelopment) form of (3), and also the potential for improvements and slacks in an extension form of (4).

2.2 Polynomials

We now introduce the classes of polynomials of interest. Given integers $n, L \geq 2$, we set $V = [n] = \{1, \ldots, n\}$ and $E = \{e \subseteq V : |e| = L\}$, so that (V, E) can be seen as the complete $L - uniform$ hypergraph on n elements. We set $m := |E| = ((_l \wedge n))$ where we omit the explicit dependence on n, L to simplify notation, and we let $\Delta m = \{x = (xe : \ e \in E \subset \mathrm{R}^m) : \ x \geq 0, \ X \ \sum_(e \in E)(xe = 1)\}$. denote the standard simplex in R^m. The elements of Δm correspond to probability vectors on m items and the barycenter $x^* = \frac{1}{m}\,(1, \ldots 1)$ of Δm corresponds to the uniform probability vector. Given an integer $d \geq 2$ we consider the following $m - variate$ polynomial in the variables $x = (xe : \ e \in E)$, which is a main player in the paper:

$$f_d(x) = \sum_{Ed} \prod_{i=1}^{n} d \frac{Xel}{|e_1 \cup \cdots \cup e_i|} \tag{5}$$

So f_d is a homogeneous polynomial with degree d. We are interested in the following optimization problem

$$f_d^*(x) = \min_{x \in \Delta m} f_d(x)$$

asking to minimize the polynomial f_d over the simplex Δm. The main conjecture, which is stated in (4), claims that the minimum is attained at the uniform probability.

Conjecture 2.1. *Given integers $n, d, L \geq 2$, is the polynomial $f_d(x)$ in (5) attains its minimum over Δm at the barycenter x^* of Δm.*

As explained in [1], the motivation for this conjecture comes from its relevance to a problem in queuing theory, that we will briefly describe in the next section. In this chapter we are only able to give a partial positive answer to this conjecture, namely, in the case $d = 2$ and in the case $d = 3$ and $L = 2$. As a first step toward understanding the polynomials fd we investigate a related, easier to analyze, class of polynomials. Given an integer $d \geq 2$ we consider the following related class of polynomials

$$p_d(x) = \sum_{e \in E^d} \frac{1}{|e_1 \cup \cdots \cup e_i|} \tag{6}$$

which are also homogeneous with degree d. Note that, for degree $d = 2$, we have $f_2 = 1Lp2$. For degree $d \geq 3$ the polynomials f_d have a related, but more complicated structure than the polynomials p_d. Here too we may ask whether the minimum of p_d over the standard simplex Δm is attained at the uniform probability vector x^*. For the polynomials p_d we are able to give a positive answer in the general case. The following is the first main result of the paper.

As we will see, the analysis of the polynomials f_d is technically much more involved than for the polynomials p_d, and we have only partial results so far. In both cases the key ingredient is showing that the polynomials are convex on the simplex, i.e., that they have positive semidefinite Hessians at any vector in Δm. It turns out that the Hessian of the polynomial p_d enters some way as a component of the Hessian of the polynomial f_d. So this forms a natural motivation for the study of the polynomials p_d, though they form a natural class of symmetric polynomials that are interesting for their own sake. Exploiting symmetry plays a central role in our proofs. Indeed, the key idea is to show that the polynomials are convex, which, combined with their symmetry properties, implies that the global minimum is attained at the barycenter of the simplex. For this we show that their Hessian matrices are positive semidefinite at each point of the simplex, which we do through exploiting again their symmetry structure and links to Terwilliger algebras.

Symmetry is a widely used ingredient in optimization, in particular in semidefinite optimization and algebraic questions involving polynomials. We mention a few landmark examples as background information. Symmetry can indeed be used to formulate equivalent, more compact reformulations for semidefinite programs. The underlying mathematical fact is Artin-Wedderburn theory, which shows that matrix $*$-algebras can be block-diagonalized. An early well-known example is the linear programming reformulation from [4] for the Theta number of Hamming graphs, showing the link to the Delsarte bound and Bose-Mesner algebras of Hamming schemes [5].

2.3 Motivation

Our motivation for the study of the polynomials p_d and f_d comes from their relevance to a problem in queuing theory. The question whether they attain their minimum at the uniform probability distribution was posed to us by the authors of [1], who conjecture this to establish a result about the asymptotic behavior of the job occupancy in a parallel-server system with redundancy scheduling in the light-traffic regime (in contrast to the heavy-traffic regime considered in [6]). In what follows we will give only a high-level sketch of this connection, and we refer to the paper [1] for a detailed exposition. We also refer to [6] for an extended review of the relevant literature. A crucial mechanism that has been considered to improve the performance of parallel-server systems in queuing theory is redundancy scheduling. The key feature of this policy is that several replicas are created for each arriving job, which are then assigned to distinct servers (and then, as soon as the first of these replicas completes (or enters) service on a server the remaining ones are stopped). The underlying idea is that sending replicas of the same job to several servers will increase the chance of having shorter queuing times. This however must be weighed against the risk of wastage of capacity. An important question is thus to assess the impact of redundancy scheduling policies. While most papers in the literature of redundant scheduling assume that the set of servers to which the replicas are sent is selected uniformly at random, the paper [1] considers the case when the set of servers is selected according to a given probability distribution, and it investigates what is the impact of this probability distribution on the performance of the system. It is shown there that while the impact remains relatively limited in the heavy-traffic regime, the system occupancy is much more sensitive to the selected probability distribution in the light-traffic regime.

We will now only introduce a few elements of the model considered in [1], so that we can make the link to the polynomials studied in this paper. We keep our presentation high level and refer to [1] for details. The setting is as follows. There are n parallel servers, with average speed μ. Jobs arrive as a Poisson process of rate $n\lambda$ for some $\lambda > 0$. When a job arrives, L replicas of it are created that are sent — with probability xe — to a subset $\mathbf{e} \subseteq [n]$ of L servers. Here, $L \geq 2$ is an integer and $x = (xe)\ e \in E$ is a probability distribution on the set $E = \{e \subseteq [n] \ : \ |e| = L\}$ of possible collections of L servers. As noted in [1] this can be seen as selecting an edge $e \in E$ with probability xe in the uniform hypergraph $(V = [n], E)$ (with edge size L). An important performance parameter is the system occupancy at time t, which is represented by a vector $(\mathbf{e}_1, \ldots, \mathbf{e}_M)$, where $M = M(t)$ is the total number of jobs present in the system and $\mathbf{e}_i \in E$ is the collection of servers to which the replicas of the i'th longest job in the system have been assigned. We need three modeling assumptions. First one needs to assume suitable stability conditions. Second, all servers should have the same speed μ and, third, the service requirements of the jobs are assumed to be independent and exponentially distributed with unit mean. Under these assumptions, the stationary distribution of the

occupancy of the above edge selection is given by

$$\pi(e_1 \dots e_M) = C \prod_{i=1}^{M} \frac{n\lambda x e_i}{\mu |e_1 \dots e_i|} \tag{7}$$

for some constant $C > 0$. let $Q_\lambda(x)$ be a random variable with the stationary distribution of the system occupancy when the edge selection is given by the probability vector $x = (xe)\ e \in E$. It then follows that, for any integer $d \geq 1$, the probability that d jobs are present in the system is given by

$$P\big[Q_\lambda(x) = d\big] = \sum_{e \in E^d} \pi(e_1 \dots e_l) \tag{8}$$

Therefore, $P\big[Q_\lambda(x) = d\big]$ is the polynomial $f_d(x)$.

3 Conclusion

It would be worth mentioning that we have two stages in the search for the generalization error bound: the first stage is based on the construction of the class of piecewise linear hypotheses whose elements are polynomials that are located as close as possible to the data sample, and the second stage is based on the construction of the bound of the fat-shattering dimension of the class of hypothesis constructed in the first stage. The minimization of the bound of the expected error using the bound of the fat-shattering dimension calculated gives rise to the Data Envelopment Analysis-based Machines (DEAM) model as a method for estimating piecewise linear production functions, which minimizes the generalization error as well as the empirical error.

References

[1] Cardinaels, Ellen, Sem Borst, and Johan SH van Leeuwaarden. "Power-of-two sampling in redundancy systems: The impact of assignment constraints." Operations Research Letters 50, no. 6 (2022): 699-706.

[2] Schrijver, Alexander. "New code upper bounds from the Terwilliger algebra and semidefinite programming." IEEE Transactions on Information Theory 51, no. 8 (2005): 2859-2866.

[3] De Klerk, Etienne, Dmitrii V. Pasechnik, and Alexander Schrijver. "Reduction of symmetric semidefinite programs using the regular-representation." Mathematical programming 109, no. 2 (2007): 613-624.

[4] Charnes, Abraham, William W. Cooper, and Edwardo Rhodes. "Measuring the efficiency of decision making units." European journal of operational research 2, no. 6 (1978): 429-444.

[5] Schrijver, Alexander. "A comparison of the Delsarte and Lovász bounds." IEEE Transactions on Information Theory 25, no. 4 (1979): 425-429.

[6] Delsarte, Philippe, and Vladimir I. Levenshtein. "Association schemes and coding theory." IEEE Transactions on Information Theory 44, no. 6 (1998): 2477-2504.

[7] Cardinaels, Ellen, Sem Borst, and Johan SH van Leeuwaarden. "Heavy-traffic universality of redundancy systems with assignment constraints." Operations Research (2022).

e-mail: `marziehmoradi99@yahoo.com`

Machine learning algorithm for the numerical solution of the epidemiological disease model

Sima naraghi[1]
Department of Mathematics, Faculty of Mathematical Sciences, Shahid Beheshti University, Email: s_naraghi@sbu.ac.ir

Hassan Dana Mazraeh
Department of Computer and Data Sciences, Faculty of Mathematical Sciences, Shahid Beheshti University, Email: h_danamazraeh@sbu.ac.ir

Kourosh Parand
Department of Computer and Data Sciences, Faculty of Mathematical Sciences, Shahid Beheshti University, Email: k_parand@sbu.ac.ir

Abstract

In this paper, we introduce a novel hybrid approach that combines support vector regression with the spectral method to solve infectious disease models. Our results demonstrate that this innovative method effectively addresses the challenges of solving dynamical systems, providing accurate and efficient solutions.

Keywords: Supervised learning algorithm, Least squares support vector regression machines, collocation method, Biology dynamical system.
Mathematics Subject Classification [2010]: 13D45, 39B42

1 Introduction

Many natural phenomena have been modeled using mathematical models such as differential equations or statistics [4, 5]. In this way, some problems in biology and medicine have been modeled, and the importance of these models appears in personalized treatment and disease control diseases [6].

In this way, infectious diseases have been modeled using differential equations and solved by various methods [1, 8]. One of the important models in epidemiology is the Susceptible-Infected-Removed (SIR) model, which was introduced by Ronald Ross and Kermack [7]. Subsequently, the researchers have been solved the model by using various methods[9, 10]. The model comprises a system of three interconnected non-linear ordinary differential equations for which no explicit analytical solution exists. The model has been developed by many researchers in form of stochastic, fractional or modified by vaccinate effect [11, 12, 13]. The main SIR model has been introduced as following:

$$\begin{cases} \dfrac{\partial S}{\partial t} = -\beta SI, \\ \dfrac{\partial I}{\partial t} = \beta SI - \upsilon I, \\ \dfrac{\partial R}{\partial t} = \upsilon I, \end{cases} \tag{1}$$

[1]Speaker

Which $R(t) = N - S(t) - I(t)$ and N shows the total population.

On the other hand, some of machine learning algorithms presented for prediction and classification on the real data such as image, text [2, 3] and recently, machine learning methods and artificial intelligence algorithms have emerged as effective solutions for solving these equations, demonstrating impressive accuracy [14]. One standout method is least squares support vector regression (LS-SVR) [15] , which has been successfully applied to a diverse range of equations since its introduction by Suykens et al[16, 17].

The method presented by Suykens and Mehrkanoon employs radial basis functions as the kernel, has gained significant attention from scientists due to its high accuracy and efficiency in solving equations and other researchers developed the method [18, 19].

This paper introduces a hybrid method that combines the strengths of LS-SVR and collocation method. Section 2 provides a brief overview of LS-SVR and legendre polynomials, followed by a detailed explanation of the combined method. Section 3 presents the results obtained, and the final section discusses and concludes the findings.

2 Legendre LS-SVR methd

In [16] the authors have presented the LS-SVR for regression problem as follows:

$$\begin{array}{ll} \underset{\boldsymbol{w},b,\boldsymbol{e}}{\text{minimize}} & \frac{1}{2}\boldsymbol{w}^T\boldsymbol{w} + \frac{\gamma}{2}\boldsymbol{e}^T\boldsymbol{e} \\ \text{subject to} & y_i = \boldsymbol{w}^T\boldsymbol{\varphi}(x_i) + b + e_i, \quad i = 1, \ldots, N, \end{array} \tag{2}$$

Here $\gamma \in \mathbb{R}^+, b \in \mathbb{R}, \boldsymbol{w} \in \mathbb{R}^h, \varphi(\cdot) : \mathbb{R} \to \mathbb{R}^h$ is the feature map and h is the dimension of the feature space. The dual solution is formed as follows:

$$\left[\begin{array}{c|c} \Omega + I_N/\gamma & \mathbf{1}_N \\ \hline \mathbf{1}_N{}^T & 0 \end{array}\right] \left[\begin{array}{c} \boldsymbol{\alpha} \\ \hline b \end{array}\right] = \left[\begin{array}{c} \boldsymbol{y} \\ \hline 0 \end{array}\right] \tag{3}$$

where $\Omega_{ij} = K(x_i, x_j) = \varphi(x_i)^T \varphi(x_j)$ is the ij-th entry of the positive definite kernel matrix. $\mathbf{1}_N = [1, \ldots, 1]^T \in \mathbb{R}^N, \boldsymbol{\alpha} = [\alpha_1, \ldots, \alpha_N]^T, \boldsymbol{y} = [y_1, \ldots, y_N]^T$ and I_N is the identity matrix.

For solving the systems of ODEs by machine learning algorithm, at first, we describe the system of differential equation as following:

$$\begin{cases} u_1(t) = F_1(t, u_1, u_2, ..., u_n), \\ u_2(t) = F_2(t, u_1, u_2, ..., u_n), \\ u_3(t) = F_3(t, u_1, u_2, ..., u_n), \end{cases} \tag{4}$$

subject to

$$u_i^{(m)}(x_0) = u_{im}, \tag{5}$$

which $m = 0, 1, ..., n_i - 1$, $i = 1, 2, .., n$. We can rewrite the method as following:

$$\begin{aligned} L_1(w_1, \lambda_1, e_1) &= \frac{1}{2}w_1^T w_1 + \frac{\gamma}{2}e_1^T e_1 - \lambda_1(u_1(t) - F_1), \\ L_2(w_2, \lambda_2, e_2) &= \frac{1}{2}w_2^T w_2 + \frac{\gamma}{2}e_2^T e_2 - \lambda_2(u_2(t) - F_2), \\ L_3(w_3, \lambda_3, e_3) &= \frac{1}{2}w_3^T w_3 + \frac{\gamma}{2}e_3^T e_3 - \lambda_3(u_3(t) - F_3). \end{aligned} \tag{6}$$

Now, by using K.K.T condition, we can reduced the optimization problem to an algebraic system of equations.

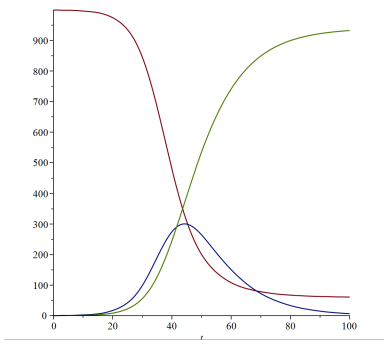

Figure 1: Legendre Least Square support Vector Regression method for numerical solution SIR model

3 Experimental Results

In this section, we demonstrate the results obtained using our proposed method for solving Eq. (1) with S(0) = 999, I(0) = 1, R(0) = 0 and $\beta = 0.0003$, $\upsilon = 0.1$. Tables 1, 2, and 3 illustrate the approximate solutions of the presented approach and we show the solution of the model by Legendre Lssvr method in figure 1.

Table 1: Table of numerical result for Suspected cases in SIR model

t	LS-SVR method
0	998.9993
20	974.5587
40	480.2506
60	108.1149
80	67.311
100	60.9674

Table 2: Table of numerical result for Infected cases in SIR model

t	LS-SVR method
0	1.0007
20	17.03959
40	274.6853
60	150.7034
80	33.1469
100	6.5646

Table 3: Table of numerical result for Removed cases in SIR model

t	LS-SVR method
0	-0.003
20	8.4050
40	245.0639
60	741.1814
80	899.5418
100	932.4678

4 Conclusion

In this paper, we presented an innovative hybrid method based on LS-SVR and Legendre collocation method for solving an epidemiological disease model described in Eq. (1). The results showed that the presented method is capable of solving this model accurately.

References

[1] H. Kheiri, M. Jafari, *Stability analysis of a fractional order model for the HIV/AIDS epidemic in a patchy environment*, Journal of Computational and Applied Mathematics, 346 (2019) 323-339

[2] D. D. Solomon, S. Kumar, K. Kanwar, S. Iyer, M. Kumar, *Extensive review on the role of machine learning for multifactorial genetic disorders prediction*, Archives of Computational Methods in Engineering, 31 (2024) 623-640

[3] S. Deng, Q. Li, R. Dai, S. Wei, D. Wu, Y. He, X. Wu, *A Chinese power text classification algorithm based on deep active learning*, Applied Soft Computing, 150 (2024) 111067.

[4] A.K. Cheng, *Mathematical modelling and real life problem solving*, in: Mathematical Problem Solving: Yearbook 2009, Association of Mathematics Educator

[5] J. Pilz, V.B. Melas, A. Bathke, *Statistical Modeling and Simulation for Experimental Design and Machine Learning Applications: Selected Contributions from SimStat 2019 and Invited Papers*, Springer Nature, 2023.

[6] J.D. Murray, *Mathematical Biology: II: Spatial Models and Biomedical Applications*, vol. 18, Springer, 2003.

[7] R.M. Anderson, *Discussion: the Kermack-McKendrick epidemic threshold theorem*, Bulletin of Mathematical Biology, 53 (1991) 1-32.

[8] M. Sohaib et al., *Mathematical modeling and numerical simulation of HIV infection model*, Results in Applied Mathematics, vol. 7, pp. 100118, 2020. Elsevier.

[9] Ö. İlhan, G. Şahin, *A numerical approach for an epidemic SIR model via Morgan-Voyce series*, International Journal of Mathematics and Computer in Engineering, 2024.

[10] Sunil Kumar, Ali Ahmadian, Ranbir Kumar, Devendra Kumar, Jagdev Singh, Dumitru Baleanu, Mehdi Salimi, *An efficient numerical method for fractional SIR epidemic model of infectious disease by using Bernstein wavelets*, *Mathematics*, vol. 8, no. 4, pp. 558, 2020, MDPI.

[11] Todd L. Parsons, Benjamin M. Bolker, Jonathan Dushoff, David JD Earn, *The probability of epidemic burnout in the stochastic SIR model with vital dynamics*, *Proceedings of the National Academy of Sciences*, vol. 121, no. 5, pp. e2313708120, 2024, National Acad Sciences.

[12] Mohammed Berir, Rania Saadeh, Mohamed A Abdoon, Ahmad Qazza, Dalal Almutairi, *A fractional study for solving the SIR model and chaotic system*, *IAENG International Journal of Applied Mathematics*, vol. 54, no. 2, 2024.

[13] Salvatore Federico, Giorgio Ferrari, Maria-Laura Torrente, *Optimal vaccination in a SIRS epidemic model*, *Economic Theory*, vol. 77, no. 1, pp. 49–74, 2024, Springer.

[14] Maziar Raissi, Paris Perdikaris, George Em Karniadakis, *Physics-informed neural networks: A deep learning framework for solving forward and inverse problems involving nonlinear partial differential equations*, *Journal of Computational Physics*, vol. 378, pp. 686-707, 2019, doi: 10.1016/j.jcp.2018.10.045.

[15] Johan AK Suykens, Joos Vandewalle, *Chaos control using least-squares support vector machines*, *International Journal of Circuit Theory and Applications*, vol. 27, no. 6, pp. 605-615, 1999, Wiley Online Library.

[16] Siamak Mehrkanoon, Tillmann Falck, Johan AK Suykens, *Approximate solutions to ordinary differential equations using least squares support vector machines*, *IEEE Transactions on Neural Networks and Learning Systems*, vol. 23, no. 9, pp. 1356-1367, 2012, IEEE.

[17] J.A. Rad, K. Parand, S. Chakraverty, *Learning with fractional orthogonal kernel classifiers in support vector machines: Theory, algorithms and applications*, Springer, 2023.

[18] K. Parand, A. A. Aghaei, M. Jani, A. Ghodsi, *Parallel LS-SVM for the numerical simulation of fractional Volterra's population model*, Alexandria Engineering Journal, vol. 60, no. 6, pp. 5637–5647, 2021, Elsevier.

[19] S. Mehrkanoon, J.A.K. Suykens, *Learning solutions to partial differential equations using LS-SVM*, Neurocomputing, vol. 159, pp. 105–116, 2015, Elsevier.

Email: `s_naraghi@sbu.ac.ir`
Email: `h_danamazraeh@sbu.ac.ir`
Email: `k_parand@sbu.ac.ir`

Study on the behavior and control of a chaotic HIV-1 system

Marzieh Pabasteh *1
Bashir Naderi*
*Department of Mathematics, Payame Noor University(PNU), Tehran, Iran.

Abstract

In this article, we investigate the behavior of the dynamic system of the HIV-1 virus and according to it, we realize that the system is chaotic. Also we controll the chaotic system by designing a linear controller based on the contraction method by applying the graphical algorithm.

Keywords: HIV-1 model, Chaotic, Control, Graphical algorithm.

AMS Mathematical Subject Classification [2010]: 37D35, 37N25

1 Introduction

There are different types of cancers that are mainly seen in patients with AIDS. AIDS begins when the virus seriously damages the immune system, leading to certain types of infections or other medical complications, including cancer. In this article, a dynamic model of the HIV-1 virus is defined by[1] , and the purpose of the model we reviewed in this article is to describe the dynamics of HIV-1 infection in cancer patients. Therefore, the model is presented as follows:

$$\begin{cases} \dot{x_1} = x_1[\beta_1(1 - \frac{x_1+x_2+x3}{\mu}) - \eta_1 x_2] \\ \dot{x_2} = x_2[\beta_2(1 - \frac{x_1+x_2+x3}{\mu}) - \sigma\eta_1 x_1 - \eta_2 x_3] \\ \dot{x_3} = \eta_2 x_2 x_3 - \rho x_3 \end{cases} \tag{1}$$

Where in the state variables are the population numbers of cancer cells (x_1), healthy cells (x_2), and HIV-infected cells (x_3). The constants β_1 and β_2 are the uncontrolled proliferation rate of cancer cells and the intrinsic growth rate of healthy cells, respectively, with $\beta_1 > \beta_2$. Parameter η_1 corresponds to the immune system's killing rate of tumor cells; η_2 is the infection rate coefficient. Moreover, μ is the effective carrying capacity of the system; σ is the losing rate of the immune cells because of the killing of cancer cells. Finally, the constant ρ represents the whole immune system killing's effect on the infected cells. The parameter values are shown in Table(1).

Remark 1.1. Notice that the growth of the populations of the cancer and the immune system cells is limited by a logistic-like function, given by $1 - \frac{x_1+x_2+x3}{\mu}$.

Table 1: Parameter values

Parameter	Parameter value
β_1	0.1775
β_2	0.03
μ	1500
η_1	0.0001
η_2	0.0005
σ	0.01
ρ	0.3
$x_{1(0)}$	678
$x_{2(0)}$	452
$x_{3(0)}$	0.25

In order to discuss the behavior of the system, first we get the equilibrium points to check the behavior of this system. We use Grobner's method to find equilibrium points. To check the stability of equilibrium points, we calculate the Jacobian matrix of the system(1).

$$J = \begin{pmatrix} \beta_1 - 2\frac{\beta_1}{\mu}x_1 - \frac{\beta_1}{\mu}x_2 - \frac{\beta_1}{\mu}x_3 - \eta_1 x_2 & -\frac{\beta_1}{\mu}x_1 - \eta_1 x_1 & -\frac{\beta_1}{\mu}x_1 \\ -\frac{\beta_2}{\mu}x_2 - \sigma\eta_1 x_2 & \beta_2 - \frac{\beta_2}{\mu}x_1 - 2\frac{\beta_2}{\mu}x_2 - \frac{\beta_2}{\mu}x_3 - \sigma\eta_1 x_1 - \eta_2 x_2 & -\frac{\beta_2}{\mu}x_2 - \eta_2 x_2 \\ 0 & \eta_2 x_3 & \eta_2 x_2 - \rho \end{pmatrix} \quad (2)$$

By placing the parameters and equilibrium points in the matrix(2), the eigenvalues are given in the table2.

Table 2: The eigenvalues of the Jacobian matrix(2) for the values of Table(1)

Equilibrium	λ_1	λ_2	λ_3
$(0,0,0)$	-0.3	0.03	0.1775
$(1500,0,0)$	-0.3	0.03	0.1775
$(0,1500,0)$	0.03	0.1775	-0.3
$(\frac{1500\beta_2}{1500\sigma\eta_1+\sigma\beta_1+\beta_2}, \frac{1500\sigma\beta_1}{1500\sigma\eta_1+\sigma\beta_1+\beta_2}, 0)$	0.1770	0.0299	-0.2989
$(0, \frac{\rho}{\eta_2}, \frac{\beta_2(1500\eta_2-\rho)}{\eta_2(1500\eta_2+\beta_2)}$	-0.2979	0.0331	0.1773
$\frac{1500\eta_1\eta_2\rho+\eta_1\rho\beta_2-1500\eta_2^2\beta_1+\eta_2\rho\beta_1}{(\sigma\eta_1-\eta_2)\eta_2\beta_1}, \frac{\rho}{\eta_2}, -\frac{(1500\eta_1\sigma\rho-1500\sigma\eta_2\beta_1+\sigma\rho\beta_1+\rho\beta_2)\eta_1}{(\sigma\eta_1-\eta_2)\eta_2\beta_1}$	0.1772	0.03229	-0.2977

Since some eigenvalues are positive, it is clear that the system(1) is unstable at the equilibrium points.

2 Main results

Since system(1) is unstable, we want to find a linear controller for the system by contraction method and with the help of graphical algorithm.

Definition 2.1. [2] A nonlinear dynamical system is called contraction if is in the conditions The beginning of a partial perturbation state variable is created, it converges exponentially to the same variable.

[1]speaker

Theorem 2.2. *[3, 4] A continuous-time dynamic system m of dimension $\dot{x} = f(x,t)$ is contraction if there exists a Jacobian matrix J such that for each $i = 1, \ldots, m$ to have:*

$$J_{ii}(t,x) < 0$$

The graph $G_d(A)$ constructed based on J described above does not contain directed loops and

$$\alpha_{ij}(t,x)\,\alpha_{ji}(t,x) \leq 1.$$

The graphical algorithm is derived from the above theorem. Now we apply the steps of the algorithm on system(1). The first step is to obtain the Jacobian matrix calculated in(2).
Using the Jacobian matrix, we write the adjacency matrix A:

$$A = \begin{pmatrix} 0 & 1 & 1 \\ 1 & 0 & 1 \\ 1 & 1 & 0 \end{pmatrix} \tag{3}$$

Next, we need to specify the direction of the edges of the graph. To determine the direction of the edges, we must first calculate $\alpha_{ij}(i \neq j)$, then obtain the directional algorithm $G_d(A)$. To calculate α_{ij}, the first condition is that $J_{i,i}$ should not be zero and in addition it should be negative. Therefore, we apply the controllers as follows:

$$u = (u_1, u_2, u_3)^T = (-nx_1, -mx_2, -kx_3)^T \quad s.t \quad n > 0, m > 0, k > 0.$$

Applying the new controllers, we recalculate the Jacobian matrix:

$$J = \begin{pmatrix} -n + \beta_1 - 2\frac{\beta_1}{\mu}x_1 - \frac{\beta_1}{\mu}x_2 - \frac{\beta_1}{\mu}x_3 - \eta_1 x_2 & -\frac{\beta_1}{\mu}x_1 - \eta_1 x_1 & -\frac{\beta_1}{\mu}x_1 \\ -\frac{\beta_2}{\mu}x_2 - \sigma\eta_1 x_2 & -m + \beta_2 - \frac{\beta_2}{\mu}x_1 - 2\frac{\beta_2}{\mu}x_2 - \frac{\beta_2}{\mu}x_3 - \sigma\eta_1 x_1 - \eta_2 x_2 & -\frac{\beta_2}{\mu}x_2 - \eta_2 x_2 \\ 0 & \eta_2 x_3 & -k + \eta_2 x_2 - \rho \end{pmatrix}$$

Now, by applying the controllers, we calculate α_{ij}:

$$\alpha_{13} = \frac{|\frac{\beta_1}{\mu}x_1|}{|-n+\beta_1-2\frac{\beta_1}{\mu}x_1-\frac{\beta_1}{\mu}x_2-\frac{\beta_1}{\mu}x_3-\eta_1 x_2|}(3-1-1) \qquad \alpha_{31} = \frac{|0|}{|-k+\eta_2 x_2-\rho|}(3-1-1)$$

$$\alpha_{21} = \frac{|-\frac{\beta_2}{\mu}x_2-\sigma\eta_1 x_2|}{|-m+\beta_2-\frac{\beta_2}{\mu}x_1-2\frac{\beta_2}{\mu}x_2-\frac{\beta_2}{\mu}x_3-\sigma\eta_1 x_1-\eta_2 x_2|}(3-1-1) \qquad \alpha_{12} = \frac{|-\frac{\beta_1}{\mu}x_1-\eta_1 x_1|}{|-n+\beta_1-2\frac{\beta_1}{\mu}x_1-\frac{\beta_1}{\mu}x_2-\frac{\beta_1}{\mu}x_3-\eta_1 x_2|}(3-1-1)$$

$$\alpha_{23} = \frac{|-\frac{\beta_2}{\mu}x_2-\eta_2 x_2|}{|-m+\beta_2-\frac{\beta_2}{\mu}x_1-2\frac{\beta_2}{\mu}x_2-\frac{\beta_2}{\mu}x_3-\sigma\eta_1 x_1-\eta_2 x_2|}(3-1-1) \qquad \alpha_{32} = \frac{|\eta_2 x_3|}{|-k+\eta_2 x_2-\rho|}(3-1-1)$$

By applying the condition $\alpha ij(t,x)\alpha_{ji}(t,x) \leq 1$, we introduce the controllers as follows, and the value of parameters n, m, and k is determined which is shown in Table(3).

$$u = (u_1, u_2, u_3)^T = (-nx_1, -mx_2, -kx_3)^T \quad s.t \quad n > 0, m < 0, k > 0.$$

Table 3: controller gain

Parameter	Parameter value
n	0.1775
m	-0.03
k	6

The results are shown in Figures (1) and (2).

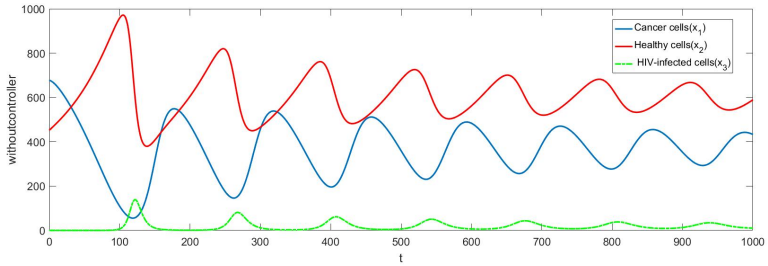

Figure 1: without controller system

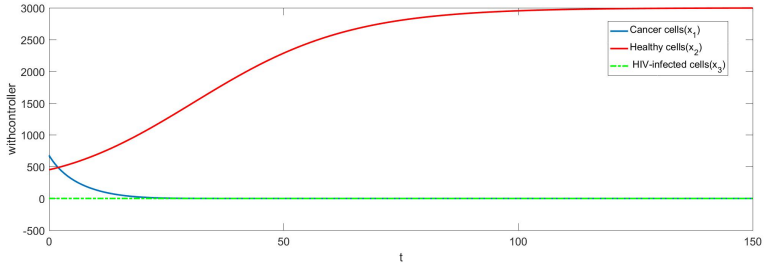

Figure 2: with controller system

References

[1] J. Lou, T. Ruggeri, and C. Tebaldi, *Modeling cancer in HIV-1 infected individuals: equilibria, cycles and chaotic behavior*, Mathematical Biosciences and Engineering, 3(2), (2006) .313-324

[2] W. Lohmiller, and J. J. E Slotine, *Control system design for mechanical systems using Contraction theory*, IEEE Transactions on Automatic Control J, 45(5) (2000), 984-989.

[3] G. Russo, M. di Bernardo, J. J. E. Slotine, *An algorithm to prove contraction, consensus, and network synchronization*, In Proceedings of the International Workshop NecSys, (2009).

[4] G. Russo, M. di Bernardo, J. J. E. Slotine, *A graphical algorithm to prove contraction of nonlinear circuits and systems*, IEEE Transactions on Circuits and Systems I, 58(2) (2011), 336-348.

e-mail: `m.pabasteh@yahoo.com`
e-mail: `b_naderi@pnu.ac.ir`

Investigating the importance of coping strategies in predicting mental well-being by using random forest model

Abbas Pak[1]
Department of Computer Sciences, Shahrekord University, Shahrekord, Iran

Iman Makhdoom
Department of Statistics, Payame Noor University (PNU), Tehran, Iran

Abstract

Mental well-being is an important aspect of the process of individual adaptation and development. Coping strategies play a pivotal role in determining individual well-being, especially in the face of stress and adversity. This article investigates the importance of different coping strategies in predicting well-being by utilizing the feature importance metrics inherent to random forest models. The results show that emotional support, active coping and positive reframing characteristics were the most important in predicting well-being.

Keywords: Mental well-being, Coping strategies, Feature importance metrics, Random forest model.
Mathematics Subject Classification [2010]: 13D45, 39B42

1 Introduction

An important indicator of mental health is well-being that can be defined as an effect of the cognitive and emotional assessment of one's own life, consisting of a high level of fulfilment in multiple areas [1]. In today's fast-paced and often stressful world, understanding the factors that contribute to individual well-being is more important than ever. Well-being, encompassing physical, emotional, and psychological health, is influenced by a multitude of factors, among which coping strategies are paramount. Coping strategies refer to the specific efforts, both behavioral and psychological, that individuals employ to manage stress and adversity.

Understanding coping strategies' impact on psychological well-being is key to identifying strategies that may serve as resources for successful adaptation. Existing research has explored the relationship between coping styles and well-being. For example, Konaszewski et al. [2] have used structural equation modelling to explore the relationships between coping strategies and well-being. Behbahani and Lajoie [3] utilized a criterion profile analysis to investigates the impact of level and pattern of coping strategies in predicting well-being. But, in none of these studies, the importance of each feature in predicting well-being has not been discussed. To address this gap, we employ a machine learning technique, namely random forests, which provides accurate predictions and offer insights into the relative importance of each feature in the prediction process.

The main contribution of this article is to explore the importance of coping strategies in predicting well-being using random forest feature importance metrics. We begin with an overview of the feature importance analysis in Section 2. In Section 3, by analyzing a practical dataset from a recent psychological study, we aim to identify which coping strategies are most influential in promoting well-being.

[1]Speaker

2 Material and Method

2.1 Data

We utilized a preexisting dataset provided by Konaszewski et al. [2] which includes well-being and coping strategies. Their study drew upon a sample of 253 juveniles, comprising 172 boys and 81 girls within the age range of 13 to 18 years. The coping strategies were measured by using the Brief COPE questionnaire that consists of 14 coping strategies [3]:

- Active coping: Taking active steps to deal with the problem.
- Planning: Developing a plan of action to address the problem.
- Using instrumental support: Seeking practical assistance or advice from others.
- Humor: The capacity to express or perceive what's funny.
- Venting: Expressing negative emotions and seeking emotional support.
- Positive reframing: Finding positive aspects or silver linings in the situation.
- Acceptance: Accepting the reality of the situation and learning to live with it.
- Religion: Finding solace and support in religious or spiritual beliefs.
- Self-distraction: Distracting oneself from the problem through engaging in other activities.
- Denial: Refusing to accept or acknowledge the reality of the situation.
- Behavioral disengagement: Giving up or withdrawing from the situation.
- Self-blame: Blaming oneself for the problem or feeling guilty.
- Substance use: Using substances such as alcohol or drugs to cope.
- Emotional support: Showing care and compassion for another person.

Further, the mental well-being was measured using the Warwick-Edinburgh Mental Well-being Scale [1].

2.2 Random Forest Model

Feature importance refers to the techniques used to identify and quantify the contribution of each input feature to the model's predictions. Random forests model inherently provides measures of feature importance through mean decrease in impurity Behbahani. The algorithm of random forest is a robust tree-based technique in machine learning. It operates by generating multiple decision trees during the training phase. Each tree is built using a random subset of the dataset, measuring a random subset of features at each split. This randomness introduces diversity among the trees, which helps reduce overfitting and enhances overall prediction accuracy. During prediction, the algorithm combines the outputs of all the trees, either through voting for classification tasks or averaging for regression tasks. This ensemble approach, leveraging the collective insights of multiple trees, ensures stable and precise results. Random Forests are extensively used for both classification and regression tasks due to their ability to handle complex data, minimize overfitting, and deliver reliable predictions across various scenarios. Here, we have used Scikit-learn library in Python for implementing the random forest algorithm.

3 Results

We employed three techniques to calculate feature importance in random forests, each offering unique insights:

- Built-in feature importance: This method measures how much the impurity (or randomness) within a node of a decision tree decreases when a specific feature is used to split the data.

- Permutation feature importance: Permutation importance assesses the significance of each feature independently by evaluating the impact of individual feature permutations on predictions.

- SHAP Values: SHAP values delve deeper by explaining the contribution of each feature to individual predictions.

Firstly, a *RandomForestRegressor* is conducted on the train data and then, the importance of features (coping strategies) is evaluated using the above mentioned approaches. The results of these techniques are shown in Figs. 1-3. It is observed that emotional support, active coping, and positive reframing were the top three features, ranked by their importance scores, as the most important features.

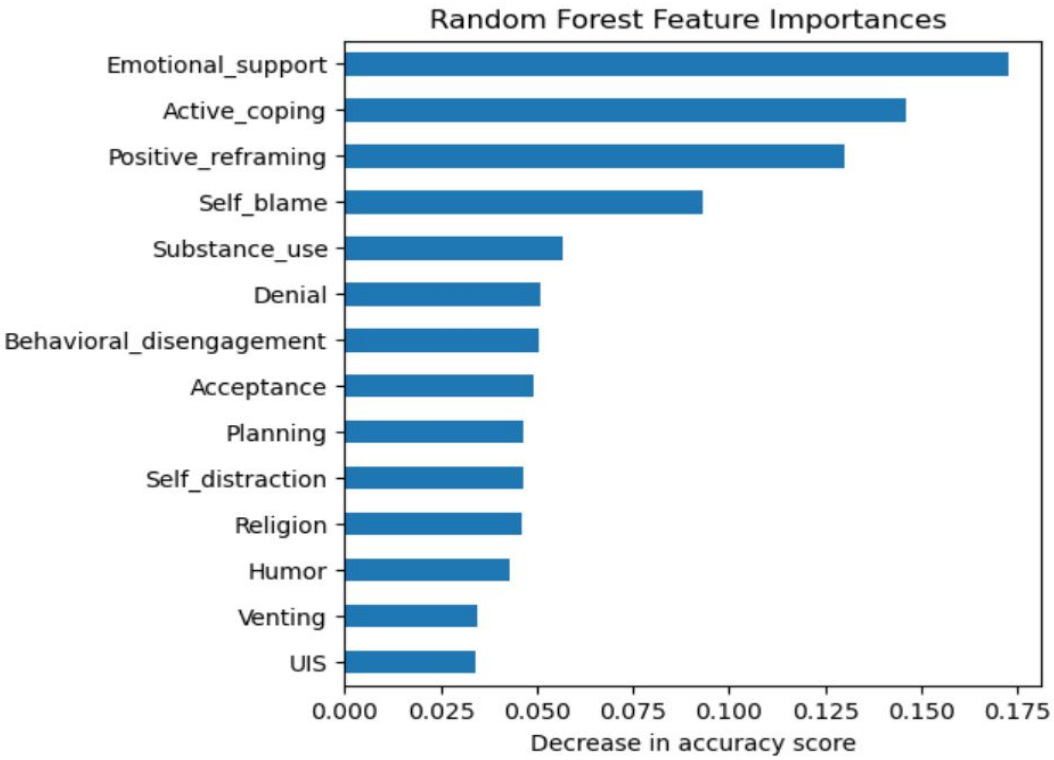

Figure 1: The amount of importance obtained by Built-in feature importance approach

4 Conclusion

This study highlights the critical role of coping strategies in predicting well-being, utilizing the robust feature importance metrics provided by the random forest model. The findings underscore the importance of emotional support, active coping and positive reframing strategies in predicticting well-being that offers valuable insights for developing targeted mental health interventions.

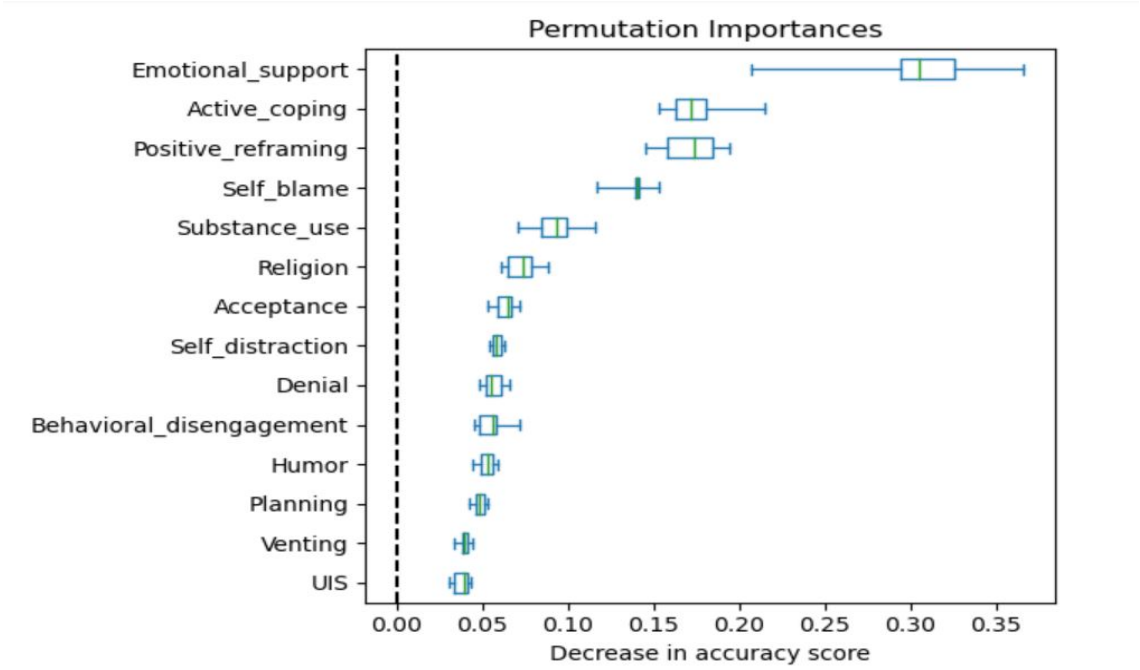

Figure 2: The amount of importance obtained by Permutation feature importance approach

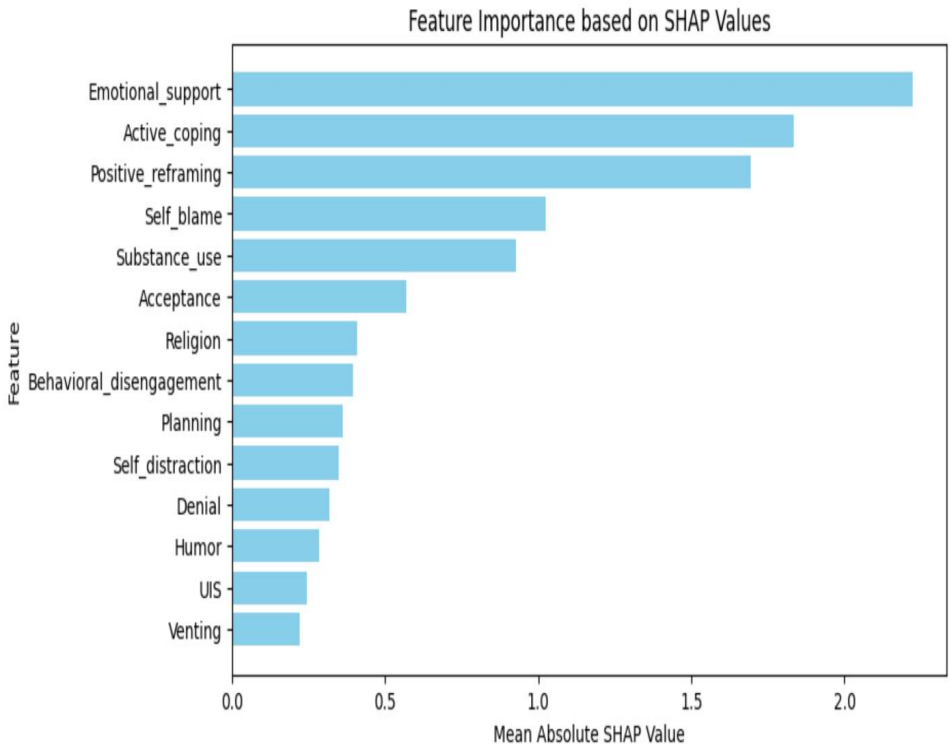

Figure 3: The amount of importance obtained by SHAP approach

References

[1] S. Stewart-Brown, K. Janmohamed, *Warwick–Edinburgh mental wellbeing scale*, User Guide Version, 2008, 1.

[2] K. Konaszewski, M. Niesiobedzka, J. Surzykiewicz, *Resilience and mental health among juveniles: role of strategies for coping with stress*, Health Qual Life Outcomes, 19(1) (2021) 58 DOI: 10.1186/s12955-

021-01701-3.

[3] M.G. Behbahani, D. Lajoie, *Patterns of individual differences in coping strategies: Criterion profile analysis of open coping strategies data*, Personality and Individual Differences, 223 (2024) 112634.

[4] Feature Importance with Random Forests. https://www.geeksforgeeks.org/feature-importance-with-random-forests/

Email: abbas.pak1982@gmail.com
Email: makhdoom@pnu.ac.ir

Bifurcation Analysis of Infectious Disease Model with Delay

Khayyam Salehi
Department of Computer Sciences, Faculty of Mathematical Sciences, Shahrekord University

Javad Alidousti
Department of Applied Mathematics, Faculty of Mathematical Sciences, Shahrekord University

Elahe Rafiean Borujeni[1]
Department of Applied Mathematics, Faculty of Mathematical Sciences, Shahrekord University

Abstract

During the outbreak of a pandemic, the information about the prevalence disseminated by the mass media or infected individuals leads to changes in the behavior of the community. The information that is generated is influenced by the delay in reporting by these infected individuals. This research proposes a delay infectious disease model to investigate the impact of delay on the system dynamics and disease prevalence. It is observed that the system experiences Hopf, double-Hopf, and Bautin bifurcations. Numerical simulations provide more evidence that the analytical findings are accurate.

Keywords: Hopf bifurcation, Double-Hopf bifurcation, Bautin Bifurcation, Delayed system
Mathematics Subject Classification [2010]: 37C75, 37G10

1 Introduction

The spread of infectious diseases is one of the major public health problems worldwide, and extensive research has been conducted in the direction of mathematical modeling regarding these diseases, including SARS, influenza, and others like them, with the objective of identifying methods to regulate the transmission of diseases [1]. Among these methods are the use of various pharmaceutical and non-pharmaceutical approaches. Non-pharmaceutical methods such as education, awareness, information, and others have been examined in [2]. Whenever a disease becomes prevalent in a community, information related to the disease prevalence and mortality rate is disseminated by the mass media or the people themselves. This information leads to behavioral changes in individuals, who then use protective measures such as wearing masks to protect themselves. These behavioral changes resulting from information ultimately impact the progression and spread of the disease [3]. As a result, this information is used as a highly effective non-pharmaceutical control intervention.

Recently, researchers have focused on examining the impact of information on the transmission of infectious diseases. In reference [4], the researchers combined the force of infection with the effect of awareness arising from the media in a $SIRS$ epidemic model, and pointed out that the impact of awareness considerably diminishes the disease's prevalence, however, it is impossible to eradicate it. From this discussion, it is clear that the progression of the disease is significantly influenced by the impact of information and the delay in its dissemination.

We examine the effect of behavioral changes induced by information in susceptible individuals in the event of a delay in the provision of information by infected individuals. We show that the system undergoes a Hopf bifurcation. We also demonstrate the stability and orientation of these periodic solutions, as well as the existence of a double-Hopf and Bautin bifurcations.

[1] Speaker

2 System Modeling and Existence of The Equilibrium Point

We consider the system introduced in [5]:

$$\begin{cases} \dfrac{dx}{dt} &= \alpha - \beta xy - \mu x - \theta\eta wx + \delta z \\ \dfrac{dy}{dt} &= \beta xy - (\mu + \xi + \gamma)y \\ \dfrac{dz}{dt} &= \gamma y + \theta\eta wx - (\mu + \delta)z \\ \dfrac{dw}{dt} &= \dfrac{ay}{1 + by} - cw \end{cases} \tag{1}$$

All parameters are considered non-negative.

In model 1, the researchers assumed that aware individuals are immediately rendered immune to the disease and are added to the recovered or immune population after taking protective measures. During the outbreak of the disease, the dissemination of information regarding the prevalence is always delayed. Therefore, we examine this delay in the dissemination of details in the system (1) to analyze the effect of this delay on the dynamics of disease transmission. Therefore, considering the system in the following manner:

$$\begin{cases} \dfrac{dx}{dt} &= \alpha - \beta xy - \mu x - \theta\eta wx + \delta z \\ \dfrac{dy}{dt} &= \beta xy - (\mu + \xi + \gamma)y \\ \dfrac{dz}{dt} &= \gamma y + \theta\eta wx - (\mu + \delta)z \\ \dfrac{dw}{dt} &= \dfrac{ay_\tau}{1 + by_\tau} - cw \end{cases} \tag{2}$$

where, $y_\tau = y(t - \tau)$. The model has a unique interior equilibrium point as $E_* = (x_*, y_*, z_*, w_*)$, where $x_* = \frac{\mu+\xi+\gamma}{\beta}$, $y_* = \frac{1}{2\,A}\left(-B + \sqrt{B^2 - 4AC}\right)$, $z_* = \frac{y_*}{\mu+\delta}\left(\gamma + \frac{\eta\theta a(\mu+\xi+\gamma)}{\beta\, c\,(by_*+1)}\right)$, $w_* = \frac{ay_*}{c\,(by_*+1)}$. moreover, $A = b(\mu + \xi) + \frac{b\mu\,\gamma}{\mu+\delta}$, $B = b\alpha\,(\frac{1}{R_0} - 1) + \frac{\mu\,(\mu+\xi+\gamma)+\delta\,(\mu+\xi)}{\mu+\delta} + \frac{\mu\eta\theta a(\mu+\xi+\gamma)}{\beta c(\mu+\delta)}$, $C = \alpha\,(\frac{1}{R_0} - 1)$, and $R_0 = \frac{\alpha\,\beta}{\mu\,(\mu+\xi+\gamma)}$. It is worth noting that R_0 is the basic reproduction number of the system.

3 Bifurcation Analysis for Time Delay ($\tau \neq 0$)

The characteristic equation of the model (2) around E_* is $\det(\lambda I - A_0 - A_\tau e^{\lambda\tau}) = 0$, where

$$A_0 = \begin{bmatrix} -\theta\,\eta w_* - \beta\,y_* - \mu & -\beta\,x_* & \delta & -\eta\theta\,x_* \\ \beta\,y_* & \beta\,x_* - \delta - \gamma - \mu & 0 & 0 \\ \theta\,\eta w_* & \gamma & -\mu - \delta & \eta\theta\,x_* \\ 0 & 0 & 0 & -c \end{bmatrix},$$

and

$$A_\tau = \begin{bmatrix} 0 & 0 & 0 & 0 \\ 0 & 0 & 0 & 0 \\ 0 & 0 & 0 & 0 \\ 0 & \frac{a}{by_*+1} - \frac{ay_*\,b}{(by_*+1)^2} & 0 & 0 \end{bmatrix}.$$

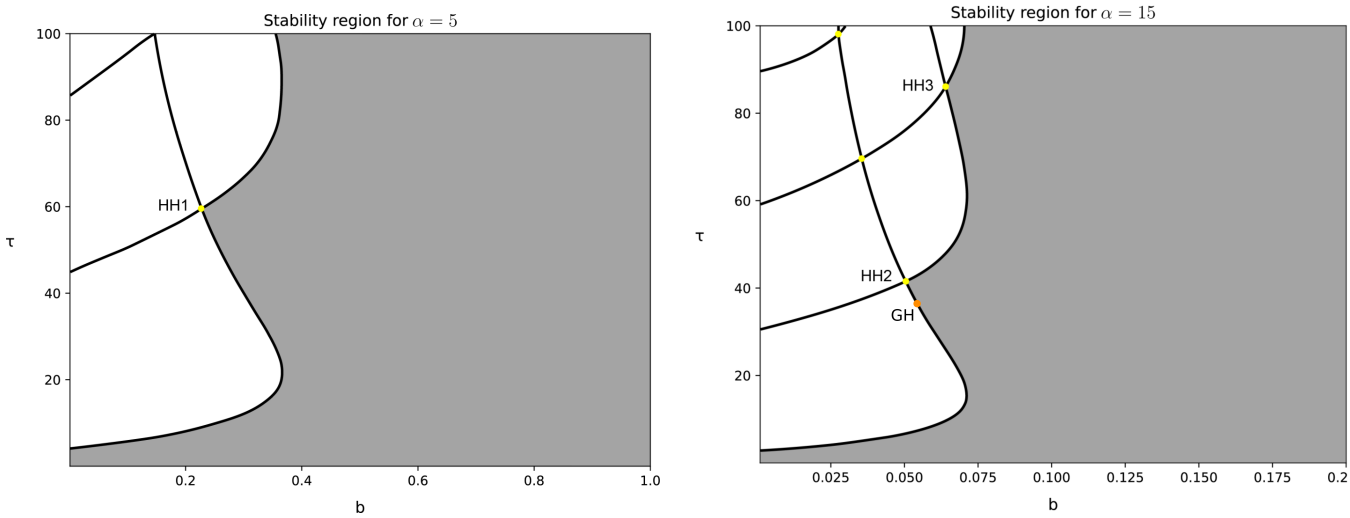

(a) (b)

Figure 1: a) The stability region at E_* for the delay system ($\alpha = 5$) is shown. The gray region represents an asymptotically stable parameter domain of equilibrium. At $HH1 : (b, \tau, \omega_1, \omega_2) = (0.227090, 59.464882, 0.124348, 0.051125)$, it represents a double-Hopf bifurcation. b) The stability region at E_* for the delay system ($\alpha = 15$) is shown. The double-Hopf bifurcation points in yellow color are $HH2 : (b, \tau, \omega_1, \omega_2) = (0.050450, 41.625812, 0.180458, 0.073561)$ and $HH3 : (b, \tau, \omega_1, \omega_2) = (0.064067, 86.232928, 0.164133, 0.104127)$. The Bautin point GH in orange color is demonstrated.

If all eigenvalues of the characteristic equation have negative real part, then the equilibrium point will be asymptotically stable whenever $\tau > 0$. By inserting the critical eigenvalue $\lambda = i\ \omega$, where $\omega > 0$, and subsequently separating the real and imaginary components, the stability region can be obtained. By setting $\mu, \gamma, \xi, \delta, \eta, \beta, a, c, b, \theta = 0.04, 0.1, 0.5, 0.5, 0.17, 0.01, 0.1, 0.1, 0.1, 0.9$ and considering bifurcation parameters as b and τ, the stability regions for $\alpha = 5$ and $\alpha = 15$ are depicted in Fig. 1. Moreover, the phase spaces around $HH2$ are depicted in Fig. 2 for transition between asymptotic behavior to unstable dynamics through double-Hopf bifurcation.

As the parameter α is increased, the area of the stability region around the equilibrium point also increases. For example, in Fig. 1(a), the stability region widens when parameter α increases from 5 to 15. It is worth noting that for higher value of α, the boundary curves intersect each other and become more complex.

In Fig 1 (b), a critical point GH is identified with the coordinates $(b, \tau) = (0.053535, 37.547558)$. This point is additionally denoted by an orange point. The critical point GH clearly separates the curve into two separate sections by different behavior. The curve lower than GH is associated with the negative value of first Lyapunov coefficient, leading to the occurrence of a supercritical Hopf bifurcation. In contrast, the curve upper than GH is associated with the positive of this value, which gives rise to a sub-critical Hopf bifurcation. This situation is referred to the Bautin bifurcation, where two distinct periodic orbits can exist simultaneously.

References

[1] M.E. Alexander, C. Bowman, S.M. Moghadas, R. Summers, A.B. Gumel, and B.M. Sahai, *A vaccination model for transmission dynamics of influenza*, SIAM Journal on Applied Dynamical Systems 3, no. 4 (2004): 503-524.

[2] S.M. Kassa and A. Ouhinou, *The impact of self-protective measures in the optimal interventions for controlling infectious diseases of human population*, Journal of mathematical biology 70 (2015): 213-236.

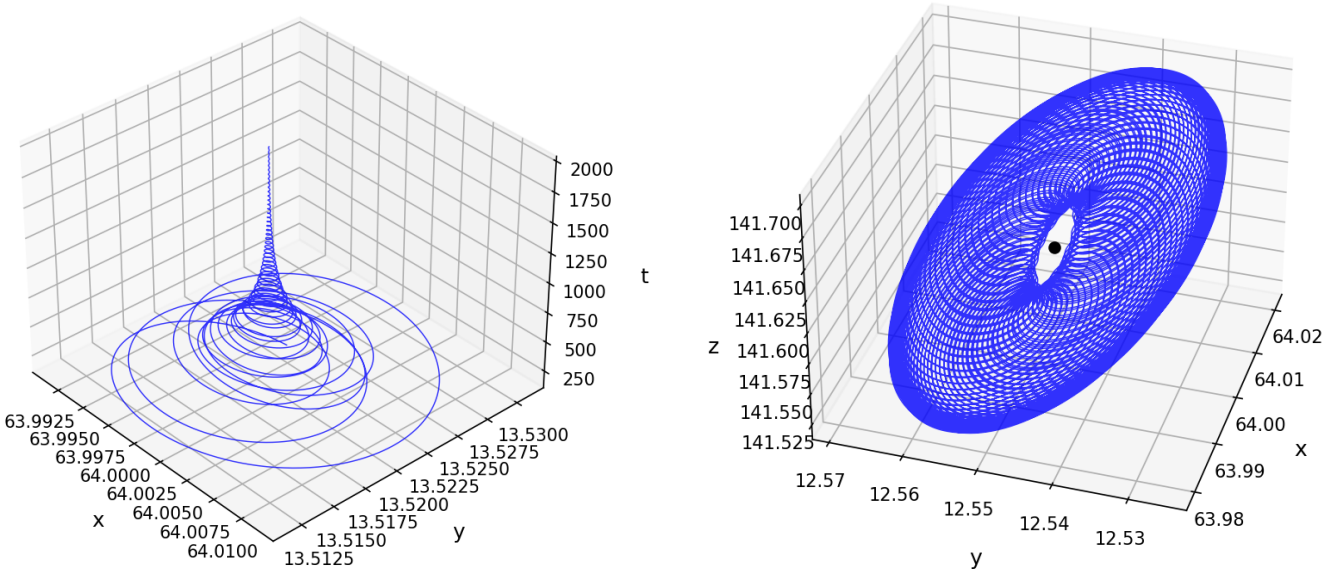

(a) (b)

Figure 2: a) The phase space corresponding to parameters in gray area of Fig. 1(b) near point $HH2$, showing that equilibrium point is asymptotically stable for $(b, \tau) = (0.065, 41.625)$. b) The phase space corresponding to parameters in boundary curve of Fig. 1(b) near point $HH2$: $(b, \tau, \omega_1, \omega_2) = (0.050450, 41.625812, 0.180458, 0.073561)$.

[3] World Health Organization, *Government of Senegal boots ebola awareness through SMS campaign*, http://www. who. int/features/2014/senegal-ebola-sms/en/. Published November (2014).

[4] Y. Liu and J. Cui, *The impact of media coverage on the dynamics of infectious disease*, International Journal of Biomathematics, 1(1):65–74, 2008.

[5] A. Kumar, P.K. Srivastava, and A. Yadav, *Delayed information induces oscillations in a dynamical model for infectious disease*, International Journal of Biomathematics 12, no. 02 (2019): 1950020.

Email: `kh.salehi@sku.ac.ir`
Email: `alidousti@sku.ac.ir`
Email: `elahe.rafieian@stu.sku.ac.ir`

سومین همایش بین‌المللی و پنجمین همایش ملّی ریاضیات زیستی
Third International and Fifth National Biomath Conference
مردادماه ۱۴۰۳

A novel method for solving quasi-equilibrium problems in Hadamard space

Mahdiyeh Shaker Sar[1]
Department of Pure Mathematics, Faculty of Mathematics,Statistics and Computer Sciences, University of Tabriz, Tabriz, Iran

Gholamreza Zamani Eskandani
Department of Pure Mathematics, Faculty of Mathematics,Statistics and Computer Sciences, University of Tabriz, Tabriz, Iran

Abstract

In this paper; we consider quasi-equilibrium problems wich extend equilibrium problems and quasi-variational inequalities as wel as variational inequalities in Hadamard space.we study Δ -convergence of the sequence generated by the extragradiant method to solution of quasi-equilibrium problem in Hadamard space.

Keywords: : Quasi-equilibrium problem, Hadamard space, Monotone mapping, Zero point
AMS Mathematical Subject Classification [2010]: 13D45, 39B42

1 Introduction

Let us present some concepts and facts regarding Hadamard spaces.
Let (X, d) be a metric space and $x, y \in X$. A geodesic path connecting points x and y is an isometry $c : [0, d(x, y)] \to X$ such that $c(0)=x, c(l)=y$ where $l := d(x, y)$ and $d(c(t), c(t'))=|t-t'|$ for all $t, t'\in[0, l]$. The set $c([0, l]) \subset X$ is denoted by $[x, y]$ and is called a geodesic segment (or geodesic) with the ends x and y. Metric space (X, d) is called a geodesic space if any two points of X can be connected by a geodesic, and it is called a uniquely geodesic space if for any two points from X there exists exactly one geodesic connecting them. Let X be a uniquely geodesic metric space, for each $x, y \in X$ and for each $t\in[0, 1]$, there exists a unique point $z\in[x, y]$ such that $d(x, z)=(1-t)d(x, y)$ and $d(y, z)=td(x, y)$. We will use the notation $tx \oplus (1-t)y$ for denoting the unique point z satisfying the above statement. A geodesic space X is called $CAT(0)$ space if for all $x, y, z\in X$ and $t\in[0, 1]$ it holds that

$$d^2(tx \oplus (1-t)y, z)\leq td^2(x, z)+(1-t)d^2(y, z)-t(1-t)d^2(x, y). \tag{1}$$

A complete $CAT(0)$ space is called an Hadamard space. Suppose that X is a metric space and C is a nonempty closed and convex subset of$X$.Moreover,$K : C \to C$ is defined asa multivalued mapping such

[1]Mahdiyeh Shaker Sar

that for all $x \in C$, $K(x)$ is a nonempty closed and convex subset of C. In addition,$f : X \times X \to R$ is a bi-function. Let x^*be a fixed pointof $K(\cdot)$. Then, the quasi-equilibrium problems QEP(f,K) consists of finding

$$f(x^*, y) \geq 0, \qquad \forall y \in K(x^*). \tag{2}$$

Let $S(f, K)$ and F(K) bethe sets respectively including all solutions of QEP(f,K) and all fixed-points of K. The associated Minty quasi-equilibrium problem isto find $x^* \in K(x^*)$ such that $f(y, x^*)\leq 0$ for all $y \in K(x^*)$. When $K(x) = C$ for all $x \in C$,the quasi-equilibrium problem QEP(f,K) and the associated Minty quasi-equilibrium problems respectively change to a classical equilibrium problemEP(f,C) and classical Minty equilibrium problems (see [5]).

For instance, quasi-variational inequality problems are considered as the quasi-equilibrium problems. Considering the duality pair as$\langle \cdot, \cdot \rangle : X^* \times X \to \mathbb{R}$ which leads to $\langle z, x \rangle = z(x)$.The map $T : X \to E^*$and $f(x, y) = \langle T(x), y - x \rangle$ are defined. Additionally, finding a point $x^* \in K(x^*)$ for every $x \in K(x^*)$, which satisfies $\langle T(x^*), x - x^* \rangle \geq 0$ is defined as the quasi-variational inequality problem QV IP(T,K). Considering these definitions, it can be demonstrated that QEP(f,K) is equivalent to QVIP(T,K).

2 Some important conditions

A sequence $\{x_n\}$ in an Hadamard space (X, d) Δ-converges to $x \in X$ if $A(\{x_{n_k}\})=\{x\}$, for each subsequence $\{x_{n_k}\}$ of $\{x_n\}$. We denote Δ-convergence in X by $\xrightarrow{\triangle}$ and the metric convergence by $\to$.

We introduce now some conditions on the bifunction f and the multivalued mapping K which are needed in the convergence analysis.

B1: $f(x, x)=0$ for all $x \in X$.

B2: $f(x, \cdot):X \to \mathbb{R}$ is convex and lower semicontinuous for all $x \in X$.

B3: $f(\cdot, y)$ is $\triangle$-upper semicontinuous for all $y \in X$.

B4: f is Lipschitz-type continuous, i.e. there exist two positive constants c_1 and c_2 such that

$$f(x, y) + f(y, z) \geq f(x, z) - c_1 d^2(x, y) - c_2 d^2(y, z), \quad \forall x, y, z \in X.$$

B5: f is pseudo-monotone, i.e. whenever $f(x, y)\geq 0$ with $x, y \in X$, it holds that $f(y, x)\leq 0$.

B6: $K_j:C \to 2^C, (1\leq j\leq M)$ are quasi-nonexpansive and demiclosed mappings with nonempty, closed and convex values.

In this section, we assume that $C \subset X$ is a nonempty, closed and convex set of an Hadamard space X. Let the bifunction $f:X \times X \to \mathbb{R}$ satisfies $B1-B5$ and let $K_j:C \to 2^C$ for all $1\leq j\leq M$ be multivalued quasi-nonexpansive mapping and satisfy in $B6$. Let $A_i:X \rightrightarrows X^*$ for all $1\leq i\leq N$ be multi-valued monotone operators. We introduce the following algorithm for finding a common element of the set of solutions of a quasi-equilibrium problem and a common zero of a finite family of monotone operators.

Algorithm1 *Initialization:* Choose $v_0, u \in C$ and fore sequences $\{\lambda_n\}$, $\{\beta_n\}$, $\{\gamma_n^i\}$ and $\{\alpha_n\}$ such that

(H1) $\{\lambda_n\} \subset [a,b] \subset \Big(0, \Big\{\min\{\frac{1}{2c_1}, \frac{1}{2c_2}\}\Big)$,

(H2) $\{\beta_n\} \subset [c,d] \subset (0,1)$,

(H3) $\{\gamma_n^i\} \subset (0,\infty)$ and $\liminf_{n\to\infty} \gamma_n^i > 0$ for $i = 1, 2, \cdots, N$,

(H4) $\{\alpha_n\} \subset (0,1)$, $\lim_{n\to\infty} \alpha_n = 0$ and $\sum_{n=0}^{\infty} \alpha_n = \infty$.

Set n=0 and go to Step 1.

Step 1: Compute

$$t_n = J_{\gamma_n^N}^{A_N} o \cdots o J_{\gamma_n^1}^{A_1}(v_n).$$

Step 2: Compute

$$w_n = P_{K_M(t_n)} o \cdots o P_{K_1(t_n)}(t_n).$$

Step 3: Compute

$$x_n = \beta_n v_n \oplus (1-\beta_n) w_n.$$

Step 4: Solve the following minimization problem and let y_n be the solution of it, i.e.

$$y_n = argmin_{y\in C}\{f(x_n, y) + \frac{1}{2\lambda_n} d^2(x_n, y)\}.$$

Step 5: Solve the following minimization problem and let z_n be the solution of it, i.e.

$$z_n = argmin_{y\in C}\{f(y_n, y) + \frac{1}{2\lambda_n} d^2(x_n, y)\}.$$

Step 6: Compute

$$v_{n+1} = \alpha_n u \oplus (1-\alpha_n) z_n.$$

Put $n := n+1$ and go to Step 1.

Suppose that Conditions $B1-B6$ hold and $S^* \neq \emptyset$. Then the sequence $\{x_n\}$ generated by Algorithm1 converges strongly to $P_{S^*}u$.

The convergence of the given algorithm is illustrated with a numerical example and figures 1,2

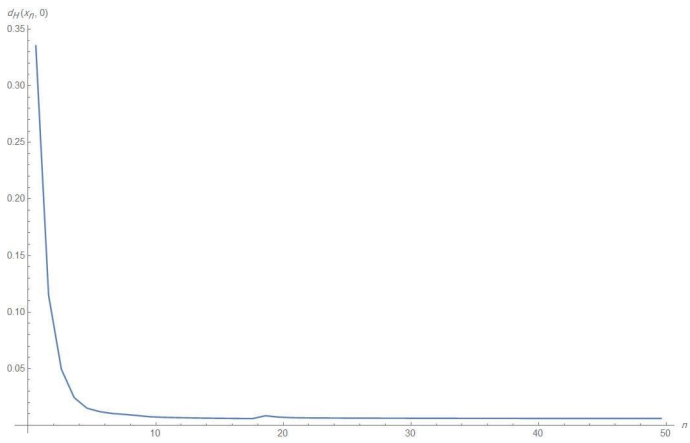

Figure 1: Plotting of $d_H(x_n, 0)$

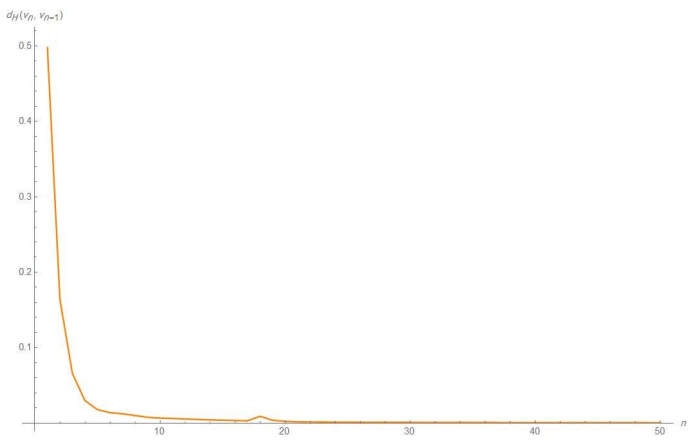

Figure 2: Plotting of $d_H(v_n, v_{n-1})$

References

[1] M. Bianchi and S. Schaible; Generalized monotone bifunctions and equilibrium problems, J. Optim. Theory Appl, 90, (1996), 31-43.

[2] O. Chadli, Z. Chbani and H. Riahi; Equilibrium problems with generalized monotone bifunctions and applications to variational inequalities, J. Optim. Theory Appl, 105, (2000), 299-323.

[3] P.L. Combettes and S.A. Hirstoaga; Equilibrium programming in Hilbert spaces, J. Nonlinear Convex Anal, 6, (2005), 117-136.

[4] B. Djafari Rouhani and V. Mohebbi; Extragradient methods for quasi equilibrium problems in Banach spaces. Journal of the Australian Mathematical Society, 112(1),(2022), 90-114. doi:10.1017/S1446788720000233

[5] B. Djafari-Rouhani and V. Mohebbi; Proximal point method for quasi-equilibrium problems in Banach spaces, Numer. Funct. Anal. Optim., 41, (2020), 1007-1026.

[6] G.Z. Eskandani, M. Raeisi and Th.M. Rassias; A hybrid extragradient method for solving pseudomonotone equilibrium problems using Bergman distance, J. Fixed Point Theory Appl, 20(132), (2018).

[7] A. Gibali, S. Reich and R. Zalas; Iterative methods for solving variational inequalities in Euclidean space, Fixed Point Theory Appl, 17(4), (2015), 775-811.

[8] A. Gibali, S. Reich and R. Zalas; Outer approximation methods for solving variational inequalities in Hilbert space, Optimization, 66(3), (2017), 417-437.

[9] A.N. Iusem, G. Kassay and W. Sosa; On certain conditions for the existence of solutions of equilibrium problems, Math. Program., 116, (2009), 259-273.

[10] A.N. Iusem and W. Sosa, On the proximal point method for equilibrium problems in Hilbert spaces, Optimization, 59, (2010), 1259-1274.

[11] H. Khatibzadeh and S. Ranjbar; Monotone operators and the proximal point algorithm in complete CAT(0) metric spaces. J. Aust. Math. Soc. 103, (2017), 70-90.

[12] M. Raeisi and G.Z. Eskandani; A hybrid extragradient method for a general split quality problem involving resolvents and pseudomonotone bifunctions in Banach spaces, Calcolo, 56(43), (2019).

[13] S. Reich and Z. Salinas; Metric convergence of infinite products of operators in Hadamard spaces, Nonlinear Anal, 18, (2017), 331-345.

[14] S. Reich and Z. Salinas, Weak convergence of infinite products of operators in Hadamard spaces. Rend Circ Mat Palermo, 65, (2016), 55-71.

[15] Pedro Jorge S. Santos and Joao Carlos de O. Souza; A proximal point method for quasi-equilibrium problems in Hilbert spaces, Optimization, (2020), doi: 10.1080/02331934.2020.1810686

سومین همایش بین‌المللی و پنجمین همایش ملی ریاضیات زیستی
Third International and Fifth National Biomath Conference
مرداد ماه ۱۴۰۳

Radiomics: Transforming Medical Imaging into Quantitative Data for Enhanced Diagnosis and Treatment

Kosar Tarvirdizade [1]

Nima Yousefivand

Tabriz University of Medical Sciences, faculty of medicine

Abstract

Radiomics converts medical imaging into quantitative data by extracting numerous features through advanced algorithms. This review highlights its principles, applications, challenges, and future directions. Radiomics focuses on feature extraction, including image acquisition, segmentation, and analysis. It shows significant promise in oncology for tumor analysis, neurology for brain tumors and neurodegenerative diseases, as well as in cardiovascular and liver disease imaging. Despite its potential, challenges like standardization, data quality, and interpretability hinder clinical adoption. Future directions involve integrating radiomics with multi-omics data, advancing AI and deep learning, and moving towards clinical application. Radiomics is poised to enhance diagnosis and treatment, improving patient care across various diseases.

Keywords: Radiomics, medical imaging, quantitative data, diagnosis, prognosis
Mathematics Subject Classification [2010]: 13D45, 39B42

1 Introduction

Radiomics is an innovative field that extracts a large number of quantitative features from medical images using advanced computational algorithms. By converting images into high-dimensional data, radiomics facilitates the discovery of patterns and correlations that are invisible to the human eye. This review discusses the principles, applications, challenges, and future directions of radiomics, highlighting its transformative potential in various medical domains.

1.1 Principles of Radiomics

1.1.1 Feature Extraction

Feature extraction is the foundation of radiomics. It involves the following steps:

Image Acquisition: High-quality images are acquired from modalities such as CT, MRI, PET, and ultrasound.

Segmentation: Regions of interest (ROIs) are delineated, either manually or using automated algorithms.

Feature Calculation: Quantitative features are extracted, categorized into:

- First-order statistics: Describing the distribution of voxel intensities (e.g., mean, standard deviation).
- Shape features: Characterizing the geometry of the ROI (e.g., volume, surface area).

[1] corresponding author

- Texture features: Capturing the spatial arrangement of voxel intensities (e.g., Gray-Level Co-occurrence Matrix [GLCM]).
- Wavelet features: Decomposing the image into multiple frequency components.

1.1.2 Data Processing and Analysis

Once features are extracted, they undergo several processing steps, including normalization, feature selection, and machine learning modeling. These steps help in reducing dimensionality and improving the robustness and interpretability of the models.

1.2 Applications of Radiomics

1.2.1 Oncology

- Tumor Characterization Radiomics has shown immense potential in oncology for tumor characterization. Studies have demonstrated that radiomic features can differentiate between benign and malignant tumors, as well as between different tumor grades and histological subtypes [1]. For example, radiomic analysis of lung cancer CT images can predict histological subtypes and genetic mutations such as EGFR and KRAS [2].
- Prognosis and Treatment Response Radiomics can also predict patient prognosis and response to treatment. Pre-treatment imaging features have been correlated with overall survival, disease-free survival, and response to therapies in various cancers [3]. In breast cancer, radiomics combined with machine learning algorithms has been used to predict response to neoadjuvant chemotherapy [4].

1.2.2 Neurology

- Brain Tumors In neuroimaging, radiomics aids in the characterization and prognosis of brain tumors. MRI-based radiomic features can distinguish between different types of brain tumors and grades, as well as predict genetic mutations such as IDH status in gliomas [5]. Radiomics can also predict treatment response and survival outcomes in patients with brain tumors [6].
- Neurodegenerative Diseases Radiomics is being explored for diagnosing and monitoring neurodegenerative diseases. For instance, radiomic features from MRI scans have been used to differentiate between Alzheimer's disease and other types of dementia, as well as to predict disease progression [7].

1.2.3 Cardiovascular Imaging

Radiomics provides valuable insights into cardiovascular diseases. Radiomic features from CT and MRI can assess plaque characteristics in coronary artery disease, predict the risk of adverse cardiac events, and evaluate myocardial tissue properties in conditions like cardiomyopathy [8].

1.2.4 Liver Disease

In liver disease, radiomics is used for diagnosing and managing conditions such as non-alcoholic fatty liver disease (NAFLD) and hepatocellular carcinoma (HCC). Radiomic features from CT and MRI can grade liver fibrosis, differentiate between benign and malignant liver lesions, and predict patient outcomes [9].

1.3 Challenges in Radiomics

1.3.1 Standardization

Standardization is a significant challenge in radiomics. Variability in imaging protocols, feature extraction methods, and data processing steps can lead to inconsistent results. Standardized guidelines and protocols are necessary to ensure reproducibility and comparability of radiomic studies [10].

1.3.2 Data Quality and Quantity

High-quality imaging data and large datasets are crucial for robust radiomic models. Ensuring data quality and obtaining large, annotated datasets can be challenging due to privacy concerns and the labor-intensive nature of manual annotations [11].

1.3.3 Interpretability

Complex machine learning models used in radiomics can be difficult to interpret. Enhancing the interpretability of these models is essential for clinical adoption. Techniques such as feature importance analysis and visualization tools can help in understanding model predictions [12].

2 Main results

Future directions in radiomics include integrating radiomic data with other omics data, such as genomics and proteomics, to provide a comprehensive understanding of disease biology and enhance predictive modeling. This multi-omics approach holds significant potential for advancing personalized medicine by offering deeper insights into the molecular underpinnings of diseases. Additionally, advancements in artificial intelligence (AI) and deep learning are poised to revolutionize radiomics. AI can automate the feature extraction process, improving the accuracy and robustness of models, while deep learning techniques can uncover novel features that traditional methods might miss, further enhancing the predictive power of radiomics.
Efforts are also focused on translating radiomic research into clinical practice. This involves the development of user-friendly software tools, validation of radiomic models through large, multi-center studies, and the creation of clinical implementation guidelines. These steps are crucial for ensuring that radiomic advancements can be effectively and safely utilized in clinical settings. Radiomics represents a significant leap in medical imaging, with applications in oncology, neurology, cardiovascular imaging, and liver disease. Despite existing challenges, ongoing research and technological progress are expected to overcome these barriers, ultimately realizing the full potential of radiomics to improve patient care.

References

[1] HJ. Aerts , ER. Velazquez, RT. Leijenaar, C. Parmar, P. Grossmann, S. Carvalho, J. Bussink, R. Monshouwer, B. Haibe-Kains, D. Rietwld, F. Hoebers, MM. Rietbergen, CR. Leemans, A. Dekker, J. Quackenbush, RJ. Gillis, P. Lambin, *Decoding tumour phenotype by noninvasive imaging using a quantitative radiomics approach*, Nature Communications, 5, 4006 (2014). DOI: 10.1038/ncomms5006

[2] ER. Velazquez, C. Parmar, Y. Liu, TP. Coroller, G. Cruz, O. Stringfield, Z. Ye, M. Makrigiorgos, F. Fennessy, RH. Mak, R. Gillies, J. Quackenbush, HJW. Aerts, *Somatic Mutations Drive Distinct Imaging Phenotypes in Lung Cancer*, Scientific Reports, 7, 5477 (2017).Cancer Res, Jul 15;77(14):3922-3930. DOI: 10.1158/0008-5472.CAN-17-0122.

[3] P. Lambin, ER. Velazquez, R. Leijenaar, S. Carvalho, RGPM. Stiphout, P. Granton, CML. Zegers, R. Gillies, R. Boellard, A. Dekker, HJ. Aerts, *Radiomics: Extracting more information from medical images using advanced feature analysis*, European Journal of Cancer, 48(4), 441-446. DOI: 10.1016/j.ejca.2011.11.036.

[4] JY. Lee, K. Lee, B.K. Seo, K.R Cho, OH. Woo, SE. Song, EK. Kim, HY. Lee, JS. Kim, J. Cha, *Radiomic machine learning for predicting prognostic biomarkers and molecular subtypes of breast cancer using tumor heterogeneity and angiogenesis properties on MRI*, Eur Radiol, 32, 650–660 (2022). DOI: 10.1007/s00330-021-08146-8.

[5] F. Zheng, L. Zhang, H. Chen, Y. Zang, X. Chen, Y. Li, *Radiomics for predicting MGMT status in cerebral glioblastoma: comparison of different MRI sequences*, Journal of Radiation Research, 65, 3, 350–359(2024) DOI: 10.1093/jrr/rrae007.

[6] TC. Booth, M. Williams, A. Luis, J. Cardoso, K. Ashkan, H. Shuaib, *Machine Learning and Glioma Imaging Biomarkers*,Clin Radiol, 75, 1, 20-32(2020) DOI: 10.1016/j.crad.2019.07.001.

[7] JJ. Lee, M. McGue, WG. Iacono, AM. Michael, CF. Chabris,*The causal influence of brain size on human intelligence: Evidence from within-family phenotypic associations and GWAS modeling*, intelligence, 75, 48-58(2019) DOI: 10.1016/j.intell.2019.01.011.

[8] M. Kolossváry, J. Karády, B. Szilveszter, P. Kitslaar, U. Hoffmann, B. Merkely, P. Maurovich-Horvat, *Radiomic features are superior to conventional quantitative computed tomographic metrics to identify coronary plaques with napkin-ring sign*, Circulation: Cardiovascular Imaging, 10(12), e006843 (2017) DOI: 10.1161/CIRCIMAGING.117.00684.

[9] WK. Jeong, N. Jamshidi, ER. Felker, SS. Raman, DS. Lu, *Radiomics and radiogenomics of primary liver cancers*, Clin Mol Hepatol. 25(1):21-29, (2019). DOI: 10.3350/cmh.2018.1007.

[10] FA. Shaikh, BJ. Kolowitz, O. Awan, HJ. Aerts, A. Reden, S. Halabi, SA. Mohiuddin, S. Malik, RB. Shrestha and C. Deible,*Technical Challenges in the Clinical Application of Radiomics*, JCO Clin Cancer Inform 1, 1-8(2017) DOI:10.1200/CCI.17.00004.

[11] RJ. Gillies, PE. Kinahan and H. Hricak,*Radiomics: Images Are More than Pictures, They Are Data*, Radiology, 278(2) 563-77(2016). DOI: 10.1148/radiol.2015151169.

[12] A. Hosny, C. Parmar, J. Quackenbush, LH. Schwartz, HJ. Aerts, *Artificial intelligence in radiology*, Nat Rev Cancer, 18(8):500-510(2018) DOI: 10.1038/s41568-018-0016-5.

[13] YB. Xi, F. Guo, ZL. Xu, C. Li, W. Wei, P. Tian, TT. Liu, L. Liu, G. Chen, J. Ye, G. Cheng, LB. Cui, HJ. Zhang, W. Qin and H. Yin, *Radiomics signature: A potential biomarker for the prediction of MGMT promoter methylation in glioblastoma*, J Magn Reson Imaging. 47(5):1380-1387(2018). DOI: 10.1002/jmri.25860.

[14] A. Defeudis, C. De Mattia, F. Rizzetto, F. Calderoni, S. Mazzetti, A. Torresin, A. Vanzulli, D. Regge and V. Giannini, *Standardization of CT radiomics features for multi-center analysis: impact of software settings and parameters*, Phys Med Biol., 29;65(19):195012 (2020) DOI: 10.1088/1361-6560/ab9f61.

[15] A. Zwanenburg, M. Vallières, MA. Abdalah,HJWL. Aerts, V. Andrearczyk, A. Apte, S. Ashrafinia, S Bakas, RJ. Beukinga, R. Boellaard, M Bogowicz, L. Boldrini, I. Buvat,GJR. Cook, C. Davatzikos, A. Depeursinge, MC. Desseroit, N. Dinapoli, CV. Dinh, S. Echegaray, I. El Naqa, AY. Fedorov, R. Gatta, RJ. Gillies, V. Goh, M. Götz, M. Guckenberger, SM. Ha, M. Hatt, F. Isensee, P. Lambin, S. Leger, RTH. Leijenaar, J. Lenkowicz, F. Lippert, A. Losnegård, KH. Maier-Hein, O. Morin, H. Müller, S. Napel, C. Nioche, F. Orlhac, S. Pati, EAG. Pfaehler, A. Rahmim, AUK. Rao, J. Scherer, MM. Siddique, NM. Sijtsema, J. Socarras Fernandez, E Spezi, RJHM. Steenbakkers, S. Tanadini-Lang, D. Thorwarth, EGC. Troost, T. Upadhaya, V. Valentini, LV. van Dijk, J. van Griethuysen, FHP. van Velden, P. Whybra, C. Richter and S. Löck, *The Image Biomarker Standardization Initiative: Standardized Quantitative Radiomics for High-Throughput Image-based Phenotyping. Radiology*, 295(2):328-338 (2020) DOI: 10.1148/radiol.2020191145.

Email: `kosar.tarvirdizade@gmail.com`

Deep Learning Model to Diagnose Diabetic Retinopathy

Kosar Tarvirdizadeh[1]
Faculty of Medicine, Tabriz University of Medical Science, Tabriz, Iran

Mahsa Tarvirdizadeh
Department of Computer Engineering, University of Daneshvaran, Tabriz, Iran.

Habib Izadkhah
Department of Computer Science, Faculty of Mathematics, Statistics, and Computer Science, University of Tabriz, Tabriz, Iran.

Abstract

Diabetic retinopathy (DR) is the leading cause of preventable blindness among adults aged 2074. Major organizations recommend regular screenings every 12 to 24 months for patients with minimal or no DR. However, the rising prevalence of diabetes challenges the efficiency of these screening programs. To improve efficiency, screenings could be tailored based on the likelihood of DR development or progression. This study introduces a deep learning model using EfficientNet-B2 to classify DR images into five stages: no DR, mild DR, moderate DR, severe DR, and PDR. The model is trained on a dataset of 35,126 images and evaluated using accuracy and confusion matrix analysis. Two-stage testing is performed with learning rates of 0.001 and 0.0001. The model achieves a maximum validation accuracy of 0.8131 and 0.8019, and test accuracy of 0.8176 and 0.8030 in the first and second stages, respectively.

Keywords: Diabetic retinopathy, Deep Learning, Convolutional neural network

Mathematics Subject Classification [2010]: 13D45, 39B42

1 Introduction

Diabetic retinopathy (DR) is a severe complication of diabetes that can cause blindness if not detected early. It damages the retina's blood vessels and has two stages: non-proliferative (NPDR) and proliferative (PDR). NPDR, the early stage, involves microaneurysms (MAs), hemorrhages (HEMs), and exudates (EXs). If untreated, it can progress to PDR, which presents with severe retinal abnormalities. Early diagnosis is crucial to prevent vision loss, but manual diagnosis by ophthalmologists is time-consuming, costly, and prone to errors. Severe NPDR presents with widespread retinal abnormalities (Fig. 1).

Deep learning (DL), particularly convolutional neural networks, has become a popular and efficient technique for medical image analysis and classification, providing significant improvements in DR detection [1].

Biomedical imaging and computer-aided systems are essential for visualizing internal organs and diagnosing conditions like DR. The prevalence of diabetes and DR is rising globally, with an estimated increase in diabetic individuals from 463 million in 2019 to 700 million by 2045. Early detection methods, including image preprocessing and machine learning (ML) techniques such as support vector machine (SVM) and K-nearest neighbors (KNN), are critical. Recent advancements in DL and image processing have led to

[1]Speaker

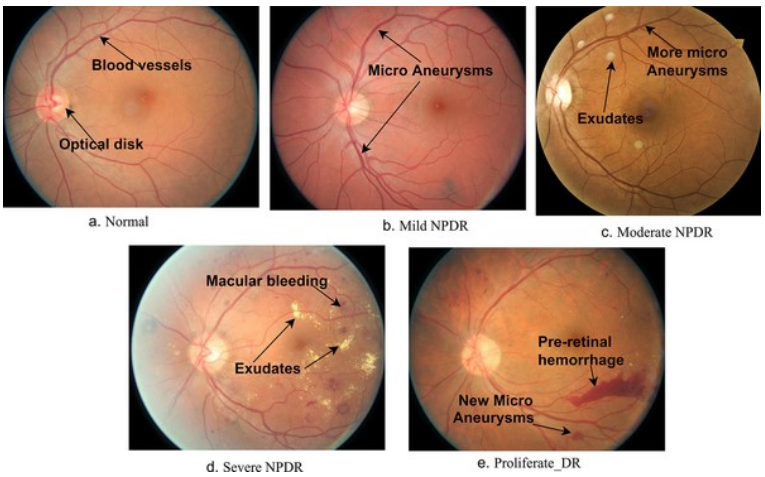

Figure 1: Different stages of DR: (a) no DR, (b) mild, (c) moderate, (d) severe, and (e) PDR.

more effective and efficient DR detection methods, reducing the burden on ophthalmologists and improving patient outcomes [2].

Diabetic patients often require hospital care for vision issues like PDR or vitreous hemorrhage. Early detection with retinal ophthalmoscopy and deep DL techniques improves diagnosis and treatment accuracy, achieving 70-85% accuracy comparable to clinical methods. However, unbalanced datasets, such as those in the 2015 EyePACS Kaggle competition, pose challenges for DL models [3]. CNNs dominate DR classification using architectures like AlexNet, Inception-v3, and ResNet for feature extraction and classification. Image preprocessing techniques improve quality and address class imbalances, including noise removal, normalization, and augmentation. Standard datasets like DIARETDB1, E-ophtha, and DRIVE aid training, using metrics such as accuracy, sensitivity, specificity, and AUC to enhance DR detection efficiency [4]. Studies automate DR lesion detection and classification using DL. Notable results include K. Xu et al. achieving 94.5% accuracy [5] in binary classification and G. Quellec et al. reporting high AUCs [6]. R. Pires et al. achieved a 98.2% AUC on Messidor-2 [7], and H. Jiang et al. reached 88.21% accuracy with pre-trained models [8]. In multi-level classification, V. Gulshan et al. [9] achieved 93% specificity using Inception-v3, while M. Abramoff et al. [10] combined CNNs with IDX-DR for a 0.98 AUC. H. Pratt et al. [11] classified DR into five stages with 75% accuracy and 95% specificity, and Wan S. et al. [12] fine-tuned VggNet-s to 95.68% accuracy. Lesion-based classification focused on specific DR lesions. J. Orlando et al. [13] used a custom CNN for red lesions, achieving a CPM of 0.4874, while P. Chudzik et al. [14] detected microaneurysms with a custom CNN, achieving an ROC score of 0.355. Adem K. et al. [15] achieved high accuracies for exudate detection. Vessel-based classification involved extracting retinal blood vessels. Vengalil S.K. et al. [16] used a modified CNN, achieving 93.94% accuracy and an AUC of 0.894 on HRF, while Oliveira A. et al. [17] achieved high accuracies for retinal vessel segmentation. Cam-Hao et al. [18] used ResNet-101 for vessel extraction, achieving 95.1% accuracy and an AUC of 0.9732 on the DRIVE dataset. Bhimavarapu et al. [19] introduced an improved activation function, achieving 99.41% accuracy with ResNet-152 on a Kaggle dataset.

This study utilized pre-trained models for diabetic retinopathy detection, leveraging: High-resolution images captured under diverse imaging conditions; and Pandas for converting trainLabels into a series and using get-dummies to encode categorical data stored in Numpy arrays.

2 Main results

In this study, pre-trained models like VGG16, ResNet18, and EfficientNet were compared, with EfficientNet-B2 ultimately selected. The model was trained and validated using transfer learning to leverage knowledge from related domains, reducing the need for extensive data labeling. EfficientNet, developed by Tan and Le, scales CNNs uniformly across width, depth, and resolution, offering better classification accuracy with

fewer parameters. The research used a public Kaggle dataset containing 35,126 images divided into five classes. The dataset was split into 60% for training, 20% for testing, and 20% for validation, and stored on Google Drive for easy access. Data Augmentation: Images were normalized and resized to 224224 pixels for compatibility with pre-trained CNN architectures. To prevent overfitting and enhance training, data augmentation was applied, including random rotations (0-180 degrees), horizontal flips, and vertical flips. Model Construction: Transfer learning was employed using the EfficientNet-B2 model to save time and improve performance by leveraging pre-learned patterns. The model was implemented and trained in Python using the PyTorch library, which provides flexibility, control, and efficient GPU processing. Due to hardware limitations, all stages of the study were conducted on Google Colaboratory, which offers free GPU resources. Data Preparation: The dataset, stored on Google Drive, was split into folders for training, validation, and testing. Labels were automatically assigned by PyTorch based on folder names (0 to 4), eliminating the need for additional labeling. Images were categorized as normal (0), mild (1), moderate (2), severe (3), and proliferative DR (4). Parameter and Hyperparameter Tuning:

- Batch Size: A batch size of 32 was used due to Google Colab's hardware constraints, balancing smooth learning with computational efficiency.
- Loss Function: CrossEntropyLoss was employed for its effectiveness in optimizing deep learning models by computing the logarithms of expected output samples.
- Optimization Algorithm: The Adam optimizer was chosen for its adaptive learning rates and quick convergence, crucial for minimizing loss functions.
- Learning Rate: The default learning rate of 0.001 was used, alongside a comparative run at 0.0001 to assess model performance.
- Number of Epochs: Due to dataset size and Google Colab's execution limits, the model was trained for 15 epochs.
- Model Implementation: The EfficientNet-B2 model was used with transfer learning. The final linear layer was adjusted to match the study's classification needs (5 classes).

Model performance was evaluated using accuracy and confusion matrix metrics, providing a quick assessment of model training and overall performance.

In this study, a dataset of 35,126 images across all five stages of diabetic retinopathy was used, split into 60% training, 20% testing, and 20% validation. The EfficientNet-B2 model was trained with the Adam optimizer, using learning rates of 0.001 and 0.0001, and a batch size of 32. The best validation accuracy was saved after each epoch, eliminating the need for early stopping. The highest validation accuracy was 0.8131 for a learning rate of 0.001 and 0.8019 for 0.0001. Test accuracy was 0.8176 and 0.8030, respectively. Confusion matrices showed that in the first run (0.001 learning rate), out of 3,871 test images, 3,792 were correctly classified, with 75 moderate and 4 high-risk images misclassified. For mild disease, 326 images were misclassified as normal, and for moderate disease, 419 were correctly identified. Severe disease saw 47 correctly classified images. Misclassifications included 18 normal, 22 moderate, and 18 severe images. The model converged better with a learning rate of 0.001 as shown in the accuracy and loss curves.

References

[1] R. F. Mansour. Evolutionary computing enriched computer-aided diagnosis system for diabetic retinopathy: a survey. IEEE Rev. Biomed. Eng. 10, 334349 (2017).

[2] Xu K, Feng D, Mi H. Deep convolutional neural network-based early automated detection of diabetic retinopathy using fundus image. Molecules. 22(12): 2054 (2017).

[3] Kaggle, Inc. Diabetic Retinopathy Detection. https://www.kaggle.com/c/diabetic-retinopathy-detection. Accessed 20 April 2020.

[4] W. Zhang, J. Zhong, S. Yang, Z. Gao, J. Hu, Y. Chen. Automated identification and grading system of diabetic retinopathy using deep neural networks. Knowl Base Syst. 175:1225 (2019).

[5] K. Xu, D. Feng, H. Mi. Deep convolutional neural network-based early automated detection of diabetic retinopathy using fundus image. Molecules. 22(12): 2054 (2017).

[6] G. Quellec, K. Charriere, Y. Boudi, B. Cochener, M. Lamard. Deep image mining for diabetic retinopathy screening. Med Image Anal. 39:17893 (2017).

[7] R. Pires, S. Avila, J. Wainer, E. Valle, M.D. Abramoff, A. Rocha. A data-driven approach to referable diabetic retinopathy detection. Artif Intell Med. 96:93106 (2019).

[8] H. Jiang, K. Yang, M. Gao, D. Zhang, H. Ma, W. Qian. An interpretable ensemble deep learning model for diabetic retinopathy disease classification. In: 2019 41st Annual International conference of the IEEE engineering in medicine and biology society (EMBC). p. 20458 (2019).

[9] V. Gulshan, P. Lily. M. Coram, M.C. Stumpe, D. Wu, A. Narayanaswamy, S. Venugopalan, K. Winder, T. Madams, J. Cuadros, R. Kim, R. Raman, P.C. Nelson, J.L. Mega, D.R. Webster. Development and validation of a deep learning algorithm for detection of diabetic retinopathy in retinal fundus photographs. Am Med Assoc. 316:240210 (2016).

[10] . M.D. Abramoff, Y. Lou, A. Erginay, W. Clarida, R. Amelon, J.C. Folk, M. Niemeijer. Improved automated detection of diabetic retinopathy on a publicly available dataset through integration of deep learning. Investig Ophthalmol Vis Sci. 57(13):52006 (2016).

[11] H. Pratt, F. Coenen, D.M. Broadbent, S.P. Harding, Y. Zheng. Convolutional neural networks for diabetic retinopathy. Procedia Comput Sci. 90:2005 (2016).

[12] S. Wan, T. Liang, Y. Zhang. Deep convolutional neural networks for diabetic retinopathy detection by image classification. Comput Electr Eng. 72:27482 (2018).

[13] J.I. Orlando, E. Prokofyeva, M. del Fresno, M.B. Blaschko. An ensemble deep learning based approach for red lesion detection in fundus images. Comput Methods Progr Biomed. 153:11527 (2018).

[14] P. Chudzik, S. Majumdar, F. Caliva, B. Al-Diri, A. Hunter. Microaneurysm detection using fully convolutional neural networks. Comput Methods Progr Biomed. 158:18592 (2018).

[15] . K. Adem. Exudate detection for diabetic retinopathy with circular Hough transformation and convolutional neural networks. Expert Syst Appl. 114: 28995 (2018).

[16] S.K. Vengalil, N. Sinha, S.S.S. Kruthiventi, R.V. Babu. Customizing CNNs for blood vessel segmentation from fundus images. In: International Conference on signal Processing and communications, SPCOM 2016. p. 14 (2016).

[17] A. Oliveira, S. Pereira, C.A. Silva. Retinal vessel segmentation based on fully convolutional neural networks. Expert Syst Appl. 112:22942 (2018).

[18] C.H. Hua, T. Huynh-The, S. Lee. Retinal vessel segmentation using round-wise features aggregation on bracket-shaped convolutional neural networks. In: Proceedings of the annual International Conference of the IEEE Engineering in Medicine and biology society, EMBS. p. 369 (2019).

[19] U. Bhimavarapu, G. Battineni. Deep Learning for the Detection and Classification of Diabetic Retinopathy with an Improved Activation Function. Healthcare (Basel).11(1):97 (2022). doi: 10.3390/healthcare11010097. PMID: 36611557; PMCID: PMC9819317.

Email: kosartarvirdizade@gmail.com
Email: izadkhah@tabrizu.ac.ir

A modification of synaptic learning rules in bio-inspired spiking neural networks

Tavangarian, Fatemeh[1]
Department of Mathematics, Malek Ashtar University of Technology, Shahin Shahr, Isfahan, Iran

Roohani Ghehsareh, Hadi
Department of Mathematics, Malek Ashtar University of Technology, Shahin Shahr, Isfahan, Iran

Abstract

Spiking Neural Networks, drawing inspiration from the neurological system, represent the third generation of neural networks. These networks employ biological inspired neuron models to carry out computations. Neurons play a crucial role in the information processing and transmission within SNNs, as they are responsible for firing spikes. In the SNN's architecture, the firing of spikes process is mathematically modeled as a non-differentiable Heaviside step function, which will cause a significant challenge in the direct training of SNNs. The non-differentiability of the Heaviside step function is tackled by introducing the surrogate gradient (SG) learning approach. Within SG, the Heaviside step function is used for controlling spikes in the forward propagation process, while an alternative differentiable function is utilized for gradient calculation during backpropagation. In recent years, various techniques have been proposed to provide differentiable approximations of the spike firing mechanism. Nevertheless, the development of new models is still of interest. In the current work, a novel approach for mathematical modeling of the spike firing mechanism inspired by the behavior of biological neurons has been presented. The Oscillatory and Laguerre Gaussian functions are introduced to tackle non-differentiability of the Heaviside step function. The effectiveness of the approach compared to other conventional approaches has been shown by solving continuous and discrete regression problems.

Keywords: Spiking neural network, Surrogate gradient, Regression
Mathematics Subject Classification [2010]: 92B20

1 Introduction

The human brain is a remarkable computational system that efficiently performs complex tasks. Artificial neural networks (ANNs), which draw inspiration from this biological structure, have demonstrated significant success in tasks such as pattern recognition, image classification, and natural language processing. Despite their achievements, ANNs often utilize simplified neuron models that do not capture the temporal dynamics observed in biological neurons. This disparity between artificial and biological intelligence has led to a growing interest in exploring spiking neural networks (SNNs)[1].

SNNs are the third generation of neural networks, taking inspiration from biological neural systems. They incorporate the concept of time and utilize spiking neurons that communicate through discrete pulses rather than continuous activation values. This additional temporal dimension allows SNNs to potentially achieve higher computational efficiency and biological plausibility compared to ANN.

One of the most importent challenge in the SNN is process of learning. To overcome this challenge some approaches like Spike-Timing-Dependent Plasticity, ANN-to-SNN conversion, and Surrogate Gradient

[1]Speaker

Learning are often used [2]. Surrogate Gradient Learning involves the use of a surrogate, which is a continuous function, to estimate the spike function during the back propagation process of a neural network. This study introduce a the Oscillatory and Laguerre-Gaussian functions for this purpose.

Initially, the concept of spiking neural networks is expressed, and Subsequently, a challenge of surrogate gradient learning is discussed. After that, introduce a way to tackle this challenge. Lastly, the proposed approach is applied to solve the Continuous and Discontinuous regression problem.

2 Brain Inspired Neural Network

This section provides an overview of the spiking neural network by contrasting it with conventional neural networks. The fundamental unit of processing in both ANNs and SNNs is the artificial neuron. ANNs employ a static neuron model. Each neuron receives weighted inputs, an activation function apply on it and at last take single output. Common activation functions include Sigmoid, Rectified linear unit (ReLU), and Tanh. However, SNNs incorporate a more biologically realistic neuron model that captures the temporal dynamics of biological neurons. There are various spiking neuron models, the Leaky Integrate-and-Fire (LIF) neuron is a popular choice due to its simplicity and effectiveness[3] that can be mathematically expressed using a differential equation that governs the voltage dynamics as follows:

$$C\frac{dV(t)}{dt} = I(t) - \frac{V(t)}{R} \tag{1}$$

where V is the voltage across the cell membrane, R is the membrane resistance, $I(t)$ is input current and C is capacity. The model equation is valid for arbitrary time-dependent input until a threshold V_{th} is reached; thereafter the membrane potential is reset. The firing frequency (spike trains) looks like:

$$spk(V) = \begin{cases} 0 & V \leq V_{\text{th}} \\ 1 & V > V_{\text{th}} \end{cases} \tag{2}$$

Using a forward Euler finite difference method to approximate a neuron model as bellow:

$$V(t+1) = (1 - \frac{\Delta t}{RC}V(t)) + I(t) - spk(V(t+1)) \tag{3}$$

Data representation plays a crucial role in how information is processed within a neural network. ANNs typically represent data as real numbers. SNNs offer a more flexible approach to data coding. They can encode information in the timing and frequency of spikes. This allows SNNs to leverage the temporal dynamics of spiking activity for information processing. The ability to represent and process temporal information natively within the network structure is a key advantage of SNNs over traditional ANNs. There exist a many way for coding data to a serise of a spike like Rate coding, temporal coding, and lower triangular coding[4].

The process through which a neural network acquires and enhances its knowledge is known as the learning paradigm. The primary learning technique in artificial neural networks (ANNs) is backpropagation.

Backpropagation has proven to be a powerful and effective approach for training deep ANNs. However, it cannot be directly used for spiking neural networks (SNNs) due to the non-differentiable nature of the spiking mechanism. In Figure (1), artificial networks are compared with spiking neural networks.

3 Learning paradigm

In this section, the mathematical model of SNN and the mentioned challenge in backpropagation will be discussed and in the following, additional information explains why backpropagation is not used, and an alternative approach involving surrogate gradients will be presented.

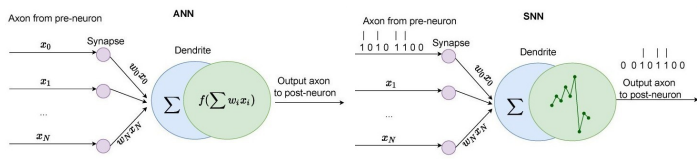

(a) (b)

Figure 1: (a) Artifitual neural network(b) Spiking neural network

3.1 Surrogate Gradient Learning

Backpropagation enables an ANN to learn by continuously adjusting the weights between neurons based on the disparity between the network's predicted output and the desired output (error). The error is then propagated backward through the network, layer by layer. Backpropagation relies on the chain rule of calculus to compute gradients, which are used to update the weights of the network during the learning process. However, the chain rule assumes that all functions involved in the computation are differentiable. In contrast, the spiking neural network model discussed previously operates using binary events called spikes. These spikes represent the firing of neurons and are not continuous in nature. As a result, the operations performed by the network are inherently discontinuous.

A L-layer spiking neural network is a mathematical function, f defined as:

$$\begin{aligned} &\mathbf{x}^{(0)} = \text{Spike trains}, \quad I_l = \mathbf{w}^{(l)} x^{(l-1)} + b^{(l)}, l = 1 \cdots L \\ &f(x, \theta) = \text{LIF} \circ I_L \circ \text{LIF} \cdots \text{LIF} \circ I_1(x^{(0)}) \end{aligned} \tag{4}$$

where $\{I_i\}_{i=1}^{L}$ is linear function and it means input current.

To train the network effectively, it is imperative to adjust the weights of the network. This can be achieved by derivation of the error concerning the network's parameters. If we consider the error of a spiking neural network as $\mathcal{L} = \sum_{\text{Data}} (f(x, \theta) - label)^2$, the weight update process can be demonstrated for a one hidden layer network, as below:

$$\frac{\partial \mathcal{L}}{\partial \mathbf{w}} = \sum_{\text{Data}} 2 \frac{\partial (f(x, \theta))}{\partial \mathbf{w}} = \sum_{\text{Data}} 2 \frac{\partial (\text{LIF} \circ I)}{\partial \mathbf{w}} = \sum_{\text{Data}} 2 \frac{\partial spk}{\partial V} \frac{\partial V}{\partial I(t)} \frac{\partial I(t)}{\partial \mathbf{w}} \tag{5}$$

The partial derivative $\frac{\partial spk}{\partial V}$ can be represented as the Dirac delta function. This implies that the weight is not update correctly. To address this issue, researchers have developed alternative methods for training spiking neural networks [5]. These methods often involve approximations or modifications to the backpropagation algorithm to handle the discontinuities caused by spikes.

3.2 Neural Learnning

In general, the derivative of the arc tangent and sigmoid functions is often used to approximate the Dirac function, as depicted in Figure (2-a). However, in this article, we aim to introduce alternative functions that closely resemble the actual neuron model.

By observing the process of spike production in the neuron, it becomes that an electric current enters the neuron to reach a threshold, resulting in the generation of a spike and a subsequent decrease in potential value. This decreases the membrane potential value to be lower than the initial value (rest value). This work introduces the alternative model, Laguerre-Gaussian (6), and Oscillatory radial (7) Functions inspired by the real behavior of membrane potential changes over tim. As shown in Figure (2-c), the functions also take negative values, which is similar to decreasing the potential below the initial value.

$$La(x) = (3/2 - |x|^2) \exp(-|x|^2) \tag{6}$$

$$Os(x) = (1 - x)_+^{12} (1 + 1x - 104x^2) \tag{7}$$

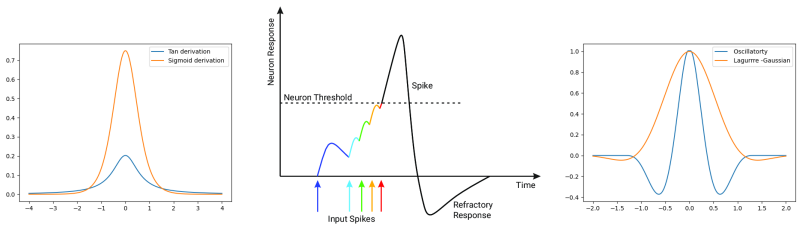

(a) (b) (c)

Figure 2: (a) derivative of the arc tangent and sigmoid functions (b) memberance potential in real neuron (c) Oscillatory and a Lagurre -Gaussian function

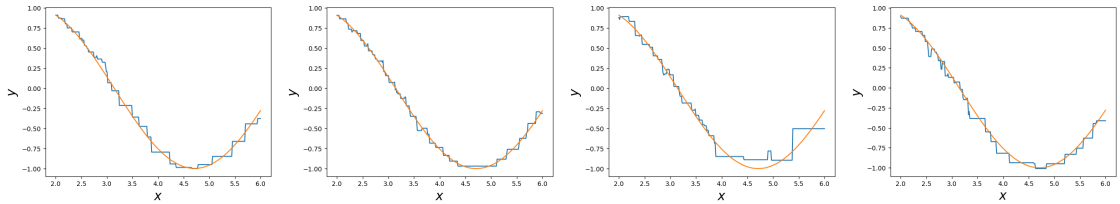

(a) (b) (c) (d)

Figure 3: The original function and the function estimated by(a)Lagurre -Gaussian function (b) Oscillatory function (c) derivation of arctangent functions (d)derivation of sigmoid functions

4 Regression with Spiking Neural Network

ANNs are primarily employed for computing the regression function, whereas spiking neural networks hold less significance owing to their discrete characteristics. Kahana et al. investigate the use of spiking neural networks for regression tasks and introduce a new coding approach[5].

In the upcoming section, we will introduce a spiking neural network. After that, we will examine two regression issues, one continuous and one discrete. We will apply various spike estimation techniques to these problems and then analyze and compare the outcomes.

A regression function is estimated using a 3-layer spiking neural network consisting of 60 neurons. The training of the spiking neural network involves the utilization of 300 randomly selected points$\{(x_i, y(x_i))\}_{i=1}^{300}$. To address this problem, the approach employed involves the implementation of the most basic form of coding and decoding, as illustrated below.

$$x \xrightarrow{\text{Coding}} \underbrace{[x, x, \cdots, x]}_{T}$$

$$[V_1^L, V_2^L, \cdots, V_T^L] \xrightarrow{\text{Decoding}} \frac{\sum_{i=1}^{T} V_i}{T} \sim f(x, \theta)$$

Such that V_i^L is the membrane potential at time step i of the last layer L, and T denotes the number of training spikes. The cost function used to train the spiking neural network assesses the difference between the expected and actual values as $\mathcal{L} = \sum_x (y(x) - f(x, \theta))^2$.

In the following, two examples of function approximation using spiking neural networks are given, and the results are compared.

Continuous function

In this section, we select the labeled points from $sin(x)$ such that $x \in [2, 6]$. The results of running the SNN with different estimates are depicted in Figure 3, and the errors of different runs are showcased in Table 1.

In Table 1, the residual for regression using the Laguerre-Gaussian function is lower compared to the others. However, the root-mean-square deviation error when using the Oscillatory function is similar to that of the Laguerre-Gaussian function. Based on the results, the regression problem's solution for estimation

Estimation Rule	Lagurre -Gaussian	Oscillatory	derivation of arctangent	derivation of sigmoid
Residual	1.14e-02	1.10e-03	5.97e-03	2.88e-03
RMSD error	0.005300	0.00267861	0.023290	0.0230253

Table 1: Results from implementing the spiking neural network using different spike derivative estimates

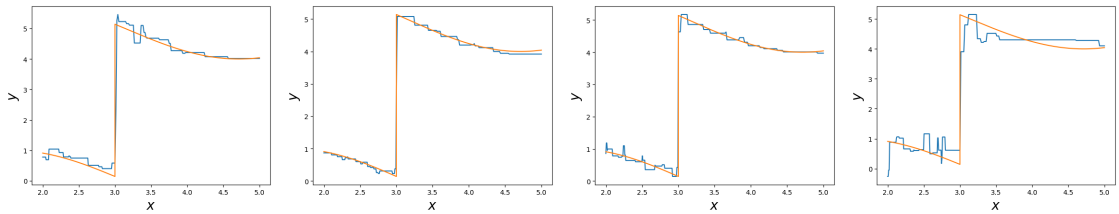

(a) (b) (c) (d)

Figure 4: The original function and the function estimated by (a)Lagurre -Gaussian function (b) Oscillatory function (c) derivation of arctangent functions (d)derivation of sigmoid functions

is better when using both Oscillatory and Laguerre-Gaussian functions compared to using arctangent and sigmoid derivative functions.

Discontinuous function

In this section, we aim to estimate a specific function 8 using the same spiking neural network. The results of the spiking neural network implementation are displayed in Figure 4.

$$y(x) = \begin{cases} sin(x) & x \in [2,3] \\ sin(x) + 5 & x \in (3,5] \end{cases} \tag{8}$$

As depicted in Figure 4 , the results obtained from the approximation using the oscillatory function yield better outcomes.

References

[1] Shiva Subbulakshmi Radhakrishnan, Amritanand Sebastian, Aaryan Oberoi, Sarbashis Das, and Saptarshi Das, *A biomimetic neural encoder for spiking neural network*, Nature communications, 12(1):2143, 2021.

[2] Schmidgall, Samuel and Ziaei, Rojin and Achterberg, Jascha and Kirsch, Louis and Hajiseyedrazi, S. Pardis and Eshraghian, Jason, *Brain-inspired learning in artificial neural networks: A review* APL Machine Learning 2,2024

[3] L.F Abbott, *Lapicque's introduction of the integrate-and-fire model neuron (1907)*, Brain Research Bulletin, 50(5):303–304, 1999

[4] Wenzhe Guo, Mohammed E. Fouda, Ahmed M. Eltawil, and Khaled Nabil Salama, *Neural coding in spiking neural networks: A comparative study for robust neuromorphic systems*, Frontiers in Neuroscience, 15, 2021

[5] Adar Kahana, Qian Zhang, Leonard Gleyzer, and George Em Karniadakis, *Spiking neural operators for scientific machine learning.*, arXiv preprint arXiv:2205.10130, 2022.

Email: `tavangarian15@gmail.com`
Email: `hadiroohani61@gmail.com`

Pretreatment of Food Industry Wastewater by Coagulation: Process Modeling and Optimization using by artificial intelligence

Zaki, GholamReza[1]
University of Tabriz

Irandoust-Pakchin, Safar
University of Tabriz

A. Jodayree Akbarfam
University of Tabriz

Abstract

In this article, the coagulation process in food industry effluents has been investigated. Coagulation processes using $FeCl_3 6H_2O$ and $Al_2(SO_4)_3 18H_2O$ as coagulants were employed and designed for chemical oxygen demand (COD) and total suspended solids (TSS) removal from food industry wastewater. We have used two types of artificial neural networks to model the performance of these two coagulants. Radial basis networks ($\mathfrak{Net}_{rb}$) and generalized regression neural networks ($\mathfrak{Net}_{grnn}$). Numerical results showed that the performance of networks $\mathfrak{Net}_{rb}$ and $\mathfrak{Net}_{grnn}$ was much better than feed-forward networks ($\mathfrak{Net}_{ff}$). After modeling, with the help of collective intelligence such as genetic algorithm (GA), we find the optimal values of these coagulants. Comparison of numerical results with other common methods such as response surface methodology (RSM) shows the superiority of the proposed method.

Keywords: genetic algorithm, artificial neural network, Coagulation, chemical oxygen demand, total suspended solids

AMS Mathematical Subject Classification [2010]: 13D45, 39B42

1 Introduction

Food industry wastewaters mainly contain leavenings, carbohydrate, organic and inorganic salts, oil and grease, cleaning products and proteins which are difficult to treat by conventional physicochemical pretreatment applications [2]. Conventional biological processes applied for the treatment of these wastewaters are insufficient to meet discharge standards in many countries and new treatment methods are needed [3]. Thus, researchers have recommended addition of chemical coagulants for treatment of these wastewaters[4, 5]. Moreover, coagulation process was used as a pretreatment application in the treatment of various food industry wastewaters. $Al_2(SO_4)_3$ was used as coagulant to treat wastewaters from instant coffee and coffee products [6] and table olive processing [7] while $FeCl_3$ was applied in the pretreatment of vegetable processing [8] and table olive processing [7] wastewaters.

[1]G. R. Zaki

Coagulation processes using $FeCl_3 6H_2O$ and $Al_2(SO_4)_3 18H_2O$ as coagulants were employed and designed for chemical oxygen demand (COD) and total suspended solids (TSS) removal from food industry wastewater.

2 Main results

In [1], the performance of each of the two coagulants $Al_2(SO_4)_3 18H_2O$ and $FeCl_3 6H_2O$ is modeled as a three-variable function using the least squares method as below

$$\begin{aligned} COD_A(x,y,z) &= 5.6875 + 3.375x - 0.0003y + 0.075z - 0.1875x^2 + 0.00025xy - 0.0xz \\ &\quad + 0.0000022y^2 - 0.00005yz - 0.002z^2. \end{aligned} \tag{1}$$

$$\begin{aligned} COD_F(x,y,z) &= 22.0125 + 4.7063x - 0.01805y - 1.57875z - 0.44375x^2 \\ &\quad + 0.001675xy + 0.06xz + 0.0000058y^2 + 0.000565yz + 0.02275z^2. \end{aligned} \tag{2}$$

$$\begin{aligned} TSS_A(x,y,z) &= 55.65 + 3.81458x - 0.00681667y + 0.22625z - 0.151042x^2 \\ &\quad + 0.00015xy + 0.00375xz + 0.0000112833y^2 - 0.00043yz + 0.0174583z^2. \end{aligned} \tag{3}$$

$$\begin{aligned} TSS_F(x,y,z) &= 37.9875 + 12.8875x - 0.11125y + 4.605z - 0.6875x^2 \\ &\quad - 0.001xy + 0.16xz + 0.000057y^2 - 0.00028yz - 0.0855z^2. \end{aligned} \tag{4}$$

where subscript A stands for coagulant $Al_2(SO_4)_3 18H_2O$ and and subscript F stands for coagulant $FeCl_3 6H_2O$. Variable x shows the pH value, variable y the Dosage (mg/L) and variable z the reaction time. The above functions are derived from the following experimental data using the least squares method. Each of the

Table 1: Input variables $X = (x, y, z)$

x	5	9	5	9	5	9	5	9	7	7	7	7	7	7	7
y	500	500	1500	1500	1000	1000	1000	1000	500	1500	500	1500	1000	1000	1000
z	15	15	15	15	5	5	25	25	5	5	25	25	15	15	15

Table 2: Output variables $Y_F = (COD_F, TSS_F)$ for $FeCl_3 6H_2O$

COD_F	19.7	22.4	27.1	38.6	26.4	28.2	28.2	34.8	28.2	37.7	21.9	42.7	28.2	28.7	29.8
TSS_F	85.9	87.2	87.5	92.8	49.7	67.7	69.5	74.7	70.1	82.8	85.1	92.2	72.7	80.1	77.3

Table 3: Output variables $Y_A = (COD_A, TSS_A)$ for $Al_2(SO_4)_3 18H_2O$

COD_A	19.7	22.4	27.1	30.8	20.8	25.6	22.9	27.7	22.9	27.7	22.9	28.7	25.0	24.5	26.1
TSS_A	77.0	82.8	84.8	91.2	76.5	85.5	80.1	89.4	72.8	89.7	87.2	95.5	80.4	81.6	83.2

above functions calculates a value by receiving a three-dimensional vector. For better results, we suggest neural networks that receive a 3D vector and calculate a 2D vector. In this way, two values COD and TSS are calculated together. In this case, unlike the above models, the optimal points of the model maximize both output variables. Table (4) and Table (5), compares the results obtained from the radial base neural network ($\mathfrak{Net}_{rb}$) and the generalized regression neural network ($\mathfrak{Net}_{grnn}$) with the measured data as well as the results obtained from formulas (1)-(4). Also, figures 1 to 4 show these comparisons. Tables 6 and 7 show the optimal points and optimal values of both coagulandts based on the proposed methods and the

method presented in [1]. Although the method presented in [1] has found better optimal values, it should be noted that this method optimizes the function for only one of the values (COD and TSS), and the optimal point of one may not be the optimal point of the other.

Table 4: $FeCl_3 6H_2O$

x	y	z	COD	TSS	COD_{rb}	TSS_{rb}	COD_{grnn}	TSS_{grnn}	COD_{lse}	TSS_{lse}
5	500	15	21.9	85.9	21.9	85.9	21.9	85.9	21.238	82.25
9	500	15	22.9	87.2	22.9	87.2	22.9	87.2	22.162	87.7
5	1500	15	30.9	87.5	30.9	87.5	30.9	87.5	31.637	87
9	1500	15	38.6	92.8	38.6	92.8	38.6	92.8	39.262	96.45
5	1000	5	26.4	49.7	26.4	49.7	26.4	49.7	27.575	52.075
9	1000	5	28.2	67.7	28.2	67.7	28.2	67.7	29.45	65.925
5	1000	25	28.2	69.5	28.2	69.5	28.2	69.5	26.95	71.275
9	1000	25	34.8	74.7	34.8	74.7	34.8	74.7	33.625	72.325
7	500	5	28.2	70.1	28.2	70.1	28.2	70.1	27.688	71.375
7	1500	5	37.7	82.8	37.7	82.8	37.7	82.8	35.788	80.925
7	500	25	21.9	85.1	21.9	85.1	21.9	85.1	23.813	86.975
7	1500	25	42.7	92.2	42.7	92.2	42.7	92.2	43.213	90.925
7	1000	15	28.2	72.7	28.9	76.7	28.9	76.7	28.9	76.7
7	1000	15	28.7	80.1	28.9	76.7	28.9	76.7	28.9	76.7
7	1000	15	29.8	77.3	28.9	76.7	28.9	76.7	28.9	76.7

Table 5: $Al_2(SO_4)_3 18H_2O$

x	y	z	COD	TSS	COD_{rb}	TSS_{rb}	COD_{grnn}	TSS_{grnn}	COD_{lse}	TSS_{lse}
5	500	15	19.7	77	21.74	77.84	19.7	77	19.95	75.112
9	500	15	22.4	82.8	21.74	77.84	22.4	82.8	23.45	82.437
5	1500	15	27.1	84.8	27.1	84.8	27.1	84.8	26.05	85.162
9	1500	15	30.8	91.2	30.8	91.2	30.8	91.2	30.55	93.087
5	1000	5	20.8	76.5	21.74	77.84	20.8	76.5	21.6	75.675
9	1000	5	25.6	85.5	25.6	85.5	25.6	85.5	25.6	83.15
5	1000	25	22.9	80.1	21.74	77.84	22.9	80.1	22.9	82.45
9	1000	25	27.7	89.4	27.7	89.4	27.7	89.4	26.9	90.225
7	500	5	22.9	72.8	21.74	77.84	22.9	72.8	21.85	75.512
7	1500	5	27.7	89.7	27.7	89.7	27.7	89.7	27.95	90.162
7	500	25	22.9	87.2	22.9	87.2	22.9	87.2	22.65	86.737
7	1500	25	28.7	95.5	28.7	95.5	28.7	95.5	29.75	92.787
7	1000	15	25	80.4	25.2	81.733	25.2	81.733	25.2	81.733
7	1000	15	24.5	81.6	25.2	81.733	25.2	81.733	25.2	81.733
7	1000	15	26.1	83.2	25.2	81.733	25.2	81.733	25.2	81.733

Table 6: $Al_2(SO_4)_3 18H_2O$

	COD	COD_{rb}	COD_{grnn}	TSS	TSS_{rb}	TSS_{grnn}
x	9	7	6.1764	9	7	6.1764
y	1493	1000	1327.8	1000	21.74	1327.8
z	25	15	22.47	25	15	22.479
$Remov$	31.2	25.2	28.7	96.2	81.733	95.5

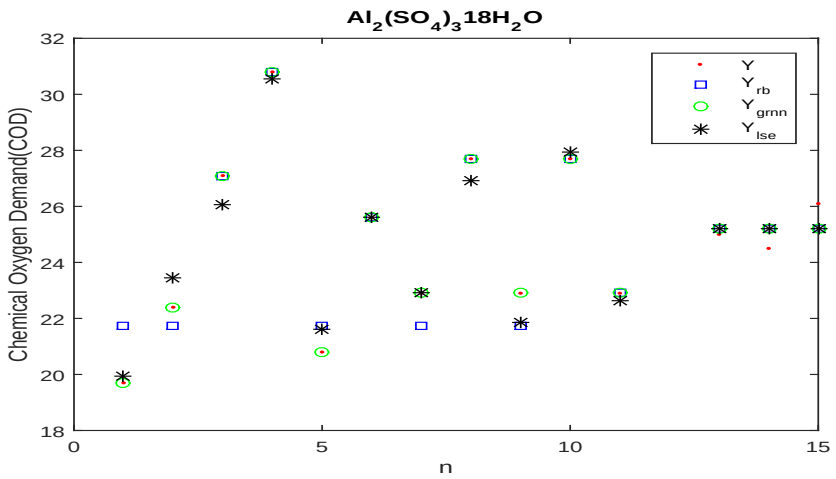

Figure 1: Comparing the measured values Y with the values obtained from the proposed models(Y_{rb} and Y_{grnn}) and the model given in [1] (Y_{lse}) for COD when using the $Al_2(SO_4)_3 18H_2O$ as a coagulant.

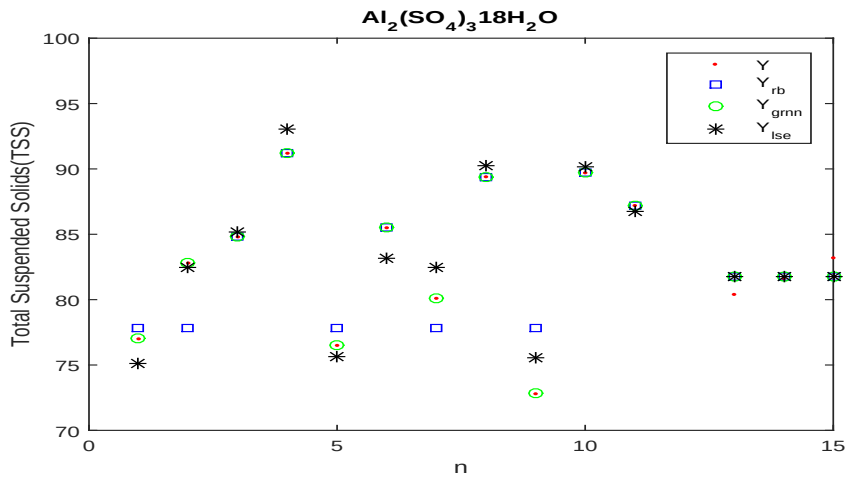

Figure 2: Comparing the measured values Y with the values obtained from the proposed models(Y_{rb} and Y_{grnn}) and the model given in [1](Y_{lse}) for TSS when using the $Al_2(SO_4)_3 18H_2O$ as a coagulant.

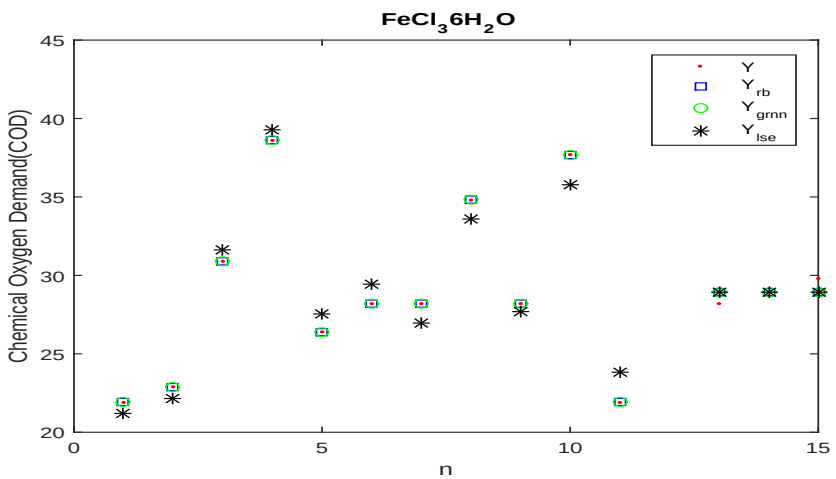

Figure 3: Comparing the measured values Y with the values obtained from the proposed models(Y_{rb} and Y_{grnn}) and the model given in [1] (Y_{lse}) for COD when using the $FeCl_3 6H_2O$ as a coagulant.

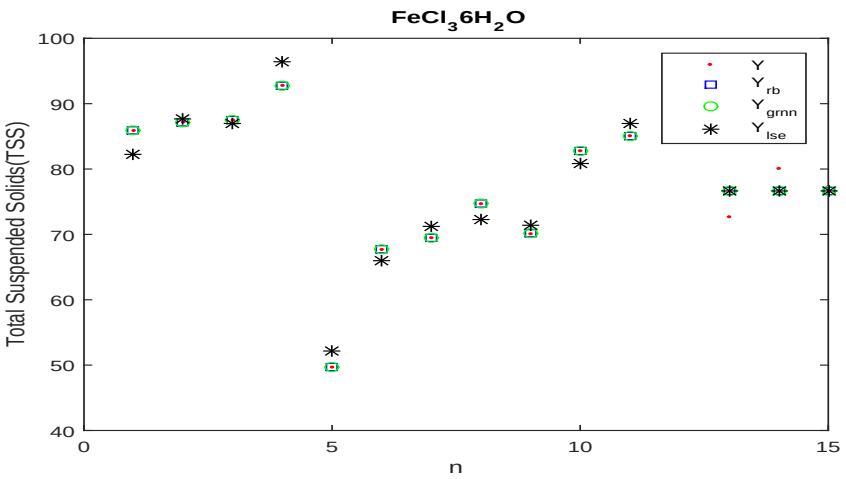

Figure 4: Comparing the measured values Y with the values obtained from the proposed models(Y_{rb} and Y_{grnn}) and the model given in [1](Y_{lse}) for TSS when using the $FeCl_3 6H_2O$ as a coagulant.

Table 7: $FeCl_3 6H_2O$

	COD	COD_{rb}	COD_{grnn}	TSS	TSS_{rb}	TSS_{grnn}
x	9	5.0001	7.5727	8.5	5.0001	7.5727
y	1500	500	1405.2	1500	500	1405.2
z	25	15	24.074	16.5	15	24.074
$Remov$	46.4	21.9	28.7	96.7	85.9	92.2

3 Conclusion

In this article, neural networks were used to model the behavior of two types of coagulants. Models $\mathfrak{Net}_{rb}$ and $\mathfrak{Net}_{grnn}$ performed much better compared to the models presented in [1]. It is clear that using a more accurate model to find the optimal values will give more reliable results. In addition, the proposed models optimize for both outputs COD and TSS together. For optimization, we use the genetic algorithm(GA).

References

[1] S. Y. Güvenç, E. C. Güven, *Pretreatment of Food Industry Wastewater by Coagulation: Process Modeling and Optimization*, Celal Bayar University Journal of Science, Volume 15, Issue 3,(2019), p 307-316. Doi: 10.18466/cbayarfbe.581611.

[2] P. Silva, T. P. Salazar, V. C. Meza, J. R. Morales, G. C. Cruz, *Physicochemical and biological combined treatment applied to a food industry wastewater for reuse*, Journal of Environmental Science and Health - Part A Toxic/Hazardous Substances and Environmental Engineering; (2009) 44(1): 108–115.

[3] Varank, G, Yazici Guvenc, S, Demir, A. 2018. *A comparative study of electrocoagulation and electro-Fenton for food industry wastewater treatment*: Multiple response optimization and cost analysis. Separation Science and Technology (Philadelphia); 53(17): 2727–2740.

[4] Beltran de Heredia, J, Dominguez, JR, Lopez, R. 2004. *Treatment of cork process wastewater by a successive chemical- physical method*, Journal of Agricultural and Food Chemistry; 52(14): 4501–4507.

[5] Minhalma, M, De Pinho, MN. 2001. *Flocculation/flotation/ultrafiltration integrated process for the treatment of cork processing wastewaters*, Environmental Science and Technology; 35(24): 4916–4921.

[6] Can, OT, Gengec, E, Kobya, M. 2019. *TOC and COD removal from instant coffee and coffee products production wastewater by chemical coagulation assisted electrooxidation*, Journal of Water Process Engineering; 28: 28–35.

[7] Ozbey-Unal, B, Balcik-Canbolat, C, Dizge, N, Keskinler, B. 2018. *Treatability studies on optimizing coagulant type and dosage in combined coagulation/membrane processes for table olive processing wastewater*, Journal of Water Process Engineering; 26: 301–307.

[8] Weng, SC, Jacangelo, JG, Schwab, KJ. 2019. *Sustainable practice for the food industry: assessment of selected treatment options for reclamation of washwater from vegetable processing*, International Journal of Environmental Science and Technology; 16(3): 1369–1378.

e-mail: GhRezaZaki@gmail.com
e-mail: s.irandoust@tabrizu.ac.ir
e-mail: akbarfam@tabrizu.ac.ir

دینامیک عملکرد بطن چپ قلب

۱ محدثه ابراهیمی و ۲ حسین خیری

چکیده. در این مقاله، هدف اصلی، بررسی دینامیک قلب به عنوان یک ارگان اصلی بدن است. ریاضیات می‌تواند برای فهم بهتر مکانیسم حرکت نقاط آناتومیکال بطن چپ قلب و مسیر حرکت آنها به کار گرفته شود. اندیس‌های بسیار مهم(از نظر بالینی) قلبی از جمله استرین، سرعت و نیرو سگمان‌های بطن چپ فرمول‌بندی شده‌اند. در پیرو این بیان براساس داده‌ها و تصاویر اکوکاردیوگرافی، حرکت و تغییر شکل نقاط آناتومیکال قلب بررسی می‌شود. سپس با استفاده از معادلات اویلر ـ لاگرانژ، مسیر حرکت بهینه هر نقطه آناتومیکال، به دست آورده شده است.

کلمات کلیدی: استرین، نیرو، معادله اویلر ـ لاگرانژ.

۱. مقدمه

قلب به عنوان ارگانی حیاتی در بدن انسان، وظیفه پمپاژ و گردش خون را بر عهده دارد. مطالعه مکانیسم قلب، ساختار، حرکت آن حین تپیدن و خونرسانی به سایر اعضای دیگر بدن بسیار حائز اهمیت است. امروزه تصاویر قلب و حفرات آن، مخصوصا بطن چپ که مهمترین حفره قلبی است توسط امواج فراصوتی بدست می‌آیند[۱، ۲]. معادلات و تکنیک‌های ریاضی، اطلاعات بسیار مهم قابل دسترس و ارزشمندی برای شناخت حرکت و تغییر شکل میوکارد بطن چپ ارائه می‌دهند. دستگاه‌های اکوکاردیوگرافی با استفاده از پروپ‌های مخصوص متصل به آن، امواج فراصوتی را با فرکانس‌های مختلف بطور پیوسته به سوی یک قسمت انتخابی ازعضله میوکارد بطن چپ منتشر می‌کنند. یکی از مسائل اصلی در این مقاله، معرفی، فرموله و محاسبه کردن اندیس‌های استرین و نیرویی که منجر به حرکت و استرین می‌شود، است[۳، ۴]. سپس هدف اصلی، ردیابی هر سگمان عضلانی میوکارد بطن چپ در حین یک دوره کامل قلب سالم است. بدین معنا که دریابیم هر نقطه آناتومیکال روی چه منحنی‌ایی حرکت می‌کند. بدین منظور با در نظر گرفتن لاگرانژین(اختلاف انرژی‌های پتانسیل و جنبشی) هر نقطه در حال حرکت در زمان، طبق قانون لاگرانژ که بیان می‌کند مسیر حرکت یک ذره، منحنی‌ای است که مقدار مجموع یا انتگرال لاگرانژین حرکت آن نقطه دریک بازه زمانی باید کمترین مقدار باشد. الگوریتم‌های طراحی شده برای محاسبات مقادیر استرین و نیرو و نمایش همزمان بردارهای متناظر نقاط آناتومیکال دلخواه هر سگمان بطن چپ و حل معادلات لاگرانژ اشاره شده، بصورت دستورات کامپیوتری کد شده‌اند و در نرم‌افزار متلب قابل اجرا هستند.

۲. دینامیک بطن چپ قلب

در این بخش سعی می‌کنیم عملکرد قلب را با استفاده از معادلات ریاضی بدست بیاوریم. برای این منظور، ابتدا معرفی و فرمول‌بندی اندیس‌های زیر الزامی است.

۱.۲. **استرین.** اگر J_{n,t_n}، فاصله بین iامین نقطه از اولین فریم تا nامین فریم باشد که یک فاصله خطی است، مقدار استرین نقطه p در زمان t_n با نمادگذاري ε به صورت

$$\varepsilon(p,t_n)=\sum_{k=1}^{n-1}\frac{(J_{k+1,t_{k+1}}-J_{k,\,t_k})}{J_{k,\,t_k}} \tag{۱.۲}$$

است. در شکل‌هاي ۱و۲ مقادير استرين(مثبت و منفي) و بردارهاي مربوطه، چند نقطه آناتوميكال انتخابی دلخواه در بطن چپ نشان داده شده است.

۲.۲. **سرعت.** بردارهای سرعت به عنوان مقادیر استرین محاسبه شده، کشیده می‌شوند. بنابراین حرکت و تغییر شکل به طور همزمان در نظر گرفته می‌شود. در شکل ۱ بردارها و مقادیر عددي سرعت در چند نقطه آناتوميكال بطن چپ نشان داده شده است.

رده بندی موضوعی۲۰۱۰: $93A30$، $35Q79$.

سخنران: محدثه ابراهیمی .

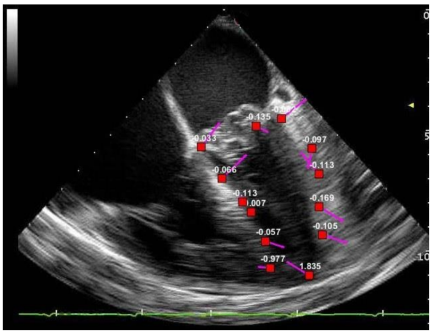

شکل ۱: مقادیر عددی و بردارهای استرین با رنگ کد شده‌اند(رنگ قرمز مقادیر منفی را نشان می‌دهد).

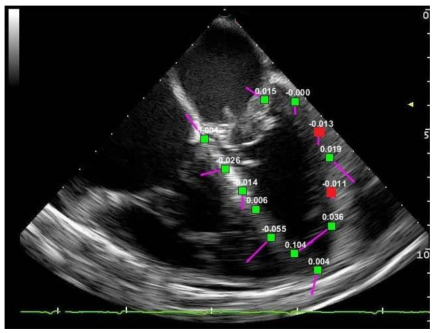

شکل ۲: مقادیر عددی و بردارهای استرین با رنگ کد شده‌اند(رنگ سبز مقادیر مثبت را نشان می‌دهد).

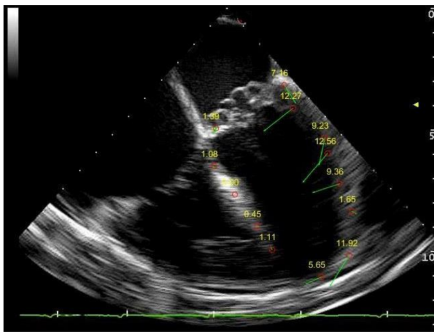

شکل ۳: سرعت‌های برداری به همراه مقادیر عددی(mm/s) در طول یک دوره قلبی با نقاط هندسی ترکیب می‌شوند.

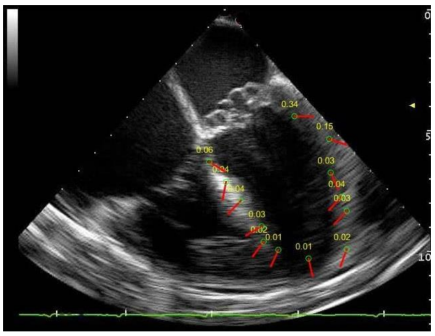

شکل ۴: بردارهای نیرو و مقادیر عددی آنها(میلی‌متر نیوتن)

۳.۲. **نیرو.** اندیس‌های نیرو براساس پارامترهای حرکت و تغییر شکل استخراج شده، فرموله و محاسبه می‌شوند(شکل ۳و۴). فرمول نیرو براساس سرعت، جابجایی، استرین و نرخ استرین به صورت زیر است:

$$f(p,n,d_n(p),v(p,n,t),\varepsilon(p,n,t_n),\varepsilon'(p,n,t_n),t_n) = \frac{2d_n(p)}{(t_n)^2} + 2\varepsilon'(p,n,t_n).[\frac{(\varepsilon(p,n,t_n)+1)d_0(p)}{t_n}] - \frac{2v(p,n,t)}{t_n} \tag{۲.۲}$$

که p همان نقطه هندسی متناظر با نقطه آناتومیکال انتخاب شده روی عضله قلبی است،
$d_n(p)$ جابجایی نقطه p در nامین فریم،
$v(p,n.t)$ سرعت نقطه p در همان فریم،
$\varepsilon(p,n,t_n)$ استرین و $\varepsilon'(p,n,t_n)$ نرخ استرین در nامین فریم هستند.
نیروی کلی نقطه p در هر دوره قلبی از حاصل جمع رابطه(۲.۲) به دست می‌آید:

$$F(P) = \sum f = \sum\{\frac{2d_n(p)}{(t_n)^2} + 2\varepsilon'(p,n,t_n) \times [\frac{(\varepsilon(p,n,t_n)+1)d_0(p)}{t_n}] - \frac{2v(p,n,t)}{t_n}\}.$$

پارامترهای مکانیکی وارد معادلات اویلر ـ لاگرانژ می‌شوند که براساس اندیس‌های استرین و مشتق اول سرعت، دوباره فرمول‌بندی می‌شوند.

۳. الگوریتم

یک نقطه هندسی$p = (p_1, p_2)$، به یک نقطه آناتومیکال در یک سگمان قلب متناظر می‌شود که p_i مختصات آن نقطه در فضای اقلیدسی دو بعدی است. نقطه p را می‌توان با دو متغیر Γ_{lp} و τ_{lp} توصیف کرد که به ترتیب تغییر شکل و حرکت در امتداد رشته عضلانی l_p را که از نقطه p عبور می‌کند، نشان می‌دهد. Γ_{lp} را می‌توان در نقطه p به شکل زیر نشان داد:

$$\Gamma_{l_p} = \sum_{1\leq i,j\leq 2} \varepsilon_{(p,i,j,l_p)} P_i P_j.$$

مولفه‌های استرین در جهات مختلف هستند که براساس مجموعه داده‌های اکوکاردیوگرافی$\varepsilon_{(p,i,j,l_p)}$ استخراج و محاسبه شده‌اند. پارامتر نیرو را در طول زمان در نقطه p می‌توان با معادله دیفرانسیل جزئی

$$F_{l_p}(p,t) := \frac{\partial(\Gamma_{l_p}\tau_{l_p})}{\partial S_{l_p}},$$

فرمول‌بندی کرد.
بردارهای سرعت از جابجایی τ_{lp} مشتق گرفته و محاسبه می‌شوند. بردارهای سرعت به صورت قدرمطلق Γ_{lp} کشیده می‌شوند(Γ_{lp} به‌عنوان مقدار استرین کلی متناظر با سگمان قلبی در امتداد رشته عضلانی l_P محاسبه می‌شود). بنابراین اندیس نیرو محاسبه و در پوشه خروجی الگوریتم ذخیره می‌شود.
گام بعدی، طراحی معادلات برای یافتن مسیر سگمان قلبی با استفاده از معادلات اویلر_لاگرانژ است. فرمول‌بندی مجدد سیستم معادلات بر اساس مجموعه داده‌های اکوکاردیوگرافی مهم، است. معادله اویلر_لاگرانژ برای یک سگمان قلبی دو بعدی(نقطه p) با فرمول‌بندی مجدد زیر بر اساس مجموعه داده‌های به دست آمده توصیف می‌شود:

$$\begin{aligned}&L(p,\dot{p},\varepsilon_p,\dot{\varepsilon}_p,t) = T(p,\dot{p},\varepsilon_p,\dot{\varepsilon}_p,t) - U(p,\dot{p},\varepsilon_p,\dot{\varepsilon}_p,t) = \\ &\frac{1}{2}\rho[\delta A_{p,n}(t_n) + p_1 p_2]\dot{p}^2 - \frac{1}{2}(\sum_{l_{p,r}\in l_p^*}(\sum_{1\leq i,j\leq 2}\varepsilon_{(p,i,j,l_{p,r})}(t)P_iP_j))p^2.\end{aligned}$$

l_p، مجموعه تمام رشته‌های عضلانی است که از نقطه ... عبور می‌کنند، $\delta A_p(t)$ تغییر مساحت نقطه p از اولین فریم به nامین فریم در زمان t_n است و $\delta A_{p,n}(t_n)$ دترمینان ماتریس استرین تعمیم‌یافته است:

$$\begin{pmatrix}\varepsilon_{p,1} & \varepsilon_{p,2}\\ \varepsilon_{p,3} & \varepsilon_{p,4}\end{pmatrix}.$$

با بازنویسی داده‌های جدید در معادلات لاگرانژی تعمیم‌یافته داریم:

$$\begin{aligned}&\frac{\partial L(p,\dot{p},\varepsilon_p,\dot{\varepsilon}_p,t)}{\partial p} - \frac{d}{dt}(\frac{\partial L(p,\dot{p},\varepsilon_p,\dot{\varepsilon}_p,t)}{\partial \dot{p}}) = \sum_{l_{p,r}\in l_p^*} F_{l_p}(p,t) = \sum_{l_{p,r}\in l_p^*}\frac{\partial(\Gamma_{l_p}\tau_{l_p})}{\partial S_{l_p}}\\ &= F(p,n,d_n(p),v(p,n,t),\varepsilon(p,n,t_n),\varepsilon'(p,n,t_n),t_n).\end{aligned}$$

این الگوریتم می‌تواند معادلات لاگرانژی را با افزودن فرمول نیرو به سمت راست آنها بصورت:

$$\begin{aligned}&\frac{\partial L(p,\dot{p},\varepsilon_p,\dot{\varepsilon}_p,t)}{\partial p} - \frac{d}{dt}(\frac{\partial L(p,\dot{p},\varepsilon_p,\dot{\varepsilon}_p,t)}{\partial \dot{p}})\\ &= F(p,n,d_n(p),v(p,n,t),\varepsilon(p,n,t_n),\varepsilon'(p,n,t_n),t_n)\\ &= \sum\{\frac{2d_n(p)}{(t_n)^2} + 2\varepsilon'(p,n,t_n).[\frac{(\varepsilon(p,n,t_n)+1)d_0(p)}{t_n}] - \frac{2v(p,n,t)}{t_n}\},\end{aligned}$$

بازنویسی کند. با اعمال فرمول‌های انرژی جنبشی و پتانسیل سگمان قلبی p در سمت چپ معادلات لاگرانژ داریم:

$$\Big[\partial\Big[\frac{1}{2}p_1p_2+\frac{1}{2}\det\begin{pmatrix}\varepsilon_{p,1} & \varepsilon_{p,2}\\ \varepsilon_{p,3} & \varepsilon_{p,4}\end{pmatrix}\dot{p}^2-\frac{1}{2}Ap^2/\partial p\Big]$$
$$-d(\Big(\partial\Big[\frac{1}{2}\rho\Big(p_1p_2+\det\begin{pmatrix}\varepsilon_{p,1} & \varepsilon_{p,2}\\ \varepsilon_{p,3} & \varepsilon_{p,4}\end{pmatrix}\dot{p}^2-\frac{1}{2}Ap^2/\partial\dot{p}/dt\Big))$$
$$=\sum\left\{\frac{2d_n(p)}{t_n^2}+2\varepsilon'(p,n,t_n)\cdot\Big[\frac{(\varepsilon(p,n,t_n)+1)d_0(p)}{t_n}\Big]-\frac{2v(p,n,t)}{t_n}\right\}.$$

که در آن A بصورت

$$\sum_{\ell_{p,r}\in\ell^*}\sum_{1\leq i,j\leq 2}\varepsilon_{p,i,j,\ell_{p,r}}(t)\cdot p_i\cdot p_j$$

می‌باشد.

۴. نتیجه گیری

هدف این مقاله بررسی پویایی قلب، عضوی حیاتی در بدن انسان بوده است. با استفاده از تکنیک‌های ریاضی، توانسته‌ایم درک عمیق‌تری از مکانیسم‌های حرکتی و مسیرهای نقاط آناتومیکال در بطن چپ قلب به دست آوریم. این مطالعه بر چندین اندیس قلبی مهم از نظر بالینی، از جمله استرین، سرعت و نیروی سگمان‌های بطن چپ تمرکز داشته است. این اندیس‌ها برای ارائه ارزیابی جامع‌تری از عملکرد قلب فرموله شده‌اند. با استفاده از داده‌ها و تصاویر اکوکاردیوگرافی، حرکت و تغییر شکل نقاط آناتومیکال قلب بررسی شده‌اند. علاوه‌براین، در این مطالعه از معادلات اویلر ـ لاگرانژ برای تعیین مسیر حرکت بهینه هر نقطه آناتومیکال در قلب استفاده کرده‌ایم.

مراجع

[1] Keith L. Moore; Arthur F. Dalley; Anne M. R. Agur. "1". Clinically Oriented Anatomy. Wolters Kluwel Health Lippincott Williams & Wilkins. pp. 127–173. ISBN 978-1-60547-652-0.

[2] Reed, C. Roebuck; Brainerd, Lee Wherry; Lee,, Rodney; Inc, the staff of Kaplan, (2008). CSET: California Subject Examinations for Teachers (3rd ed. ed.). New York, NY: Kaplan Pub. p. 154. ISBN 978-1-4195-5281-6. Archived from the original on 6 October 2014. Retrieved 5 November 2015. cite book: |edition= has extra text (help).

[3] Abraham TP, Dimaano VL, Liang HY. Role of tissue Doppler and strain echocardiography in current clinical practice. Circulation 2007;116: 2597-609.

[4] Takigiku K, Takeuchi M, Izumi C, Yuda S, Sakata K, Ohte N, et al. Normal range of left ventricular 2-dimensional strain: Japanese Ultrasound Speckle Tracking of the Left Ventricle (JUSTICE) study, Circ J, 2012, vol. 76 (pg. 2623-32).

ایران ـ تبریز ـ دانشگاه تبریز ـ دانشکده ریاضی، آمار و علوم کامپیوتر
Email address: m.ebrahimi@tabrizu.ac.ir

ایران ـ تبریز ـ دانشگاه تبریز ـ دانشکده ریاضی، آمار و علوم کامپیوتر
Email address: h-kheiri@tabrizu.ac.ir

مدل سازي رياضي جريان خون پالسی در رگ با گرفتگی مخروطی

۱ احمدرضا حقیقی

چکیده. در این مقاله یک مدل ریاضی برای جریان خون پالسی و دوبعدی درطول سرخرگ مخروطی ارایه شده است. مشخصات جریان خون از معادله ساختاری میکروپلار ارینگن توصیف می شود. رگ شبیه سازی شده بصورت دو گرفتگی، مخروطی، وابسته به زمان و الاستیک فرض می شود. معادلات حاکم برجریان با اعمال یک نگاشت مناسب و با انتخاب شرایط اولیه و مرزی با استفاده از روش عددی تفاضلات متناهی حل شده است. مشخصه های اصلی جریان از جمله سرعت بی بعد محوری و چرخشی و دبی حجمی ومقاومت در برابر جریان بررسی می شود.

کلمات کلیدی: روش تفاضلات متناهی، رگ مخروطی، سیال میکروپلار، جریان خون

۱. مقدمه

یکی از شایع ترین بیماری های قلبی_ عروقی آترواسکلروز است که در اثر تجمع چربی در دیواره رگ بوجود می آید. حقیقی و شهبازی اصل [۱] شبیه سازی یک مدل دوبعدی و دولایه ای ازجریان خون ناپایدار درطول سرخرگ گرفته شده با استفاده از روش تفاضلات متناهی استفاده کردند، که در آن نوع گرفتگی هندسه نسبت به جهت محوری غیر متقارن و نسبت به جهت شعاعی متقارن در نظر گرفتند. سنکارو لی [۲] بافرض جریان خون بصورت سیال غیرنیوتونی یک مدل ریاضی برای جریان خون ارایه داده اند که جریان خون در این مطالعه بصورت پالسی و متقارن محور فرض شده است و معادلات حاکم از روش اختلال حل شده اند.

۲. فرمول بندی ریاضی

سیستم مختصات استوانه ای(r, θ, z) به ترتیب شعاع، زاویه و مختصات طول نقطه درراستای محور رگ رانشان می دهد. هندسه وابسته به زمان برای گرفتگی به صورت زیر می باشد. (شکل(1)) [۳] :

(۱.۲)

$$R(z,t) = \begin{cases} \Bigg[(mz+1) - \frac{\tau_m \cos(\theta)(z-d)}{l_0} \\ \quad \times \Big\{11 - \frac{94(z-d)}{3l_0} + \frac{32(z-d)^2}{l_0^2} - \frac{32(z-d)^3}{3l_0^3}\Big\}\Bigg] a_1(t), & d \le z \le d + \frac{3}{2}l_0 \\ (mz+1)a_1(t), & \text{O.W} \end{cases}$$

که در آن $m = tan(\psi)$، $R(z,t)$ شعاع رگ در ناحیه گرفتگی، a شعاع ثابت رگ قسمت باز رگ، ψ زاویه مخروطی وتابع وابسته به زمان $a_1(t)$ بصورت $a_1(t) = 1 + k_r cos(\omega t - \phi)$ می باشد، فرکانس زاویه ای ω بصورت $\omega = 2\pi f_b$ فرکانس پالسی و b یک ثابت است. معادلات بی بعد پیوستگی و مومنتوم برای جریان

رده بندی موضوعی۲۰۱۰: ۹۲B۰۵، ۹۲A۰۸ .
سخنران: احمدرضا حقیقی .

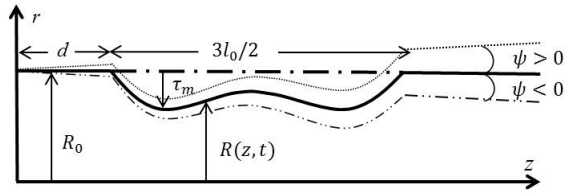

شکل ۱. هندسه ی گرفتگی

سیال تراکم ناپذیر میکروپلاردر سیستم استوانه ایی (r, θ, z) بصورت زیر است [۴]:

$$\frac{\partial u}{\partial t} + v\frac{\partial u}{\partial r} + u\frac{\partial u}{\partial z} = -\frac{\partial p}{\partial z} + \frac{1}{Re}\left(\frac{\partial^2 u}{\partial r^2} + \frac{1}{r}\frac{\partial u}{\partial r} + \frac{\partial^2 u}{\partial z^2}\right) + \frac{m}{Re}\left(\frac{\partial w}{\partial r} + \frac{w}{r}\right) \tag{۲.۲}$$

$$\frac{\partial v}{\partial t} + v\frac{\partial v}{\partial r} + u\frac{\partial v}{\partial z} = -\frac{\partial p}{\partial r} + \frac{1}{Re}\left(\frac{\partial^2 v}{\partial r^2} + \frac{1}{r}\frac{\partial v}{\partial r} + \frac{\partial^2 v}{\partial z^2} - \frac{v}{r^2}\right) + \frac{m}{Re}\left(\frac{\partial w}{\partial z}\right) \tag{۳.۲}$$

$$\begin{aligned}\frac{JM}{1-m}\left(\frac{\partial w}{\partial t} + v\frac{\partial w}{\partial r} + u\frac{\partial w}{\partial z}\right) = &-\frac{2N}{Re}w + \frac{N}{Re}\left(\frac{\partial v}{\partial z} - \frac{\partial u}{\partial r}\right) + \\ &\frac{1}{Re}\left(\frac{\partial^2 w}{\partial r^2} + \frac{1}{r}\frac{\partial w}{\partial r} + \frac{\partial^2 w}{\partial z^2} - \frac{w}{r^2}\right)\end{aligned} \tag{۴.۲}$$

$$\frac{\partial u}{\partial z} + \frac{\partial v}{\partial r} + \frac{v}{r} = 0, \tag{۵.۲}$$

شرایط مرزی بی بعد بصورت زیر می باشند:

$$\text{on } r = 0: \quad v(r,z,t) = w(r,z,t) = 0, \frac{\partial u(r,z,t)}{\partial r} = 0 \tag{۶.۲}$$

$$\text{on } r = R: \quad u(r,z,t) = 0, v(r,z,t) = \frac{\partial R}{\partial t}, w(r,z,t) = -\lambda\frac{\partial u}{\partial r}, 0 < \lambda < 1 \tag{۷.۲}$$

به منظور شبکه بندی کردن سرخرگ مفروض [۵]، ابتدا نگاشت $\xi = \frac{r}{R}$ روی معادلات حاکم بر جریان خون و شرایط مرزی و اولیه اعمال می شود. در نتیجه اعمال این نگاشت، دیواره رگ به صورت غیر الاستیک و ثابت تبدیل شده و سرخرگ گرفته شده به سرخرگ مستطیل شکل تبدیل شود تا بتوان شبکه تولید شده را روی سطح سرخرگ اعمال کرد. نتیجه اعمال نگاشت مفروض روی معادله پیوستگی و مومنتوم و شرایط مرزی بصورت زیر است:

$$\begin{aligned}\frac{\partial u}{\partial t} = &-\frac{\partial p}{\partial z} + \frac{1}{R}\frac{\partial u}{\partial \xi}\left[\xi\left(u\frac{\partial R}{\partial z} + \frac{\partial R}{\partial t}\right) - v\right] - u\frac{\partial u}{\partial z} + \frac{1}{Re}\left[\frac{1}{R^2}\left\{1 + (\xi\frac{\partial R}{\partial z})^2\right\}\right. \\ &\left.\frac{\partial^2 u}{\partial \xi^2} + \frac{1}{\xi R^2}\left\{1 + 2(\xi\frac{\partial R}{\partial z})^2 - \xi^2 R\frac{\partial^2 R}{\partial z^2}\right\}\frac{\partial u}{\partial \xi} + \frac{\partial^2 u}{\partial z^2}\right] + \frac{m}{Re}\left(\frac{1}{R}\frac{\partial w}{\partial \xi} + \frac{w}{\xi R}\right)\end{aligned} \tag{۸.۲}$$

$$\frac{\partial w}{\partial t} = \frac{1}{R}\frac{\partial w}{\partial \xi}\left[\xi\left(u\frac{\partial R}{\partial z} + \frac{\partial R}{\partial t}\right) - v\right] - u\frac{\partial w}{\partial z} + \frac{1-m}{MReJ}\left[N\left(-2w + \frac{\partial v}{\partial z} - \frac{\xi}{R}\frac{\partial R}{\partial z}\frac{\partial v}{\partial \xi} - \frac{1}{R}\frac{\partial u}{\partial \xi}\right) + \left\{\frac{1}{R^2}\left(1 + (\xi\frac{\partial R}{\partial z})^2\right)\frac{\partial^2 w}{\partial \xi^2} + \frac{1}{\xi R^2}\left\{1 + 2(\xi\frac{\partial R}{\partial z})^2 - \xi^2 R\frac{\partial^2 R}{\partial z^2}\right\}\frac{\partial w}{\partial \xi} + \frac{\partial^2 w}{\partial z^2} - \frac{w}{(\xi R)^2}\right\}\right] \tag{۹.۲}$$

$$\frac{1}{R}\frac{\partial v}{\partial \xi} + \frac{v}{\xi R} + \frac{\partial u}{\partial z} - \frac{\xi}{R}\frac{\partial R}{\partial z}\frac{\partial u}{\partial \xi} = 0 \tag{۱۰.۲}$$

$$\text{on } \xi = 0: \quad v(0,z,t) = 0, w(0,z,t) = 0, \frac{\partial u(0,z,t)}{\partial \xi} = 0 \tag{۱۱.۲}$$

$$\text{on } \xi = 1: \quad u(1,z,t) = 0, v(1,z,t) = \frac{\partial R}{\partial t}, w(1,z,t) = -\frac{\lambda}{R}\frac{\partial u}{\partial \xi} \tag{۱۲.۲}$$

برای محاسبه سرعت شعاعی از معادله پیوستگی استفاده می شود، برای بدست آوردن این پروفیل معادله (۱۰.۲) را در ξR ضرب کرده نسبت به ξ دربازه ی 0 تا ξ انتگرال گرفته می شود. برای محاسبه سرعت محوری و سرعت چرخشی از فرمول تفاضلات متناهی مرکزی برای تقریب مشتقات مکانی و فرمول تفاضلات متناهی پیشرو برای تقریب مشتق زمانی استفاده می شود. مقدار u در (ξ_j, z_i, t_k) توسط $u^k_{i,j}$ نشان داده می شود. بعد از محاسبه پروفیل سرعت، مقادیر بی بعد مربوط به دبی حجمی (Q) ومقاومت دربرابر جریان (Λ) به صورت زیر بدست می آید:

$$Q^k_i = 2\pi(R^k_i)^2\int_0^1 \xi_j(u)^k_{i,j}d\xi_j, \quad \Lambda^k_i = \frac{\left|L\left(\frac{\partial p}{\partial z}\right)^k_i\right|}{Q^k_i}. \tag{۱۳.۲}$$

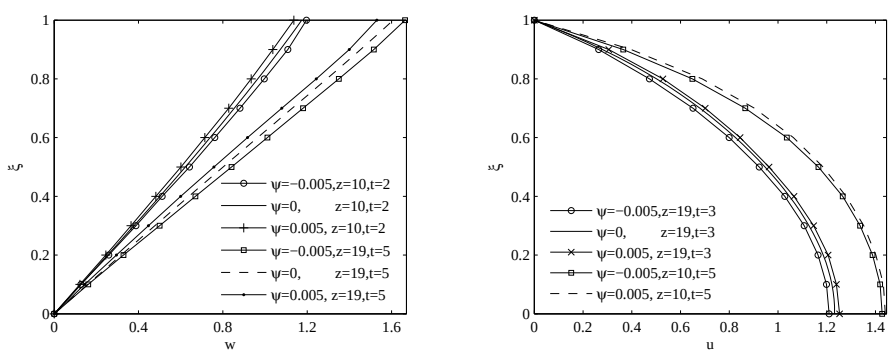

(ب) سرعت چرخشی میکروپلار بی بعد

(آ) سرعت محوری بی بعد

شکل ۲

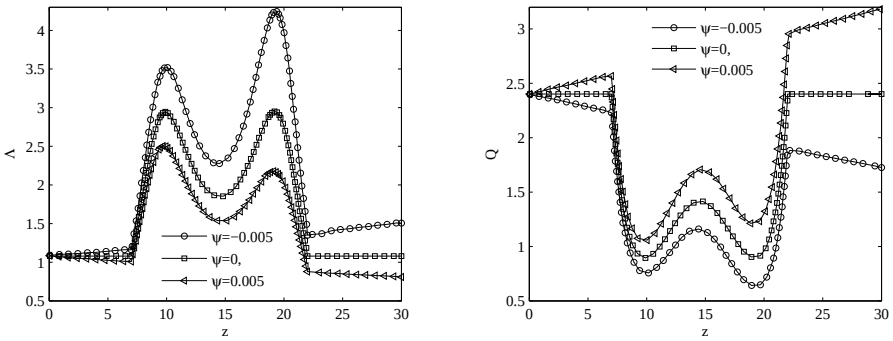

(آ) پروفیل دبی حجمی بی بعد

(ب) پروفیل مقاومت دربرابرجریان بی بعد

شکل ۳

۳. بحث های عددی

در نتایج عددی ارائه شده از پارامترهای زیر استفاده می کنیم:

$$\Delta t = 0.0001,\ \Delta\xi = 0.125,\ \Delta z = 0.1,\ L_1 = 15,\ Re = 300,\ A_0 = 0.1,\ A_1 = 0.2A_0,$$
$$k_r = 0.05, \phi = 0,\ f_p = 1.2,\ L = 30,\ N = 1,\ M = 1,\ m = 0.85,\ d = 7,\ R_0 = 1.52$$

با مشاهده ی شکل ۲ ـ آ می توان دید که مقدار سرعت محوری در رگ مخروطی منقبض شونده در مقایسه با رگ مخروطی منبسط شونده مقدار بالاتری دارد و منحنی رگ غیر مخروطی در بین آنها قرار دارد. سرعت چرخشی در راستای شعاع بی بعد در زمان $t = 3$ برای زوایای مخروطی مختلف در شکل ۲ ـ ب نشانگر این است که در رگ منقبض شونده در مقایسه با رگ مخروطی منبسط شونده مقدار بیشتری دارد. باتوجه به این نمودار برای هر نقطه و در هردو زمان با افزایش زاویه مخروطی کاهش می یابد. شکل ۳ ـ آ پروفیل دبی حجمی بی بعد را برای زوایای مختلف نشان می دهد. رفتار دبی حجمی مربوط به هندسه ی گرفتگی طوری است که در زمان شروع گرفتگی نرخ دبی حجمی کاهش یافته است ودر بیشتر نقطه ی گرفتگی به پایین ترین سطح خود می رسد. واضح است که دبی حجمی با افزایش زاویه مخروطی افزایش می یابد. مقاومت دربرابر جریان در رگ گرفته برای زوایای مخروطی مختلف در زمان های $t = 1$ درشکل ۳ ـ ب نشان داده شده است. دبی حجمی و مقاومت در برابر جریان رفتار عکس دارند. بنابراین برخلاف دبی حجمی در مقایسه با مقاومت دربرابرجریان با افزایش زاویه مخروطی کاهش می یابد.

۴. نتیجه گیری

در این مقاله یک شبیه سازی عددی برای جریان خون بی بعد ناپایدار پالسی در طول سرخرگ گرفته شده با استفاده از معادلات سیال میکروپلار ارینگن ارایه شده که حل عددی آن با استفاده از روش تفاضلات متناهی انجام شده است. نتایج نشان می دهند که رگ مخروطی ویژگی های جریان خون را به طور قابل توجهی مورد تاثیر قرار می دهد. مخروطی فرض شدن رگ یک عامل مهم در توسعه فشار است. با افزایش زاویه مخروطی سرعت محوری و دبی حجمی روند افزایشی دارند. با افزایش زاویه مخروطی سرعت چرخشی سیال میکروپلار و مقاومت دربرابر جریان کاهش می یابد. بیشترین مقدار دبی حجمی و مقاومت دربرابر جریان در نقطه ی اوج گرفتگی رخ داده است.

مراجع

[۱] حقیقی، احمدرضا، شهبازی اصل،محمد، *شبیه سازي عددي جريان خون غيردائم در طول سرخرگ الاستیک با گرفتگی غیرمتقارن*، انتشارات دانشگاه تربیت مدرس،تهران، ۱۳۹۳

[2] D. Sankar, U. Lee,, *Mathematical modeling of pulsatile flow of non- Newtonian fluid in stenosed arteries*, Communications in Nonlinear Science and Numerical Simulation, Vol. 14, No. 7, pp. 2971-2981, 2009 .

[3] S. Chakravarty and P. K. Mandal , *A nonlinear two-dimensional model of blood flow in an overlapping arterial stenosis subjected to body acceleration*, Math. Comput. Model. 24(1) (1996) 43–58.

[4] M. A. Ikbal, S. Chakravarty and P. K. Mandal , *Two-layered micropolar fluid flow through stenosed artery: Effect of peripheral layer thickness*, Comput. Math. Appl. 58(7) (2009) 1328–1339.

[5] M Fahim, M Sajid, N Ali ,Pulsatile pressure-driven non-Newtonian blood flow through a porous stenotic artery: A computational analysis, Numerical Heat Transfer, Part A: Applications,(2024) 1-21

عضو هیات علمی گروه ریاضی،دانشکده آمار،ریاضی و رایانه،دانشگاه علامه طباطبائی ـ تهران ـ ایران
Email address: ah.haghighi@gmail.com

بررسی انتشار آلاینده ناشی از نیروگاه حرارتی و گازی تبریز و آسیب های جبران ناپذیر آن

۱ قادر درخوشی و ۲ کریم ایواز

چکیده. امروزه گسترش شهر نشینی ،رشد جمعیت، صنعتی شدن، عدم ساماندهی سیستم حمل و نقل و ترافیک شهری و کمبود فضای سبز موجب افزایش غلظت آلودگی هوا در شهرها، بویژه شهرهای بزرگ شده است بر این اساس، توجه به مسئله آلودگی هوا و شناخت عواملی که موجب افزایش غلظت آلاینده ها می شوند از اهمیت زیادی برخوردار است در این پژوهش، با مدل های ریاضی حاکم بر قدیم انتشار آلاینده در هوا بررسی می شوند مدل مناسب را انتخاب کرده و شبیه سازی عددی را انجام می دهیم.

کلمات کلیدی: آلودگی هوا۱ ، معادله پخش و انتشار ۲ ، تفاضلات متناهی ۳.

۱. مقدمه

مدلهاي رياضی براي شبيه سازي پراكندگی آلودگی در هوا استفاده می شوند . اين نوع مدل سازي ميتواند به عنوان يک ابزار مناسب در كنترل آلودگی هوا، بررسی اثرات آلودگی هوا، مكانيابی كارخانجات آلاينده و برنامه ريزي و مديريت شهري بكار رود بيشتر مدلهاي انتشار آلودگی در هوا بر اساس حل تحليلی معادله انتقال - انتشار استوار هستند. در اين مدلها غلظت آلاينده بصورت تابعی با فرم بسته رياضی بر حسب ساير پارامترهاي مرتبط بيان می شوند، [۱] آلاینده های جوی پس از تخلیه از منابع مرتفع از سطح زمین مانند دودکش کارخانه ها، بوسیله جریان باد و نوسانات تلاطم هوا منتقل می شوند و توزیعی از غلظت آلاینده را در محیط اطراف ایجاد میکنند. بيشتر مدلهاي رايج پراكندگی آلودگی در هوا مدل هاي گوسی هستند. مدلهاي گوسی می توانند لحظه اي يا دائمی باشند در روابط انتشار آلاينده لحظه اي گوسی يا آلاينده دائمی گوسی تغييرات مكانی سرعت باد و ضريب انتشار در نظر گرفته نميشود كه اين امر باعث ايجاد خطاي نسبتاً چشم گيري در نتايج به دست آمده می شود. [۲] براي مثال در اين مدلها از تغييرات ضرايب پخش نسبت به مكان و زمان صرفنظر شده و اين ضرايب در جهات مختلف $(k_x = k_y = k_z = k)$. يكسان فرض شده است همچنين با توجه به اينكه سرعت باد در ارتفاعات مختلف متفاوت است نميتوان يک سرعت ثابت را براي تمام ارتفاعات بكار برد. براي حصول دقت بيشتر، ضريب پخش و سرعت باد بايد بصورت توابعی از مكان در نظر گرفته شوند [۳]. در ادامه به آلودگی هوای کلانشهر تبریز که یکی از عوامل آن آلاینده های ناشی از نیروگاه حرارتی تبریز است می پردازیم نیروگاهی که برق شمال غرب کشور را تامین می کند و بسیار با اهمیت است.

۲. بيان مسئله و معادلات حاكم

معادله حاكم بر پراكندگی آلودگی در هوا بوسيله معادله انتقال - انتشار بيان ميگردد. فرم سه بعدي اين معادله در دستگاه مختصات متعامد بصورت زير ميباشد:

$$\frac{\partial c}{\partial t} + v\frac{\partial c}{\partial x} + u\frac{\partial c}{\partial y} + w\frac{\partial c}{\partial z} = k_x\frac{\partial^2 c}{\partial x^2} + k_y\frac{\partial^2 c}{\partial y^2} + k_z\frac{\partial^2 c}{\partial z^2} + S(x,y,z,t) \qquad (۱.۲)$$

كه درآن c غلظت آلاينده، v, u, w به ترتيب مولفه های سرعت باد در جهات x, y, z و k_x, k_y, k_z به ترتيب ضرايب پخش در جهات x, y, z می باشد فرضيات برای ساده كردن (۱.۲) بر اساس شرايط جغرافيای منطقه مورد بحث متفاوت است. موضوع اين مقاله در مورد خروج و پخش آلاينده از دودكش نيروگاه حرارتی شهر

رده بندی موضوعی۲۰۱۰: .....
سخنران: قادر درخوشی .

منطقه	α
دریاها و دریاچه ها	.07
بیابان ها و صحراها	.1
گیاهان کوتاه	.13
مراتع	.15
زمین های کشاورزی	$.24 - .26$
جنگل ها و شهرها	0.39

جدول ۱: مقادیر ضریب αدر مناطق مختلف

تبریز که با سوخت فسیلی مازوت کار می کند و آلاینده های ناشی از آن اکثر زمین های و باغات روستاهای اطراف خود را تحت تاثیرقرار داده است .

الف) شرایط به صورت ماندگار یک دوره شش ماهه فصل های سرد سال مهر تا آخر اسفند که وارونگی دما زیاد اتفاق می افتد در نظر گرفته می شود. $\frac{\partial c}{\partial t} = 0$

ب) شرایط به صورت دو بعدي و در جهت افقی و قائم در نظر گرفته می شود $u\frac{\partial c}{\partial y} = 0, \quad k_y\frac{\partial^2 c}{\partial y^2} = 0$

ج) سرعت باد در جهت محور x در نظر گرفته شده است $u = w = 0$

د) از انتقال آلاینده توسط انتشار متلاطم مولکولی در قیاس با انتقال توسط جریان باد صرف نظر می شود $k_x\frac{\partial^2 c}{\partial x^2} = 0$

تحت شرایط فوق معادله (۱.۲)به معادله زیر تبدیل می شود

$$V\frac{\partial c}{\partial x} = k_z\frac{\partial^2 c}{\partial z^2} + S(x,z) \tag{۲.۲}$$

روابط تخمین سرعت باد و ضریب انتشار

انتقال آلاینده توسط باد به میزان زیادي وابسته به سرعت باد میباشد. بیشتر مدلهاي موجود مانند مدل هاي لحظه اي و دائمی گوسی در این زمینه مقدار ثابتی را براي سرعت باد در نظر میگیرند، اما در حقیقت سرعت باد در این تحقیق با تغییرات ارتفاع تغییر میکند رابطه نمایی تغییرات سرعت باد براي تخمین سرعت باد بکار میرود. بر این اساس رابطه تغییرات سرعت باد نسبت به ارتفاع بصورت زیر توصیف می شود [۴]

$$v(z) = V_{10}\Big(\frac{z}{10}\Big)^{\alpha} \tag{۳.۲}$$

V_z سرعت باد در ارتفاع z از سطح زمین ، V_{10} سرعت باد در ارتفاع 10 متری از سطح زمین که از داده های ایستگاه هواشناسی بدست می آید. و α توانی است که بستگی به شرایط زبری زمین دارد و از جدول زیر بدست می آید. براي لحاظ کردن تغییرات مکانی ضریب انتشار از رابطه زیر استفاده می شود

$$k_z = \Big(\frac{\sigma_w^2}{\overline{V}}\Big)x \tag{۴.۲}$$

که در آن σ_w انحراف معیار تغییرات سرعت باد، $\overline{V}$ متوسط سرعت باد در جهت محور طول ها و x فاصله نقطه مورد نظر از منبع آلاینده در جهت وزش باد می باشد

اعمال شرایط مرزی شرایط مرزي روابطی هستند که میزان غلظت یا تغییرات آن را در مرزهاي دامنه حل بیان می کنند.

۱) $\left.\frac{\partial c}{\partial z}\right|_{z=0} = v_d$ یعنی الاینده ها با سرعت v_d جذب خاک می شوند

۲) $\left.\frac{\partial c}{\partial z}\right|_{z=H} = 0$ یعنی در شرایط وجود وارونگی، آلودگی نمیتواند از انتهاي لایه وارونه شده خارج شود.در حالتی که وارونگی وجود ندارد شرط مرزي انتهایی در راستاي قائم بصورت $z \to \infty$ انگاه $c \to 0$

۳) $\left.\frac{\partial c}{\partial z}\right|_{x=L} = 0$ یعنی تغییرات غلظت در فاصله افقی نسبتاً دور از منبع آلاینده تقریبا ناچیز است

۴) با توجه به سرعت باد، میزان غلظت در راستاي قائم بجز گره روي منبع آلاینده $x = 0$ برابر صفر است. با

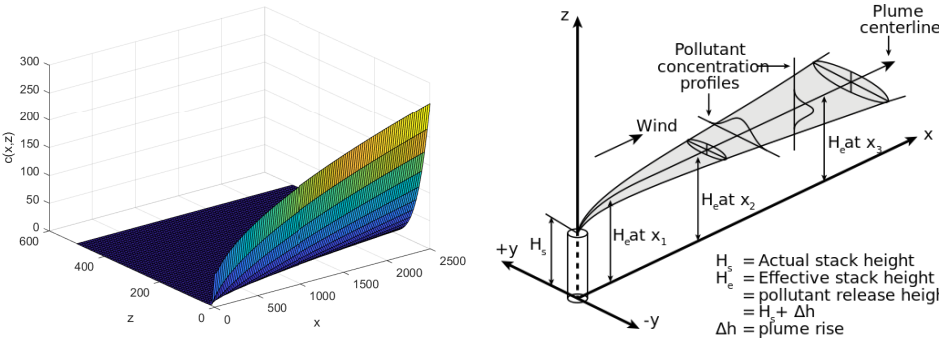

شکل ۱: سمت راست دود کش نیروگاه و سمت چپ آن توزیع انتشار و پراکندگی آلاینده را نشان میدهد

توجه به اینکه منبع آلاینده مرتفع از سطح زمین به عنوان یک منبع نقطه اي در نظر گرفته می شود، شرط مرزي گره روي منبع آلاینده به صورت زیر تعریف می شود:

$$V_{10}\Big(\frac{z}{10}\Big)^{\alpha} c\Big|_{x=0}^{z=H} = S.\delta(z-H). \tag{۵.۲}$$

که در آن H ارتفاع منبع آلاینده از زمین، S نرخ جرمی خروجی آلودگی از منبع ،عملگر δ نشان دهنده تابع دلتاي ديراك می با شد [۵]. با این توضیحات مسئله انتشار و پراکندکی آلودگی هوا در حالت دو بعدی و ماندگار از دودکش نیروگاه برقی تبریز که با سوخت مازوت کار می کند به شکل زیر می توان نوشت.

$$\begin{aligned} &v(z)\frac{\partial c}{\partial x} = k_z\frac{\partial^2 c}{\partial z^2} + S(x,z) \;\; 0 \le z \le H \quad 0 \le x \le L \\ &V_{10}\Big(\frac{z}{10}\Big)^{\alpha} c(0,H) = S.\delta(z-H), \quad \frac{\partial c}{\partial x}(L,z) = 0, \\ &\frac{\partial c}{\partial z}(x,0) = c(x,0).v_d, \quad \frac{\partial c}{\partial z}(x,H) = 0, \end{aligned} \tag{۶.۲}$$

گسسته سازي معادله به روش تفاضلات متناهی

با جاگذاری روابط (۳.۲) و (۴.۲) در معادله (۲.۲)

$$V_{10}\Big(\frac{z}{10}\Big)^{\alpha}\frac{\partial C}{\partial x} = \Big(\frac{\sigma_w^2 x}{\overline{V}}\Big)\frac{\partial^2 C}{\partial z^2} + S(x,z) \tag{۷.۲}$$

با جایگذاري تقریبهاي مشتقات عددي پسرو و مرکزي به ترتیب بجاي پارامترهای انتقال و انتشار در معادله (۸.۲) فرم گسسته شده این معادله بصورت زیر بدست می آید

$$V_{10}\Big(\frac{z_j}{10}\Big)^{\alpha}\frac{C_{i,j}-C_{i-1,j}}{\Delta X} = \Big(\frac{\sigma_w^2 X_i}{\overline{V}}\Big)\frac{C_{i,j+1}+2C_{i,j}+C_{i,j-1}}{\Delta Z^2} + S(x,z) \tag{۸.۲}$$

چون $\Delta T = 0$ پس معادله (۸.۲) همواره پایدار است. در این تحقیق لازم به ذکر است پهنای زمین های اطراف نیروگاه به شعاع $L = 2500$ متر و ارتفاع از منبع آلودگی را با در نظر گرفتن ارتفاع وارونگی دما در فصل های سرد سال $H = 500$ متر تعیین شده است. معادله (۸.۲) با اعمال شرایط مرزی و اولیه تبدیل به یک دستگاه معادلات می شود که به روش تکرار گوس سایدل حل می شود.

۳. نتیجه گیری

نمودار حاکی از آن است که با در یک پریود زمان ثابت ، با شروع حرکت آلاینده از دود کش با نرخ جرمی معین در ارتفاعات کمتر غلظت آلاینده کمتر بوده ، سپس تا یک ارتفاع معین تا رسیدن به حداکثر طول معین افزایش می یابد چنانکه در نمودار نشان داده شده است بعد از گذشت یک ارتفاع معین دیگر غلظت آلاینده به صفر می رسد اگر سرعت باد زیاد باشد آلاینده ها پراکنده شده از منطقه اطراف دور می شود و با توجه به جغرافیای اقلیمی در فصل تابستان بادهای مدیترانه که از غرب می وزند به همراه بادهای محلی این آلاینده ها وارد شهر تبریز شده و بر حجم آلایندهای شهر که از منابع مختلف بوجود آمده ،افزوده می شود و این خوش ترین حالت ممکنه است چون در فصل بهار و تابستان سوخت نیروگاه گاز طبیعی است .

در فصل های سرد با توجه به افزایش مصرف گاز خانگی ،سوخت نیروگاه که از خط لوله ایکه از پالایشگاه تبریز کشیده شده با مصرف ۳۲۰۰ تن مازوت در شبانه روز تغییر می کند که خطرناکترین آلاینده ناشی از آن روزانه مقدار زیادی گوکرد وارد جوی و محیط زیست می شود و این در حالی است به دلیل پدیده وارونگی دما که عمدتا در روز های سرد سال اتفاق می افتد که گاهی چندین روز هم ادامه پیدا می کند در چنین شرایطی که بدترین حالت ممکنه است آلاینده با حجم وسیعی منطقه اطراف نیروگاه را فرا گرفته و ادامه این پدیده وارونگی دما وسعت آلودگی هوا زیادتر شده ، که با وزش باد و از بین رفتن پدیده وارونگی حجم زیادی از آلاینده ها وارد کلانشهر تبریز می شود که با آلاینده های سوخت گاز خانگی فاجعه زیست محیطی فراوان به بار خواهد آورد و یا با بارش برف یا باران این الاینده ها را که عمدتا دی اکسید سولفات هستند با خود تحت عنوان باران های اسیدی(اسید سولفوریک) جذب درختان و خاک روستاهای اطراف نیروگاه می شود خشک شدن درختان و بی حاصل شدن زمین های کشاورزی باغ معروف و کوجوار.. ،گواه این واقعیت است.

مراجع

[۱] A. S. Pal. *Modeling and parameterization of near-source diffusion in weak winds.*، Journal of Applied Meteorology and Climatology ۳۴.۵ :(۱۹۹۵) .۱۱۱۲-۱۱۲۲

[۲] W. Sérgio، et al. *A new analytical approach to simulate the pollutant dispersion in the PBL.*، Atmospheric Environment ۳۹.۱۲ :(۲۰۰۵) .۲۱۷۱-۲۱۷۸

[۳] S. Maithili، and Suman Gupta، *Two-dimensional analytical model for estimating crosswind integrated concentration in a capping inversion: eddy diffusivity as a function of downwind distance from the source.*، Atmospheric Environment ۳۶.۱ :(۲۰۰۲) .۹۷-۱۰۵

[۴] S. F.B. .(۱۹۵۷) *The diffusion of smoke from a continuous elevated plume source into a turbulent atmosphere.*، Journal of Fluid Mechanics، :۲ —۴۹ .۷۶

[۵] T. G.، et al. .(۱۹۵۷) *On modeling dry deposition of long-lived and chemically reactive species over heterogeneous terrain.*،Journal of atmospheric chemistry ۴۲ :(۲۰۰۲) .۱۲۳-۱۵۵

[۶] A. Narjes، and BAYGI MOHAMMAD MOUSAVI. *A ۲-D Numerical Model for Steady Air Pollutant Dispersion by Considering the Spatial Variation of Wind Velocity and Diffusivity Coefficient*:(۲۰۱۰)، .۴۵-۵۷

دانشگاه تبریز دانشکده ریاضی،آمار و علوم کامپیوتر
E-mail address: gaderdarkhooshi1352@gamil.com

دانشگاه تبریز دانشکده ریاضی،آمار و علوم کامپیوتر
E-mail address: ivaz@tabriz u.ac.ir

بررسی روند انتشار بیماری با استفاده از شبکه‌های چندلایه

۱ هاله عشّاقی و ۲ یوسف جمالی

چکیده. شبکه‌ها ابزاری مفید برای مدل‌سازی سیستم‌های پیچیده هستند. از آنجایی که شبکه‌های پیچیده واقعی ناهمگن هستند، بسیاری از وابستگی بین اجزا توسط شبکه‌های تک‌لایه قابل تفهیم نمی‌باشد. بدین منظور، برای توضیح این منبع پیچیدگی، به یک چارچوب کلی‌تری نیاز است. این نوع شبکه‌ها به‌عنوان شبکه‌های چندلایه شناخته می‌شوند. یکی از چالش‌هایی که امروزه در مدل‌سازی شیوع بیماری‌های همه‌گیر وجود دارد، توسعه روش‌هایی برای کنترل انتقال بیماری است؛ لذا هدف این است با استفاده از شبکه چندلایه که در یک‌لایه نحوه انتقال بیماری و در لایه دیگر تعامل تفکرات افراد جامعه در مورد واکسیناسیون است را مورد بررسی قرار دهیم که چگونه طرز تفکر افراد جامعه در مورد واکسیناسیون بر انتشار بیماری در جمعیتی که در تعامل هستند تأثیر می‌گذارد.

کلمات کلیدی: شبکهٔ چندلایه، انتشار بیماری، تبادل عقاید.

۱. مقدمه

دنیای ما پر از سیستم‌هایی است که سیستم پیچیده [1] نامیده می‌شود. "سیستم پیچیده" گروه یا سازمانی است که از بسیاری از بخش‌های متقابل تشکیل شده است که بر هم اثر گذارند. نمایش این نوع سیستم‌ها در قالب شبکه است که گره‌هایش عناصر سیستم و یال‌هایش برهم‌کنش‌های میان‌شان است. ازاین‌رو مفهوم شبکه در تعریف گراف که مستلزم نمایش بصری مجموعه‌ای از گره‌ها و یال‌هاست، صدق می‌کند. بدین سبب مدل‌سازی ریاضی شیوع بیماری‌های واگیر به ابزار مهمی برای تخمین میزان اپیدمی تبدیل شده است [۱، ۲]. دانش یا اطلاعاتی که در مورد یک ویروس و نحوه‌ی انتقال آن بین افراد وجود دارد، نقش اساسی در مهار یک بیماری همه‌گیر دارد. بدین سبب درک تعامل بین دینامیک بیماری و رفتار انسان یک نکته مهم و ضروری برای کنترل عفونت است [۳]. دربرخی موارد شیوع بیماری را می‌توان با واکسیناسیون تحت تأثیر قرارداد؛ لذا ریشه‌کنی بیماری یا مصونیت جمعیت هدف واکسیناسیون است. از سوی دیگر، تصمیمات هر فرد در مورد واکسیناسیون تحت تأثیر تصمیمات دیگران است. از آنجایی که روند انتشار بعضی از بیماری‌ها وابسته به واکسیناسیون است، ازاین‌رو طرز تفکر افراد جامعه در مورد دریافت واکسن و عدم دریافت واکسن می‌تواند در روند انتقال بیماری نقش داشته باشد. مدل شبکه چندلایه [2] یکی از قدرتمندترین شبکه‌هاست که می‌تواند شبکه‌های چند رابطه‌ای را مدل‌سازی کند. [۴] از آنجایی که هدف مدل ما بررسی اثر واکسیناسیون است که در یک شبکه دولایه مورد بررسی قرار می‌گیرد، ازاین‌جهت مدل‌هایی که برای دینامیک هر لایه در نظر گرفته می‌شود باید در عین سادگی بتوانند به‌خوبی پدیده مد نظر را بیان کنند. دینامیک حاکم در لایه اول که مربوط به انتشار بیماری می‌باشد، بر اساس مدل SIRDV [3] است [۵] و دینامیک حاکم در لایه‌ی دوم که مربوط به تبادل عقاید در مورد واکسیناسیون می‌باشد، بر اساس مدل Q-VOTER است. مدل Q-VOTER بر روی جمعیتی با اندازه N تعریف می‌شود که در آن هر فرد i نظری دارد که با یک متغیر باینری $si = \pm 1$ مشخص می‌شود [۶]. دو دینامیک بر روی یک شبکه دولایه عمل می‌کند. شکل (۱) بیانگر این مدل می‌باشد:

سخنران: هاله عشاقی .

[1] Complex system
[2] Multilayer networks
[3] Susceptible-Infectious-Recovered-Death-Vaccinated

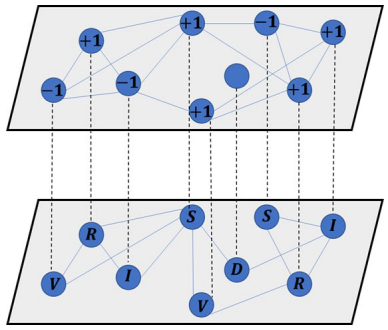

شکل ۱. نمایش مدل دولایه $(SIRDV - QVOTER)$

این شبکه دولایه، علاوه بر تعاملات درون لایه‌ای، یک سری تعاملات بین لایه‌ای نیز دارد که از هم اثر می‌پذیرند. در لایه‌ی اول گره‌ها در حالت (S) مستعد، (I) آلوده، (R) بهبودیافته، (V) واکسینه شده و (D) افراد فوت شده می‌باشند. همین گره‌ها در لایه بالایی یک ویژگی تحت عنوان عقاید مثبت و منفی نسبت به واکسیناسیون را به خود اختصاص داده‌اند. یعنی هر گره در شبکه علاوه بر این که یکی از پنج حالت (S) مستعد، (I) آلوده، (R) بهبودیافته، (V) واکسینه شده و (D) فوت شده(بدون عقیده)، یک عقیده نسبت به واکسن نیز دارد که می‌تواند عقیده مثبت یا منفی باشد که ناشی از لایه دوم شبکه دولایه است. این شبکه‌ی دولایه علاوه بر دینامیکی که به طور مجزا در هر لایه جریان دارد، یک سری تعاملات نیز دارد که ناشی از تأثیر لایه اول بر روی لایه دوم و تأثیر لایه دوم بر روی لایه اول است. باتوجه به مدل $SIRDV - QVOTER$، و تاثیرپذیری لایه اول از دوم هریک از $S(t)$، $I(t)$، $R(t)$، $D(t)$ و $V(t)$ در لایه بیماری دارای دینامیکی هستند که توسط معادلات زیر نشان داده شده است:

$$\frac{dS_+(t)}{dt} = -\alpha S_+(t) - \gamma S_+(t)I(t) \tag{۱.۱}$$

$$\frac{dS_-(t)}{dt} = -\gamma S_-(t)I(t) \tag{۲.۱}$$

$$\frac{dI(t)}{dt} = \gamma S_-(t)I(t) + \gamma S_+(t)I(t) - (\delta_1 + \delta_2)I(t) \tag{۳.۱}$$

$$\frac{dR(t)}{dt} = \delta_1 I(t) \tag{۴.۱}$$

$$\frac{dD(t)}{dt} = \delta_1 I(t) \tag{۵.۱}$$

$$\frac{dV(t)}{dt} = \alpha S_+(t) \tag{۶.۱}$$

به طور خلاصه در این مدل تعامل بین افراد یا عامل‌ها [۴] به‌صورت حالات زیر است:

- $S(+1) \xrightarrow{\alpha} V$:یک عامل مستعد با عقیده مثبت با نرخ α واکسینه می‌شود.
- $S(+1) \xrightarrow{\gamma} I$: یک عامل مستعد با عقیده مثبت با نرخ γ آلوده می‌شود.
- $S(-1) \xrightarrow{\gamma} I$:یک عامل مستعد با عقیده منفی با نرخ γ آلوده می‌شود.
- $I \xrightarrow{\delta_1} R$: یک عامل آلوده با نرخ δ_1 بهبود می‌یابد.
- $I \xrightarrow{\delta_2} D$: یک عامل آلوده با نرخ δ_2 می‌میرد.

[4] Agent

۲. تأثیرپذیری لایه‌ها از یکدیگر

در این قسمت به بررسی نتایج حاصل از شبیه‌سازی مدل موردنظر پرداخته می‌شود. شبیه‌سازی زمانی استفاده می‌شود که به دلیل وجود پیچیدگی سیستم موردنظر، روش‌های تحلیلی برای حل مسئله موردنظر غیرعملیاتی است. ما شبیه‌سازی را با محیط برنامه‌نویسی پایتون انجام دادیم. از جمله شبکه‌های مورداستفاده در شبیه سازی که مورداستفاده قرار گرفتند می‌توان به شبکه‌های اردوش رینی و واتس استروگاتز [۷] اشاره کرد که شبکه‌ی واتس استروگاتز به دلیل ضریب خوشه‌بندی بالایی که دارد گزینه‌ی مناسبی است. جامعه‌ی مورد بررسی که همان گره‌های شبکه می‌باشد از $N = 5 \times 10^3$ نفر تشکیل شده است. ما دو شبکه با اندازه یکسان در نظر گرفتیم که گره‌های موجود در هر دو شبکه با هم همپوشانی [۵] دارند. کل مدت زمانی که دینامیک مدل در آن مورد بررسی قرار گرفته، معادل ۵۰۰ روز در نظر گرفته شده است. در حین اجرا هیچ پارامتری تغییر نمی‌کند و از آنجایی که فرآیند شبیه سازی تصادفی است، لذا برای حفظ پایین‌بودن سطح افت‌وخیز، از اجراها به تعداد ۲۰ بار میانگین گرفته شده است. مقادیر پارامترها به صورت $\alpha = 0.3$ ، $\gamma = 0.25$ ، $\delta_1 = 0.35$ ، $\delta_2 = 0.05$ و $p = 0.5$ (نرخ تبادل عقاید) می‌باشد. در ابتدای شبیه سازی در لایه‌ی بیماری حدود ۰۵.۰ از افراد کل جامعه مبتلا به بیماری بوده و سایر افراد، مستعد بیماری هستند و در لایه‌ی عقاید حدود ۹.۰ افراد کل جامعه دارای عقیده مثبت نسبت به واکسیناسیون هستند. قسمت (آ) شکل ۲ دینامیک عقاید افراد جامعه را در طول

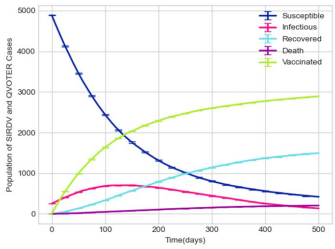

(ب) نمایش دینامیک مدل $SIRDV - QVOTER$.

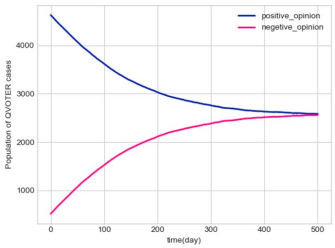

(آ) نمایش دینامیک عقاید افراد جامعه در طول زمان.

شکل ۲

زمان نشان می‌دهد. با گذشت زمان می‌بینیم که افراد جامعه به دلیل تعاملات عقایدی بر هم اثر می‌گذارند و بعد از گذشت 500 روز تقریباً 50% جامعه دارای عقیده منفی و 50% دارای عقیده مثبت می‌شوند. دینامیک لایه بیماری در صورت وجود لایه عقاید در قسمت (ب) شکل ۲ نشان‌داده‌شده است. در این مدل تعداد افراد آلوده روند صعودی داشته و بعد از گذشت تقریباً 130 روز از تعداد آنها کاسته شده و روند نزولی را سیر می‌کنند. افراد واکسینه شده روند صعودی داشته و تقریباً 3000 نفر از جمعیت کل واکسینه شده‌اند که ناشی از حضور لایه‌ی دوم و تبادل عقاید درمورد واکسینه شدن می‌باشد. ما در شرایط اولیه حدود 90% از افراد جامعه را با عقیده مثبت در نظر گرفته‌ایم. به عبارتی لایه‌ی بیماری از لایه‌ی عقاید تأثیر می‌پذیرد و از آنجایی که افراد مستعد جامعه دارای قدرت تصمیم‌گیری درمورد واکسینه شدن هستند، هر چه تعداد افراد مستعد با عقیده مثبت زیادتر باشد، آمار افراد واکسینه شده بیشتر می‌شود و آمار افراد آلوده شده و فوت شده کاهش می‌یابد. لایه بیماری نیز بر دینامیک حاکم در لایه عقاید تأثیرگذار است. در این حالت افراد فوت شده و آلوده شده به بیماری بر روی عقاید سایر افراد جامعه تأثیر می‌گذارند. در واقع در صورت اعمال‌کردن تأثیر لایه بیماری بر عقاید، چون افراد فوت شده و آلوده به بیماری بر روی عقاید همسایگان خود تأثیر می‌گذارند، ممکن است در مجاورتشان فرد واکسینه شده باشد و اگر دارای عقیده منفی نسبت به واکسیناسیون باشند عقیده خود را به حالت مثبت تبدیل

[5] Overlap

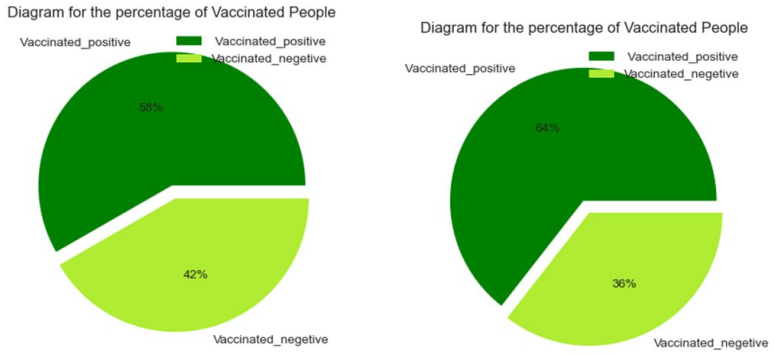

(آ) نمایش درصد افراد واکسینه شده دارای عقاید مثبت و منفی درصورت تاثیر گذاری لایه بیماری بر عقاید.

(ب) نمایش درصد افراد واکسینه شده دارای عقاید مثبت و منفی درصورت عدم تاثیر گذاری لایه بیماری بر عقاید.

شکل ۳. تاثیر لایه بیماری بر عقاید.

کنند. بدین صورت در شکل ۳ شاهد هستیم که عقاید افراد واکسینه شده در صورت تأثیرپذیری لایه عقاید از بیماری از 58% عقیده مثبت به 64% رسیده است.

در حالت کلی‌تر تأثیرپذیری لایه عقاید از بیماری، بر روی عقاید اکثریت افراد جامعه تأثیر می‌گذارد و افراد جامعه در مجاورت با فرد فوت شده و یا آلوده شده عقیده خود را به عقیده مثبت تبدیل می‌کنند. این تأثیرگذاری در عقاید افراد جامعه به‌وضوح دیده می‌شود. به شکل ۴ دقت شود.

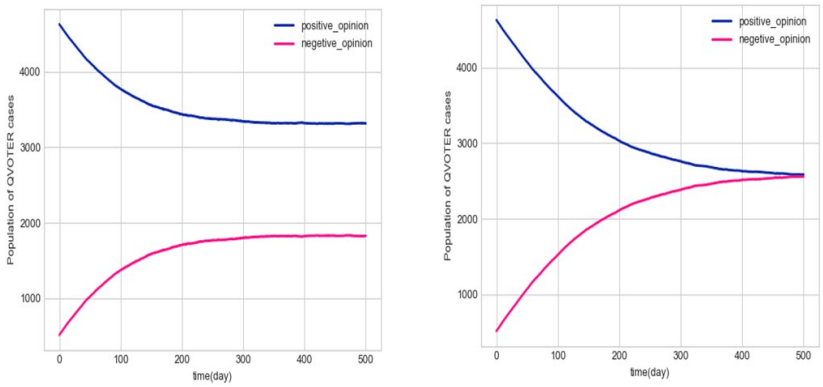

(آ) عدم تاثیر پذیری لایه عقاید از بیماری.

(ب) تاثیر پذیری لایه عقاید از بیماری.

شکل ۴. نمایش دینامیک عقاید افراد جامعه.

با اضافه‌شدن این تأثیرگذاری می‌بینیم که شیب منحنی مربوط به افراد با عقاید مثبت نسبت به قسمت (آ) شکل ۴ کمتر است و افراد جامعه در سطح بالایی از عقاید مثبت باقی‌مانده‌اند و اکثریت افراد جامعه بعد از

گذشت 500 روز به سبب اینکه تأثیرگذاری لایه بیماری بر عقاید به مدل اضافه شده است دارای عقیده مثبت نسبت به واکسینه شدن هستند. هم چنین شیب منحنی افراد با عقیده منفی نیز در مقایسه با قسمت (ب) شکل ۴ کمتر است که حاکی از پایین‌بودن سرعت تبادل عقاید منفی بین افراد جامعه است و در نهایت بعد از گذشت 500 روز تعداد افراد دارای عقیده منفی در حالتی که تأثیرگذاری لایه بیماری بر عقاید در نظر گرفته شده است کمتر از حالتی است که این تأثیرگذاری در نظر گرفته نشده است.

در تأثیرپذیری لایه دوم از لایه اول دیدیم که عقاید افراد جامعه نیز تا حدودی تحت تأثیر لایه اپیدمی قرار دارد. به صورتی که افراد آلوده به بیماری عقاید منفی خود را بعد از ابتلا به بیماری به عقیده مثبت تغییر می‌دادند و به سبب این تأثیر پذیری لایه دوم از لایه اول شاهد افزایش افراد واکسینه شده و افزایش جامعه آماری افراد با عقیده مثبت شدیم. به دلیل وجود تعامل عقیدتی بین افراد جامعه این تغییر عقیده از حالت منفی به مثبت منجر می‌شد که همسایگان فرد موردنظر تحت تأثیر قرارگرفته و عقیده خود را به حالت مثبت تغییر دهند. بدین ترتیب تأثیری که لایه اول بر روی لایه دوم داشت منجر به بازگشت تأثیر مثبت لایه دوم بر روی لایه اول گردید.

مراجع

[1] Pastor-Satorras, R., et al., Epidemic processes in complex networks. Reviews of modern physics, 2015. 87(3): p. 925.

[2] de Arruda, G.F., F.A. Rodrigues, and Y. Moreno, Fundamentals of spreading processes in single and multilayer complex networks. Physics Reports, 2018. 756: p. 1-59.

[3] Zhu, P., et al., Investigation of epidemic spreading process on multiplex networks by incorporating fatal properties. Applied Mathematics and Computation, 2019. 359: p. 512-524.

[4] Hammoud, Z. and F. Kramer, Multilayer networks: aspects, implementations, and application in biomedicine. Big Data Analytics, 2020. 5(1): p. 2.

[5] Usherwood, T., Z. LaJoie, and V. Srivastava, A model and predictions for COVID-19 considering population behavior and vaccination. Scientific reports, 2021. 11(1): p. 12051.

[6] Jankowski, R. and A. Chmiel, Role of time scales in the coupled epidemic-opinion dynamics on multiplex networks. Entropy, 2022. 24(1): p. 105.

[7] Barrat, A., M. Barthelemy, and A. Vespignani, Dynamical processes on complex networks. 2008: Cambridge university press

آدرس مولف اول: گروه ریاضی کاربردی، دانشکده علوم ریاضی، دانشگاه تربیت مدرس، تهران، ایران
Email address: h.oshaghii@gmail.com

آدرس مولف دوم: گروه ریاضی کاربردی، دانشکده علوم ریاضی، دانشگاه تربیت مدرس، تهران، ایران
Email address: y.jamali@gmail.com

تحليل داده هاي تابعي با استفاده شبكه هاي عصبي

۱ سيده اوين قيصري و ۲ اميد خادم نوع

چکیده. در این مقاله به مطالعه تحلیل رگرسیونی خواهیم پرداخت که در آن متغیر مستقل متغیری تابعی مقدار و متغیر پاسخ یک متغیر اسکالر مقدار است. با استفاده از شبکه عصبی پیش‌خور، روش را برای پیش‌بینی متغیر پاسخ اسکالر مورد مطالعه قرار خواهیم داد که ماهیت تابعی متغیر پیشگو را در نظر می‌گیرد. با استفاده از این روش به پیش‌بینی میزان چربی موجود در نمونه‌های گوشت داده به کمک طیف‌سنجی نورهای نزدیک نورمادون‌قرمز به عنوان متغیر پیشگوی تابعی خواهیم پرداخت.

کلمات کلیدی: داده‌های تابعی، رگرسیون متغیر تابعی، شبکه عصبی پیش‌خور، طیف‌سنجی نورهای نزدیک نورمادون قرمز.

۱. مقدمه

امروزه با توجه به پیشرفت تکنولوژی امکان ثبت داده‌ها با سرعت و دقت بیشتری امکان‌پذیر شده است. از این رو تحلیل داده‌های تابعی (FDA) یک حوزه روبه رشد در آمار و یادگیری ماشین است که به تحلیل داده‌های منحنی، یا سطح (تابع مقدار) می‌پردازد. یکی از روش‌های تحلیل داده‌های تابعی، بررسی رگرسیون و پیش‌بینی یک متغیر پاسخ حقیقی مقدار با یک متغیر مستقل تابعی مقدار است [۱]. این نوع تحلیل رگرسیون در بسیاری از تحقیقات علمی و کاربردهای عملی مانند پیش‌بینی میزان کل بارندگی سالیانه بر اساس تابع دما در طول سال، پیش‌بینی مواد مغذی در نمونه‌های غذای با استفاده از طیف‌سنجی نورهای با طول موج‌های متفاوت، مورد استفاده قرار می‌گیرد [۲]. در روش رگرسیون خطی تابعی، یک رابطه خطی تابعی بین متغیر تابعی و پاسخ اسکالر وجود دارد. فرض کنید Y نشان‌دهنده پاسخ اسکالر و $X(t)$ متغیر پیشگوی تابعی که برای $t \in \tau$ باشد. در این حالت مدل رگرسیون خطی تابعی به صورت زیر تعریف می‌شود:

$$\mathrm{E}(Y|X) = \alpha + \int_{\tau} \beta(t)X(t)dt$$

که در آن αعرض از مبدأ و $\beta(t)$ ضریب تابعی است که اثر کلي خطی $X(t)$ را بر Y را نشان می‌دهد[۳]. چنین مدلی اغلب در مواقعی مورد استفاده قرار می‌گیرد که متغیر پاسخ Y دارای توزیع نرمال است. هنگامی که پاسخ اسکالر از یک توزیع خانواده نمایی پیروی کند، آنگاه مدل رگرسیون خطی تابعی به مدل خطی تعمیم‌یافته زیر گسترش پیدا می‌کند.

$$\mathrm{E}(Y|X) = g\left(\alpha + \int \beta(t)X(t)dt\right)$$

که در آن g(.) نشان دهنده تابع پیوند است. در این مدل‌ها با استفاده از توابع پایه می‌توان تقریبی را برای تابع شیب بدست آورد و با استفاده از یک سری تکنیک‌ها تحلیل رگرسیونی مورد نظر پیش برد. در حالتی که تابع پیوند فرم پارامتری نداشته باشد، می‌توان برای بررسی ارتباط متغیر پیشگوی تابعی با پاسخ اسکالر از

رده بندی موضوعی۲۰۱۰: .....
سخنران: نام سخنران .

Functional data analysis

رگرسیون ناپارمتری تابعی استفاده کرد. هریک از این روش در مواقع که مفروضات لازم برقرار باشد کارایی خوبی دارد. در این مقاله با استفاده از ادغام روش‌های تحلیل داده‌های تابعی با شبکه عصبی عمیق، روشی را پیشنهاد خواهیم داد که دقت بالایی برای پیش‌بینی متغیراسکالر بر اساس ورودی متغیر تابعی مقدار دارد.

۲. شبکه عصبي با ورودي تابعي و پاسخ اسکالر

در ادامه، یک چارچوب کلی برای مدل‌سازی وزن‌های تابعی در شبکه‌های عصبی را توضیح می‌دهیم. با توجه به یک متغیر تابعی $X(t)$ که در آن $t \in \tau$ تغییر می‌کند، ما به دنبال توسعه شبکه عصبی هستیم که می‌تواند این متغیرهای تابعی را در فرآیند یادگیری ادغام کند. که شامل معرفی وزن‌های تابعی است که در طول فرآیند بهینه‌سازی تغییر می‌کنند. اولین گام، نمونه‌گیری از متغیر تابعی $X(t)$ در نقاط زمانی مختلف t_i، $i = 1, \ldots, n$ است. این نمونه‌ها سپس به لایه‌های بعدی شبکه منتقل می‌شوند. لایه‌های پنهان در شبکه عصبی تابعی مشابه لایه‌های پنهان در شبکه‌های عصبی کلاسیک هستند، اما با یک تفاوت که وزن‌های مرتبط با هر ورودی تابعی، خود توابعی از زمان هستند. فرم نورون با ورودي متغير تابعي در لايه اول به اين صورت است:

$$\nu_i^{(1)} = g(\int_\tau \beta_i(t) x dt + b_i^{(1)})$$

مي توان تابع وزن $\beta_i(t)$ را به صورت ترکیب خطي از توابع پایه بیان کرد:

$$\beta_i(t) = \sum\nolimits_{m=1}^{M} c_{im}\, \phi_i(t) = \underset{i}{\mathbf{c}}^T \boldsymbol{\phi}_i(t)$$

که در آن $\boldsymbol{\phi}_i(t) = (\phi_{i1}(t), ..., \phi_{iM}(t))^T$ یک بردار از تابع پایه و $\mathbf{c}_i = (c_{i1}, ..., c_{iM})^T$ ضرایب پایه خطي هستند. ضرایب پایه برای $\beta_i(t)$ توسط شبکه مقداردهی اولیه می‌شوند؛ این مقداردهی‌های اولیه سپس با یادگیری شبکه به‌روز می‌شوند. با استفاده از این تقریب‌های پایه‌ای از $\beta_i(t)$، می‌توانیم به صورت ساده بیان کنیم که فرم یک نورون تنها $v_i^{(1)}$ به صورت زیر است:

$$\begin{aligned} v_i^{(1)} &= g\left(\int_\tau \beta_i(t) x(t)\, dt + b_i^{(1)}\right) \\ &= g\left(\int_\tau \sum_{m=1}^{M} c_{im} \phi_{im}(t) x(t)\, dt + b_i^{(1)}\right) \\ &= g\left(\sum_{m=1}^{M} c_{im} \int_\tau \phi_{im}(t) x(t)\, dt + b_i^{(1)}\right) \end{aligned}$$

لایه ورودی را همانطور که در شکل ۱ ارائه شده است، در نظر مي گیریم. فرم کلی لایه اول به صورت زیر است:

$$v_i^{(1)} = g\left(\sum_{m=1}^{M} c_{im} \int_\tau \phi_{im}(t) x(t)\, dt + b_i^{(1)}\right)$$

پس از اجرای نورون‌های اولیه در لایه اول و محاسبه تابع هاي فعال ساز برای لایه‌های بعدی، می‌توانیم به یک مقدار نهایی برسیم که خروجی تک‌بعدی خواهد بود. برای ارزیابی عملکرد شبکه، می‌توان از مجموع مربعات میانگین،R، به صورت زیر استفاده کرد:

$$R(\theta) = \sum_{i=1}^{N} (y_i - \hat{y}_i(\theta))^2$$

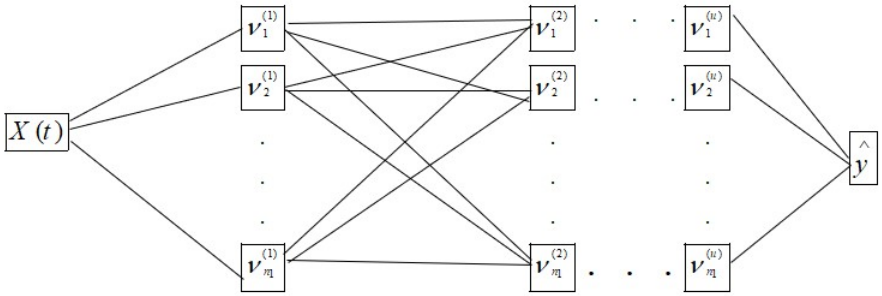

شکل ۱: شکل یک شبکه عصبی تابعی برای زمانی که ورودی تابع $x_k(t)$ و پاسخ این شبکه یک مقدار اسکالر $\hat{y}$ است.

در ادامه توضيح مي دهيم كه تعداد پارامترها در شبکه عصبی تابعی ارائه شده در اینجا می‌تواند اغلب کمتر از تعداد پارامترهای مورد نیاز در شبکه‌های عصبی کلاسیک باشد. فرض کنیم اندازه‌گیری‌های تکراری از متغیر کمکی تابعی در $P = 100$ نقطه داریم. به این معناست که تعداد پارامترها در لایه اول برابر با $(P + 1) \cdot n_1$ خواهد بود، که n_1 تعداد نورون‌ها در لایه پنهان اول است. در شبکه ما، تعداد پارامترها در لایه اول برابر با تعداد توابع پایه‌ای است که برای تعریف وزن تابعی استفاده می‌کنیم. تعداد توابع پایه M کمتر از P خواهد بود زیرا به درون يابي تابع وزنی که تمام نقاط مشاهده شده ما را دربرگیرد نیازي نیست ،ما ترجیح می‌دهیم که اثری هموار روي دامنه داشته باشیم تا از تطبیق با نویز(بیش برازش) جلوگیری کنیم. با توجه به توضیحاتي که ارائه شد تعداد پارامترها در لایه اول شبکه ما برابر با $(M + 1) \cdot n_1$ است. از طرفي نتايج عملي بدست آمده نشان می‌دهد که در آن $M < P$.

کل فرآیند شبکه را در الگوریتم ۱ خلاصه میکنیم.

جدول ۱: الگوریتم ۱

الگوريتم ۱: شبكه ي عصبي با ورودي تابعي
ورودی: $x_k(t)$ برای $j = 1, 2, \ldots, J$، γ، تعداد لایه‌ها،
نورون‌ها در هر لایه، توابع فعال‌سازی، نرخ کاهش، تقسیم اعتبارسنجی،
تعداد بسط پایه وزن تابعی، توابع پایه وزن تابعی،
دامنه‌های وزن تابعی، تعداد ایپوک ها، اندازه دسته، توقف زودهنگام،
آستانه بهبود حداقل، انتخاب تابع خطا، دراپ‌اوت
خروجی: مجموعه پارامترهایی که شبکه عصبی را تعریف می‌کنند، θ

در ادامه با استفاده از روشي كه ارائه شد به تحليل يک مثال كاربردي مي پردازيم. از مجموعه داده Tecator [۲] برای پیش‌بینی مقدار چربی در نمونه‌های گوشت استفاده کردیم. این داده‌ها شامل ۲۱۵ منحنی جذب نزدیک به مادون قرمز (طول موج ۸۵۰-۱۰۵۰ نانومتر) هستند که یک متغیر تابعی و یک متغیر اسکالر دارند.

هدف ما مقایسه عملکرد شبکه عصبي تابعي(FNN) که در این مقاله توضیح داده شده با سایر روش‌های شبکه‌های عصبی مانند شبکه‌های عصبی کانولوشن (CNN)، شبکه‌های عصبی با حافظه بلندـ کوتاه‌ـ مدت (LSTM) و واحدهای بازگشتی دروازه‌دار (GRU) است. که این روش‌ها بدون در نظر گرفتن ماهیت تابعي متغیر پیشگو مورد استفاده قرار می‌گیرند. در این تحلیل ما یک متغیر تابعی $x_k(t)$ را با استفاده از ۲۹ تابع پایه فوریه بسط دادیم و از ۳ تابع پایه برای بسط تابع وزن استفاده کردیم. طبق جدول نتایج نشان داد که خطای پیش‌بینی میانگین مربعات اعتبارسنجی متقابل (MSPE) برای FNN کمتر از سایر روش‌ها است. علاوه بر این، تعداد پارامترهای مورد نیاز برای FNN کمتر از بقیه بوده است. تعداد پارامتر براي FNN برابر با ۴۰۲۹ بود، در حالی که تعداد پارامترها براي روش CNN ۶۳۵۷ بوده ، در حالتهاي مختلف CNN تعداد پارامترها بین ۳۲۳۲۵ تا ۸۷۶۴۵ بوده ،براي روش LSTM تعداد پارامترها ۲۲۲۴۱ ،براي حالت دو طرفه آن تعداد پارامترها ۴۳۲۳۳و همچنین براي روش GRU تعداد پارامترها ۱۸۰۱۷ بوده است.

Model	MSPE	SE
CNN 1 (Kernel Size: 2; Filters: 64)	5.86	0.962
CNN 2 (Kernel Size: 2; Filters: 32)	5.19	0.967
CNN 3 (Kernel Size: 3; Filters: 64)	>10	0.314
CNN 4 (Kernel Size: 2; Filters: 16)	6.24	0.959
LSTM	4.35	0.971
LSTM Bidirectional	5.5	0.964
GRU	5.2	0.966
Conventional neural networks	7.43	0.952
Functional neural networks	3.63	0.976

۳. نتایج

به‌طور کلی، نتایج نشان داد که شبکه‌های عصبی تابعی در پیش‌بینی متغیرهای وابسته با استفاده از متغیرهای تابعی و چندمتغیره عملکرد بهتری نسبت به سایر مدل‌ها دارند و همچنین نه تنها از نظر دقت عملکرد بهتري دارد بلکه پارامترهای کمتری نسبت به سایر روش‌ها نیاز دارند.

مراجع

[1] Ramsay, J., and Silverman, B. (2005), Functional Data Analysis, New York:Springer.

[2] Thodberg, H. H. (2015), Tecator Meat Sample Dataset, StatLib Datasets Archive

[3] Cardot, H., Ferraty, F., and Sarda, P. (1999), "Functional Linear Model,"Statistics and Probability Letters, 45, 11–22.

[4] Barinder Thind, Kevin Multani , Jiguo Cao (2022): Deep Learning with Functional Inputs, Journal of Computational and Graphical Statistic.

[5] Müller, H.-G., and Stadtmüller, U. (2005), "Generalized Functional Linear Models," The Annals of Statistics, 33, 774–805

[6] Jiang, C.-R., and Wang, J.-L. (2011), "Functional Single Index Models for Longitudinal Data," The Annals of Statistics, 39, 362–388

آدرس مولف اول

Email address: awingheisari@gmail.com

آدرس مولف دوم

Email address: khademnoe@znu.ac.ir

Functional neural networks
Convolutional neural network
Long short-term memory
Gated recurrent unit
Mean Squared Prediction Error

نمونه‌هایی از مدل‌سازی ریاضی در درمان سرطان

مریم مسعودی آرانی

چکیده. ما در این مقاله برخی از مدل‌های ریاضی ارائه شده برای بعضی از روش‌های جدید درمان سرطان را معرفی خواهیم کرد. همچنین نتایج حاصل از به‌کار گیری این مدل‌سازی‌ها در تشخیص بدخیمی، عوامل موثر بر درمان و چگونگی دست‌یابی به درمانی بی‌خطر و یا کم‌خطر بررسی خواهد شد. مدل‌های ریاضی ارائه شده مربوط به گرمادرمانی سرطان به ویژه تومور کبد، جلوگیری از متاستاز استخوان، ویفرتراپی نوعی تومور مغزی به نام گلیوبلاستوما همچنین درمان فتودینامیکی تومورهای مغزی می‌باشد.

کلمات کلیدی: مدل‌سازی ریاضی، گرمادرمانی، ویفرتراپی، فوتودینامیک‌تراپی

۱. مقدمه

دانش ریاضیات همواره برای دست‌یابی به تحلیل‌های دقیق، درک و شناخت روابط بین پدیده‌ها و نیز دقیق‌تر شدن پیش‌بینی‌ها مورد استفاده علوم مختلف بوده است. از جمله کاربردهای بسیار ارزشمند ریاضیات، کاربرد آن در پزشکی است. در حقیقت استفاده از ریاضیات یکی از روش‌های اصولی پژوهش در پزشکی است. رشد بیماری‌ها قوانینی دارد که پزشکان با استفاده از ریاضیات و همفکری و همکاری با ریاضی‌دانان می‌توانند در کشف این قوانین و بررسی آنها موفق‌تر بوده و به درمان اصولی‌تر بیماری‌ها دست یابند. از جمله این بیماري‌ها رشد تومورها است که قوانین رياضي دارد و معمولاً به شکل سیستم‌هاي ديناميكي و معادلات ديفرانسيل است. ما در این مقاله ضمن آشنایی با روش‌های نوینی که در درمان بیماری سرطان به کار می‌رود، به معرفی مدل‌سازی‌های ریاضی ارائه شده در ارتباط با آنها و نقش کلیدی این مدل‌سازی‌ها در شناخت عوامل بیماری‌زا و دست‌یابی به درمان‌هایی دقیق‌تر، مفیدتر و با آسیب کمتر خواهیم پرداخت.

۲. نتایج اصلی

ما دراین بخش بعضی از مدل‌های ریاضی ارائه شده در درمان و تشخیص برخی از بدخیمی‌ها را مورد مطالعه قرار خواهیم داد. مدل‌های ریاضی مربوط به گرمادرمانی سرطان به ویژه تومور کبد، جلوگیری از پیشرفت متاستاز استخوان، ویفرتراپی نوعی تومور مغزی بدخیم به نام گلیوبلاستوما و درمان فتودینامیکی تومورهای مغزی از جمله‌ی آنهاست. همچنین نتایج استفاده از مدل‌های ریاضی ارائه شده و تاثیر آنها در تشخیص بیماری، روند درمان و دست‌یابی به درمان‌هایی کم‌خطر و یا بی‌خطر بررسی خواهد شد.

۱.۲. **استفاده از مدل‌سازی ریاضی در گرمادرمانی بیماری سرطان به‌ویژه تومور کبد.** از جمله روش‌های مقابله با تومورها در انسان، گرما درماني است. در این روش با استفاده از روش‌های مختلف، دمای بافت تومور تا دمایی بالاتر از دمای نرمال افزایش می‌یابد. استفاده از گرمادرمانی همراه با شیمی‌درمانی یا پرتودرمانی می‌تواند باعث بهتر شدن اثر آنها باشد. بنابر [۱] گردش خون در بافت تومور محدودتر از بافت‌های سالم است. گرما نیز می‌تواند مانعی برای رسیدن اکسیژن و مواد غذایی به بافت تومور باشد. بنابراین گرمادرمانی باعث تغییر پروتوئین‌های بافت تومور خواهد شد. از آنجا که این پروتئین‌های تغییر یافته برای سیستم ایمنی بدن ناشناخته هستند، سیستم ایمنی بدن سلول‌های تومور را راحت‌تر شناسایی می‌کند. برای آن‌که گرمادرمانی با بهترین نتیجه

رده بندی موضوعی۲۰۱۰: ۹۷M۱۰، ۹۳A۳۰، ۹۲B۰۵.
سخنران: مریم مسعودی آرانی .

همراه باشد، لازم است عوامل موثر بر آن به‌خوبی بررسی شوند. این عوامل عبارتند از عوامل فیزیولوژیکی و عواملی که در درمان مورد استفاده قرار می‌گیرند. عوامل فیزیولوژیکی مانند موقعیت بافت سرطانی، شبکه خون‌رسانی به بافت سرطانی، نوع بافت سرطانی و بافت‌های سالم اطراف بافت سرطانی. عواملی که در درمان مورد استفاده قرار می‌گیرند مانند نوع منبع ایجاد حرارت و چگونگی ایجاد گرما. برای مطالعه جزئیات بیشتر توضیحات بالا می‌توانید به [۱] مراجعه نمایید.

آیاتی و همکاران در [۱] دو مدل ریاضی برای بررسی گرمادرمانی سرطان و عوامل موثر بر آن ارائه نموده‌اند. در مدل اول بافت یک تومور عمقی شبیه‌سازی شده و اثر عوامل مختلف مثل نوع بستر بافت تومور و نوع شبکه خون‌رسانی به بافت تومور و بافت‌های اطراف آن بررسی شده‌اند. در این مدل از امواج فراصوت تخت برای ایجاد گرما در تومور استفاده شده است. در مدل دوم تاثیر نوع منبع حرارتی به صورت کیفی بررسی شده است. به این ترتیب که اثر نوع منبع حرارتی با توجه به میزان فرکانس منبع تولید گرما، بررسی شده است. با توجه به نتایج حاصل از این بررسی ملاحظه می‌شود در حالتی که از منبع حرارتی مانند لیزر برای ایجاد گرما استفاده شود، باید تغییرات دمای شبکه خون‌رسانی مویرگی نیز مورد توجه باشد. این درحالی است که اگر فرکانس منبع تولید گرما پایین باشد، می‌توان تعادل حرارتی خون مویرگی و بافت را به عنوان فرض اولیه در نظر گرفت. لذا با توجه به نتایجی که از هر دو مدل به‌دست آمده است، برای مدلسازی ریاضی گرمادرمانی سرطان، لازم است اطلاعات کامل و دقیقی از بافت سرطانی، بافت بستر آن، خواص ترموفیزیکی بافتها، شبکه خون‌رسانی بافت سرطانی و بافتهای اطراف و نوع منبع حرارتی که برای ایجاد گرما استفاده می‌شود، در دسترس باشد.

معرفت و همکاران در [۴] یک مدل ریاضی برای تحلیل حرارتی بافت کبد در گرمادرمانی سرطان کبد به وسیله لیزر ارائه کرده‌اند. در این مدل بافت تومور به شکل یک کره در میان بافت سالم در نظر گرفته شده است. سپس با حل معادلات غیرخطی حاصل، توزیع دما در بافت تومور طی گرمادرمانی، در زمان‌های مختلف محاسبه شده است. با استفاده از این محاسبات اثر پارامترهای مختلف مانند مشخصات لیزر و تغییرات ضرایب اپتیکی بر محدوده اثرگذاری لیزر بررسی شده است. نتایج حاصل می‌تواند پزشکان را برای بدست آوردن یک روش برای گرمادرمانی بی‌خطر به وسیله لیزر برای از بین بردن بافت سرطانی راهنمایی نماید، به‌طوری که آسیب بافت‌های سالم به حداقل برسد.

۲.۲. استفاده از مدل‌سازی ریاضی در درمان متاستاز استخوان. زمانی که سرطان از مکان اولیه خود به مناطق دیگری از بدن گسترش می‌یابد، در اصطلاح متاستاز نامیده می‌شود. ازجمله متاستاز استخوان. متاستاز استخوان زمانی ایجاد می‌شود که سلول‌های سرطانی از مکانی دیگر مانند ریه، کبد، پروستات و ... خود را به استخوان رسانده و در آن رشد می‌کنند. در [۶] یک مدل ریاضی در مورد متاستاز استخوان بر اثر سرطان سینه ارائه شده است. در [۶] مدل ارائه شده یک دستگاه معادلات دیفرانسیل جزیی غیرخطی می‌باشد که هدف از ارائه آن پیدا کردن دستور بهینه استفاده از دارو برای مینیمم کردن حجم تومور با استفاده از کنترل بهینه می باشد. نتایج شبیه‌سازی نشان می‌دهد که با استفاده از دارو طبق دستور بهینه به‌دست آمده برای درمان متاستاز استخوان، تراکم تومور نسبت به مدل بدون دارو کاهش داشته است.

۳.۲. استفاده از مدل‌سازی ریاضی برای رشد و ویفرتراپی نوعی تومور مغزی. ع. فروحی در [۲] یک مدل ریاضی برای بررسی رشد نوعی تومور مغزی به نام گلایوما ارائه کرده است. گلایوما توموری است که از سلول‌های غیرنورونی دستگاه عصبی مرکزی و دستگاه عصبی پیرامونی به نام گلایال در مغز نشأت می‌گیرد. یکی از بدخیم‌ترین انواع گلایوماها، گلیوبلاستوما یا GBM نام دارد. درمان معمول برای GBM جراحی و بعد از آن پرتودرمانی یا شیمی‌درمانی است. امروزه روش‌های درمانی جدیدی برای شیمی‌درمانی مستقیم تومورهای مغزی معرفی شده‌اند. یکی از این روش‌های جدید ویفرتراپی است که در [۷] معرفی شده است. ویفر عبارت است از یک دیسک نازک که در آن داروی ضد سرطان کارموستین بین زنجیره‌های یک نوع پلیمر قرار دارد.

Gliomas
Glial
Glioblastoma
Wafer Therapy
Carmustine

بعد از آن‌که تومور با جراحی برداشته شد، در حفره ایجاد شده به جای تومور چند ویفر قرارد داده می‌شود. کارموستین از ویفر جای‌گذاری شده به مغز نفوذ کرده و تا حدی رشد تومور را مهار می‌کند. به دلیل اینکه در مغز ساختارهای مهم و بافت‌ها بسیار به هم نزدیک هستند، جراحی و برداشتن تومورها در مغز با دشواری و محدودیت‌های زیادی همراه است. همچنین نتیجه پرتودرمانی و شیمی‌درمانی بستگی زیادی به موقعیت، اندازه و بافت تومور و عوامل بیولوژیک دارد. امیدواریم با کمک گرفتن از مدل‌های ریاضی بتوان به شناخت بهتر و بیشتری از چگونگی تشکیل و رشد این تومورها دست یافت.

در مدل ریاضی که در [۲] ارائه شده است، اثر عوامل ژنتیکی، فیزیکی و فیزیولوژیکی بر رشد تومور و همچنین اثر ویفرتراپی به عنوان یک روش درمانی جدید گنجانده شده است. اهمیت این مدل به شرح زیر است.

۱. با استفاده از این مدل به جای معرفی کیفی، می‌توان رشد تومور را به صورت کمی معرفی نمود.
۲. با استفاده از این مدل می‌توان رشد تومور را در اندازه‌هایی که با دستگاه‌های MRI و CT ممکن نیست، شناسایی نمود.
۳. از این مدل می‌توان برای اهدافی مانند رادیوتراپی و شیمی‌درمانی همزمان با ویفرتراپی به جای ویفرتراپی تنها استفاده نمود.
۴. با استفاده از این مدل می‌توان از روشهای کمی در توسعه پیش‌کلینیکی داروهای ضد سرطان استفاده نمود.
۵. از این مدل می‌توان برای تعیین زمان عود تومور بعد از عمل جراحی و ویفرتراپی استفاده نمود.

۴.۲. استفاده از مدل‌سازی ریاضی در درمان فوتودینامیکی تومور مغزی. فوتودینامیک‌تراپی یا PDT یک روش درمانی است که در آن نوعی دارو که به نور حساس است به بیمار تزریق می‌شود. عمده این داروها فوتوفرین است. این دارو به طول موج خاصی از نور واکنش نشان می‌دهد و در زمان تابش آن طول موج به دارو، اکسیژن بسیار فعال منفرد را تولید کرده و سلول‌های مجاور خود را از بین می‌برد [۳] . امروزه فوتودینامیک‌تراپی برای درمان انواع مختلفی از بیماری سرطان مورد استفاده قرار می‌گیرد. بنابر [۵] در این روش درمانی، دارویی که به بیمار تزریق می‌شود طی چند ساعت در تمامی بافت‌های نرم توزیع می‌شود. این دارو تا زمان پرتودهی غیر فعال باقی می‌ماند. ۷۲ــ۴۸ ساعت پس از تزریق مقدار زیادی از این دارو که در بافت‌های سالم جذب شده است، دفع می‌شود. این در حالی است که غلظت دارو در سلول‌های تومور حتی بعد از ۱۰ــ۷ روز نیز چندان کاهش نمی‌یابد. از آنجا که دارو در تمامی بدن توزیع شده است، لازم است بیمار تا مدتی از مواجه با طول موج‌های موثر بر دارو دور باشد. زیرا نور خورشید یا نور مصنوعی قادر است مقادیر باقی مانده از دارو در بافت‌های سالم را فعال کرده و موجب تخریب سلول‌های سالم شود. تخریب سلول‌های تومور توسط اکسیژن فعال منفردی که از فعل و انفعال بین اکسیژن پایه و داروی فعال شده از تابش نور ایجاد شده است، انجام می‌شود. لذا روش PDT به شدت تحت تاثیر وجود اکسیژن ملکولی در بافت است.

کیوان و همکاران در [۳] در روش درمان فوتودینامیکی تومور مغزی، نحوه توزیع اکسیژن در بافت بعد از تابش لیزر و شروع درمان را با استفاده از یک مدل ریاضی که در آن تومور کره فرض شده است، بررسی نموده‌اند. همچنین برای حل معادلات حاصل از مختصات کروی استفاده شده است. با استفاده از این مدل و حل معادلات ریاضی حاصل در [۳]، نتایج زیر در مورد نحوه توزیع اکسیژن در بافت بعد از تابش لیزر و شروع درمان مشخص شده است.

۱. هرچه به مناطق عمیق‌تر تومور نزدیک می‌شویم، مقدار اکسیژن کمتر می‌شود تا جایی که به صفر می‌رسد.
۲. در نواحی نزدیک بافت سالم بیشترین مقدار اکسیژن وجود دارد و در نواحی دورتر که مربوط به نواحی عمیق‌تر تومور است، غلظت اکسیژن به شدت کاهش می‌یابد.
۳. غلظت اکسیژن ۱ ثانیه بعد از تابش لیزر در تمام نقاط تومور محاسبه شده است که مشاهده می‌شود در تمام این نقاط غلظت اکسیژن کاهش یافته است.
۴. به منظور فهم بهتر موضوع، تحولات تغییر غلظت اکسیژن بر حسب زمان برای یک موقعیت خاص ۴۰ میکرو متری از شعاع تومور مشخص شده است. ملاحظه می‌شود که ۷ ثانیه بعد از تابش لیزر غلظت اکسیژن نزدیک به صفر و تقریبا ثابت شده است.

Photodynamic Therapy
Photofrin

با توجه به نتایج بالا، مشخص می‌شود طی درمان فوتودینامیکی به دلیل مصرف اکسیژن، در تمام نقاط بافت تومور اکسیژن کاهش می‌یابد. در این شرایط ادامه تابش لیزر تاثیری در پروسه‌ی درمان نخواهد داشت. بنابراین پس از مقداری تابش می‌توان تابش لیزر را قطع نمود تا اکسیژن از دست رفته دوباره تولید شود و پس از آن درمان ادامه یابد.

۳. نتیجه گیری

مطالعه ساختار بدن انسان به عنوان یک سیستم و به تبع آن به‌کارگیری مدلسازی‌ها و معادلات ریاضی حاکم بر آن ما را به درک بهتر و دقیق‌تری از بدن انسان و چگونگی مقابله با عوامل بیماری‌زا رهنمون خواهد شد. پرواضح است که تکامل مدل‌های ریاضی ساخته شده و در نظر گرفتن فرضیه‌های دقیق‌تر ما را به نتایج صحیح‌تر و به واقعیت نزدیک‌تر خواهد رساند.

مراجع

[۱] م. ب. آیاتی، ج. ابوالفضلی اصفهانی، م. بلالی و م. س. مهاجر، *روش‌های مدل‌سازی درمان حرارتی سرطان*، مجموعه مقالات دومین همایش کاربرد ریاضیات و نظریه کنترل در پزشکی (۲۰۰۹)، ۱۲ـ۳۰.

[۲] ع. فروحی، *مدل ریاضی برای رشد و ویفرتراپی گلایوبلاستوما*، مجله دانشگاه علوم پزشکی گیلان ۱۹ (۱۳۸۹)، شماره ۷۳، ۱ـ۱۲.

[۳] م. ا. کیوان، ف. رضایی و ش. تشکری، *مدل سازی ریاضی روش درمان فتودینامیکی در تومور مغزی با بررسی نرخ مصرف اکسیژن*، مجموعه مقالات بیست و سومین کنفرانس اپتیک و فوتونیک و نهمین کنفرانس مهندسی و فناوری فوتونیک ایران (۱۳۹۵)، ۶۵۳ـ۶۵۶.

[۴] م. معرفت، م. مختاری دیزجی و ز. حداد سلیمانی، *مدلسازی لیزر درمانی بافت کبد با در نظر گرفتن اثر ذوب چربی*، مهندسی پزشکی زیستی ۳ (۱۳۸۸)، شماره ۳.

[۵] م. ح. میران بیگی، م. نجفی و ن. نقوی، *مدل سازی روش فوتودینامیکتراپی در درمان سرطان پستان با پیشرفت قفسه سینه‌ای*، لیزر پزشکی ۴ (۱۳۸۵)، شماره ۴، ۲۲ـ۲۹.

[۶] م. نیکبخت، ع. فخارزاده جهرمی و ع. حیدری، *ارائه یک مدل ریاضی برای جلوگیری از پیشرفت متاستاز استخوان با استفاده از کنترل بهینه*، تحقیق در عملیات در کاربردهای آن ۱۲ (۱۳۹۴)، شماره ۴، ۶۰ـ۴۷.

[7] Hammoud, DA., Belden, CJ, HO AC., Dal Pan, GJ., Herskovits, EH., Hilt, DC., Brem, H., & Pomper, MG.(2003). The Surgical Bed After BCNU Polymer Wafer Placement for Recurrent Glioma. *Serial Assessment on CT and MRI Imaging*, 180, 1469-1475.

گروه ریاضی، دانشگاه فنی و حرفه‌ای، تهران، ایران
Email address: masoudiar@gmail.com

مدل‌سازی آماری داده‌ها بر اساس آمار توصیفی

مهدی مهدی‌زاده

چکیده. در بسیاری از مسائل استنباط آماری پارامتری، تعیین دقیق توزیع احتمالی اهمیت ویژه‌ای دارد. یک انتخاب نامناسب برای توزیع جامعه می‌تواند به نتایج نادقیق و حتی گمراه کننده منجر شود. گشتاورها یکی از مشخصه های مهم برای هر توزیع هستند. این مقاله به موضوع انتخاب مدل احتمالی برای داده‌ها بر اساس ضرایب چولگی و کشیدگی گشتاوری می‌پردازد. با استفاده از نرم‌افزار R ، کاربرد روش مطرح شده را در مورد یک مجموعه داده پزشکی نشان می‌دهیم.

کلمات کلیدی: ضریب چولگی، ضریب کشیدگی، مدل‌سازی آماری.

۱. مقدمه

نظریه توزیع‌ها ابزاری قوی برای مدل‌سازی آماری پدیده‌ها در علوم مختلف بوده و تحقیقات زیادی در این زمینه انجام شده است. تحت شرایطی، روش‌های آماری توسعه یافته بر مبنای فرض‌های توزیعی، نسبت به معادل ناپارامتری خود کاراتر هستند. به عنوان نمونه می‌توان به توزیع‌های نرمال و نمایی اشاره کرد که شکل ریاضی انعطاف پذیری دارند و رویه‌های آماری بسیاری بر اساس آنها پیشنهاد شده‌اند.

انتخاب توزیعی که برازش مناسب به داده‌ها دارد، یک گام مهم در استنباط آماری پارامتری است. در این مقاله، روش انتخاب چنین توزیعی را بر اساس گشتاورها مطالعه می‌کنیم. در بخش ۲ ، ابتدا گشتاورهای مختلف یک توزیع را معرفی کرده و قضیه‌ای درباره مشخصه‌سازی یک توزیع بر حسب گشتاورهای آن بیان می‌کنیم. سپس، ضرایب چولگی و کشیدگی گشتاوری ارائه می‌شوند. در پایان، روش انتخاب مدل احتمالی مناسب برای داده‌ها بر اساس این ضرایب را مطرح می‌کنیم. در بخش ۳، کاربرد روش معرفی شده را به کمک نرم‌افزار R نشان می‌دهیم.

۲. انتخاب توزیع بر اساس ضرایب چولگی و کشیدگی

می‌دانیم اطلاع کامل درباره متغیر تصادفی X در تابع جرم یا چگالی احتمال آن وجود دارد. اما در برخی کاربردها، تنها آگاهی از چند مشخصه یا پارامتر در مورد X کافی است. گشتاورها یکی از مشخصه‌های مهم برای هر متغیر تصادفی هستند. تحت شرایطی، گشتاورها توزیع یک متغیر تصادفی را به طور یکتا مشخص می‌کنند.

گشتاور مرتبه r ام متغیر تصادفی X حول مبدأ به صورت زیر تعریف می‌شود

$$\mu'_r = E(X^r),$$

که در آن r یک عدد طبیعی است. μ'_1 امید ریاضی متغیر تصادفی X نامیده می‌شود و آن را با μ نشان می‌دهیم. طبق قضیه زیر، هر توزیع به طور یکتا توسط μ'_r ها مشخص می‌شود (روهتگی و احسانز صالح [۴] ، ص ۸۹).

رده بندی موضوعی۲۰۱۰: ۶۲G۰۵، ۹۷K۴۰.
سخنران: مهدی مهدی‌زاده.

قضیه ۱.۲. فرض کنید μ'_r دنباله گشتاورهای متغیر تصادفی X حول مبدأ است. اگر برای یک t مثبت، سری

$$\sum_{r=1}^{\infty} \frac{\mu'_r}{r!} t^r$$

مطلقاً همگرا باشد، آنگاه توزیع X به طور یکتا توسط μ'_r ها مشخص می‌شود.

گشتاور مرکزی مرتبه r ام متغیر تصادفی X به صورت زیر تعریف می‌شود

$$\mu_r = E(X-\mu)^r,$$

که در آن r یک عدد طبیعی است. μ_2 واریانس متغیر تصادفی X نامیده می‌شود و آن را با σ^2 یا $Var(X)$ نشان می‌دهیم. به کمک بسط دو جمله‌ای می‌توان گشتاورهای مرکزی را بر حسب گشتاورهای حول مبدأ بیان کرد.

برخی شاخص‌های مهم توزیعی بر حسب گشتاورها بیان می‌شوند. ضریب چولگی و ضریب کشیدگی دو شاخص مهم برای شکل توزیع هستند که به ترتیب عبارت‌اند از

$$\gamma_1 = \frac{\mu_3}{\sigma^3},$$

و

$$\gamma_2 = \frac{\mu_4}{\sigma^4} - 3.$$

یک ضریب چولگی غیر صفر، عدم تقارن توزیع را نشان می‌دهد. ضریب کشیدگی، وزن دُم‌های توزیع را در مقایسه با توزیع نرمال اندازه می‌گیرد که برای آن، مقدار ضریب کشیدگی برابر است با ۳.

فرض کنید $x_1, \ldots, x_n$ مشاهدات یک نمونه تصادفی به حجم n از جامعه مورد نظر باشند. در این صورت، برآورد ضرایب فوق به ترتیب عبارت‌اند از

$$g_1 = \frac{m_3}{m_2^{1.5}},$$

و

$$g_2 = \frac{m_4}{m_2^2} - 3,$$

که در آن

$$m_r = \frac{1}{n}\sum_{i=1}^{n}(x_i - \bar{x})^r, \quad r = 2, 3, 4, \ldots,$$

گشتاور مرکزی مرتبه r ام نمونه، و $\bar{x}$ میانگین نمونه است. شایان ذکر است که شکل اصلاح شده‌ای از برآوردگرهای فوق وجود دارد که نااریب هستند:

$$G_1 = \frac{\sqrt{n(n-1)}}{n-2} g_1,$$

و

$$G_2 = \frac{n-1}{(n-2)(n-3)} \left[(n+1)g_2 + 6\right].$$

برای جزئیات بیشتر درباره این برآوردگرها به جوآنز و گیل [۲] مراجعه کنید.

قضیه ۱.۲ اهمیت گشتاورهای یک توزیع را نشان می‌دهد. ضرایب چولگی و کشیدگی، توابعی از گشتاورها هستند که اطلاعات مفیدی درباره شکل توزیع در بر دارند. بنابراین، انتخاب مدل احتمالی برای یک مجموعه داده می‌تواند بر مبنای این ضرایب باشد. یک روش منطقی آنست که توزیعی را انتخاب کنیم که دامنه مقادیر ضرایب چولگی و کشیدگی آن، شامل مقادیر ضرایب G_1 و G_2 برای مجموعه داده مورد نظر باشد. کولن و فری [۱] نمودار چولگی‌ـ کشیدگی را پیشنهاد کردند که استفاده از روش فوق را آسان می‌کند. در بخش بعد، از بسته fitdistrplus در نرم‌افزار R برای رسم این نمودار استفاده می‌کنیم. این بسته، امکانات مفیدی برای برازش توزیع‌های احتمالی به انواع داده‌ها دارد (دلیگنت‌ـ مولر و داتنگ [۳]).

۳. کاربرد

داده‌های موسسه ورزش استرالیا به طور گسترده در مطالعه توزیع‌های چوله استفاده شده‌اند. این داده‌ها شامل اندازه‌گیری ۱۳ متغیر در مورد ۲۰۲ ورزشکار (۱۰۰ زن و ۱۰۲ مرد) استرالیایی هستند. یکی از این متغیرها، تعداد گلبول‌های قرمز خون است که در این بخش از آن استفاده می‌شود. برای دسترسی به داده‌های این متغیر، ابتدا بسته sn را در نرم‌افزار R نصب می‌کنیم. با اجرای دستورات زیر، داده‌های مربوط به زنان ورزشکار در بردار RBC ذخیره می‌شود:

```
library(sn)
data(ais)
RBC=ais[,3][1:100]
```

برای تشخیص توزیع مناسب، ابتدا بسته fitdistrplus را نصب و سپس دستورات زیر را به کار می‌بریم:

```
library(fitdistrplus)
descdist(RBC)
```

مقدار آماره‌های توصیفی به صورت زیر در خروجی گزارش می‌شود:

```
> descdist(RBC)

summary statistics
------
min:  3.8   max:  5.33
median:  4.385
mean:  4.4045
estimated sd:  0.3208964
estimated skewness:  0.7032466
estimated kurtosis:  3.382149
```

که در آن ضرایب چولگی و کشیدگی بر اساس G_1 و G_2 محاسبه شده‌اند. با توجه به مقدار این ضرایب می‌توان دید که توزیع متغیر مورد نظر، چولگی مثبت دارد و کشیدگی آن نسبت به توزیع نرمال بیشتر است.

نمودار چولگی ـ کشیدگی متناظر نیز در شکل ۱ آمده است. نقطه مرجع در این نمودار (دایره آبی رنگ توپُر)، مقادیر G_1^2 و G_2 را برای داده‌ها را نشان می‌دهد. ناحیه متناظر با مقادیر γ_1^2 و γ_2 برای توزیع‌های رایج نیز رسم شده است. مقدار چولگی و کشیدگی برخی توزیع‌ها (مثل نرمال، یکنواخت، لوژستیک و نمایی)، مستقل از پارامترها بوده و یک عدد ثابت است. بنابراین، توزیع با یک نقطه روی نمودار مشخص می‌شود. مجموعه مقادیر ممکن برای چولگی و کشیدگی در برخی توزیع‌ها (مثل گاما و لگ‌نرمال) به صورت یک خط، و در برخی توزیع‌های دیگر (مثل بتا) شامل نواحی بزرگتر است. هر چقدر نقطه مرجع به ناحیه متناظر یک توزیع نزدیکتر باشد، آن توزیع برای برازش به داده‌ها مناسب‌تر است. با توجه به موقعیت نقطه مرجع، توزیع‌های گاما و لگ‌نرمال را برای مدل‌سازی داده‌های تعداد گلبول‌های قرمز خون به کار می‌بریم. توزیع بتا به دلیل محدود بودن تکیه‌گاه آن، انتخاب نمی‌شود.

به عنوان مثال، برای برازش توزیع گاما با روش ماکسیمم درستنمایی به داده‌ها کافی است دستورات زیر را اجرا کنیم:

```
mle.g=fitdist(RBC,"gamma")
summary(mle.g)
```

خروجی متناظر در پنجره R Console به صورت زیر است:

```
> mle.g=fitdist(RBC,"gamma")
> summary(mle.g)

Fitting of the distribution ' gamma ' by maximum likelihood
Parameters :
       estimate Std. Error
shape 195.44155  27.613943
rate   44.37324   6.277526
```

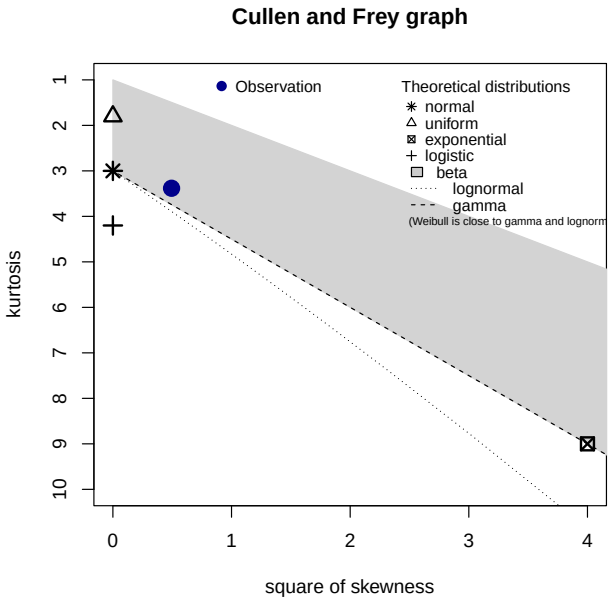

شکل ۱: نمودار چولگی_ کشیدگی برای داده‌های تعداد گلبول‌های قرمز خون

```
Loglikelihood:  -26.2235   AIC:  56.44701   BIC:  61.65735
Correlation matrix:
          shape      rate
shape 1.0000000 0.9987209
rate  0.9987209 1.0000000
```

اگر چند توزیع رقیب برای برازش به یک مجموعه داده وجود داشته باشند، می‌توان آنها را بر اساس شاخص‌هایی با هم مقایسه کرد. یک معیار ساده، لگاریتم تابع درستنمایی به ازای برآورد ماکسیمم درستنمایی پارامترها است. هر چقدر این کمیت بزرگتر باشد، توزیع متناظر برازش بهتر دارد. استفاده از این معیار زمانی مجاز است که توزیع‌های رقیب دارای تعداد پارامتر یکسان باشند. در غیر این صورت، می‌توان از معیار اطلاع آکائیکه (AIC) و معیار اطلاع بیزی (BIC) استفاده کرد. هر چقدر این کمیت‌ها کوچکتر باشد، توزیع متناظر برازش بهتر دارد. شایان ذکر است که افزایش تعداد پارامترها در شاخص BIC بیشتر جریمه می‌شود.

مراجع

[1] A.C. Cullen, H.C. Frey. *Probabilistic Techniques in Exposure Assessment, 1st Edition.* Plenum Publishing Co., 1999.

[2] D. Joanes, C. Gill. *Comparing measures of sample skewness and kurtosis Comparing measures of sample skewness and kurtosis.* Journal of the Royal Statistical Society: Series D (The Statistician) 47 (1998), 183-189.

[3] M.L. Delignette-Muller, C. Dutang. *fitdistrplus: An R Package for Fitting Distributions.* Journal of Statistical Software 64 (2015), 1–34.

[4] V.K. Rohatgi, A.K.Md. Ehsanes Saleh. *An Introduction to Probability and Statistics, 3rd Edition.* Wiley, New York, 2015.

گروه آمار، دانشگاه حکیم سبزواری

E-mail address: mahdizadeh.m@hsu.ac.ir, mahdizadeh.m@live.com

شناسایی رفتار دینامیکی داده‌های رشد-مهار بیماری به‌وسیله‌ی ابزار یادگیری ماشین

۱ دکتر حسین خیری و ۲ یونس یوسف‌پور

چکیده. در حالی‌که مدل‌های یادگیری ماشین با نرخ دقت بالای خود، نمایش‌های امیدوارکننده‌ای از خود بروز می‌دهند، یک چالش دایمی در عدم تفسیرپذیری آن‌ها نهفته است. توانایی ادراک و توصیف فرآیندهای تصمیم‌گیری این مدل‌ها در جلب اعتماد و تسهیل پذیرش آن‌ها در محیط‌های مراقبت بهداشتی در دنیای واقعی بسیار مهم است. در پاسخ به این چالش‌ها، تلفیق چارچوب‌های ریاضی با شیوه‌های یادگیری ماشین پاسخ قانع‌کننده‌ای ارائه می‌دهد که نقاط قوت هر دو رویکرد را در هم می‌آمیزد. در این مقاله با نگرشی به کاربرد ریاضیات در علوم پزشکی سعی کرده‌ایم تا با به‌کارگیری تکنیک‌های یادگیری ماشین به شناسایی دینامیک الگو از روی داده‌های موجود بپردازیم.

واژه های کلیدی: شناسایی دینامیک، یادگیری ماشین، الگوی ریاضی.

۱. پیش‌گفتار

پدیده‌ی هوش مصنوعی و یادگیری ماشین در سال‌های اخیر تحولی شگرف در بسیاری از کاربردها به‌ویژه شاخه‌های گوناگون علوم ایجاد کرده است. یادگیری ماشینی دسته‌ای از توان‌مندی‌های رایانشی است که سبب می‌شود رایانه‌ها بدون نیاز به یک برنامه‌ی صریح، در مورد یک موضوع ویژه یاد بگیرند[۴]. دانش یادگیری ماشین در دهه‌ی کنونی به‌لطف فن‌آوری یادگیری ژرف جهش‌های خیره‌کننده‌ای داشته است و در بسیاری زمینه‌ها از جمله علوم، مهندسی، کسب و کار، زبان‌شناسی و پزشکی کاربرد دارد[۳]. همچنان‌که هر پدیده‌ی نوظهوری می‌تواند هم‌زمان، سودبخشی‌ها و آسیب‌هایی به‌همراه داشته باشد، پدیده‌ی هوش مصنوعی نیز از این ویژگی مستثنی نیست، لیکن آثار مثبت آن بسیار بارز است.

آلن تورینگ نخستین کسی بود که در زمینه‌ای که خود، آن‌را هوش ماشینی نامید، پژوهش‌های بنیادین انجام داد[۵]. هوش مصنوعی به‌عنوان یک رشته‌ی دانشگاهی در سال ۱۹۵۶.م بنیان‌گذاری شد. این دانش نوپا، پله‌های پیشرفت را یکی پس از دیگری پشت سر گذاشت، اما پس از مدتی، دوره‌هایی از افول را که به‌عنوان زمستان هوش مصنوعی شناخته می‌شود، تجربه نمود[۶]. پس از سال ۲۰۱۲.م، زمانی که یادگیری ژرف از تمام شگردهای هوش مصنوعی پیشی گرفت، سرمایه‌گذاری‌ها و گرایش‌ها را به سمت خود جلب کرد[۶].

۲. توصیف و بررسی الگو

رویکردهای مدل‌سازی ریاضی در تحقیقات پزشکی به‌ویژه بیماری سرطان، پرکاربرد هستند، چراکه این رویکردها به‌واسطه‌ی کمّی بودن، می‌توانند اعتبار فرضیه‌های گوناگون مرتبط با پویایی سرطان را بهبود بخشیده، به تبَع آن، روشنگری‌های ارزنده‌ای درخصوص سازوکارهای پیوسته و پیچیده در این زمینه داشته باشند [۲]. در اینجا قصد آن داریم تا به‌عنوان نمونه به یک الگوی رشد و درمان توموری که در [۱] ارائه شده است پرداخته، روند آن را با گذشت

رده بندی موضوعی۲۰۱۰: ...،...
سخنران: یونس یوسف پور .

Artificial intelligence
Machine learning
Deep learning
Alan Turing

جدول ۱: شرح پارامترها و مقادیر آن‌ها [۱]

پارامتر	عنوان	مقدار	یکا
r	سرعت رشد درونی تومور	$(0.006, 0.03)$	day^{-1}
K	بیشینه گنجایش پیرامونی برای رشد تومور	10^3	cm^3
δ	بیشینه نرخ نابودی تومور به‌وسیله‌ی سیتوکین	0.1	day^{-1}
m	ثابت نیمه‌اشباع نرخ نابودی تومور	1.0	cm^3
β	بیشینه نرخ تولید $\mathrm{CD4^+T}$	$varied$	day^{-1}
k	ثابت نیمه‌اشباع نرخ تولید $\mathrm{CD4^+T}$	10	cm^3
a	نرخ مرگ و میر سلولهاي $\mathrm{CD4^+T}$	$(0.01, 0.18)$	day^{-1}
α	بیشینه نرخ تولید سیتوکین	0.1	day^{-1}
b	ثابت نیمه‌اشباع نرخ تولید سیتوکین	0.1	cm^3
μ	نرخ از دست دادن سیتوکین	$(47, 77)$	day^{-1}
I_1	درمان به‌وسیله‌ی $\mathrm{CD4^+T}$	$varied$	$\mathrm{cm}^3\mathrm{day}^{-1}$
I_2	درمان به‌وسیله‌ی سیتوکین	$varied$	$\mathrm{cm}^3\mathrm{day}^{-1}$

زمان با به‌کارگیری ابزارهای پیش‌بینی کننده‌ی یادگیری ماشینی بررسی نماییم. مدل پیشنهادی به این‌صورت است:

$$\begin{aligned} \dot{x}(t) &= rx\Big(1 - \frac{x}{K}\Big) - \frac{\delta xz}{m + x} \ , \\ \dot{y}(t) &= \frac{\beta xy}{k + x} - ay + I_1 \ , \\ \dot{z}(t) &= \frac{\alpha xy}{b + x} - \mu z + I_2 \ . \end{aligned} \tag{۱.۲}$$

در این الگو، x، y و z به‌ترتیب نشانگر شمار سلول‌های توموری، سلول‌های $\mathrm{CD4^+T}$ و مقدار سیتوکین در زمان t هستند. مبنای طرح این الگو بر به‌کارگیری ظرفیت‌های ایمنی‌درمانی است. به‌عبارتی رفتار درازمدت ایمنی‌درمانی صرفا با تقویت سامانه‌ی ایمنی بدن و بدون به‌کارگیری درمان‌های تضعیف کننده‌ی بدن، هدف اساسی از طرح این مدل است. بررسی نقاط تعادل این دستگاه دینامیکی و نوع پایداری آن‌ها در [۱] موجودند، همچنین شرح پارامترها و مقادیر آنها در جدول ۱ آمده است. وجود جواب، مثبت بودن و کرانداری آن به ازای شرایط آغازین نامنفی در [۱] بررسی شده‌اند. مولفان در این پژوهش، نتایج تحلیلی ارائه شده‌ی خود را بر اساس ارزیابی‌های مقادیر پارامتر برگرفته از منابع، از جمله داده‌های تجربی به‌دست آمده از پژوهش‌های خود و دیگر محققان، به‌دست آورده‌اند.

۳. آموزش‌پذیری دینامیک الگو با فرآیندهای یادگیری ماشینی

شیوه‌های عددی به‌ویژه در حل معادلات دیفرانسیل، سهم به‌سزایی در گره‌گشایی بن‌بست‌های محاسباتی و تحلیلی مسائل دارند. با این وجود، به‌سبب وابستگی پاسخ‌ها به نقاط آغازین، همچنین طول گام انتخابی، از آنجا که محاسبات، اغلب به‌صورت گام‌به‌گام پیش می‌روند، هرگونه تغییر در شرایط معادله، از جمله جابه‌جایی نقطه‌ی مطلوب، به احتمال زیاد منجر به بازنگری محاسبات از ابتدا خواهد شد. این محدودیت می‌تواند به وسیله‌ی پیاده‌سازی مدل در قالب شبکه‌های عصبی مصنوعی و ارتقای آن با فنون یادگیری ماشین برچیده شود. کاری که در این پژوهش انجام دادیم، نخست انتخاب مجموعه‌ای از نمونه‌های متوالی بود که می‌خواستیم توسط ماشین آموزش دیده شود. این نمونه ممکن است برگرفته از داده‌های یک موسسه‌ی درمانی یا آزمایشگاهی درباره‌ی دسته‌ی مشخصی از نوعی بیماری باشد که ما در اینجا بیماری سرطان را برگزیدیم. برای شفافیت بیشتر موضوع، داده‌ها را از روی مدل (۱.۲)

cytokine

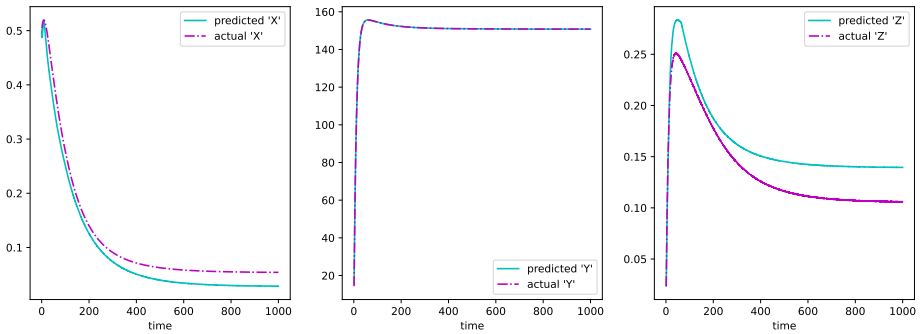

(آ) عدم انطباق کافی

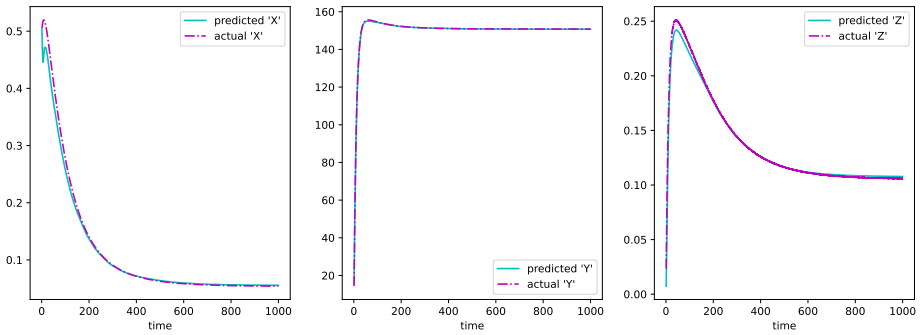

(ب) حذف آشفتگی با به‌کارگیری الگوریتم میانگین متحرک

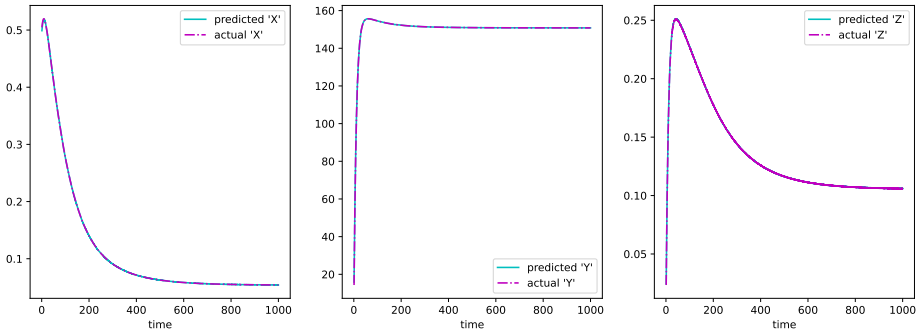

(ج) حذف آشفتگی با رویکرد افراز مجموعه‌ی داده‌ها

شکل ۱: پیش‌بینی و شناسایی دینامیک الگو به‌وسیله‌ی ابزار پیش‌بینی کننده‌ی یادگیری ماشین (نمودار انطباقی)

و ترجیحا به‌وسیله‌ی یکی از روش‌های عددی حل معادلات به‌دست آوردیم. در ادامه با به‌کارگیری زبان برنامه‌نویسی پایتون و قابلیت‌های ابزار کتابخانه‌ای مناسب، از روی داده‌های در دسترس، نتایج حاصل از یادگیری و پیش‌بینی را به‌دست آوردیم. ما این کار را با استفاده از ابزار کتابخانه‌ی tensorflow.keras انجام دادیم. این کتابخانه یک

Python

رابط برنامه نویسی کاربردی (API) شبکه‌های عصبی سطح بالاست که به زبان پایتون نوشته شده است و ایجاد و آموزش مدل‌های یادگیری ماشین، به ویژه شبکه‌های عصبی ژرف را ساده می‌کند، همچنین دارای رویکردی کاربرپسند برای ساخت، آموزش و ارزیابی مدل‌های یادگیری ماشین است. پس از آنکه داده‌ها در اختیار برنامه گذاشته شد، آن‌ها را وارد چرخه‌ی آموزش شبکه‌ای نمودیم. عملکرد کلی در این مرحله چنین است که پس از هر گذر رو به جلو در شبکه، وزن‌های شبکه تا اندازه‌ای که خروجی آن با خروجی واقعی به تطابق کافی برسد، اصلاح می‌شوند، سپس شبکه، خروجی را با توجه به داده‌ی جدید پیش‌بینی می‌کند. یعنی با به‌کارگیری تابع مناسب، عملیات محاسباتی روی داده‌های ورودی انجام گرفته، پارامترهای شبکه که پیش‌تر اصلاح شده‌اند، در تولید خروجی، مورد استفاده قرار می‌گیرند.

با این‌حال پس از اجرای برنامه، آن‌چه انتظار داشتیم به‌طور کامل برآورده نشد. درواقع با چالشی جدید مواجه شدیم. بخش‌های قابل توجهی از داده‌های پیش‌بینی شده نه‌تنها با داده‌های واقعی مطابقت نداشتند، بلکه دچار آشفتگی‌های زیادی شده بودند (شکل۱ آ). به همین سبب برآن شدیم تا با پیاده‌سازی الگوریتم میانگین متحرک به مقابله با این مشکل بپردازیم. این کار تا حد زیادی امیدوارکننده بود. درواقع آشفتگی‌ها از بین رفته بودند ولی عدم تطبیق در برخی مقادیر مشهود بود (شکل۱ ب). از این‌رو شیوه‌ی دیگری درپیش گرفته شد تا اینکه بتوانیم به تطابق قابل قبول دست یابیم. این شیوه عبارت بود از افراز داده‌ها. یعنی در این شیوه، پیش بینی‌ها روی زیرقطعه‌های مشخصی از داده‌ها انجام گرفته، در نهایت به هم الحاق شدند (شکل۱ ج). با این‌حال هرکدام از شیوه‌های گفته شده در شرایطی خاص می‌تواند بر دیگری برتری داشته باشد.

۴. نتیجه‌گیری

آنچه در این پژوهش به آن پرداخته شده، بررسی آموزش‌پذیری داده‌های یک بیماری است. به‌عبارتی دیگر، تلاشی است برای پاسخ به این پرسش که آیا ماشین، این توان‌مندی را دارد که دینامیک یک الگو را درک کرده و در گامی فراتر، رفتار آن را پیش‌بینی کند؟ بررسی‌های عددی به‌طور ضمنی پاسخی مثبت به این پرسش می‌دهند. قابلیت شناسایی و درک‌پذیری الگوها توسط ماشین می‌تواند بستر بسیار مناسبی برای پژوهش‌های بیشتر در این حوزه پدید آورد.

مراجع

[1] Anderson, Luke, Sophia Jang, and Jui-Ling Yu. "Qualitative behavior of systems of tumor–CD4+–cytokine interactions with treatments." Mathematical Methods in the Applied Sciences 38, no. 17 (2015): 4330-4344.

[2] Padmanabhan, Regina, Nader Meskin, and Ala-Eddin Al Moustafa.*Mathematical models of cancer and different therapies.* Singapore: Springer, 2021.

[3] Russell, Stuart J., and Peter Norvig, *Artificial intelligence: a modern approach.* Pearson, 2016.

[4] Piryonesi, S. Madeh, and Tamer E. El-Diraby, *Data analytics in asset management: Cost-effective prediction of the pavement condition index.*, Journal of Infrastructure Systems 26, no. 1 (2020): 04019036.

[5] Copeland, B. Jack, ed. The essential turing. Clarendon Press, 2004.

[6] Russell, Stuart J., and Peter Norvig. Artificial intelligence: a modern approach. Pearson, 2016.

گروه ریاضی کاربردی دانشگاه تبریز
Email address: h-kheiri@tabrizu.ac.ir

گروه ریاضی کاربردی دانشگاه تبریز
Email address: yonesmail4@gmail.com

Application Programming Interface
Moving Average

بررسی آموزش مدلسازی ریاضی و ایجاد ارتباط بین علوم ریاضی و زندگی روزمره بر پیشرفت تحصیلی ریاضی دانش آموزان

۱ فاطمه یوسف زاده درزی

چکیده. هدف از این مطالعه بررسی تاثیر آموزش مدلسازی ریاضی و ایجاد ارتباط بین علوم ریاضی و زندگی روزمره بر پیشرفت ریاضی دانش آموزان می باشد.جامعه آماری مورد این پژوهش را دانش آموزان متوسطه اول (پایه نهم) شهرستان سیمرغ ۴۳۲ نفر تشکیل می دهد. با استفاده از روش نمونه گیری در دسترس،تعداد نمونه که ۱۱۰ نفر بودند که ۵۵ نفر در گروه آزمایش و ۵۵ نفر که در گروه کنترل قرار داشتند، برنامه اجرا گردید.سپس برای گروه آزمایش برنامه آموزش به روش حل مسائله مدلسازی ریاضی اجرا گردید و گروه کنترل به روش قبلی آموزش دیدند.در این پژوهش، برای جمع آوری داده ها از آزمون معلم ساخته استفاده شد. روایی و پایایی ابزار توسط معلمان ریاضی و سرگروه آموزشی به تایید رسیده است. جهت تجزیه و تحلیل داده های به دست آمده ازآزمون تی مستقل استفاده شد. نتایج این تحقیق نشان می دهد که پیشرفت تحصیلی ریاضی و نمره ریاضی گروهی که در برنامه آموزش مدلسازی ریاضی شرکت می کنند به طور معنا داری بیشتر ازگروه کنترل می باشد. همچنین دانش آموزانی که در درس ریاضی ضعیف بودند بیش از دانش آموزان قوی از برنامه آموزش مدلسازی ریاضی سود بردند.

کلمات کلیدی: مدلسازی ریاضی، پیشرفت تحصیلی

۱. مقدمه

یکی از موضوعات با اهمیت قرن ۱۲ توانایی افراد در حل مسائل در زمینه های واقعی است.توانایی به کارگیری ریاضی در دنیای واقعی و حل مسائل خارج از کلاس درس، چیزی فراتر از داشتن دانش ریاضی است که مدلسازی می تواند در این زمینه مفید باشد. مدلسازی ریاضی این امکان را فراهم می کند تا دانش آموزان ارزش واقعی ریاضیات را به عنوان یک ابزار اساسی و کاربردی در جامعه، درک کنند.با توجه به اهمیت روز افزون ریاضیات در تکنولوژی و زندگی در عصر جدید، مدلسازی به یکی از موضوعات برجسته در دهه های اخیر تبدیل شده است. مدلسازی به عنوان یک روش قدرتمند برای دست یافتن به یادگیری معنادار در ریاضیات است، زیرا درک دانش آموزان را از مفاهیم کلیدی تقویت می کند.مدلسازی ریاضی به عنوان پلی عمل می کند که بین ریاضی یاد گرفته شده در مدرسه و ریاضی به کاربرد شده در جامعه رابطه برقرار می نماید. مدلسازی ریاضی این فرصت را برای دانش آموزان ایجاد می کند تا بتوانند دانش خود را در زمینه های واقعی به کار برند.مدلسازی می تواند به این سوال پاسخ گوید که فایده یادگیری ریاضیات چیست؟ زیرا در برخی موارد، از نظردانش آموزان ، ریاضیات مدرسه ای به عنوان فعالیتی است که جدا از زندگی واقعی افراد می باشد و تنها در حل مسائل مطرح شده در کلاس درس، کاربرد دارد. با این حال ریاضیات یک روش نظام مند تفکر است که با استفاده از مدلسازی راه حل هایی برای موقعیت های واقعی تولید می کند و یکی از کارآمد ترین ابزارها در جهت جست و جوی راه حل هایی برای مسائل دنیای واقعی است.امروزه افراد در جامعه با داده های بسیار زیادی توسط ها روبه رو هستند.تا پیش از این کار، کار را با داده های پیچیده تا این اندازه مورد نیاز نبوده است.دنیا پیوسته در حال تغییر است.بنابراین رویکرد جدیدی برای حل مسائل و تصمیم گیری مورد نیاز است. این رویکرد جدید رویکرد مدلسازی است.یعنی باید به کاربردهای ریاضیات در حوزه های مختلف توجه کنیم که این توجه می تواند در قالب مدلسازی، ارائه شود.(نیس و گالبریت ، ۲۰۱۷). یکی از اهداف آموزش ریاضی در عصر جدید رشد فهم افراد از مفاهیم ریاضی ارتقای آنها در استفاده

رده بندی موضوعی۲۰۱۰: ....،...
سخنران: فاطمه یوسف زاده درزی .

از استراتژی های مختلف و افزایش توانایی آنان در به کار بردن ریاضی در موقعیت های اجتماعی و حرفه ای است. (اسکلورک،۲۱۱۲) .آموزش ریاضی باید موقعیت های چالش برانگیز را ایجاد کند. به تقویت خلاقیت و رشد مهارتهای ریاضی بپردازند و مهمترین اصل در این مورد این می باشد که باید توانایی به کار بردن ریاضی را در زندگی واقعی برای افراد ایجاد کند .درنتیجه یادگیری ریاضیات باید شرایطی را ایجاد کند که فرد را در پیشرفت زندگی اجتماعی آینده شغلی و تحصیلات مقاطع بالاتر یاری کنند مدل سازی ریاضی با ایجاد شرایطی میتواند آموزش گران را در رسیدن به این اهداف یاری کند .در مدل سازی افراد به تغییر یک موقعیت واقعی و طراحی یک مدل ریاضی می پردازند.مدل های ریاضی با اهداف مختلفی مورد استفاده قرار می گیرند که از این بین می‌توان اهداف به اقتصادی و محیطی که به عنوان منبع اصلی برای تصمیم گیری در سطوح مختلف اجتماعی استفاده می شونداشاره کرد(هانت، ۲۰۰۷).استفاده از مدل های ریاضی در کلاس درس می تواند به فهم دانش آموزان در مورد چگونگی و چرایی یادگیری ریاضیات کمک کند تحقیق در مورد مدل سازی در آموزش ریاضی درتمامی کشورها به صورت بین المللی مورد توجه قرارگرفته است واین فعالیت از سال ۱۹۰۶ به طور جدی ترین پیگیری شد.(بلوم ،۱۹۹۵) .هدف اولیه در استفاده از مدل ها باید این موضوع باشد که به دانش آموزان در ساختن دانش ریاضی بر اساس دیدگاه شخصیتی شان کمک نماید. (گرامجر، ۱۹۹۴).

۱.۱. **اهداف تحقیق.** هدف از تحقیق حاضر ،بررسی تاثیر آموزش مدلسازی ریاضی و کاربرد آن در دنیای واقعی بر پیشرفت تحصیلی دانش آموزان در ریاضیات می باشد. در این تحقیق بر بهره گیری دانش آموزان از راهبردهای آموزش مدلسازی در کلاس درس ریاضی تاکید شده و سپس تاثیر آن بر پیشرفت تحصیلی درس ریاضی مورد بررسی قرار گرفته است. هدف دیگر این پژوهش،مقایسه تاثیر افزایش مهارت های مدلسازی در دانش آموزان ضعیف و متوسط بود.

۲.۱. **سوالات تحقیق.**

(۱) آیا گروهی که در برنامه آموزش راهبرد های آموزش مدلسازی شرکت می کنند ،نسبت به گروه کنترل که با روش سنتی آموزش می بینند ،نمره بیشتری در درس ریاضی کسب می نمایند؟

(۲) آیا تاثیر برنامه آموزش مهارت های مدلسازی بر دانش آموزان قوی متفاوت از دانش آموزان ضعیف و متوسط است، به عبارت دیگر،کدام دسته از دانش آموزان بهره بیشتری از برنامه آموزش مدلسازی می برند؟

۲. روش‌ها و ابزارها

۱.۲. **فرضیه پژوهش.** نمره ریاضی گروهی که در برنامه آموزش راهبرد های مدلسازی شرکت می کنند به طور معنا داری بیشتر از گروه کنترل است.

۲.۲. **روش پژوهش.** جامعه آماری این تحقیق دانش آموزان متوسطه اول پایه نهم شهرستان سیمرغ ۴۳۲ نفر می باشد . نمونه شامل ۱۱۰ دانش آموز (۵۵ پسر و ۵۵ دختر) پایه نهم می باشد که در چهار کلاس مشغول به تحصیل بودند. شیوه انتخاب بدین صورت بود که از هر کدام از مدارس دخترانه و پسرانه یک کلاس به طور تصادف به عنوان گروه آزمایشی و کلاس دیگر به عنوان گروه کنترل در نظر گرفته شد. گروه کنترل و آزمایشی هر مدرسه را معلمی واحد اداره می کرد تا عامل معلم کنترل شود. جدول زیر بیانگر عده آزمودنیهای هر گروه است:

جدول ۱: تعداد افراد نمونه

جنس گروه	دختر	پسر	جمع
آزمایشی	26	29	55
کنترل	26	29	55
جمع	52	58	110

برنامه در دو مرحله اجرا شد. ابتدا دو تن از معلمان پایه نهم (یک معلم مدرسه پسرانه ویک معلم مدرسه دخترانه) مورد

آموزش قرار گرفتند ودرباره مدلسازی ریاضی و نقش آن در پیشرفت تحصیلی ،چگونگی ارتقای فعالیت مدلسازی و کاربرد آن در دنیای واقعی در دانش آموزان مطرح شد. معلمان پس از آشنایی با اهداف تحقیق وموضوع آن درباره چگونگی اجرای روش آزمایشی در کلاس درس تمرین کردند و نمونه ای از این شیوه را حضور محقق اجرا کردند. در مرحله دوم برنامه که شش هفته به طول انجامید،معلمانی که با روش آموزش مدلسازی ریاضی و نحوه اجرای آن آشنا بودند ،آن را در کلاس درس خود)گروه های آزمایشی(به کار بردند. معلمان گرروه آزمایشی ابتدا دانش آموزان را به گرو های۴-۵ نفری تقسیم کردند به گونه ای که در هر گروه دانش آموز قوی ،متوسط و ضعیف وجود داشته باشد. معلم پس از ارائه درس که مطابق معمول صورت می گرفت برنامه آموزش مدلسازی ریاضی و کاربرد آن در دنیای واقعی را آغاز کرد. برنامه آموزش مدلسازی ریاضی در۲۰ دقیقه کلاسی اجرا شد و طی آن معلم برگه هایی که شامل مسائل و تمرینات مربوط به درس می شد را در اختیار گروه ها قرار داد. دانش آموزان با توجه به مطالب ارائه شده توسط معلم و با استفاده از دانسته های قبلی و تعامل و همفکری هم شروع به حل مسائل کردند و راه حل های خود را بررسی کردند. از دانش آموزان خواسته می شود که روش استدلال خود را در گروه توضیح دهند.در تمام این مدت معلم به عنوان راهنما بوده و به سوالات احتمالی دانش آموزان پاسخ می دهد. گروه کنترل مطابق روش سنتی آموزش می دیدند و هیچ گونه تغییر خاصی در برنامه آموزشی آنان ایجاد نشد.روش آزمایشی به مدت شش هفته)در طول ماه بهمن و اسفند (اجرا شد.

۳.۲. **ابزار پژوهش.** ابزار این تحقیق آزمون معلم ساخته ای بود که در پایان برنامه آموزشی از دانش آموزان هر دو گروه به عمل آمد. این آزمون از نوع معلم ساخته و پرسشها برای هر دو گروه کنترل و آزمایشی یکسان بود. به اعتقاد پینتریچ و دی گروت)(۱۹۹۰ آزمون های معلم ساخته بیشتر شبیه امتحانات معمولی مدارس هستند،به عنوان ابزار پژوهش مناسب تر از آزمون های استاندارد هستند. به منظور روایی و پایایی میان نمره گذاران ،برگه ها پس از تصحیح نمره گذار اول،در اختیار معلم دیگر قرار گرفت و مشاهده شد که توافق این دو نمره گذار۹۵٪ است.

از نمره ریاضی سال قبل دانش آموزان)خرداد ماه(به عنوان پیش آزمون استفاده شد تا تفاوتی که دانش آموزان از قبل در ریاضی داشته اند،کنترل شود.

۲.۴. **شیوه گردآوری و تجزیه و تحلیل داده ها.** برای مقایسه کردن میانگین نمره ریاضی گروه آزمایشی و گروه کنترل و هم چنین برای مقایسه کردن میانگین نمرات دانش آموزان دختر و پسر یا مقایسه کردن میانگین نمرات دانش آموزان قوی و ضعیف از آزمون تی استفاده شد.

۳. نتایج

برای بررسی فرضیه اصلی تحقیق مبنی بر وجود تفاوت معنی دار میان میانگین نمرات پیشرفت تحصیلی ریاضی دانش آموزان گروه کنترل و آزمایشی، ابتدا نمرات ریاضی سال گذشته این دو گروه با استفاده از آزمون تی مورد استفاده قرار گرفت. نتیجه این مقایسه که در جدول زیر مشاهده می شود، بیانگر آن است که این دو گروه در قبلی درس ریاضی با یکدیگر مشابه هستند و تفاوت معنی داری با یکدیگر ندارند. پیشرفت

جدول ۲: آزمون تی برای مقایسه میانگین دو گروه در نمره قبلی درس ریاضی

گروه	عده	میانگین	انحراف معیار	مقدار تی	درجه آزادی	سطح معناداری
آزمایشی	55	32.42	3.48	0.38	116	0.00
کنترل	55	82.00	3.8			

نتیجه فوق بدان معنی است که در پایان آزمایش اگر تفاوتی میان دانش آموزان گروه کنترل و آزمایشی مشاهده شود، این تفاوت را می توان به تاثیر برنامه آموزشی و به عبارت دیگر ،به تاثیر آموزش مدلسازی نسبت داد. به همین دلیل ،میانگین دو گروه آزمایشی و کنترل در آزمون ریاضی پایان دوره آزمایشی با استفاده از آزمون تی مورد مقایسه قرار گرفت.

جدول ۳: آزمون تی برای مقایسه نمره تغییر سه گره قوی و متوسط و ضعیف

گروه	عده	میانگین	انحراف معیار	مقدار تی	درجه آزادی	سطح معناداری
قوی	11	0.59	0.27	7.98	116	0.00003
متوسط	16	1.25	0.25			
ضعیف	28	2.21	0.19			

۴. نتیجه‌گیری

یافته ها بیانگر تاثیر برنامه آموزشی مدلسازی بر پیشرفت تحصیلی درس ریاضی می باشد. همانطور که ملاحظه شد دانش آموزان ابتدا در گروه های ۵-۴ نفره به بحث و استدلال درباره راه حل ها می پرداختند و به کمک دانسته های قبلی و آموزش های معلم ،مسئله جدید را حل می کردند و جواب های هم را مقایسه می کردند. در این روش، معلم نقش راهنما و هدایت کننده را داشت و دانش آموزان به طور فعال در گروه ها با تعامل و همفکری به حل مسائل می پرداختند و در مقایسه با یادگیرندکان گروه کنترل که هیچ گونه آموزش مدلسازی نداشتند، نمره بیشتری در امتحان ریاضی کسب کردند. افزایش نمرات ریاضی دانش آموزان گروه آزمایشی در حالی بود که این دانش آموزان زمان بیشتری را صرف یادگیری ریاضی در کلاس نمی کردند و مقدار و ساعت آموزشی آنان تغییر نکرده بود. این نتایج هماهنگ با پژوهش های موجود در زمینه مدلسازی است. یافته ها نشان می دهد که با آموزش مدلسازی می توان به دانش آموزان کمک کرد تا در یادگیری ریاضی فعال تر باشند و به درک بیشتر نایل آیند. در این روش همانطور که بیان شد یادگیرندگان دانش را خودشان بنا می کنند پیشنهاد می شود معلمان ریاضی با توجه به رویکرد کتاب های درسی که بر اساس فعالیت هایی کاربردی از زندگی روزمره است موقعیت های یادگیری را طوری فراهم کنندکه دانش آموزان در گرو ه های مختلف با موضوع درسی کتاب یا مسائل مربوطه رو به رو شوند. در واقع نقش معلم ،ایجاد چالش در تفکرات دانش آموز ان است.(دوفی و جانسون ۱۹۹۶).

مراجع

[۱] انگلیش، لین؛ وارن، الیزابت، *معرفی متغیر از طریق الگویابی*، ترجمه ی سهیال غالم آزاد، آموزش ریاضی ۵۴ ،دفتر انتشارات کمك آموزشی، ۱۳۸۰.

[۲] رفیع پور، ابوالفضل؛ گویا، زهرا گویا، *چرایی و چگونگی آموزش هندسه در برنامهی درسی ریاضی مدرسه‌ای*، مجله آموزش ریاضی، ۱۳۸۶.

[۳] علم الهدایی و همکاران، *تاثیر مسائل مدل سازی ریاضی بر تجربه های شوق دانش آموزان*، ۱۳۹۹.

[۴] علم الهدایی و همکاران، *ظرفیت مدلسازی مسائل مدلسازی برای تغییر نگرش دانش آموزان نسبت به ریاضی*، ۱۳۹۶.

[۵] فرود نتال، هانس، *مسائل تحقیقی در آموزش ریاضی*، ترجمه ی زهرا گویا، نشر اثر اصلی ۲۸۹۱.رشد آموزش ریاضی، ۱۳۸۰.

مدرسه شهابی سیمرغ

E-mail address: fyosefzade141@gmail.com

دلتان شاد

لبتان خندان